CHINHOYI UNIVERSITY OF TECHNOLOGY

INSTITUTE OF MATERIALS SCIENCE, PROCESSING AND ENGINEERING TECHNOLOGY

DEPARTMENT OF MATERIALS SCIENCE AND ENGINEERING

Design and Fabrication of Chiral Photoelectrodes for the Generation of Hydrogen through Photoelectrocatalytic Water Splitting

Rufaro Brenda Kawondera
(C21144165L)

Supervisors: Prof W. Mtangi
Dr S. Nyoni
Prof G. Mehlana

A THESIS SUBMITTED IN FULFILMENT OF THE REQUIREMENTS THE DEGREE OF DOCTOR OF PHILOSOPHY IN MATERIALS SCIENCE AND ENGINEERING

July 2024

Approval Form

The doctoral thesis entitled: "**Design and Fabrication of Chiral Photoelectrodes for the Generation of Hydrogen through Photoelectrocatalytic Water Splitting**," submitted by Rufaro B. Kawondera meets the regulations governing the award of Doctor of Philosophy in Materials Science and Engineering at Chinhoyi University of Technology and is approved for its contribution to knowledge and literary presentation.

10/07/2024

(Signature of Main Supervisor) Date

Declaration

I, Rufaro Brenda Kawondera (C21144165L), do hereby declare to Chinhoyi University of Technology that the thesis entitled, "**Design and Fabrication of Chiral Photoelectrodes for the Generation of Hydrogen through Photoelectrocatalytic Water Splitting"** is my original work and has never been submitted to any other university for academic award. All other sources of material used have been duly acknowledged and referenced.

10/07/2024

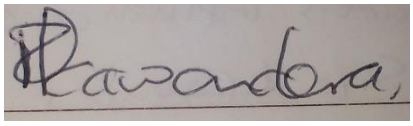

(Signature of student) Date

Dedication

This thesis is dedicated to my late maternal grandparents, Mr and Mrs Chiwashira.

Acknowledgements

Firstly, I would like to thank the Lord God Almighty for giving me the strength to carry out this study. I am very grateful to my main supervisor, Professor W. Mtangi for affording me the opportunity to carry out this PhD project, for working industriously and providing funding, expert academic assistance and most importantly teaching me how to think logically and scientifically.

Thanks also go to Dr S. Nyoni for helping me and for your patience, this project would not be possible without your kindest help.

I would also like to thank Prof G. Mehlana (MSU), his great knowledge in material synthesis and characterization is greatly appreciated. I would like to thank members of the Department of Chemical Sciences at Midlands State University for welcoming and embracing me during my research visits. Many thanks go to the members of the CO_2 Project Research Group at MSU, for their assistance during my research visits.

Special thanks go to Prof. C. Fontanesi (University of Modena*)*, Prof Massimo and Marco (University of Florence*)* for their assistance, patience and for pushing me to a better academic.

I would also like to thank Prof Makhubela and Pamela, Department of Chemical Sciences University of Johannesburg for assistance with ICP-OES measurements.

Many thanks go to the following organizations for the different grants and awards:

1. Green Chemistry for Life
2. Chinhoyi University of Technology, Vice-Chancellor' Scholarship of Excellence
3. Green Sciences for Sustainable Development Foundation
4. International Union of Crystallography
5. International Center for Diffraction Data
6. Fondazzione Alessandro Volta

Chinhoyi University of Technology Management, Materials Science and Engineering staff, The Innovation Hub staff members as well as the Chemistry department members, I am grateful for all the academic and moral support you rendered effortlessly throughout my studies.

Lastly, to my mother, siblings and nephews who never understood why I had to leave home, thank you for your support and patience.

List of conferences attended and posters/talks presented

1. Chinhoyi University of Technology Research Day, April 2021 (Oral)

   Chiral photoelectrodes for efficient generation of hydrogen through water splitting.

2. 13th Green Chemistry Summer School Online July 2021 (Oral + Poster)
   Chiral photoelectrodes for efficient generation of hydrogen through photoelectrocatalytic water splitting.

3. 14th Green Chemistry Summer School. Venice, Italy July 2022 (Oral + Poster)
   Chiral metal organic frameworks in photoelectrocatalytic water splitting
4. 3rd Pan African Conference on Crystallography Nairobi, Kenya. January 2023 (Oral)
   Novel amine functionalized Metal Organic Framework for photoelectrocatalytic water splitting.
5. 5th Chinhoyi University of Technology International Conference February 2023. Chinhoyi, Zimbabwe (Oral)
   Application of an Iron based Metal Organic Framework and its chiral derivatives in photoelectrocatalytic water splitting.

6. 3rd International School on Porous Materials: MOFschool2023 June 2023, Como, Italy (Poster).
   Enhanced Water splitting capabilities of L-Cysteine doped Metal Organic Frameworks
7. Chinhoyi University of Technology Residence week February 2024, Chinhoyi, Zimbabwe.
   Design and Fabrication of chiral electrodes for generation of hydrogen through photoelectrocatalytic water splitting (Oral).
8. MOF Global Seminar, 1 July 2024, Virtual
   Chiral doped MOFs for photoelectrocatalytic water splitting (Oral).

List of Publications

1. **Kawondera R.,** Bonechi M., Maccioni I., Giurlani W., Salzillo T., Venuti E., Mishra D., Fontanesi C., Innocenti M., Mehlana G., Mtangi W., (2023), Chiral “doped” MOFs: an electrochemical and theoretical integrated study, *Frontiers in Chemistry* (11) DOI=10.3389/fchem.2023.1215619
2. Bonechi M., Bettoni D., Maccioni I., Biffoli F., Giurlani W., Salzillo T., **Kawondera R**., Mtangi W., Fontanesi C. and Innocenti M., (2023) An Electrochemical and Spectroscopic Characterization of Chiral MIL-53(Fe) Metal-Organic Framework *ECS - The Electrochemical Society ECS Meeting Abstracts*, Volume MA2023-01, E02: Electrodeposition for Advanced Manufacturing DOI 10.1149/MA2023-01221562mtgabs
3. **Kawondera R.B**., Nyoni S., Mehlana G., Bonechi M., Mishra D., Fontanesi C., Innocenti M., Mtangi W., (2024) Chiral Metal Organic Framework Decorated Photoelectrodes for Photoelectrocatalytic Water Splitting, *ChemElectroChem*, Under Review

Abstract

The prevailing energy challenges, compounded by depletion of non-renewable resources and the effects of climate change, have resulted in the global community investing in renewable and sustainable energy. Green hydrogen stands out as a favourite candidate owing to its higher energy density and a benign combustion by-product (water), which can be further split to produce more hydrogen, thereby creating a hydrogen circular economy. The principle of the Chirality Induced Spin Selectivity (CISS) effect, which states that electron spin control is introduced in chiral photocatalysts, brings new prospects to photoelectrocatalytic water splitting. In this work, the synthesis and application of Iron (MIL 53) as well as Zinc (Zn (bdc)(bpcda)) based Metal Organic Frameworks (MOFs) and their chiral derivatives suitable for hydrogen generation through photoelectrocatalytic water splitting in the visible range is discussed. Characterization using: Nuclear Magnetic Resonance (NMR), Fourier Transform Infrared Spectroscopy (FTIR), Powder X-Ray Diffraction Spectroscopy (PXRD), Thermogravimetric Analysis (TGA), Scanning Electron Microscopy coupled with Energy Dispersive Spectroscopy (SEM-EDS), Field Emission Scanning Electron Microscopy (FESEM) and UV-vis Spectroscopy has been carried out to confirm the: completion of reaction in synthesis, functional groups, phases, thermal stability, surface morphology, elemental analysis as well as the photocatalytic activity of the MOFs. The parent MOFs, were doped using R- (-) and S- (+) camphor sulphonic acid as well as L-Cysteine. The synthesized MOFs have been found to have better absorbances in the visible range, making them suitable for utilising the available radiation within the solar spectrum. The photoelectrocatalytic activities of the synthesized MOFs, have been evaluated using electrochemical techniques including: Cyclic voltammetry, Linear sweep voltammetry and Chronoamperometry under illumination with an AM 1.5 G Solar simulator. The chiral MOFs demonstrate higher current densities under illumination. Results revealed production of greater current densities in chiral doped MOFs with the iron-based MOFs producing larger current densities than the zinc-based MOFs. Mixed-metal MOFs were synthesized by incorporation of nickel and cobalt into the MOF framework, as post synthesis modification of Zn-MOF, a tandem device incorporating α-Fe_2O_3 nanoparticles was also fabricated, this was meant to address the low current densities observed in the zinc-based MOFs. Remarkable improvement in the current densities has been observed in the mixed-metal MOFs as well as the tandem device. Evaluation of the effect of the chiral MOFs on the overpotential of photoelectrodes was done using Tafel plot analysis, it has been observed that the iron-based MOFs have lower overpotentials compared to the zinc-based MOFs. The introduction of the α-Fe_2O_3 nanoparticles further reduces the overpotential. This can be attributed to the ferromagnetic nature of the iron that is present in MIL 53 and α-Fe_2O_3. The improved water splitting capabilities observed for ferromagnetic and chiral MOFs

has been attributed to the Chirality Induced Spin Selectivity (CISS) effect whereby chiral and/or ferromagnetic photoelectrodes have the ability to control the spin of transmitted electrons. When the electrons are spin filtered, production of triplet oxygen is enhanced, thereby minimizing the production of hydrogen peroxide and resulting in improved hydrogen yield. From the results of this study, it has been observed that the introduction of chiral moieties in the metal organic framework greatly improves the performance of the photoelectrochemical cell by minimizing production of hydrogen peroxide. These results indicate the importance of controlling the spin of electrons in the efficiency of artificial photosynthesis in producing green hydrogen.

Abbreviations and symbols

PEC	Photoelectrochemical Cell
CISS	Chiral Induced Spin Selectivity
NHE	Normal Hydrogen Electrode
SHE	Standard Hydrogen Electrode
HER	Hydrogen Evolution Reaction
OER	Oxygen Evolution Reaction
PV	Photovoltaic
FTIR	Fourier Transform Infrared Spectroscopy
SEM	Scanning Electron Microscopy
FESEM	Field Emission Scanning Electron Microscopy
PXRD	Powder X-Ray Diffraction Spectroscopy
UV-Vis	Ultra-Violet-Visible Spectroscopy
Uv-DRS	Ultra-Violet Diffuse Reflectance Spectroscopy
FTO	Fluorine-Doped Tin Oxide
ITO	Indium-Doped Tin Oxide
EDS	Energy Dispersive Spectroscopy
LSV	Linear Scan Voltammetry
CV	Cyclic Voltammetry
OCP	Open Circuit Potential
EIS	Electrochemical Impedance Spectroscopy
MOF	Metal Organic Framework
MM-MOF	Mixed-Metal Metal Organic Framework
bdc	benzene-1,4-dicarboxylic acid

DMF	Dimethylformamide
R-CSA	R- Camphor Sulphonic Acid
S-CSA	S-Camphor Sulphonic Acid
SE	Secondary Electrons
BSE	Back Scattered Electrons
EPD	Electrophoretic Deposition
CCDC	Cambridge Crystallographic Data Centre
CSD	Cambridge Structural Database
GCE	Glassy Carbon Electrode
WE	Working Electrode
CE	Counter Electrode
RE	Reference electrode
R_s	electrolyte resistance
R_{ct},	Charge transfer resistance
R_w	Warburg resistance
C_{dl}	Double layer capacitance

Table of contents

CONTENTS

List of Figures

List of schemes

List of tables

1 INTRODUCTION

1.1 BACKGROUND OF THE STUDY

The marked increase in global population and the zeal of the global community to go green; for instance, the adoption of the electric vehicle has added the burden on the global energy grid to cope with energy demands. Currently, the world derives the majority of its energy from non-renewable energy sources, mainly fossil fuels (Holechek et al., 2022). According to British Petroleum, the main sources of energy are oil (32.8%), Natural gas (20.7%) and coal (25.5%) and all these are fossil based and not renewable.

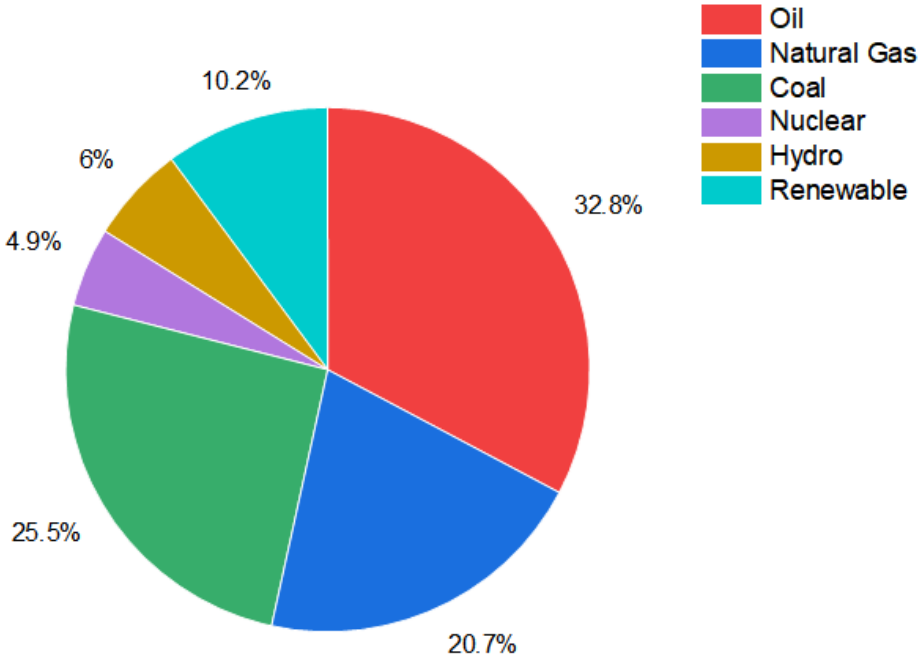

Figure 1.1: Current energy sources as of 2019 (BP Energy Outlook, 2023)

The scarcity of economic and sustainable alternative energy generation technologies, coupled with higher energy demands results in more fossil fuels being utilized, resulting in an increasing greenhouse gas being emitted. There has been a dramatic increase the anthropogenic greenhouse gas emitted owing to industrialization and this has been blamed for the adverse climate changes. The use of fossil carbon sources in the energy, industry and

transport sectors has led to increased atmospheric concentrations of CO_2, CH_4 and N_2O (Jones et al., 2023).

1.1.1 What are greenhouse emissions?

Greenhouse emissions refer to the release of greenhouse gases into the atmosphere. These gases, which include carbon dioxide (CO_2), methane (CH_4) and nitrous oxide (N_2O), and fluorinated gases, trap heat from the sun and contribute to the greenhouse effect, leading to global warming and climate change (Jones et al., 2023).

The sources of greenhouse emissions include burning fossil fuels for energy, industrial processes, agriculture, deforestation, and waste management. The increase in these emissions is one of the primary drivers of the current climate crisis. Although the ggreenhouse emissions are made up of different gases, the most important is CO_2 because it remains in the atmosphere, longer than the others (Jones et al., 2023).

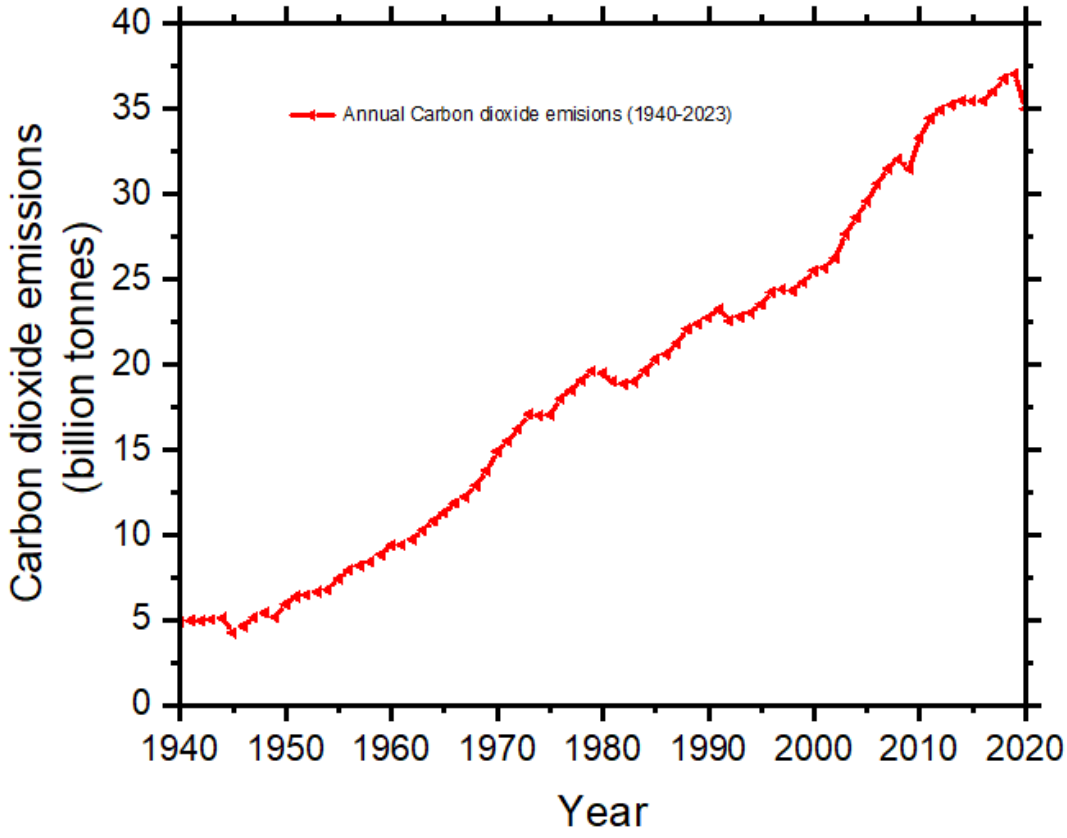

Figure 1.2: Annual carbon dioxide emissions (in billion tonnes)

Source : (Friedlingstein et al., 2023)

1.1.2 Climate change induced natural disasters

The current adverse climate change effects, driven by greenhouse gas emissions have become a major concern to all human-kind. The effects of climate change on human life are promising to have tremendous consequences. According to the World Metrological Organization, weather related disasters have increased five-fold over the past fifty years and they are expected to increase (WMO Atlas, 2021). The weather related disasters vary from storms for instance Hurricane Katrina (USA, 2005) and Cyclone Idai (Mozambique and Zimbabwe, 2019) to landslides (Philippines, 2006) and extreme temperature conditions classified as heatwaves (Europe, 2003) (WMO Atlas, 2021).

Table 1.1: Summary of weather induced human and capital cost between 1970 and 2019 Source: (WMO Atlas, 2021).

Region	Recorded weather induced disasters	Lives lost	Estimated economic loss (US$)
Africa	1695	731747	5 billion
Asia	3454	975622	2 trillion
South America	867	34854	39.2 billion
North America, Central America and the Caribbean	1977	74839	1.7 trillion
South-West Pacific	1407	65391	163.7 billion
Europe	1672	159438	476.5 billion

The results shown in table 1.1 have motivated fervent research into alternative, sustainable renewable energy sources. As a result, current trends in energy sources are moving towards green and clean energies such as wind, geothermal, hydropower and solar energy; particularly in how solar energy can be utilised in obtaining green hydrogen.

Hydrogen is a clean source of energy with a high energy-to-mass ratio compared to all other fuel sources (Gielen et al., 2019) and is regarded as the fuel for the future. Researchers project hydrogen to be the most dominant fuel beyond the 2050s (Espegren et al., 2021; Holechek et al., 2022; Staffell et al., 2019). Hydrogen is favorable as it can be recycled, as well, through its benign combustion, which produces water. The usage of hydrogen as a fuel requires its

production to be done efficiently and economically. This scenario results in a hydrogen circular economy, where the source of fuel is water, and burning the fuel produces water.

One way of producing green hydrogen is through photoelectrocatalytic water splitting. Photoelectrocatalytic water splitting harvests the solar energy and stores it as hydrogen energy (Landman et al., 2017). Indeed, hydrogen can be obtained from the electrolysis of water, but in a very energy consuming process, hence the need to find cheaper routes of producing the hydrogen. Data published by NASA shows that on average the earth receives 4.4×10^{16} Watts of solar energy per annum (Ward, 2005.), while it takes 237 KJ to produce one mole of hydrogen (Hisatomi et al., 2014).

In 1972, Fujishima and Honda demonstrated that water can be split into hydrogen and oxygen (Fujishima & Honda, 1972), and since then, significant research towards photoelectrochemical water splitting has been made. Technologies for hydrogen generation, from the steam forming of methane, (Ávila-Neto et al., 2009; Chen et al., 2011) electrolysis of water and photoelectrochemical (PEC) water splitting exist (Ehlers et al., 2023; Jin et al., 2023; Xu et al., 2022). However, these processes involve a significant overpotential, rendering them uneconomic and inefficient; as such limiting their widespread use. The overpotential represents a kinetic barrier for the electron transfer process and is sensitive to the electrode and/or photocatalyst material; as such, major efforts in the area of water splitting has led to research aimed at the discovery and development of useful and superior photocatalysts (Bhartiya et al., 2022; Feng et al., 2023; K. B. Ghosh et al., 2019; S. Ghosh et al., 2020; Mtangi et al., 2015, 2017; Zhang et al., 2018, 2021).

Nature has also given us a cue, water splitting is an efficient process used by green plants, during photosynthesis. In nature, the components responsible for water oxidation in the natural process, e.g., the cytochrome are chiral and it has been demonstrated through studies by Carmeli, and co-workers that electron transmission through photosystem I is spin selective (Carmeli et al., 2014). Chirality exists when the mirror image reflection of a configuration at an sp^3-hybridized center cannot be superimposed, on the original (Roos & Roos, 2015) .

The use of chiral systems either as electrode or electrolyte has been noted to increase the efficiency of the photoelectrochemical cell by minimizing hydrogen peroxide formation, through a phenomenon called the Chiral Induced Spin Selectivity (CISS) effect (Gazzotti et al., 2018, 2020; K. B. Ghosh et al., 2019; S. Ghosh et al., 2020; Mtangi et al., 2017; Waldeck et al., 2021; Zhang et al., 2018, 2021). According to the CISS effect, electrons moving through a chiral photocatalyst become spin polarised, i.e., there is a preference to have the spin aligned either parallel or antiparallel to the electron's velocity. This spin filtering is also observed in ferromagnetic materials (Naaman et al., 2019).

Metal Organic Frameworks (MOFs) are porous materials in which metal centres are held together by organic linkers (Furukawa et al., 2013; Yaghi et al., 2003). MOFs have attracted attention because of their large surface area, porosity and tuneability as well as post synthetic modification. These properties promote the use of MOFs in gas sensing and adsorption, energy storage as well as catalysis (Ma et al., 2019) .

This study, looks at the fabrication and characterization of chiral Metal Organic Framework based photoelectrodes for use in photoelectrocatalytic water splitting. Chirality was induced by incorporating (1R)- (-)- 10-Camphor Sulphonic Acid and 1S-(+)- 10-Camphor Sulphonic Acid as well as L-Cysteine into the MOF framework as part of the linker MOFs. The metals iron and zinc were selected as the preferred metal centres because they have been used in water splitting before and they are relatively abundant.

1.2 PROBLEM STATEMENT

The use of non-renewable fossil fuels has resulted in the emission of dangerous greenhouse gases such as CO, CO_2, SO_x and NO_x which have been blamed for the adverse effects of climate change. Water splitting is an attractive method for producing green hydrogen but its economic application remains in the future owing to high overpotentials associated with the process.

1.3 AIM

The project seeks to design and fabricate chiral Metal Organic Frameworks (MOFs) based photoelectrodes for hydrogen production in photoelectrocatalytic water splitting**.**

1.4 OBJECTIVES

The objectives of the work were:

a) To synthesize and characterize chiral Metal Organic Frameworks for use in photoelectrocatalytic water splitting
b) To fabricate chiral photoelectrodes for use in the photoelectrochemical cell.
c) To evaluate the electrochemical properties of the chiral photoelectrodes.
d) To evaluate the effectiveness of the chiral photoelectrodes in water splitting by quantifying the amount of hydrogen peroxide produced.
e) To quantify the amount of hydrogen produced during photoelectrocatalytic water splitting.

1.5 PURPOSE OF THE STUDY

The primary purpose of the study was to design and fabricate chiral Metal Organic Framework-based photoelectrodes for use in photoelectrocatalytic water-splitting.

1.6 RESEARCH HYPOTHESIS

The use of MOF-based chiral photoelectrodes in a photoelectrochemical cell can improve the efficiency of photoelectrocatalytic water splitting by minimizing the amount of hydrogen peroxide formed.

1.7 RESEARCH QUESTIONS

1. Can chiral Metal Organic Frameworks be synthesized for use in photoelectrocatalytic water splitting?
2. What is the effect of using chiral photoelectrodes on the amount of hydrogen peroxide formed during water splitting?
3. What is the yield of hydrogen produced from photoelectrocatalytic water using chiral MOF-based photoelectrodes?
4. Does the use of chiral photoelectrodes improve the efficiency of the water splitting process?

1.8 LIMITATIONS

Due to unavailability of equipment some tests such as Brunauer−Emmett−Teller (BET), to evaluate the total surface area and pore size of the chiral MOFs were not done.

1.9 DELIMITATIONS

For this research, the photoelectrocatalytic water splitting measurements were not carried under direct sunlight. Measurements were carried out under simulated solar conditions using an A.M 1.5 G solar simulator.

1.10 THIS THESIS

This works seeks to provide new insight into the oxygen evolution reaction mechanisms from the perspective of electron spin control using chiral and ferromagnetic photocatalytic systems. Chiral MOFs will be synthesised and deposited on the glass conducting substrate (FTO) to fabricate the chiral photoelectrodes which will then be used in photoelectrocatalytic water splitting.

In chapter 2 of the thesis, current knowledge on photoelectrocatalytic water splitting, synthesis and characterization of metal organic frameworks, application of Metal of Organic Frameworks

in photoelectrocatalytic water splitting as well the characteristics of the selected MOFs will be explored in an extensive literature review.

Chapter 3 covers the experimental section, the materials and methods used in synthesis and characterization of the chiral MOFs as well as the fabrication and application of the chiral photoelectrodes in water splitting.

Chapter 4 will present and discuss the results on synthesis and characterization of the Zn-MOF as well as the fabrication of the chiral photoelectrodes based on the Zn-MOF including their performance in photoelectrocatalytic water splitting.

Chapter 5 will present and discuss the results on synthesis and characterization of the MIL 53 as well as the fabrication of the chiral photoelectrodes based on the MIL 53 (Fe) including their performance in water splitting.

Chapter 6 will present and discuss the results from the remedial action taken from the results obtained from the water splitting experiments.

Chapter 7 will give recommendations for further studies as well as conclusions on the study.

Chapter 8 gives the Appendices.

1.11 REFERENCES

1) Ávila-Neto, C. N., Dantas, S. C., Silva, F. A., Franco, T. V., Romanielo, L. L., Hori, C. E., & Assis, A. J. (2009). Hydrogen production from methane reforming: Thermodynamic assessment and autothermal reactor design. Journal of Natural Gas Science and Engineering, 1(6). https://doi.org/10.1016/j.jngse.2009.12.003
2) Bhartiya, P. K., Srivastava, M., & Mishra, D. (2022). Chiral-induced enhanced electrocatalytic behaviour of cysteine coated bifunctional Au–Ni bilayer thin film device for water splitting application. *International Journal of Hydrogen Energy*, *47*(100), 42160–42170. https://doi.org/10.1016/j.ijhydene.2021.08.219
3) BP. (2023). *BP Energy Outlook 2023 Edition*, 16-18 https://www.bp.com/content/dam/bp/business-sites/en/global/corporate/pdfs/energy-economics/energy-outlook/bp-energy-outlook-2023.pdf
4) Carmeli, I., Kumar, K. S., Heifler, O., Carmeli, C., & Naaman, R. (2014). Spin Selectivity in Electron Transfer in Photosystem I. *Angewandte Chemie*, *126*(34), 9099–9104. https://doi.org/10.1002/ange.201404382
5) Chen, Y. M., Zhao, Y. C., Zhang, J. Y., & Zheng, C. G. (2011). Thermodynamic and kinetic analyses for hydrogen production via methane autothermal reforming. *Ranliao Huaxue Xuebao/Journal of Fuel Chemistry and Technology*, *39*(8).
6) Ehlers, J. C., Feidenhans'l, A. A., Therkildsen, K. T., & Larrazábal, G. O. (2023). Affordable Green Hydrogen from Alkaline Water Electrolysis: Key Research Needs from an Industrial Perspective. In *ACS Energy Letters* (Vol. 8, Issue 3). https://doi.org/10.1021/acsenergylett.2c02897
7) Espegren, K., Damman, S., Pisciella, P., Graabak, I., & Tomasgard, A. (2021). The role of hydrogen in the transition from a petroleum economy to a low-carbon society. *International Journal of Hydrogen Energy*, *46*(45), 23125–23138. https://doi.org/10.1016/j.ijhydene.2021.04.143
8) Feng, T., Chen, W., Xue, J., Cao, F., Chen, Z., Ye, J., Xiao, C., & Lu, H. (2023). Spin Polarization of Chiral Amorphous Fe-Ni Electrocatalysts Enabling Efficient Electrochemical Oxygen Evolution. *Advanced Functional Materials*, *33*(27), 1-10. https://doi.org/10.1002/adfm.202215051
9) Friedlingstein, P., O'Sullivan, M., Jones, M. W., Andrew, R. M., Bakker, D. C. E., Hauck, J., Landschützer, P., Le Quéré, C., Luijkx, I. T., Peters, G. P., Peters, W., Pongratz, J., Schwingshackl, C., Sitch, S., Canadell, J. G., Ciais, P., Jackson, R. B., Alin, S. R., Anthoni, P., … Zheng, B. (2023). Global Carbon Budget 2023. *Earth System Science Data*, *15*(12), 5301–5369. https://doi.org/10.5194/essd-15-5301-2023

10) Fujishima, A., & Honda, K. (1972). Electrochemical photolysis of water at a semiconductor electrode. *Nature*, *238*(5358), 37-38, https://doi.org/10.1038/238037a0
11) Furukawa, H., Cordova, K. E., O'Keeffe, M., & Yaghi, O. M. (2013). The chemistry and applications of metal-organic frameworks. In *Science* (Vol. 341, Issue 6149). https://doi.org/10.1126/science.1230444
12) Gazzotti, M., Arnaboldi, S., Grecchi, S., Giovanardi, R., Cannio, M., Pasquali, L., Giacomino, A., Abollino, O., & Fontanesi, C. (2018). Spin-dependent electrochemistry: Enantio-selectivity driven by chiral-induced spin selectivity effect. *Electrochimica Acta*, *286*, 271–278. https://doi.org/10.1016/j.electacta.2018.08.023
13) Gazzotti, M., Stefani, A., Bonechi, M., Giurlani, W., Innocenti, M., & Fontanesi, C. (2020). Influence of Chiral Compounds on the Oxygen Evolution Reaction (OER) in the Water Splitting Process. *Molecules*, *25*(17). https://doi.org/10.3390/molecules25173988
14) Ghosh, K. B., Zhang, W., Tassinari, F., Mastai, Y., Lidor-Shalev, O., Naaman, R., Möllers, P., Nürenberg, D., Zacharias, H., Wei, J., Wierzbinski, E., & Waldeck, D. H. (2019). Controlling Chemical Selectivity in Electrocatalysis with Chiral CuO-Coated Electrodes. *Journal of Physical Chemistry C*, *123*(5), 3024–3031. https://doi.org/10.1021/acs.jpcc.8b12027
15) Ghosh, S., Bloom, B. P., Lu, Y., Lamont, D., & Waldeck, D. H. (2020). Increasing the Efficiency of Water Splitting through Spin Polarization Using Cobalt Oxide Thin Film Catalysts. *Journal of Physical Chemistry C*, *124*(41), 22610–22618. https://doi.org/10.1021/acs.jpcc.0c07372
16) Gielen, D., Boshell, F., Saygin, D., Bazilian, M. D., Wagner, N., & Gorini, R. (2019). The role of renewable energy in the global energy transformation. *Energy Strategy Reviews*, *24*, 38–50. https://doi.org/10.1016/j.esr.2019.01.006
17) Holechek, J. L., Geli, H. M. E., Sawalhah, M. N., & Valdez, R. (2022). A Global Assessment: Can Renewable Energy Replace Fossil Fuels by 2050? *Sustainability (Switzerland)*, *14*(8), 1-22. https://doi.org/10.3390/su14084792
18) Jin, H., Xu, J., Liu, H., Shen, H., Yu, H., Jaroniec, M., Zheng, Y., & Qiao, S. Z. (2023). Emerging materials and technologies for electrocatalytic seawater splitting. In *Science Advances* (Vol. 9, Issue 42). https://doi.org/10.1126/SCIADV.ADI7755
19) Jones, M. W., Peters, G. P., Gasser, T., Andrew, R. M., Schwingshackl, C., Gütschow, J., Houghton, R. A., Friedlingstein, P., Pongratz, J., & Le Quéré, C. (2023). National contributions to climate change due to historical emissions of carbon dioxide, methane, and nitrous oxide since 1850. *Scientific Data*, *10*(1). https://doi.org/10.1038/s41597-023-02041-1

20) Landman, A., Dotan, H., Shter, G. E., Wullenkord, M., Houaijia, A., Maljusch, A., Grader, G. S., & Rothschild, A. (2017). Photoelectrochemical water splitting in separate oxygen and hydrogen cells. *Nature Materials*, *16*(6), 646–651. https://doi.org/10.1038/nmat4876

21) Ma, M., Lu, L., Li, H., Xiong, Y., & Dong, F. (2019). Functional metal organic framework/SiO2 nanocomposites: From versatile synthesis to advanced applications. In *Polymers* (Vol. 11, Issue 11). MDPI AG. https://doi.org/10.3390/polym11111823

22) Mtangi, W., Kiran, V., Fontanesi, C., & Naaman, R. (2015). Role of the Electron Spin Polarization in Water Splitting. *Journal of Physical Chemistry Letters*, *6*(24), 4916–4922. https://doi.org/10.1021/acs.jpclett.5b02419

23) Mtangi, W., Tassinari, F., Vankayala, K., Vargas Jentzsch, A., Adelizzi, B., Palmans, A. R. A., Fontanesi, C., Meijer, E. W., & Naaman, R. (2017). Control of Electrons' Spin Eliminates Hydrogen Peroxide Formation during Water Splitting. *Journal of the American Chemical Society*, *139*(7), 2794–2798. https://doi.org/10.1021/jacs.6b12971

24) Naaman, R., Paltiel, Y., & Waldeck, D. H. (2019). Chiral molecules and the electron spin. *Nature Reviews Chemistry*, *3*(4), 250–260. https://doi.org/10.1038/s41570-019-0087-1

25) Roos, G., & Roos, C. (2015). Isomers and Stereochemistry. *Organic Chemistry Concepts*, 43–54. https://doi.org/10.1016/B978-0-12-801699-2.00003-1

26) Staffell, I., Scamman, D., Velazquez Abad, A., Balcombe, P., Dodds, P. E., Ekins, P., Shah, N., & Ward, K. R. (2019). The role of hydrogen and fuel cells in the global energy system. In *Energy and Environmental Science* (Vol. 12, Issue 2, pp. 463–491). Royal Society of Chemistry. https://doi.org/10.1039/c8ee01157e

27) Waldeck, D. H., Naaman, R., & Paltiel, Y. (2021). The spin selectivity effect in chiral materials. *APL Materials*, *9*(4). https://doi.org/10.1063/5.0049150

28) Ward, A. (2005.). *NASA Facts The Balance of Power in the Earth-Sun System* pg1-6. www.nasa.gov

29) World Meteorological Organization. (2021). *WMO Atlas of Mortality and Economic Losses from Weather, Climate and Water Extremes (1970–2019)*. World Meteorological Organization

30) Xu, X., Shao, Z., & Jiang, S. P. (2022). High-Entropy Materials for Water Electrolysis. In *Energy Technology* (Vol. 10, Issue 11). https://doi.org/10.1002/ente.202200573

31) Yaghi, O. M., O'Keeffe, M., Ockwig, N. W., Chae, H. K., Eddaoudi, M., & Kim, J. (2003). Reticular synthesis and the design of new materials. *Nature*, *423*(6941), 705–714. https://doi.org/10.1038/nature01650

32) Zhang, W., Banerjee-Ghosh, K., Tassinari, F., & Naaman, R. (2018). Enhanced Electrochemical Water Splitting with Chiral Molecule-Coated Fe3O4 Nanoparticles. *ACS Energy Letters*, *3*(10), 2308–2313. https://doi.org/10.1021/acsenergylett.8b01454

33) Zhang, W., Wang, W., Hu, Y., Guan, H., & Hao, L. (2021). Take a cue from nature: Promoting electrocatalytic water splitting with a helping hand of hemoglobin. *International Journal of Hydrogen Energy*, *46*(5), 3504–3509. https://doi.org/10.1016/j.ijhydene.2020.10.154

2 LITERATURE REVIEW

2.1 INTRODUCTION

The current global climate and energy challenges have prompted research into renewable energy research with production of hydrogen from photoelectrocatalytic water splitting being identified as a potential solution. Hydrogen from photoelectrocatalytic water splitting, has been attractive because it does not only offer a cleaner production process with no emissions, through the use of abundant raw materials; sunlight and water, but has benign combustion by-products and offers the possibility of a circular economy.

This chapter introduces the basics of photoelectrocatalytic water splitting, the different methods of water splitting as well as the challenges associated with water splitting. It will also look at the electrochemical techniques, their principles, as well as their application in water splitting. An introduction to Metal Organic Frameworks (MOFs), the different types of linkers that are used in MOF synthesis, MOF synthesis and characterization techniques, as well as highlighting their advantages, is also presented. The synthesis and application of mixed- metal MOFs are also explored. The concept of Chiral Induced Selectivity (CISS) is introduced with a comprehensive review on chiral photoelectrodes being presented. Finally, photoelectrode architectures are explored, citing the advantages and applications of the different architectures.

2.2 WATER SPLITTING

2.2.1 Water Splitting in Nature

Water splitting into H_2 and O_2 is a multiple electron and multiple proton process that consist of half redox reactions as shown below.

Oxidation $4H_2O \rightarrow 4H^+ + O_2 + 4e^-$ (+1.23 V vs RHE) Equation 2.1

Reduction $4H^+ + 4e^- \rightarrow 2H_2$ (0 V vs RHE) Equation 2.2

Plants perform this conversion through natural photosynthesis. In photosynthesis, plants split water into oxygen and hydrogen ions. The hydrogen ion combines with CO_2 to form the carbohydrates, while the O_2 is released into the atmosphere as a gas. **Figure 2.1**, shows the schematic diagram of the photosynthesis process.

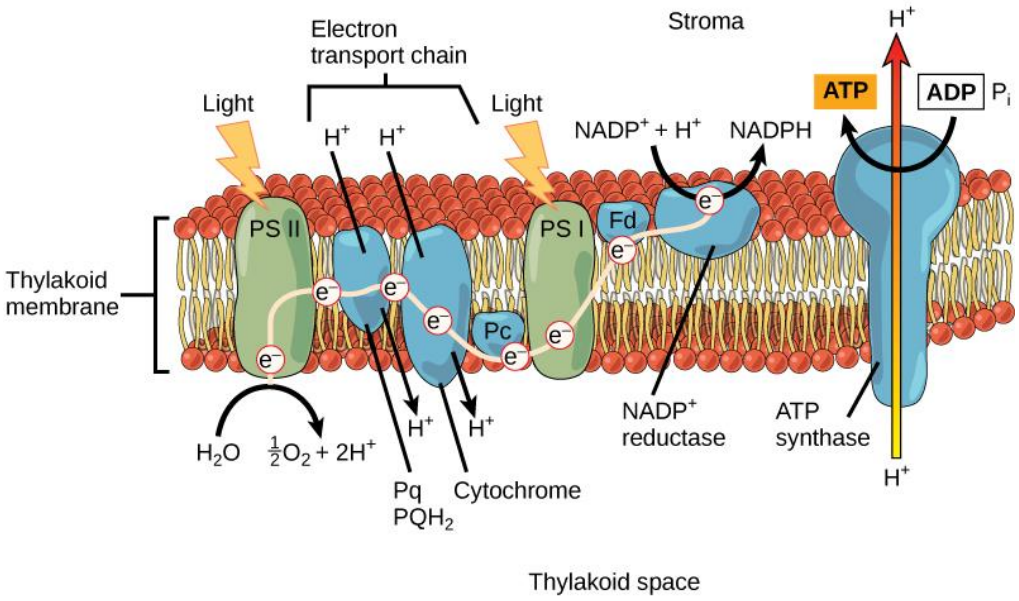

Figure 2.1: Scheme of PSII showing the light driven reactions of photosynthesis.

Source (Molnar & Gair, 2015)

Photosynthesis occurs in two stages. In the first stage, H_2O is oxidized to O_2, generating a proton (H^+) which gets bound to $NADP^+$ to give the energy carrier NADPH. In the second stage, the NADPH is used to reduce CO_2 to glucose. Light induced catalytic water splitting takes place on a metal complex which is embedded in a large membrane called Photosystem II (Cox et al., 2014). Photosystem II is made up of four Manganese atoms and one calcium atom which are joined by a network of oxygen bridges and is coordinated by a framework of surrounding amino acids (Cox et al., 2014). Water splitting occurs when the chlorophylls in P680 absorb light of wavelengths around 700 nm which leads to water oxidation producing four H^+ ions, an oxygen molecule, O_2 and four electrons (El-Khouly et al., 2017; Nocera, 2012). These electrons are transferred through the cytochrome b6f complex to PSI where H^+ ions are reduced. The two photon systems employed by plants is referred to as the z-scheme and is one way of achieving overall water splitting. The z-scheme is composed of hydrogen evolving photocatalyst on the oxygen evolving photocatalyst and an electron mediator (Kudo, 2011).

The fact that molecular oxygen is paramagnetic gives an indication that the electrons transferred through the b6f are spin polarized (Carmeli et al., 2014). Research has shown that electron transmission through the cytochrome is spin specific (Carmeli et al., 2014). As such, spin conservation plays an important part the efficiency of the water splitting process. An understanding of the mechanism behind the efficiency of natural photosynthesis is crucial for improving the artificial photosynthesis process. Successful mimicry of the natural process can guarantee efficiency of the artificial photosynthesis process.

2.2.2 Artificial Photosynthesis

Despite the demonstration by Fujishima and Honda that water can be split on a TiO_2 surface using UV light (Fujishima & Honda, 1972), several attempts have been made to generate hydrogen in an economic way, but with minimal success. The major challenge has been the fact that water splitting on TiO_2 and similar photocatalysts produce hydrogen peroxide which is a competing process to the hydrogen and oxygen evolution processes (Mtangi et al., 2017). Production of hydrogen using the artificial process (photoelectrochemical water splitting) has been observed to suffer from the need to supply an extra potential above the thermodynamically predicted value (1.23 V versus NHE), usually referred to as an over-potential of approximately 0.60 V versus NHE.

2.2.3 Photoelectrocatalytic water splitting

Water splitting is a process in which water is decomposed into hydrogen and oxygen, while photoelectrocatalytic water splitting is the conversion of abundant solar energy into clean and renewable hydrogen energy on a large scale (Z. Wang et al., 2019). This process takes place when a photocatalyst is irradiated with light possessing energy equal to or greater than the band gap of a semiconductor based photocatalyst (H. H. Mohamed, 2022), resulting in the excitation of an electron, which migrates from the filled valence band to the vacant conduction band. When the electron moves to the conduction band, a hole is created in the valence band as shown in **Figure 2.2**.

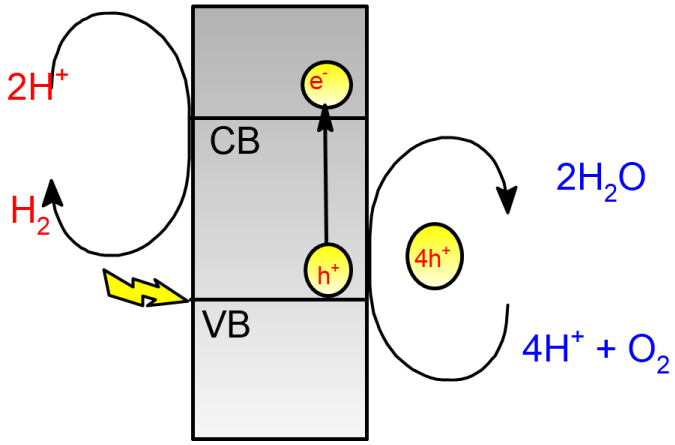

Figure 2.2: Processes taking place on the photoanode

The energy level at the bottom of the conduction band defines the reduction potential of the photoelectrons while the highest one of the valence band determines the oxidising power of photo-holes respectively (Serpone & Salinaro, 1999). The photo-generated electrons are involved in the reduction process while the holes are consumed in the oxidation process (Altaf et al., 2018).

To split water, a semiconducting photocatalyst should have a valence band with a more positive potential than H_2O/O_2 couple (1.23 eV) and a conduction band with a more negative potential than the H_2O/H_2 couple (0.00eV) (Altaf et al., 2018). Based on the above criterion several semiconductors have been identified for hydrogen evolution or oxygen evolution or both. Semiconductors such as TiO_2, $SrTiO_3$, $BaTiO_3$, $FeTiO_3$, ZrO_2 and ZnO whose conduction band potential lies above the proton reduction potential can reduce water to H_2 (Schumacher et al., 2024: H.Zhang et al., 2023). While Fe_2O_3, SnO_2 and WO_3 can oxidise water to H_2 (Al-Aisaee et al., 2023: Piccinin, 2019. A band gap of less than 3.00eV is required for an active visible light photocatalyst (Zhao et al., 2022). Different materials have been used as photocatalysts because their band gaps are suitable, with TiO_2, Fe_2O_3, $BiVO_4$, WO_3, ZrO_2, $KTaO_3$, and $SrTiO_3$ having been extensively studied (Jafari et al., 2016; Tee et al., 2017) .

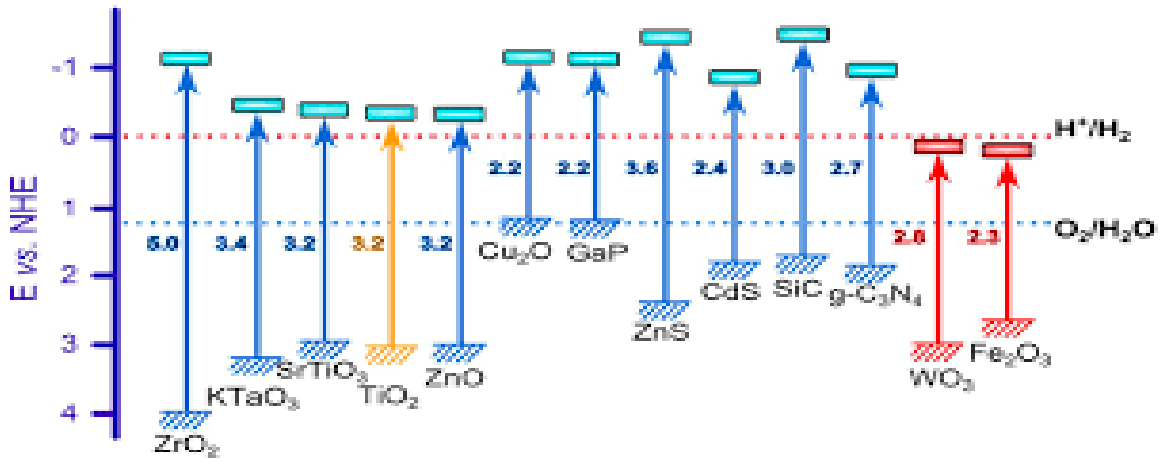

Figure 2.3: Band gap energies, conduction and valence band positions against the NHE potential at 0 pH of different semiconductors in relation to the redox potentials of water splitting. Source:(Samal & Das, 2023)

Figure 2.3 shows the band gap energies as well as conduction band positions of different semiconductor materials versus the NHE at pH of zero. For a photocatalyst to be used as a photoelectrode in a photoelectrochemical cell (PEC) water splitting device, it should meet critical requirements which include; but not limited to: a suitable band gap and appropriate valence and conduction band positions relative to the water oxidation and reduction potentials. A photoelectrode is a photoactive electrode that has the ability to convert incident photons into electron-hole pairs (Vilanova et al., 2024) . For some semiconductors/ photocatalysts such as SiC, ZnO and CdS; even though their band gaps fit well into the water splitting redox potential, they have not been used as photocatalysts because of their susceptibility to photo-corrosion. Photo-corrosion occurs when the anion from the photocatalyst is oxidised by the photogenerated holes instead of water (Nguyen et al., 2017).

2.2.4 The photoelectrochemical cell

Water splitting into H_2 and O_2 is a multiple electron and multiple proton process that consist of half redox reactions shown as Equation 2.1 and Equation 2.2 in section 2.1.

Equation 2.1 shows the oxygen evolution reaction while equation 2.2 shows the hydrogen evolution reaction. Photoelectrocatalytic water splitting takes place in a photoelectrochemical cell as shown in **Figure 2.4**.

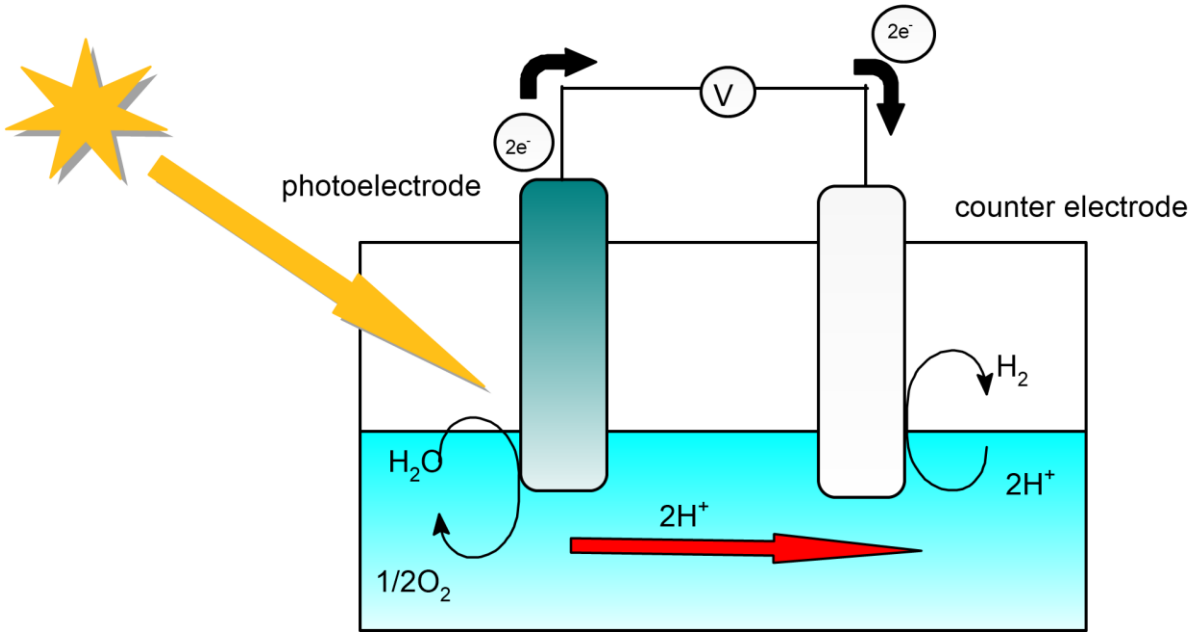

Figure 2.4: Photoelectrochemical Cell

The photoelectrochemical cell consists of a working electrode also known as the photoanode and the counter electrode. The photoanode is made up of the photocatalyst. Upon irradiation of the photoanode, redox reactions are initiated. The redox reactions take place in the PEC with oxidation taking place on the photoanode while reduction takes place on the counter electrode, to produce hydrogen.

2.2.5 Thermodynamics of water splitting

In terms of energy, water splitting is an uphill reaction that requires an external energy source to drive it, (Hisatomi et al., 2014) the Gibbs free energy increases by 237kJ/mol. The energy needed to drive photocatalytic and PEC water splitting is provided by sunlight. The theoretical maximum efficiency of solar energy conversion using a single photocatalyst increases with the wavelength available for the water splitting reaction. Since water is transparent to visible light, a light harvester is often employed (Sun et al., 2022).

2.2.6 Challenges associated with water splitting

The process of artificial photosynthesis faces a number of challenges which results in the reduced efficiency of the process. The challenges encountered during artificial photosynthesis include: high overpotential, hydrogen peroxide formation on surfaces as well as slow oxygen evolution.

2.2.6.1 Overpotential

Overpotential is defined as the difference between the equilibrium potential for a given reaction (also called the thermodynamic potential) and the potential at which the catalyst operates at a specific current under specific conditions (Appel & Helm, 2014). The origin of the overpotential has been meticulously studied through theoretical and experimental means, however, there is no clear indication of its exact origins (Mondal et al., 2018). One challenge facing water splitting research, is the fact that the mechanism behind the formation of the oxygen molecule is not well understood (Bozoglian et al., 2009; Jaque et al., 2007; Yamaguchi et al., 2012; X. Yang & Baik, 2008). Theoretical studies have suggested that the overpotential required for splitting water into hydrogen and oxygen comes from electrons' spin restrictions in forming the ground state triplet oxygen molecule (X. Yang & Baik, 2008). Researchers have suggested that when non- magnetic electrodes are used, oxygen can be produced only in an excited nonmagnetic state without violating the conservation of angular momentum, since neither water nor hydrogen is magnetic (Torun et al., 2013).

Results from theoretical and experimental studies have demonstrated the dependence of the OER, hence the overpotential on the magnetic properties of the anode material. **Figure 2.5.** below, shows the different type of electrodes and the overpotential that they exhibit.

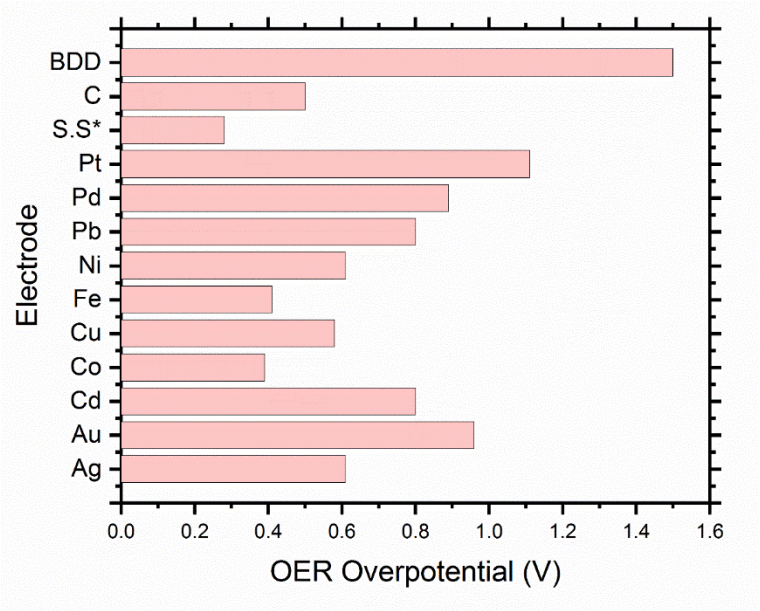

Figure 2.5: The OER overpotential of different electrode materials recorded in 1 Molar KOH in water at 25°C and J = 1mA/cm^2. (Adopted from (Heard & Lennox, 2020)

From **Figure 2.5.**, it can be observed that the overpotential is low for ferromagnetic electrodes, with cobalt (Co) and iron (Fe) having values of around 0.4 V. Stainless steel, (SS*) also shows a low overpotential of around 0.28 V and it can be noted that stainless steel contains iron, a ferromagnetic material. It can also be observed that with non-magnetic electrodes, the overpotentials are around 0.6 V and above; with the highest being Boron Doped Diamond, BDD which has an overpotential of around 1.5 V. The use of ferromagnetic materials has confirmed a reduction in the overpotential from both theoretical and experimental observations.

DFT calculations by (Rossmeisl et al., 2005) and co-workers to investigate the origin of the overpotential for elemental electrodes showed that an oxygen layer has to be formed on the metal surface in order for oxygen evolution to occur. The establishment of this oxygen layer has been explained as the source of the high overpotential since it demands a high potential to be stabilized (Rossmeisl et al., 2007). Studies have previously shown that oxide materials, particularly rutile type oxides like RuO_2, IrO_2 are better as oxygen-evolving electrodes than elemental metals (Rossmeisl et al., 2005). Lower overpotentials have also been predicted theoretically (Rossmeisl et al., 2007; Torun et al., 2013) and observed experimentally (Jirkovský et al., 2006; Nocera, 2012) with metal oxides; RuO_2 (Rossmeisl et al., 2005, 2007; Torun et al., 2013) IrO_2 (Rossmeisl et al., 2007), Co-Pi (Nocera, 2012). Strikingly, these materials exhibit some magnetic properties hence their high efficiencies as good oxygen evolution catalysts since they contain magnetic moments on the surface which help to align adjacent spins (Ping et al., 2015; Torun et al., 2013).

2.2.6.2 H_2O_2 formation on surfaces

It has been observed that photoelectrocatalytic water splitting is hampered by the formation of hydrogen peroxide during the process and its efficiency still remains a major concern (Brillet et al., 2010; Gray, 2009; Mayer et al., 2012; Prévot & Sivula, 2013). Since water splitting requires that a water molecule must be oxidized at the anode producing an oxygen molecule and releasing electrons which must reduce protons on the counter electrode; efficient production of the oxygen molecule is essential for the efficiency of the proton reduction process.

Many reports have indicated that during water splitting, oxygen is produced as a final product from the disproportionation of hydrogen peroxide (Kohl et al., 2009; Salvador & Decker, 1984). This has been explained as part of a two-step process in which hydrogen peroxide is formed first (Juan Liu et al., 2015). This is consistent with the fact that the formation of hydrogen peroxide is kinetically favorable compared to triplet oxygen formation.

Formation of hydrogen peroxide during photoelectrocatalytic water splitting is well documented (K. B. Ghosh et al., 2019; S. Ghosh et al., 2020; Mtangi et al., 2017; W. Zhang et al., 2018). Wang et al demonstrated the simultaneous generation of H_2O_2 and H_2 on TiO_2 nanoparticle surfaces with very high efficiencies (L. Wang et al., 2019) . This exceptional activity is attributed to the more favourable two-electron oxidation of water to H_2O_2. Liu *et al* also demonstrated the generation of H_2 and H_2O_2 on Pt/C_3N_4 surfaces. They attributed the difficulty in O_2 release to the kinetically competitive reactions of two-electron water oxidation to peroxides, such as H_2O_2. The work by Liu et al and Wang et al demonstrates that hydrogen peroxide formation is a competing process to the oxygen evolution process (Mondal et al., 2018). Significant research has been performed to catalyze the disproportionation reaction of H_2O_2 (Freire et al., 2020; Sengupta et al., 2016). From a thermodynamic point of view, H_2O_2 production from water requires more energy which might be the source of the over-potential in water splitting.

Efforts to minimise hydrogen peroxide formation has resulted in the inclusion of chiral molecules in the photoelectrochemical cell. Chiral moieties have been used either as chiral photoelectrodes (T. Feng et al., 2023; K. B. Ghosh et al., 2019; S. Ghosh et al., 2020; Mtangi et al., 2015, 2017; W. Zhang et al., 2018, 2021) or as the bulk electrolyte (Gazzotti et al., 2018, 2020)

2.2.6.3 Oxygen evolution

During water splitting, hydrogen is produced at the cathode, while oxygen is produced at the anode, a process that involves a net transfer of four electrons (Juan Liu et al., 2015; Nocera, 2012). The anodic process, which is the oxygen evolution reaction, OER, has previously been identified as the bottleneck of the water splitting process and has been attributed to be the source of the high overpotential (Rossmeisl et al., 2007). Ground state oxygen exists in a triplet state, thus, the sluggishness in the OER arises from spin constraints that exist in the elementary reaction steps for its formation, posing a considerable overpotential requirement (K. B. Ghosh et al., 2019). Solution pH has been observed to affect the efficiency of the process as it has an effect on these undesired pathways (Obata et al., 2020). Even though it has been demonstrated that the formation of peroxide and superoxide radicals depends on solution pH; where at high pH, it is less favourable because of the stability of the products, while at neutral pH, peroxides and superoxide radicals are more stable (K. B. Ghosh et al., 2019); spin restrictions can still affect the Faradaic efficiency of the reaction (Carmeli et al., 2014).

The importance of spin has been investigated on the OER using theoretical and experimental methods, and has been correlated to the observed overpotential using ferromagnetic and non-

magnetic surfaces. The significance of the number of unpaired electrons in the catalyst's active centre to allow for ferromagnetic-like exchange interactions between the oxygen radical intermediates and the catalyst has been demonstrated theoretically (Suntivich et al., 2011). However, in these particular studies, the effect of the electrode on suppressing peroxide and superoxide radical formation was not reported; neither was a mechanism behind the O-O bond formation given nor the origins of the overpotential investigated. Garcés-Pineda et al demonstrated a doubled hydrogen output of a water-splitting electrolyzer using a simple magnet (Garcés-Pineda et al., 2019). The results produced by Garces-Pineda et al demonstrate that an enhanced production of hydrogen by applying a magnetic field to a PEC using ferromagnetic Nickel electrodes in alkaline media is an experimental confirmation of the effect of the magnetic field on the oxygen evolution reaction. Their work also demonstrated the suppression of hydrogen peroxide at pH 11. They attributed this to the effect of the external magnetic field on the parallel alignment of the oxygen radicals during formation of the O-O bond. They also observed that maximum enhancement was achieved in highly magnetic electrodes.

The use of chiral molecule modified electrodes versus their achiral moieties has demonstrated a pronounced effect on the OER and overall water splitting efficiency (K. B. Ghosh et al., 2019; S. Ghosh et al., 2020; Mtangi et al., 2017; W. Zhang et al., 2018) . Experimental observations have demonstrated that the control of electron spin through the CISS effect has an effect on the process and concomitantly reduces the overpotential. It has also been confirmed that controlling the electron spin suppresses H_2O_2 formation. This has been attributed to the fact that the water oxidation process occurs on a triplet surface, which in turn enhances the formation of the triplet oxygen (W. Zhang et al., 2018).

Experimental results where ferromagnetic electrodes and chiral molecule modified electrodes have been employed demonstrate the significance of spin alignment and control in improving the efficiency of the OER and electrochemical water splitting. These findings clearly suggest the importance of considering spin constraints in the design of electrodes for efficient electrochemical water splitting.

The reduced overpotential with ferromagnetic metal oxide electrodes suggests their abilities to control spin alignment in the magnetic oxygen as suggested by Torun et.al and probably inhibits/reduces peroxide formation (Torun et al., 2013). Experimental observations in which the spin conservation was achieved also confirmed these predictions. These findings strongly indicate that the control of spin alignment in the formation of the triplet oxygen during water splitting is essential in improving the efficiency of the oxygen evolution reaction, OER process.

Based on these theoretical and experimental observations, there seem to be a strong correlation between the formation of hydrogen peroxide during water splitting, spin alignment control and the overpotential, as was previously explained by Mtangi in 2015 (Mtangi et al., 2015)

2.3 ELECTROCHEMICAL TECHNIQUES

2.3.1 Introduction

Water splitting experiments are carried out using different electrochemical techniques. The electrochemical techniques are classified according to the parameters that are assessed during the measurements, according to **Figure 2.6**.

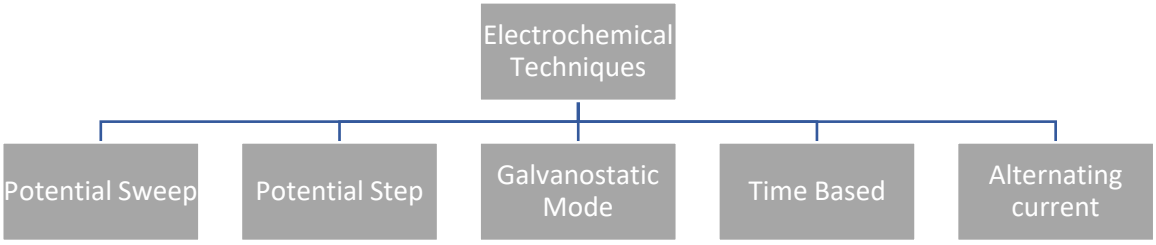

Figure 2.6: Types of electrochemical techniques

Different types of electrochemical techniques exist and they are classified depending on the parameters that are varied during an experiment. Electrochemical techniques such as Linear Sweep Voltammetry (LSV) and Cyclic Voltammetry (CV) are classified as potential sweep techniques. In potential sweep techniques, the electrochemical behaviour of photoelectrodes is evaluated as the potential is steadily increased. Chronoamperometry is classified as a potential step technique because the potential (voltage) can be changed from one discrete value to another as the change in current is recorded, while open circuit potential falls under the time-based measurements. Electrochemical Impedance Spectroscopy (EIS), under which the Mott-Schottky measurements, Nyquist plots as well as Bode plots is classified as an alternating current technique. The electrochemical techniques that were used during this study are discussed in the following section.

2.3.2 Linear Sweep Voltammetry

Linear Sweep Voltammetry (LSV) is an electrochemical technique in which the potential is varied linearly from an initial (lower) value (E_i) to the final (upper) value (E_f). In LSV measurements, the current response is plotted as a function of the voltage in a curve called a voltammogram. The characteristics of the LSV voltammogram, depend on:

- Rate of electron transfer
- Chemical reactivity of the electroactive species as well as
- The scan rate (v)

The scan rate is the variation of the electrode potential with time. LSV can be approximated as the first half-cycle of a cyclic voltammogram. Scanning starts at a potential where no electrochemical reaction occurs. Current is detected at the potential where charge transfer begins, which increases with the potential, however, after a maximum value (peak current plateau) it starts to decrease due to the depletion of the reacting species at the interface. LSV measurements can be carried out under darkness and under illumination to evaluate the OER mechanisms of the fabricated photoelectrodes. LSV measurements in which the light source is periodically chopped ON/OFF are also carried out to evaluate the photocatalytic nature of the photoelectrodes (Bedoya-Lora et al., 2021). A typical OER voltammogram is shown in **Figure 2.7 (a)** while a typical voltammogram under chopped light is shown in **Figure 2.7 (b).**

a) b)

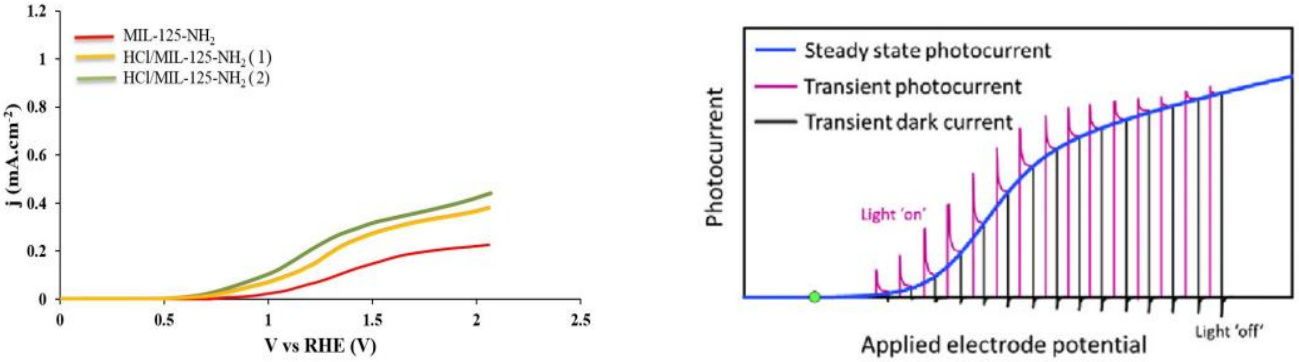

Figure 2.7: a) Typical LSV curve for OER measurements (Afzali et al., 2020). b) Chopped potential voltammogram for a typical photoelectrode (Bedoya-Lora et al., 2021)

2.3.3 Cyclic Voltammetry

Cyclic voltammetry (CV) is a common electrochemical technique frequently used to examine the reduction and oxidation processes of molecular species. CV is helpful in studying electron transfer-initiated chemical reactions, which includes catalysis. A CV profile is called a voltammogram or cyclic voltammogram. The x-axis represents a parameter that is imposed on the system, while the y-axis is the response, usually the resulting current (*i*) passed. Each CV contains an arrow showing the direction in which the potential was scanned to record the data. The arrow is used to show the beginning and sweep direction of the first segment usually referred to as the "forward scan". An important parameter reported together with CVs is the scan rate(υ). The scan rate is used to show that during the experiment the potential was varied linearly at the speed (scan rate) of e.g. 0.01V per second ($0.01Vs^{-1}$). Two conventions are commonly used to report Cyclic Voltammetry data namely the US Convention and the IUPAC convention (Elgrishi et al., 2018), as shown in **Figure 2.8**

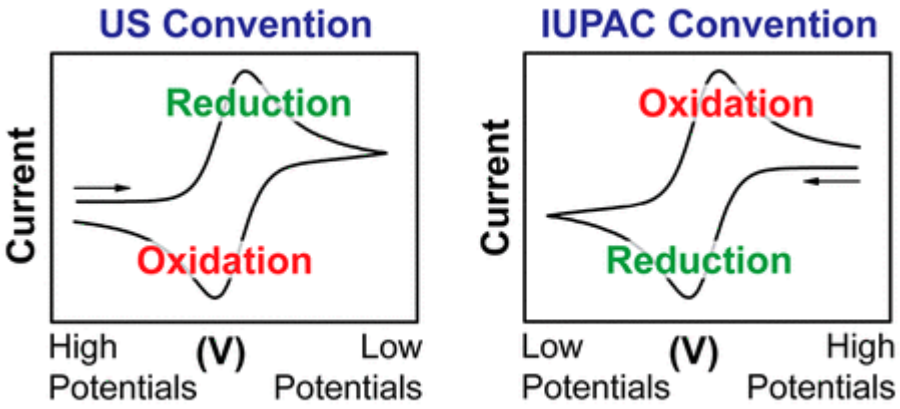

Figure 2.8: Typical Cyclic Voltammograms Source (Elgrishi et al., 2018)

2.3.4 Chronoamperometry

Chronoamperometry is an electrochemical method in which a square wave potential is applied to the working electrode. The current of the electrode is measured as a function of time (Guy & Walker, 2016). Chronoamperometry (CA) is sometimes referred to as constant potential bulk electrolysis, controlled potential amperometry or potential pulse electrolysis. At the beginning of the chronoamperometry measurement, the potential of the working electrode is held at E_i as shown in **Figure 2.9 (a)**, the whole cycle is 2τ seconds long. At t=0, the potential is instantaneously changed to a new value E_i and after τ seconds the potential changes to E_f. The corresponding current time response is recorded and is shown as **Figure 2.9 (b)**.

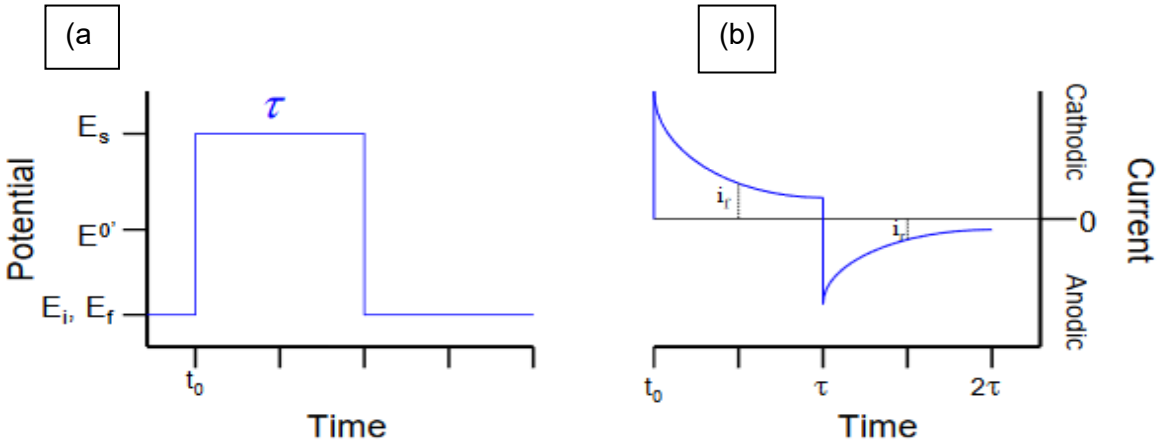

Figure 2.9: Typical chronoamperometric curves

The observed current is calculated using the Cottrel Equation:

$$i_t = \frac{nFAC_0D_0^{\frac{1}{2}}}{\pi^{\frac{1}{2}}t^{\frac{1}{2}}} \qquad \text{Equation 2.3}$$

Where

n	stoichiometric number of electrons involved
F	Faraday's constant (96500C/mol)
A	Electrode Area (cm^2)
C_0	Concentration of electroactive species (mol/cm^3)
D_0	Diffusion constant for electroactive species (cm^2/s)

In water splitting, chronoamperometry is used to assess the transient photocurrent densities when light is switched ON/OFF and can be used to give an insight into the mass transfer kinetics of the photoelectrodes under study (Afzali et al., 2020; Hendi et al., 2020).

2.3.5 Open Circuit Potential

The difference of electrical potential between two terminals of a device when disconnected from any circuit is called Open Circuit Potential (OCP). OCP can also be used to assess the photocatalytic activity of photoelectrodes, an effective photoelectrode will exhibit different

OCPs under dark and light conditions. OCP measurements are carried out to evaluate the stability of an electrochemical system as well as revealing the electrochemical potential state of a material using an electrolyte over time (Bedoya-Lora et al., 2021). The OCP measurements can also be described as the tendency of the electrode to take part in electrochemical corrosion reaction with the electrolyte. An electrode with low OCP values, can be regarded as noble. A high OCP value indicates a driving force for water oxidation and it limits the variance, between hole-quasi-Fermi-level of the semiconductor heterojunction and the redox potential of the electrolyte. However, OCP does not provide surface reaction kinetics.

2.3.6 Electrochemical Impedance Spectroscopy

Electrical Impedance Spectroscopy (EIS) technique is used to study how a material's properties change over time. It involves applying a small Alternating Current (AC) to the material and recording the resulting voltage (Lazanas & Prodromidis, 2023). The material's resistance and capacitance can be determined by analysing the relationship between current and voltage. EIS provides insight into how materials respond to electrical stimulation. EIS plays an important role in energy storage technologies. For the determination of capacitance, Mott-Schottky measurements are often carried out while Nyquist plots which record changes in resistance are used to evaluate the charge transfer kinetics.

2.3.6.1 Mott-Schottky measurements

The quality of a semiconductor contact determines its performance, poor contacts will result in undesired effects which include high leakage currents and low barrier heights. The quality of the semiconductor is determined by a number of factors, some of which include the mismatch between the Fermi-energies of the metal and semiconductor, the semiconductor processing steps (cleaning and annealing) prior to contact fabrication and the contact fabrication techniques. These contacts are considered to be ohmic or rectifying (Schottky) as governed by their response to an applied external bias (Mtangi, 2012).

Mott-Schottky involves the measurement of the differential capacity of the electric double layer at the semiconductor-electrolyte interface (Hankin et al., 2019). In a PEC system, the semiconductor and electrolyte interface form a junction similar to a Schottky diode (Ma & Wang, 2017). The in-built electric field due to charge distribution in the semiconductor and at the semiconductor/electrolyte interface is the driving force that separates photoexcited carriers. For an n-type semiconductor, the Fermi level is close to its conduction band minimum (CBM) and higher than the electrochemical potential of the electrolyte. Thus, the majority carrier of electrons will flow from the semiconductor to the electrolyte after contact until the

Fermi level of the semiconductor and the electrochemical potential of the electrolyte are aligned. The energy band edges in the semiconductor are shifted due to the change of carrier concentrations in a phenomenon called band bending as shown in **Figure 2.10**.

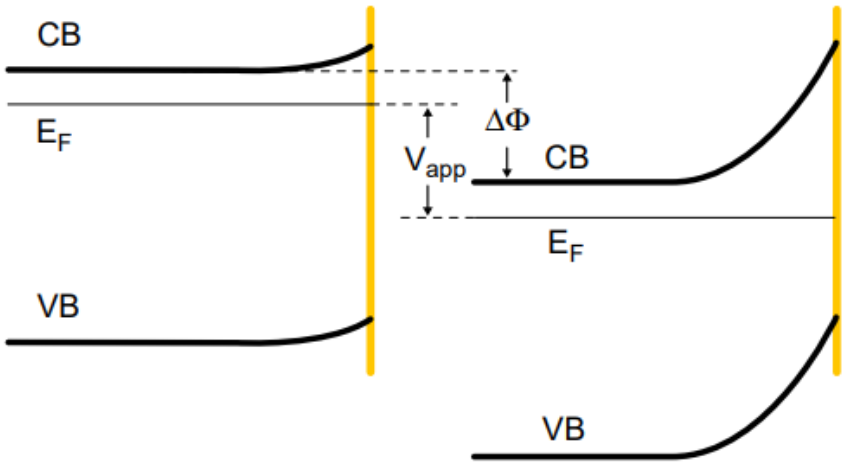

Figure 2.10: Band diagrams of an n-type semiconductor and the electrolyte before (left) and after (right) contact. Source:(Ma & Wang, 2017)

The Fermi level in a photocatalyst can be controlled by the application of a bias potential, which changes the band bending. If the applied potential causes flattening of the band edges, then it is called flat band potential (V_{bi}). This results in a lack of differences between the potential at the surface and in the bulk of the semiconductor. If the applied potential is higher than V_{bi}, the potential causes higher band bending.

The total capacitance of the interfacial double layer ($C_{interface}$), is made up of contributions from semiconductor capacitance (C_{sc}) and capacitance of the Helmhotz layer in the electrolyte, (C_H), which are in series with each other.

$$\frac{1}{C_{interface}} = \frac{1}{C_{SC}} + \frac{1}{C_H} \qquad \text{Equation 2.4}$$

The semiconductor capacitance is described by the Mott Schottky equation, which is a plot of $\frac{1}{C^2_{interface}}$ as a function of E.

$$\frac{1}{C^2} = \frac{2}{\varepsilon\varepsilon_o q N_D}\left(E - V_{bi} - \frac{kT}{q}\right) \qquad \text{Equation 2.5}$$

Where:

C The capacitance,

N_D (cm^{-3})	Donor density,
ε	Relative permittivity of the photocatalyst,
ε_0	Vacuum permittivity (8.854 × 10−12 F m^{-1}),
E	Applied potential,
k	Boltzmann constant (1.381 × 10^{-23} J K^{-1}), and
T	Temperature (298 K).

The $C_{interface}$, is obtained from EIS measurements, while the flat band potential, (V_{bi}), is determined from the intercept of the linear portion of the Mott-Schottky plot ($\frac{1}{C^2}$ vs. E) with the potential axis, when $\frac{1}{C^2} = 0$. The flat band potential is the potential at which the inversion between cathodic and anodic currents occurs (Hankin et al., 2019). The charge carrier concentration can also be determined from the gradient of the Mott-Schottky plot, if the relative permittivity is known. The slope of the Mott Schottky plot can be used to determine the nature of the semiconductor material, a negative gradient is typical of a p-type semiconductor while a positive slope points towards n-type nature of a semiconductor, (Kusmierek, 2020).

In the case where a metal oxide semiconductor–electrolyte interface is present, charge transfer and separation are governed by the magnitude of band bending. The band bending is determined by the difference in the electrode potential of the electrons in the semiconductor and the formal solution potential of the electrolyte. In the metal oxide semiconductor–electrolyte system, the potential at which no space charge layer exists, when the potential drop between the bulk and the surface of the semiconductors zero, is known as the flat band potential (V_{bi}). The flat band potential is an important parameter used to locate the position of conduction band or valence band, and can be determined experimentally.

2.3.6.2 Nyquist Plots

A plot of negative imaginary vs real parts of the complex impedance of individual electrodes or chemical cells is called the Nyquist plot (Mei et al., 2018). In Nyquist plot measurements, the frequency is varying from high frequencies to low frequencies. The high frequencies are usually of the Mega Hertz ranges. During EIS measurements, two plots are produced: the Bode Plot and the Nyquist plot which are shown in **Figure 2.11**.

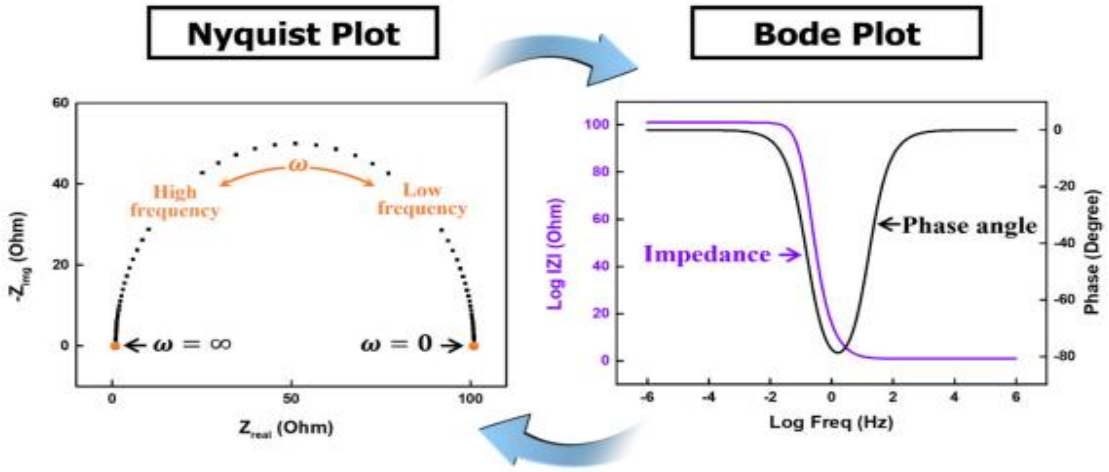

Figure 2.11: Typical relationship between a Nyquist plot and a Bode plot Source (Choi et al., 2020)

The Bode plot that shows the phase shift and magnitude changes in the applied frequency ranges while the “Nyquist plot” that represents the real and imaginary parts of Z(ω) using cartesian coordinates (Choi et al., 2020). The Bode plot is often used in sensors and transistors in electronic devices, the Nyquist plot is used to analyse the characteristics of photoelectrochemical cells because of its convenience in analysing the active reaction mechanism (Choi et al., 2020).

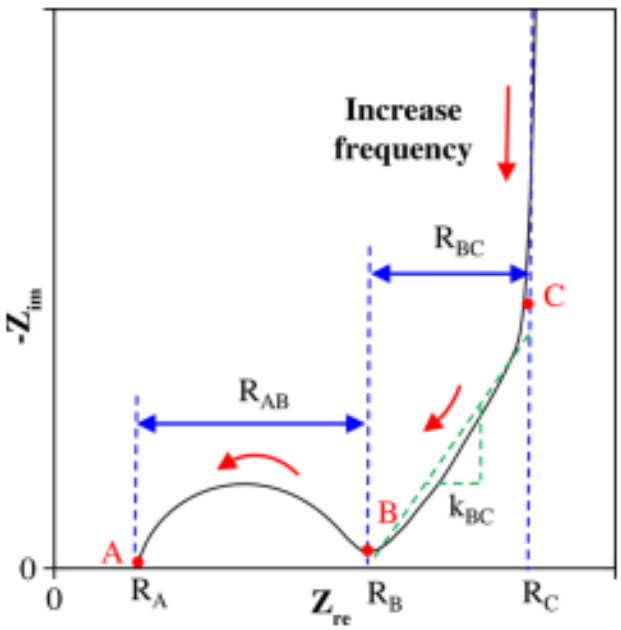

Figure 2.12: Typical Nyquist plot Source (Mei et al., 2018)

In the interpretation of the Nyquist plot, the resistance R_A at point A (**Figure 2.12**) can be attributed to the bulk electrolyte resistance or the equivalent series resistance (ESR) also known as the internal resistance which is also the sum of the resistances of the bulk electrolyte, the electrode, and the contact resistance between the electrode and the current collector. The diameter of the semicircle $R_{AB} = R_B - R_A$ in **Figure 2.12** is often assigned to the electrolyte resistance in the pores of the electrodes or the charge transfer resistance (Mei et al., 2018). The evaluation of the charge transfer is important in water splitting measurement.

The Nyquist plot offers an understanding into the possible mechanism or governing phenomena in an equivalent circuit model system. The circuit model for EIS consists of electrical circuit components such as Resistors, Capacitors as well as Inductors. A circuit model representing the whole system of the electrochemical cell can be developed. To construct an accurate circuit model, suitable electrical components that represent the overall system are employed. The purpose is to construct a circuit model that is physically meaningful and minimizes the number of variables (Choi et al., 2020). A typical Nyquist plot and the associated circuit are shown in **Figure 2.13.**

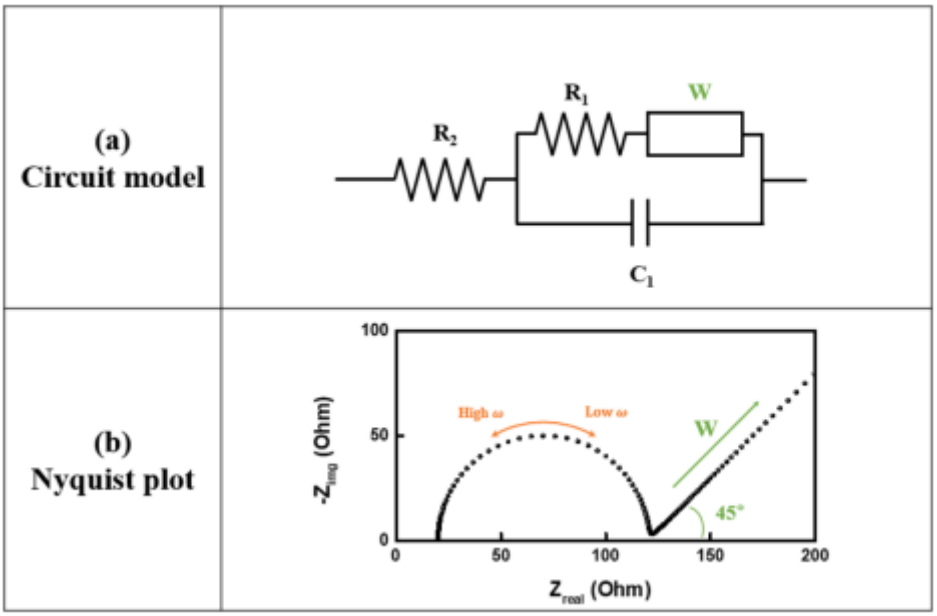

Figure 2.13: Typical Nyquist plot and corresponding circuit Source (Choi et al., 2020)

2.3.7 Tafel Plot

A Tafel plot describes the relationship between the electrochemical reaction rate and the overpotential of the surface of the electrode. Tafel plots are used in a bid to unravel the reaction kinetics as well as the oxygen evolution reaction mechanism. Tafel plots are also used to evaluate the catalytic properties of various photocatalysts that may be under study (Aralekallu et al., 2020).

Using the Tafel equation, the overpotential can be evaluated using the Tafel Equation, given in Equation 2.6.

$$\eta = \pm A \log \frac{i}{i_o} \qquad \text{Equation 2.6}$$

Where

η Overpotential in V

A Tafel slope in V

i Current Density in A/m^2

i_0 Exchange current density in A/m^2

± (+) Anodic process (-) Cathodic process

A Tafel plot shows the relationship between the current generated in an electrochemical cell and the electrode potential of a specific metal. The overpotential can be determined from the Tafel plot, as the Tafel slope which is the linear region within the Tafel plot (van der Heijden et al., 2024). The Tafel slope is also used to determine the rate determining step during water splitting (Anantharaj & Noda, 2022).

2.3.8 Efficiency of the PEC

2.3.8.1 Spectrophotometric titration

The efficiency of a PEC may also be evaluated using spectrophotometric titration. The spectrophotometric method measures the presence of hydrogen peroxide in the presence of ortho-tolidine as an indicator. During this method, chronoamperometry measurements are conducted for 30-40 minutes. The presence of hydrogen peroxide is verified by the colorimetric test titration experiment of the used electrolyte, with o-tolidine as a redox indicator. In the colorimetric measurements, generally 0.8mL of an o-tolidine solution prepared according to

the Elmms-Hauser method is added to 4 mL of the electrolyte solution obtained from the electrochemical cell and left to react for 30 minutes. In the presence of H_2O_2 a yellow colour is detected with an absorption peak at around 436 nm from UV-vis absorption spectroscopy (Mtangi et al., 2017).

2.4 CHIRAL-INDUCED SPIN SELECTIVITY EFFECT

2.4.1 Introduction

In 2012, Naaman and Waldeck discovered the Chiral Induced Spin Selectivity (CISS) effect in which they concluded that electrons moving through a chiral molecule become spin polarised and that there is a preference to have the spin aligned either parallel or antiparallel to the electron's velocity (Naaman & Waldeck, 2012). They also concluded that spin filtering is also observed in ferromagnetic materials.

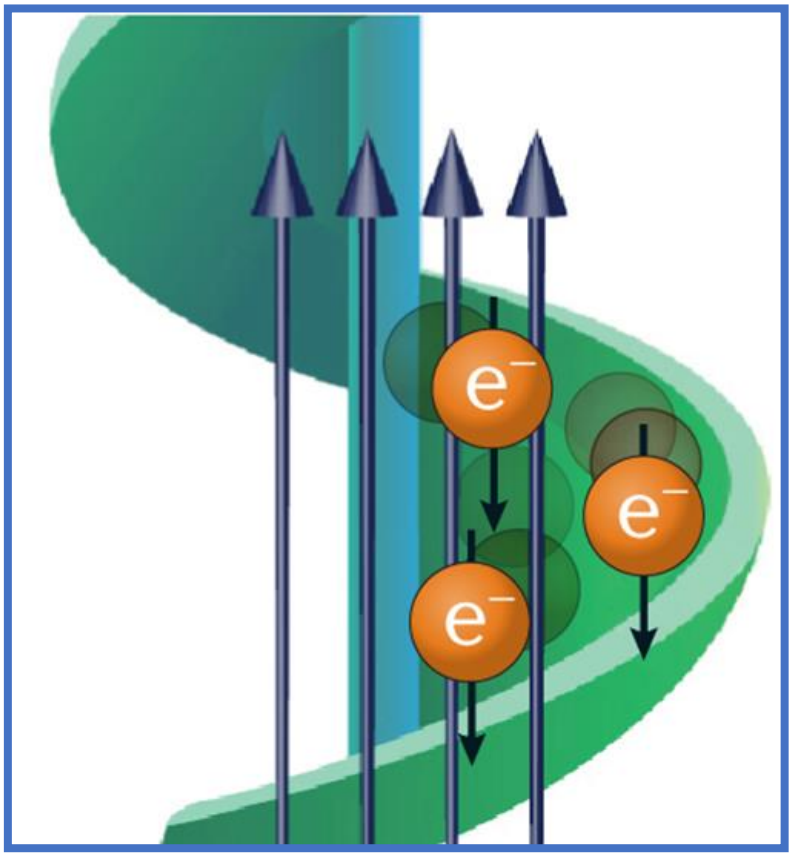

Figure 2.14: Spin filtration during CISS Source (Naaman et al., 2019)

As shown **Figure 2.14**, the electrons are going through a chiral photocatalyst, their spin is filtered and, in this case, only electrons with a downward spin are transmitted. When the spin of the electron is not filtered the formation of hydrogen peroxide is thermodynamically favoured, but when the spin of the electrons is regulated, formation of triplet oxygen ground-state ${}^{3}\Sigma_{g}({}^{g}O_{2})$ is favoured. The H_2O_2 will not be produced together with ${}^{3}O_2$, since the formation of H_2O_2 is spin forbidden on the triplet potential surface (W. Zhang et al., 2018).

2.4.2 Chirality in water splitting

A series of experiments have shown that the high OER barrier and generation of hydrogen peroxide arises from the lack of correlation between the electrons transferred in the reaction. It has been noted that chiral substances have a special capability of filtering the spin state of the electrons. This is because the electrons are spin polarised when they pass through the helical electric field of chiral substances (Naaman et al., 2020).

The great overpotential of water splitting originates from the prerequisite that oxygen atoms must be in close proximity to enable the exchange interactions between them (Mondal et al., 2018) and this causes their spin alignment to allow the formation of molecular oxygen in the triplet ground state. In this scenario, electron spin alignment of the intermediate radicals ($*OH$) should reduce the overpotential of the OER because it allows the formation of ${}^{3}O_2$ to occur with a higher cross section on a triplet surface. The formation of hydrogen peroxide is spin forbidden as it occurs on a triplet surface which is beneficial for protecting the electrodes.

It has also been noted that the spin-dependent charge reorganisation observed in chiral molecules suggests that the interaction between a chiral molecule and a magnetised surface should be enantio-specific (Naaman 2020). The interaction energy for the molecule forming a chemisorption bond with a metal spin-orbital will depend on whether the spins are aligned antiparallel (singlet) or parallel (triplet). For achiral molecules, the charge redistribution in the molecule as it approaches and binds to the surface is not spin dependent and no apparent spin selectivity is observed. As a chiral molecule approaches the surface it undergoes spin-dependent charge redistribution so that one enantiomer interacts along a singlet reaction coordinate and the other enantiomer interacts along a triplet reaction coordinate.

Magnetic materials have also been investigated for inducing chirality. In 2008 Rosenberg showed that low-energy spin polarised secondary electrons that are produced by the irradiation of a magnetic substrate can induce chiral-selective chemistry (Rosenberg et al., 2008). Naaman et al, also report that in ferromagnetic substances, if the ferromagnetic substrate has not been magnetized, its surface is made up of a mixture of up and down areas

(Naaman et al., 2020). The electronic interaction at the interface between chiral molecules and the ferromagnetic substrate, disrupts the spin degeneracy so that one spin is preferred at the expense of the other (Naaman et al., 2020).

Chirality can be induced in the photoelectrochemical cell through various ways. Bulk chiral electrolytes (Gazzotti et al., 2018, 2020) as well as chiral photoelectrodes (K. B. Ghosh et al., 2019; Mtangi et al., 2017; Zhang et al., 2018) have been used in water splitting. Chiral photoelectrodes have been fabricated by decorating the conducting substrate such as FTO with chiral molecules or by soaking the molecules in chiral solutions (W. Zhang et al., 2020).

Photoelectrodes have been fabricated using different types of metal salts as well as chiral molecules and a summary is given in Table 2.1

Table 2.1: A summary of chiral photoelectrodes that have been used in water splitting

Electrode	**Chiral molecules used**	**Comments**	**Source**
Titanium Dioxide	S-Zn S-TPyA	The final electrolyte produced negligible quantities of H_2O_2 when compared to the electrolyte from the achiral photoelectrodes	(Mtangi et al., 2017)
Iron Oxide Nanoparticles	L-A3 L-A11	Chiral molecules chemisorbed onto Iron oxide nanoparticles	(W. Zhang et al., 2018)
Cobalt Oxide	L-meso-tartaric acid	Electrodeposition was used to create the chiral electrodes	(S. Ghosh et al., 2020)
	D-meso-tartaric acid		
CuO	Cu (II) tatrate	Chiral electrodes produced through electrodeposition	(K. B. Ghosh et al., 2019)

2.5 PHOTOELECTRODE ARCHITECTURE

2.5.1 Introduction

Different photoelectrode architectures have been used in the design and fabrication of photoelectrodes that are used in water splitting. Photoelectrode architecture involves optimisation of parameters such as thickness, porosity, pore size and particle size (Zhu et al., 2022) as well as selection of the appropriate semiconductor material, metal oxides vs perovskites vs metal organic frameworks. To improve charge separation, optimize on light harvesting and provision of enough driving force to overcome overpotential beyond +1.23V different electrode configurations have been developed (Martinez-Garcia et al., 2018). Different photoelectrode architectures have been developed to address issues with charge separation, light harvesting and photo-corrosion. Surface modification by means of doping and post-synthetic treatment which includes acid treatment and surface hydrogenation, have been employed to introduce band bending (Chatterjee & Shyamal, 2023). Herein we discuss the different electrode architectures that are commonly used which include heterostructure electrodes, nanostructured electrodes and tandem junctions.

2.5.2 Nanostructured electrodes

Nanostructured photoelectrodes are thin films or surfaces that have been purposefully engineered at the nanoscale to improve their performance in photoelectrochemical processes. Nanostructures which include nanoparticles, nanowires, nanotubes, nanorods and nanobelts have found application in water splitting devices (Maçaira et al., 2013) . Nanomaterials are especially favoured in catalysis because they can have very high specific surface areas of up to several hundred of $m^2\ g^{-1}$. Photoelectrodes fabricated using nanomaterials have the ability to allow the adsorption of a large amount of sensitizer molecules in a monolayer configuration. However, nanosized materials tend to affect the way electrons are transported through the photoelectrode structure and special attention should be paid to the shape of the nanostructures as it tends to shorten the transport path (Harris-Lee et al., 2023).

For high performance, the catalyst nanoparticles must form charge-carrier-selective contacts with the underlying light-absorbing semiconductor, facilitating either hole or electron transfer while inhibiting collection of the opposite carrier (Laskowski et al., 2020). Different materials and configurations including Fe_3O_4 nanoparticles (W. Zhang et al., 2018), CdSe nanoparticles

(Mtangi et al., 2015), TiO_2 nanoparticles (Mtangi et al., 2015, 2017), ZnO nanorods (Guler et al., 2023), and MoS_2 nanosheets, (Ali et al., 2019) have been used in the fabrication of nanostructured photoelectrodes. The nanoparticles have been deposited onto the glass conducting substate such as Fluorine-doped Tin Oxide (FTO) and Indium Tin Oxide (ITO) using drop casting, electrophoretic deposition and spin coating (W. Zhang et al., 2020). To confirm the adherence of the nanoparticles to the FTO surfaces, high resolution SEM images are often taken, with results as shown in **Figure 2.15.**

(a) (b)

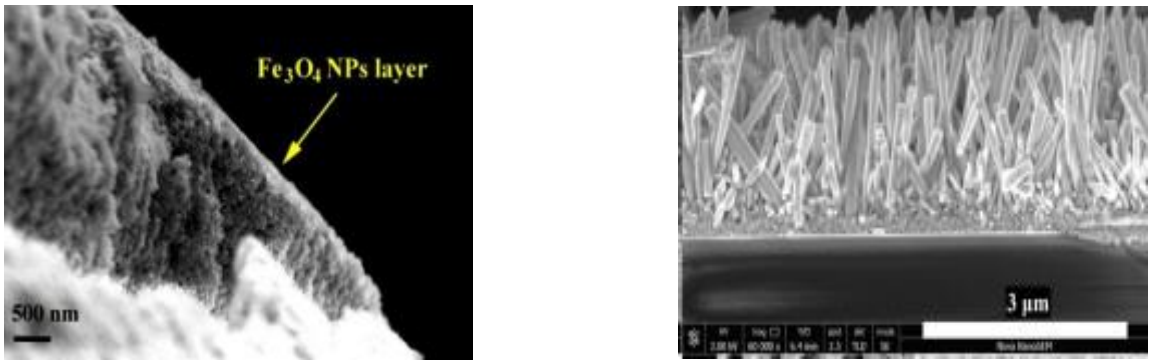

Figure 2.15: SEM images of (a) Fe_3O_4 nanoparticle layer deposited on FTO Source (W. Zhang et al., 2018) (b) ZnO nanorods deposited on FTO (Guler et al., 2023)

Nanostructured photoelectrodes also include nanocomposites. Nanocomposites are multiphase solid materials that incorporate nanosized particles into the matrix standard materials. Nanocomposites are often used in the fabrication of photoelectrodes as nanomaterials can be engineered to improve the light harvesting properties of the photoelectrodes. Nanocomposites that use Metal Organic Frameworks as the photocatalyst in the PEC have also been synthesized. MOFs such as UIO-67 and Zr-MOFs have been explored in the fabrication of photoelectrodes (Altaf et al., 2018) . An in-depth exploration of the use of MOFs in photoelectrocatalytic water splitting is made in section 2.6. In summary, nanostructured photoelectrodes play a pivotal role in advancing renewable energy technologies by harnessing sunlight for various applications.

2.5.3 Heterojunctions

A heterojunction refers to the interfacial area at the interaction point of two semiconductors (Li et al., 2022). Ideally the PEC photoelectrodes should be able to utilise as much sunlight as possible and one photocatalyst cannot meet these demands. Heterojunctions are created

when a composite of two or more semiconductors are joined for enhanced interfacial charge transfer (Chatterjee & Shyamal, 2023) and they are usually fabricated by combining a wide bandgap material with a small bandgap material. Heterojunctions are used when there is need to improve, the process of light absorption, charge transport, and interfacial charge transfer (J. W. Yang et al., 2021). The heterojunctions can be classified into three main groups, namely: Type I heterojunction called a straddling gap, Type II called a staggered gap and Type III called the broken gap. The z-Scheme also falls under the heterojunctions. The heterojunctions are also classified as n-n junctions, p-p junctions and p-n junctions. **Figure 2.16** shows the different types of heterojunctions.

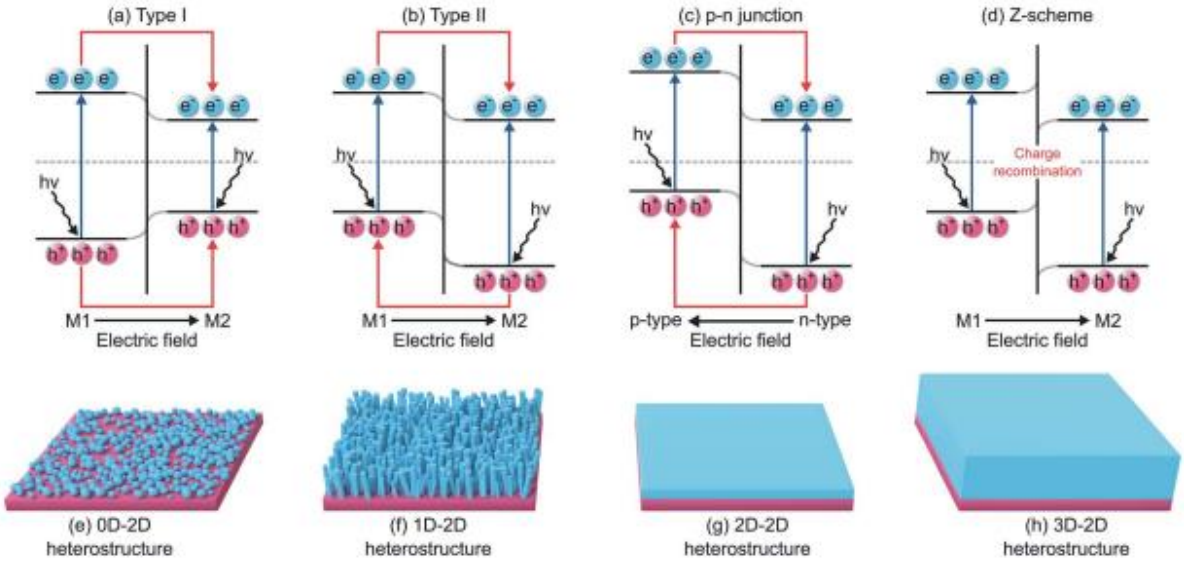

Figure 2.16: (a-d), the possible charge transfer mechanism (e-h) different configurations of the heterojunctions. Source (Fareza et al., 2022)

Fabrication of heterojunctions has been achieved by using top-down methods, such as mechanical exfoliation, liquid phase exfoliation as well as intercalation while bottom-up methods that stack up material, atom-by-atom have also been used and these include Chemical Vapour Deposition (CVD), Chemical Bath Deposition (CBD) as well as successive ionic layer adsorption and reaction.

2.5.3.1 Z-Scheme and s scheme

A z-scheme is a mechanism that is used in photocatalysis to describe the transfer of photogenerated electrons between two photocatalysts with a staggered band alignment, as the name suggests, the charge transfer pathway is shaped like a Z (Li et al., 2022). A z-scheme is based on a two-step photoexcitation mechanism, achieved by combining two

semiconductors with different bandgaps (Z. Wang & Wang, 2021) so as to broaden the light harvesting range of the photoelectrode. A z-scheme is composed of n-type and p-type semiconductor photocatalysts which will be the oxidation photocatalyst and a reduction photocatalyst. Usually, the oxidation photocatalyst possesses a lower valence band, while the reduction photocatalyst possesses a high conduction band (Xu et al., 2018). A traditional Z-scheme is shown in **Figure 2.17.**

Figure 2.17: Typical Z scheme Source (Xu et al., 2018)

Advantages of using the z-scheme include: preservation of the reductive and oxidative abilities of the photoelectrode, effective separation of the reductive and oxidative sites, high charge separation and extended light harvesting range (Xu et al., 2018). There also exists an S-scheme which is composed of two n-type semiconductors. The Z-scheme is inspired by the natural photosynthesis, while the S-scheme is named for its staggered band structure.

2.5.4 Tandem Junction

A tandem device junction is made up of two or more light absorbing species which target different parts of the solar spectrum to generate voltage necessary for water splitting (Sherman et al., 2016). Tandem cells are an emerging field in unassisted water splitting (K. Zhang et al., 2016) and configuration of dual-absorber tandem systems has been increasingly more attractive for unassisted overall water splitting (Chen et al., 2018). There are three different tandem cell configurations namely i) The PEC tandem cells ii) the integrated photovoltaic

PEC/PV tandem cell and iii) the PV/Electrolyser hybrid (K. Zhang et al., 2016). The simplest configuration of a tandem cell is a one-sided light absorption semiconductor.

In a PEC tandem cell, the device configuration is made up of a two-sided light-absorption component with both the anode and cathode **(Figure 2.18 (a)).** The spontaneous water redox which takes place via the simultaneously excitable anode and cathode and reduces the basic requirement of band edge potentials, which is critical for the use of a single semiconductor. Furthermore, the two semiconductors can have smaller bandgaps because each need to provide only a half-reaction. Additionally, the smaller bandgaps can increase the light absorption in the visible-wavelength radiation, which represents the majority of photon flux from the sun (K. Zhang et al., 2016).

Another device configuration used in unassisted water splitting is an integrated PEC cell and PV device also called the PEC/PV tandem cell, which is shown in **Figure 2.18 (b).** The PEC device is combined with a PV cell in a tandem configuration (K. Zhang et al., 2016). When the solar energy reaches the rear PV device after passing through the front PEC electrode, the carrier (electron or hole) photoinduced by the PEC electrode is recombined with that from the PV component, the remaining carrier contributes to the half-reaction of water splitting, and the charge remaining from the PV device is transferred to the counter electrode for another half-reaction of water splitting (K. Zhang et al., 2016). In this configuration, the photovoltage provided by a PV device is regarded as an external bias for unassisted water splitting. (K. Zhang et al., 2016)

The final tandem cell arrangement is a combined PV and electrolyser device, as shown in **Figure 2.18 (c)**. The PV device is used for only the photo absorber to generate charge carriers (electricity), which are transferred to the electrolyser (K. Zhang et al., 2016). The PV devices provide direct current (DC) to enable the reduction reaction at the cathode, and the oxidation reaction takes place at the anode. These PV devices are separated from the water electrolyte physically, which can prevent the degradation of PV by water (K. Zhang et al., 2016).

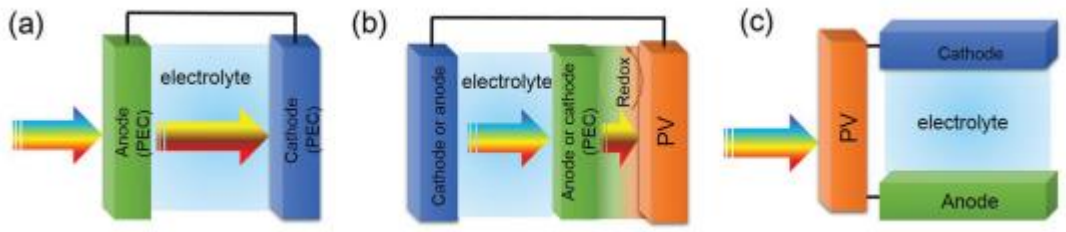

Figure 2.18: The three major tandem cell conformations for unassisted water splitting: a) a PEC tandem cell, b) a PEC/PV tandem cell and c) a PV/electrolyser tandem cell. Source (K. Zhang et al., 2016)

2.6 METAL ORGANIC FRAMEWORKS

2.6.1 Introduction

Metal- Organic Frameworks (MOFs) are a class of porous structures made by linking inorganic and organic units by strong bonds (Furukawa et al., 2013). They are created by joining metal-containing units called secondary building units (SBUs) to organic linkers using strong bonds to create open crystalline frameworks with permanent porosity (Yaghi et al., 2003). MOFs are also called Porous Coordination Polymers (PCPs). Some of the first MOFs using different linkers are shown in **Figure 2.19**.

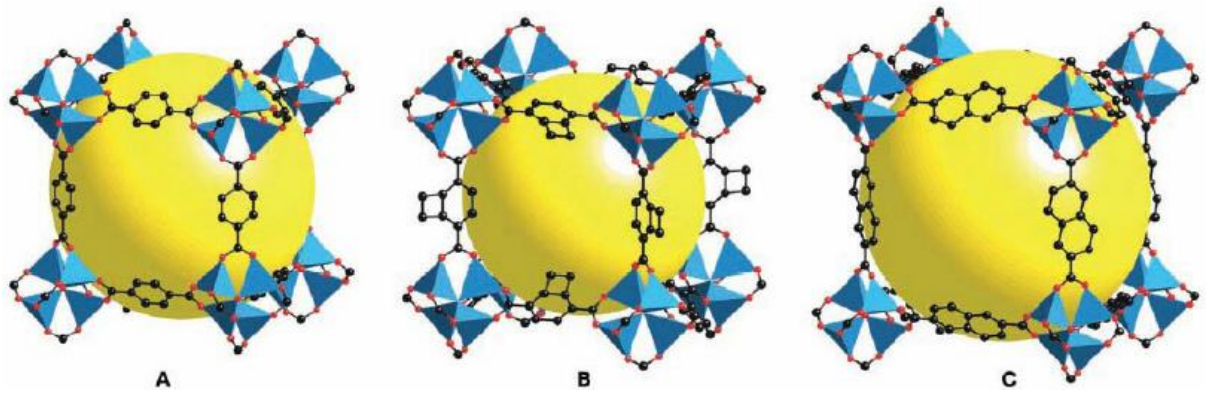

Figure 2.19: Examples of MOF structures A = IRMOF-1, B= IRMOF-6 and C= IRMOF-8

Source (Bureekaew et al., 2008)

MOFs exhibit different properties which include high porosity, diverse composition, tuneable pore structure and versatile functionality. MOFs have large porosity and large internal surface area which range from micro to mesoporous (S. N. Zhao et al., 2018). This makes them good for gas adsorption and separation especially of dihydrogen (Meyer et al., 2015). Metal-Organic Frameworks have different properties which include magnetism, electrical conductivity, luminescence and tuneable light absorption. They are capable of extraordinary physical contortions in response to adsorption and desorption of guest molecules, thermal and photon irradiation as well as mechanical force. They are known to demonstrate swelling, breathing, linker rotation and rearrangement, sub-network displacement and phase changes

induced by deformations at Secondary Building Units (SBUs) (Meyer et al., 2015). MOFs are used as heterogeneous catalysts because of their porous nature (Remya & Kurian, 2019).

2.6.2 MOF Linkers

Organic linkers or ligands are the bridging organic compounds which connect the aggregates or metal centres into prolonged framework structures through coordinate bonding. The linker should possess at least one lone pair of electrons and can be neutral or anionic. The linker can possess multiple binding sites, they can be mono-, di-, tri- or tetravalent. The bridging ligand reacts with a metal ion with more than one vacant or labile site (Sharmin & Zafar, 2016). How the linker binds to the metal node may generate one-dimensional (1D), two-dimensional (2D) or a three-Dimensional (3D) arrangement (Loera-Serna & Ortiz, 2016). The ligands are typically polycarboxylates, phosphonates, amines, pyridyl, sulphonates, imidazolates and phenolates (Sharmin & Zafar, 2016). The chain length of the organic linker varies; however, the use of long linkers can increase the space between vertices, providing expanded structures with large pores (Konstas et al., 2012). MOFs made from large linkers possess interpenetrated structures with a high surface area but they tend to have low porosity. For open structures with large pores and high rigidity, rigid linkers can be used.

The most common linker types, their characteristics and examples of MOFs in which they are used are discussed in the following section.

2.6.2.1 Organic Linkers

2.6.2.1.1 Carboxylates

The carboxylates are also known as O^- donor ligands. They contain the carboxylate group (COO^-). They can be ditopic, tritopic or tetratopic, meaning they have 2-, 3-, or 4-.bonding sites respectively. Ditopic carboxylate linkers are greatly popular because they are readily accessible and they are easy to combine with different SBUs (Aljammal et al., 2019). MOFs constructed from carboxylate-based linkers have been reported to exhibit exceptional stability in water due to the stronger bonds incorporated in the frameworks(Yuan et al., 2018). The most common carboxylate linkers are 1,4-benzene dicarboxylic acid and 2,6- naphthalene dicarboxylic acid which have been used in the synthesis of UiO-67. Terephthalic acid (1,4-benzene dicarboxylic acid) is widely used as it has the ability of carrying additional functional groups such as the amino substituent (Pullen & Ott, 2016). The structures of the most commonly used organic linkers are shown in **Figure 2.20**.

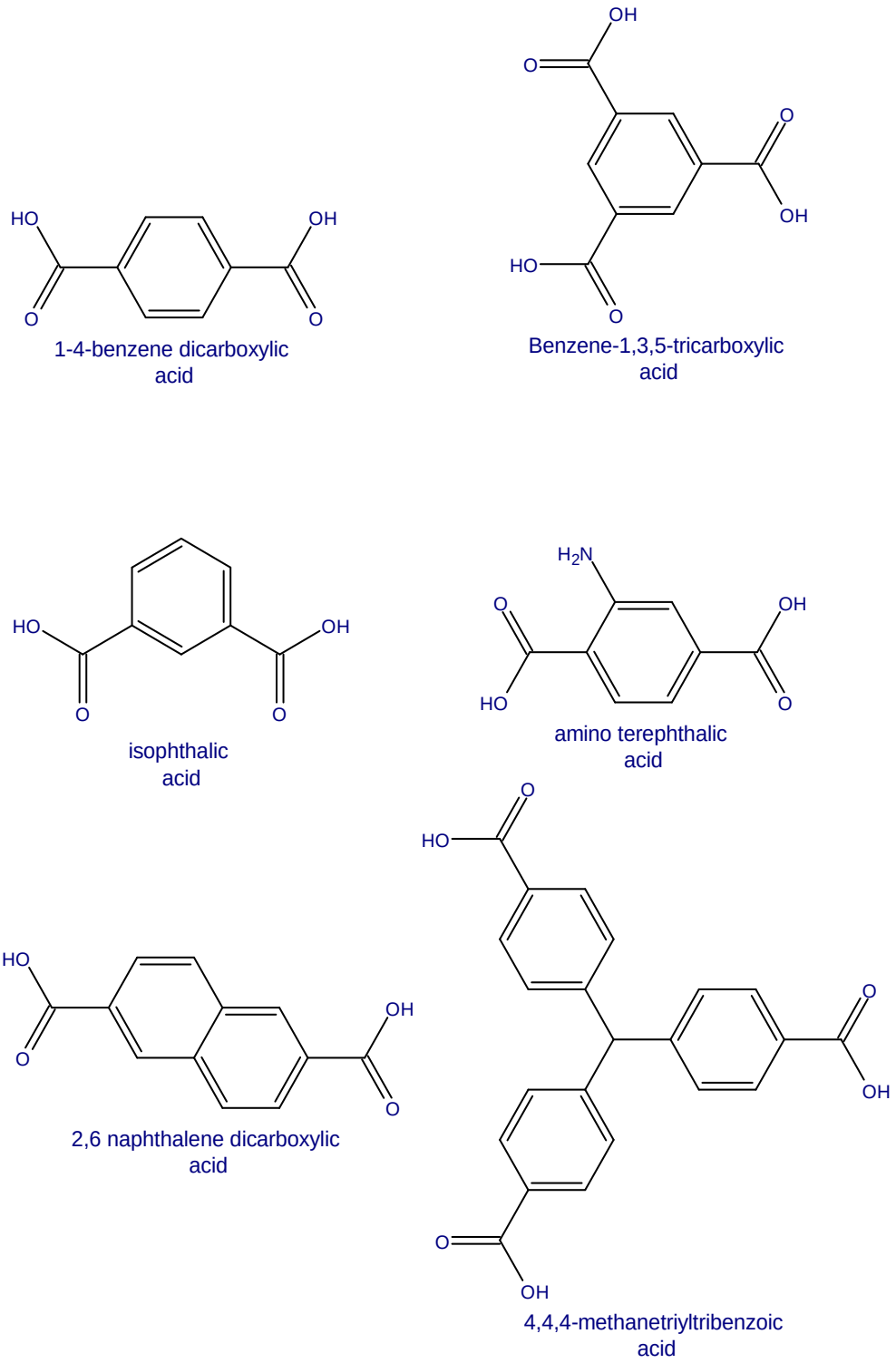

Figure 2.20: Structures of common carboxylate-based linkers.

2.6.2.1.2 Metalloporphyrins

Porphyrins are biological chemicals used in light harvesting and molecular sensing. Porphyrins are heterocyclic macromolecule organic compounds (Aziz et al., 2017). They have been successfully used as linkers in the synthesis of MOFs with excellent photocatalyst

performance (D. Feng et al., 2018) affording catalyst light harvesting and selective sorption in liquid and gas phases. The photocatalytic properties of the porphyrin molecule can be modified in the presence of metal cations within the ring and metalation of the porphyrin units by Zinc and Copper enhances photocatalytic water splitting and CO_2 respectively (Aziz et al., 2017). Metalloporphyrin complexes offer a good opportunity by serving a channel for electron transfer by the hoping mechanism (Cichocka et al., 2020). Examples of porphyrins that have been used as linkers include meso-tetra (4 carboxy-phenyl) porphyrin (TCCP) and 5,10,15,20-tetra (1H-pyrazol-4-yl) porphyrin (H_4TPP). Porphyrin based MOFs include MMPF 5 made using 5,10,15,20-tetrakis (3,5 dicarboxylphenyl) porphyrin as linker (Pereira et al., 2016) , PCN-222 which uses TCCP as the linker (D. Feng et al., 2018) and Al-PMOF (Fateeva et al., 2012).

2.6.2.1.3 Polypyridyl organometallic complexes

Polypyridyl organometallic complexes are coordination complexes which contain the polypyridine ligands which serve as building blocks in supramolecules. Polypyridyl organometallic complexes are multidentate ligands and some of them have the ability to strongly absorb visible light. Most common polypyridyl organometallic complexes include bpy 2.2'-bipyridine and ppy 2 phenylpyridine. Ru-Pt@UiO-67, UiO-67-Ru(bpy)3 and NU-1000 are some of the MOFs that use polypyridyl organometallic complexes as linkers. Examples of pyridine-based linkers are shown in **Figure 2.21**.

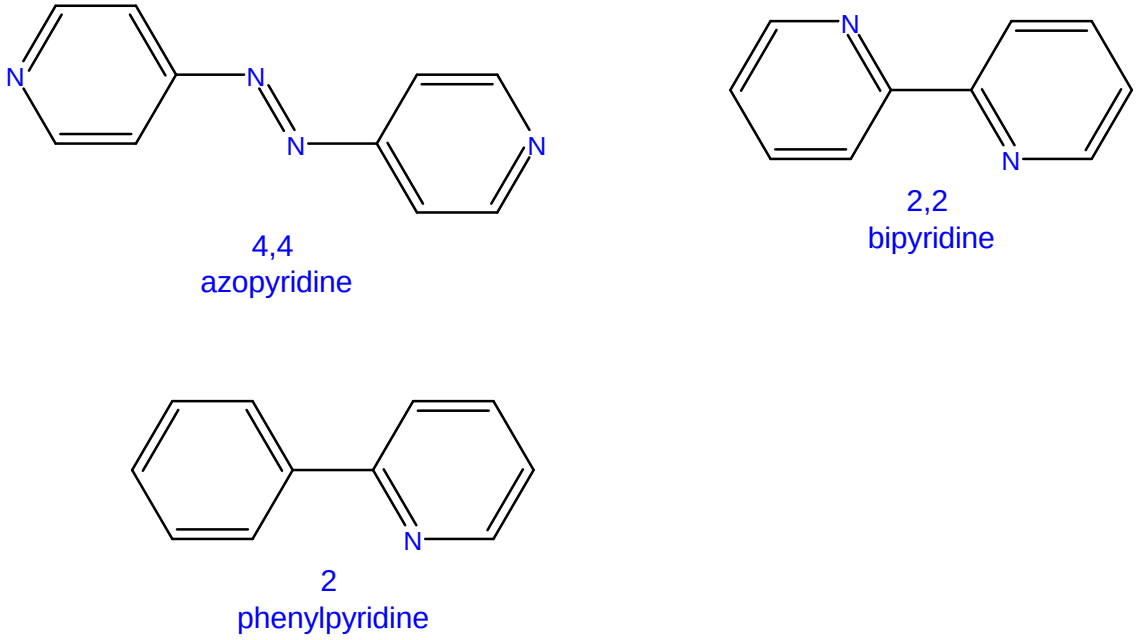

Figure 2.21: Pyridine based linkers

2.6.2.2 Phosphonates

These are phosphonate-based linkers (Salcedo-Abraira et al., 2021). The resulting MOFs are called P –MOFs and they are mainly used in gas separation. P-MOFs have improved thermal, chemical and mechanical stability. Low commercial availability, poor solubility and difficulty in elucidation of resulting structures are some of the challenges encountered when dealing with phosphonate-based MOFs. 2,4,6-tris[4-(phosphonomethyl) phenyl- 1,3,5 triazine is an example of a phosphonate linker and it has been used in the synthesis of IEF-13.

2.6.3 Metal-organic frameworks (MOFs) in water splitting

MOF based photocatalysts have been successfully used for water splitting (Song et al., 2017). Metal-organic frameworks such as MIL-125 (Ti), UiO-66(Zr), MIL-53 (Al), MIL-101 (Cr), PCN-222 and ZIF-8 are the most studied for photocatalytic hydrogen production (N. M. Mohamed et al., 2018). Metal-organic frameworks have a large surface area which allows a high density of catalytic sites for the water splitting reaction to take place. The extremely high porosity of MOFs is responsible for fast and unhindered transport and diffusion of substrates and products from catalytic sites. It is easy to remove MOFs from the water splitting systems as such, they can be used several times. This extends the lifespan of the photocatalyst and reduces waste and contamination. Some MOFs are known to maintain their structure thereby increasing their lifespan and making them cost effective (Fateeva et al., 2012). Metal-organic frameworks can be modified after synthesis and this allows the functional group inside a parent MOF to be transformed into a target group. They have the potential to impart mutable physical, chemical and electrical properties to water-splitting (Meyer et al., 2015)

The availability of an unlimited choice of metal centers, organic linkers in MOFs offers the possibility to expand the use of the spectrum of sunlight. MOFs are versatile in that they can integrate different components such as photosensitizers as well as catalytic constituents in a single material by immobilizing the active sites on metal nodes, organic linkers or encapsulated guest molecules inside the pores (S. N. Zhao et al., 2018).

MOFs have been investigated extensively and they have found use in catalysis, separation, storage and sensing (Song et al., 2017), however, there are also challenges associated with their use which include; toxicity, high fabrication costs, poor selectivity, low capacity and difficulties in recycling/ regeneration. Mohammed et al report that the greatest challenge of MOF- based photocatalysts is their water sensitivity and this limits the application on water-splitting. MOF-based photocatalysts have shown better performances in the presence of noble metals such as Ruthenium and Platinum. However, these noble metals are rare and

expensive, and these are not economically viable. Complex and expensive linkers also present challenges to researchers as it is difficult to predict how they will react.

MOFs are good candidates for chiral functionalization because they have a large number of active sites, they have permanent porosity, they have a large surface area and are generally regarded as stable (Ashraf & Wang, 2018). Compared with other porous materials, homochiral MOFs for asymmetrical catalysis can be synthesized relatively easily using enantiotropic ligands. Chiral MOFs offer a chemically and thermally stable skeleton, mild reaction conditions and reusability of the catalysts. In chiral based MOFs, the reactions can take place in the inner pores which serve as reaction chambers (Bhattacharjee et al., 2018). The use of chiral molecules in water splitting improves the light-harvesting properties of the MOFs.

2.6.4 Mixed-Metal Metal Organic Frameworks

Mixed-Metal Metal Organic Frameworks (MM-MOFs) are Metal Organic Frameworks that contain two or more different metal ions as nodes in their framework (Abednatanzi et al., 2019). MM-MOFs offer opportunities for multifunctionality and tuning (Masoomi et al., 2019)

MM-MOFs can be synthesized during one pot synthesis using multiple metal salts during conventional hydrothermal method (Abednatanzi et al., 2019). For successful one pot synthesis, metal ions with the same coulombic charge, ionic radius and similar chemical behavior are used.

Post synthesis can also be used to synthesize MM-MOFs by soaking in a process called transmetalation. Transmetalation is achieved by soaking the MOFs in a metal solution usually of nitrates or chlorides salts for several days at room temperature or elevated temperature.

Characterization of MM MOFs must go far and beyond to show the presence of two different metals. Often advanced characterization techniques such as XANES and EXAFS are necessary to prove the synthesis of one pot synthesis MM MOF.

X-Ray diffraction is used primarily to identify crystalline phases and for determining crystalline structure. The absence of separate crystal phases is considered as the first indication of successful metal mixing. XRD can also reveal unwanted phase formation and in some cases occurrence of non-metallic phases.

EPR spectroscopy can be used to identify incorporation of paramagnetic metal ions in the framework metal nodes, via the detection of hyperfine interactions with the magnetic nuclei. MM MOFs are used in water splitting to produce hydrogen.

2.6.5 MOF synthesis methods

Metal organic frameworks have been synthesized using different methods. The MOF synthesis methods have evolved from the simplest, the hydrothermal (solvothermal) to methods that manipulate some phenomenon (such as microwaves and ultrasound waves) to speed up the synthesis. Current MOF synthesis methods include: Hydrothermal Method, Microwave assisted, Sonochemical method as well as the Electrochemical method

2.6.5.1 Hydrothermal Method (Solvothermal)

Hydro-(solvo)-thermal strategies are the most universal strategies for preparing MOFs (Q. Zhang et al., 2023). The hydrothermal method is sometimes referred to as the solvothermal method. Hydrothermal synthesis is a process undertaken in a closed vessel known as a hydrothermal autoclave reactor (Tomar & Singh, 2021). The reactor is placed in a conventional oven and the MOFs are synthesized through the conventional electric heating for a given amount of time at a set temperature. The reaction takes place in a solvent medium provided the reaction temperature is higher than the boiling point of the solvent. Besides the sealed hydrothermal autoclave reactors, vials as well as sealed NMR tubes can be used in solvothermal method (Lee et al., 2013). The solvothermal method has been a powerful tool in the discovery of new MOF structures. MOFs synthesised using the hydrothermal method include MOF-5, UiO-66, Cr-MIL-101, IRMOF-3 and Fe-MIL-53 (Lee et al., 2013).

2.6.5.2 Microwave assisted synthesis

Microwave assisted synthesis of MOFs is carried in a closed chamber, where the reaction is carried out under a set temperature for a required amount of time. The reaction mixture is taken in a Teflon lined vessel and placed inside the chamber where microwave irradiation assists molecular rotation that generates heat (Tomar & Singh, 2021). In the microwave method, an oscillating electric field coupled with a permanent dipole moment of the molecules in the synthesis medium is applied and this induces molecular rotations which result in the swift heating of the liquid phase. The microwave synthesis techniques have been used in the accelerated synthesis of nanoporous materials under hydrothermal conditions. It offers fast crystallization, phase selectivity, narrow particle size distribution as well as facile morphology control (Lee et al., 2013). Microwave equipment that has controllable power, fibre optic temperature and pressure controllers is commercially available. MOF synthesised using the microwave assisted method include MOF-5, Cr-MIL-101, Fe-MIL-101-NH_2 Fe-MIL-53 and ZIF-8. The microwave assisted method can be summarised as shown in **Figure 2.22**.

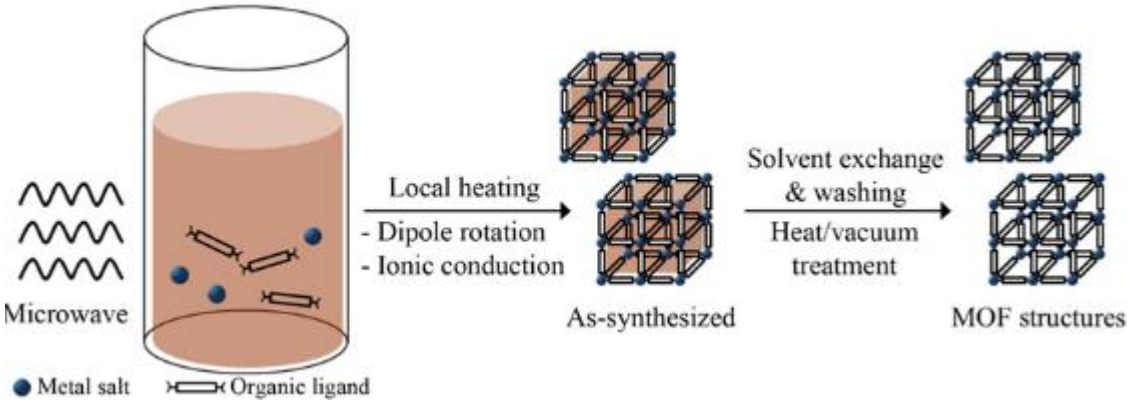

Figure 2.22: Microwave Assisted MOF synthesis (Lee et al., 2013)

2.6.5.3 Sonochemical method

Sonochemical methods in which MOF synthesis is achieved using a sonicator have also been used for MOF synthesis. In sonochemical synthesis, accelerated nucleation can also achieve a reduction in crystallization time and significantly smaller particle size than those obtained in the conventional hydrothermal synthesis. During the sonochemical synthesis, a substrate solution mixture for MOF structure is introduced to a horn-type Pyrex reactor fitted to a sonicator bar with controllable power output. During the sonication, the formation and collapse of bubbles in the solution, during acoustic cavitation, responsible for extremely high local temperatures (~5,000 K) and pressures (~1,000 bar) results in extremely fast heating and cooling rates (>1010K/s) resulting in fine crystallites (Lee et al., 2013). MOFs made using sonochemical methods, include MOF-5, ZIF-8, HKUST-1 and Co-MOF-74.

2.6.5.4 Electrochemical method

In the electrochemical synthesis of MOFs, synthesis is obtained by applying an electric current between two or more electrodes separated by an electrolyte (Tomar & Singh, 2021). The metal input is given by the metal anode under the action of an electric field and the synthesis occurs at the electrode-electrolyte interface. Metal ions are provided continuously through the anodic dissolution of the metal source, which react with the dissolved linker, usually a conducting salt is also added to the reaction medium. Metal deposition on the cathode is prevented by the use of protic solvents, however, during the process hydrogen gas is generated. When using the electrochemical method, it is possible to continuously run the reaction to produce higher solids content than in ordinary batch reactions (Lee et al., 2013). Some of the MOFs synthesised using the electrochemical method, include HKSUT, Al-MIL-101, Al-MIL-53-NH_2

Al-MIL-53 and ZIF-8. The setup for the electrochemical method for the synthesis of MOFs is shown **Figure 2.23.**

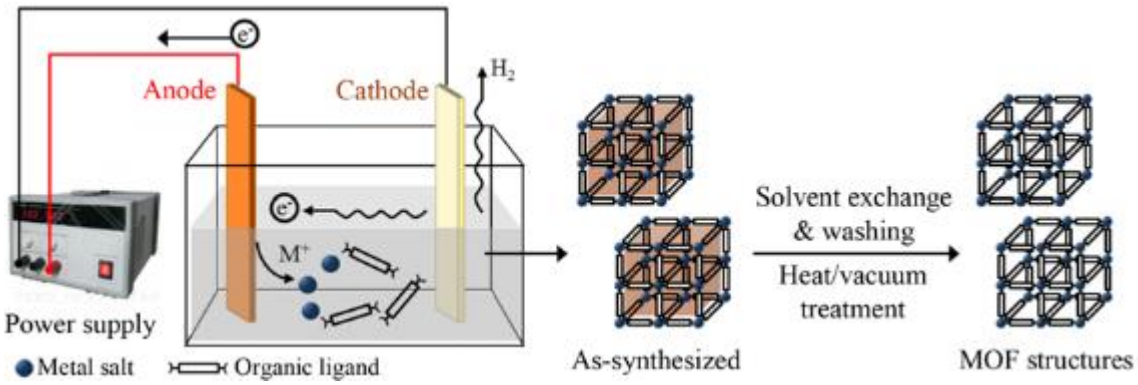

Figure 2.23: Electrochemical method of MOF synthesis (Lee et al., 2013)

2.6.6 Characterization of MOFs

After synthesis, Metal Organic Frameworks are characterised to confirm different parameters. Characterization can be done to evaluate composition, analyse the surface morphology as well as determining the structure of the MOF. When characterizing chiral MOFs, additional methods can be used to confirm chirality of these structures.

2.6.6.1 Nuclear Magnetic Resonance (NMR) Spectroscopy

NMR is an advanced spectroscopic method used to determine the linker ratio, the basic framework, the ligand ratio, and its purity (Tariq et al., 2023). NMR establishes the number and connectivity of certain atoms in a molecule. NMR takes advantage of the magnetic properties of certain nuclei and records the absorption of energy between quantized nuclear energy levels. During an NMR experiment, the spectrophotometer is set to a frequency of a particular nucleus and the spectrum reveals all such nuclei being investigated. In MOF synthesis, NMR is valuable for the study of ligand (linker) formation, since the ligands are generally organic compounds, with NMR active nuclei ^{1}H, ^{13}C, and selected elements such as Pt or Si (Sergeev & Klabunde, 2013).

2.6.6.2 Chemical Composition

The chemical composition of the synthesized MOFs is evaluated by Fourier Transform Infrared Spectroscopy (FTIR). Fourier transform infrared spectroscopy (FTIR) is a technique based on the measurement of the absorption of electromagnetic radiation with wavelengths within the mid-infrared (IR) region (Faraji et al., 2021). The infrared (IR) spectral range provides highly

valuable information due to the excitation of specific fundamental vibrational and vibro-rotational transitions characteristic of molecular species (López-Lorente & Mizaikoff, 2016). In FTIR chemical compounds are identified based on changes in vibrations of atoms when they absorb Infrared (IR) waves as each material has a unique composition and accordingly different arrangement of atoms, no two compounds produce the exact same IR spectrum (Dutta, 2017). The IR spectroscopy can result in a positive identification (qualitative analysis) of every kind of material, additionally, the peak size in the spectrum is a direct indication of the amount of material present.

The absorption of infrared light due to the excitation from the ground vibrational energy state to a higher energy level provides information on the molecular structure (particularly individual functional groups), molecular interactions as well as supramolecular assemblies (Dendisová et al., 2018) .

When the infrared light is irradiated into the sample, depending on the molecular structure the molecule may vibrate, stretch or twists and because the bonding is different in each molecule, the vibrations are also different.

The FTIR spectrum gives the transmittance versus the wavenumber (reported in cm^{-1}), where the wavenumber is the inverse of the wavelength. A typical FTIR spectrum is as shown in **Figure 2.24**.

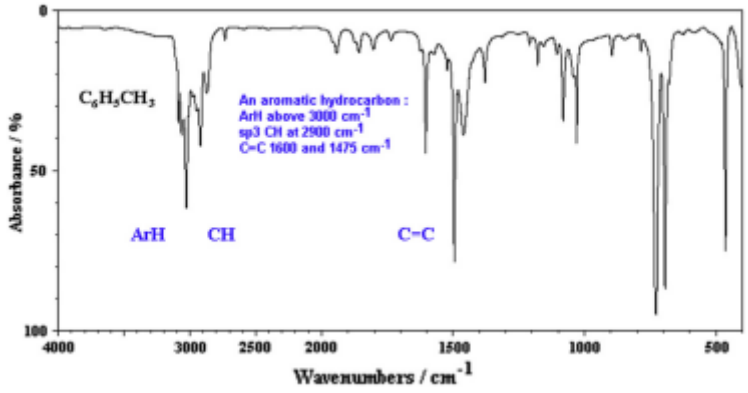

Figure 2.24: Typical FTIR spectrum (Dutta, 2017)

All organic molecules absorb IR radiation and depending on which energies of radiation are absorbed, bonds between atoms will vibrate by stretching, bending and twisting. The

molecules will only vibrate at a specific frequency. Depending on the molecule, each vibration will absorb specific wavelengths of IR radiation which are also shown as the reciprocal of the wavelength. Infrared tables are used to then assign the different peaks to the different chemical compounds.

There are also several modes of IR spectroscopy. The first one is transmission IR spectroscopy, which involves passing the IR beam through the sample and an alternative method, which uses reflecting methods such as ATR IR spectroscopy (H. Wang & Chu, 2013).

Infrared spectroscopy permits the detection of functional groups as well as molecules that are adsorbed on different surfaces, it also allows the monitoring changes of the surface chemistry (López-Lorente & Mizaikoff, 2016).

2.6.6.3 Surface Morphology

Scanning Electron Microscopy (SEM) is a microscopic technique that is used to evaluate the surface morphology of the MOFs. A Scanning Electron Microscope (SEM) uses a focused beam of electrons to create a magnified image of a sample. The electron beam is scanned in a regular pattern across the surface of the sample and the electrons ejected from the sample are used to create an image. SEM images have no colour.

SEM uses two different types of detectors, namely: a secondary electron detector and backscattered electron detector. Secondary electrons are produced when the incident electrons excite electrons in the sample and lose part of its energy in the process. The excited electrons move towards the surface of the sample and if they have sufficient energy, they excite the surface. Backscattered electrons consist of high energy electrons that are reflected or back - scattered out of the specimen of interest. The shades of grey in a secondary electron image are created by the topography of the sample while the shades of grey in a backscattered electron image stem from the atomic weight of the constituent elements in the sample. Typical SEM images are shown in **Figure 2.15**.

SEM is used to characterize the properties of crystals such as size, quality, structure, and composition through optical analysis (Tariq et al., 2023). Field Emission Scanning Electron Microscopy (FESEM) is also used to evaluate the microstructure of materials. In FESEM, the electrons are liberated by a field emission source.

2.6.6.4 Energy dispersive spectroscopy

SEM can be used to determine the elemental composition of materials, when coupled with the Energy Dispersive Spectrometer (EDS), to give SEM-EDS. SEM-EDS, sometimes referred to as SEM-EDX can be used to evaluate the elemental composition of the MOFs. EDX utilizes the X-Rays emitted from the sample, during the bombardment by the electron beams to identify the different elements that will be present in a sample. The electron beam hits the inner shell of an atom, removing an electron from the shell, at the same time leaving a positively charged electron hole. When the electron is removed, it attracts another electron from an outer shell to fill the vacancy as shown in **Figure 2.25**. As another electron passes from the outer higher-energy to the inner lower-energy shell of the atom, there is excess energy given off and this is released in the form of an X-ray. The energy of this X-ray is particular to the exact element and resulting transition.

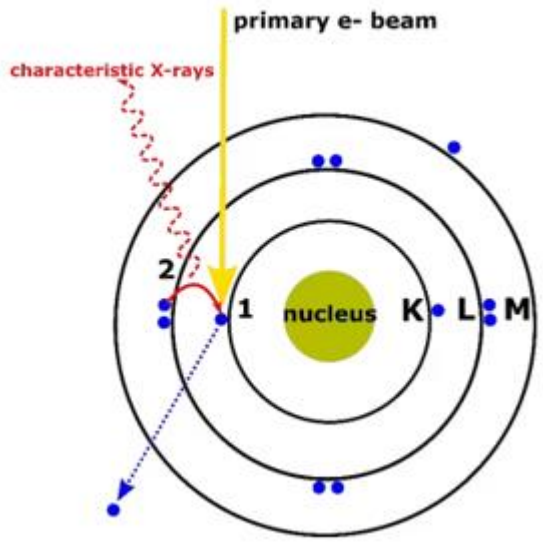

Figure 2.25: The processes taking place during EDS. Source (Nanakoudis, 2019)

The X-rays that are emitted during the process are then collected by a silicon drift detector, which measures the signal and interprets it using software. The obtained chemical information can be visualized in many different ways including line scans and elemental mapping. In this way, X-rays can be used to identify each element that exists in a sample (Antonis Nanakoudis,

2019). EDS is used for both qualitative and quantitative analysis, making it possible for users to identify the type of element that are present as well as the percentages of each element's concentration in a given sample.

Additional methods such as: X-Ray Photoelectron Spectroscopy (XPS), Electron Energy Loss Spectroscopy (EELS) as well as Auger Electron Spectroscopy (AES) are also used to evaluate the composition, as well as the surface analysis of the MOFs (W. Zhang et al., 2020).

2.6.6.5 Photocatalytic activity

Photocatalytic activity of the MOFs is evaluated using Ultra-Violet Diffuse Reflectance Spectroscopy (UV-DRS) for solid samples while a UV-Vis Spectrophotometer is used to evaluate the photocatalytic activity of liquid samples. Ultraviolet–visible (UV–vis) spectroscopy encompasses absorption spectroscopy and reflectance spectroscopy in the UV–vis spectra (H. Wang & Chu, 2013). UV-Vis spectroscopy is an analytical technique that measures the amount of discrete wavelengths of UV or visible light that are absorbed by or transmitted through a sample in comparison to a reference or blank sample usually $BaSO_4$ for UV-DRS and distilled water for UV-Vis. Molecules that have pi-electrons or non-bonding electrons can absorb ultraviolet or visible light energy and be excited to higher anti-bonding molecular orbitals (H. Wang & Chu, 2013). Uv-Vis can be used to qualitatively identify materials based on the λ_{max}, the maximum wavelength at which the material absorbs the ultra-violet and/or visible light. When evaluating the photocatalytic activity of a material, it is important to evaluate the band gap energy. The band gap energy of a material is the energy needed to excite an electron from the valence band to the conduction band (Makula et al., 2018). There are a number of methods for evaluating the band gap energy for a photocatalyst which include Tauc plots. Tauc plots are utilized in estimating the band gap energy of the photocatalysts using the Tauc method, which is expressed using equation 2.7.

$$(\alpha h\nu)^n = (h\nu - E_g) \qquad \text{Equation 2.7}$$

Where h is Planck's constant, (6.63×10^{-34} J/s)

v is the speed of light (3.0×10^8 m/s)

α is the absorption coefficient

E_g is the band gap energy

2.6.6.6 Thermal Stability

The thermal stability of the MOFs is evaluated using Thermogravimetric Analysis (TGA). Thermogravimetric Analysis is a technique in which the mass of a substance is monitored as a function of temperature or time as the sample specimen is subjected to a controlled temperature program in a controlled atmosphere. In TGA the sample's weight is measured as it is heated in a furnace. Incorporated within the TGA machine is a sample pan which is supported by a precision balance. The pan is housed in a furnace and is heated during the experiment. The changes in mass of the sample is closely monitored during the experiment. To control the environment, a sample purge gas is used. This gas may be inert (Argon, Helium or Nitrogen) or a reactive gas (Oxygen) that flows over the sample and exits through an exhaust. This technique is used as a means of analysing the thermal stability of a sample as well as the composition/purity of a sample. TGA results are communicated through a thermal curve. The TGA thermal curve is displayed from left to right. The descending TGA thermal curve indicates a weight loss occurred.

2.6.6.7 Crystallinity

The crystallinity nature of a photocatalyst used in water splitting greatly affects its performance, when the photocatalyst is crystalline in nature better charge separation is achieved as the electrons and holes can move freely without being trapped or combined (Nishioka et al., 2023; Takanabe, 2017). The crystal structure and size are evaluated using X-Ray Diffraction (XRD). X-ray diffraction (XRD) uses X-rays to investigate and quantify the crystalline nature of materials by measuring the diffraction of X-rays from the planes of atoms within the material. XRD is sensitive to both the type of and relative position of atoms in the material as well as the length scale over which the crystalline order persists. Since material has particular lattice structure, specific diffraction pattern will be formed based on Bragg's equation.

$$n\lambda = 2d \sin\theta \qquad \text{Equation 2.8}$$

Where

d	distance between neighboring diffracting planes
θ	incident angle between incident wave and planes
λ	wavelength of incident wave and
n	any integer.

The analysed material is finely ground, homogenized, and average bulk composition is determined.

2.6.6.8 Evaluation of Chirality

Chirality is an interdisciplinary phenomenon and as a concept, chirality is often conveyed in terms of the left and right hands specular images, which however is an oversimplified picture of a much more complex subject [Andrea Steffani]. The most common method of evaluating chirality is circular dichroism as well as electrochemical methods such as cyclic voltammetry in chiral recognition. Chiral recognition is a chemical interaction, frequently occurring in living systems, by which a given chiral molecule (receptor/host) recognizes a particular stereoisomer (substrate/guest) (Pappalardo & Parisi, 2008). Chiral molecules may create a totally different effect on many processes such as biological processes in nature and life. In general, just one out of a pair of enantiomers produces the characteristic effect and the other either has no effect or has a totally different (and sometimes toxic) effect due to the pair interaction energy of the two. Various techniques such as: polarimeter, enzymes (found in living systems), Nuclear Magnetic Resonance Spectroscopy (NMR), cyclic voltammetry (CV) and electrochemical impedance spectroscopy (EIS), chromatography, liquid chromatography, capillary electrophoresis, etc., have been applied in chiral recognition (Stefani et al., 2023).

2.6.6.9 Inductively Coupled Plasma-Optical Emission Spectroscopy (ICP-OES)

Inductively Coupled Plasma-Optical Emission Spectroscopy is an analytical technique that is used to identify the atomic composition of a given sample. The technique, makes use of the unique photophysical signals of each element to successfully detect the type and relative amount of each element in the complexity of a compound. ICP-OES has advantages which include: fast and simultaneous determination of multiple elements, determination at trace-level concentrations of metals, as well as tracing little concentration changes. Additionally, ICP-OES has good reproducibility and wide dynamic linear range (Faraji et al., 2021).

2.6.7 MOFs used in this study

2.6.7.1 Zn-MOF

The Zn-MOF used in this study was first reported by Altaf et al in 2018 (Altaf et al., 2018). The Zn-MOF can be classified as a multivariate metal organic framework (MTV MOF) because it contains more than one linker. Zn-MOF is synthesized using two different linkers :

terephthalic acid (H_2BDC or bdc) and N,N'-bis(pyridin-4-ylmethyl)cyclohexane-1,4-diamine (bpcda).

2.6.7.1.1 Structural description of the Zn-MOF

The structure of the as-synthesised Zn-MOF was deduced to show, each bdc dianion connecting to adjacent Zn^{2+} centres in a bridging trans-monodentate mode which results in zigzag chains that are further extended by the bpcda linkers to form a three-dimensional diamondoid framework (Altaf et al., 2018). The Zn^{2+} compound has a dia like topology by considering Zn^{2+} centre as 4-connected nodes and bpcda, bdc as linkers. Each Zn^{2+} centre node is connected to four neighbours, to form an adamantine-like cage, which is a characteristic building block for a diamondoid framework. The crystallographic data of the Zn-MOF as deposited by Altaf et al is available in Cambridge Crystallography Data Centre (CCDC) as number 1452209 (Muhammad Altaf et al., 2017). According to the deposited data, the Zn-MOF is identified as catena-[(μ-N1,N4-bis[(pyridin-4-yl)methyl]cyclohexane-1,4-diamine)-(μ-terephthalato)-zinc] with molar mass of 525.89g/mol has the molecular structure as shown in **Figure 2.26.**

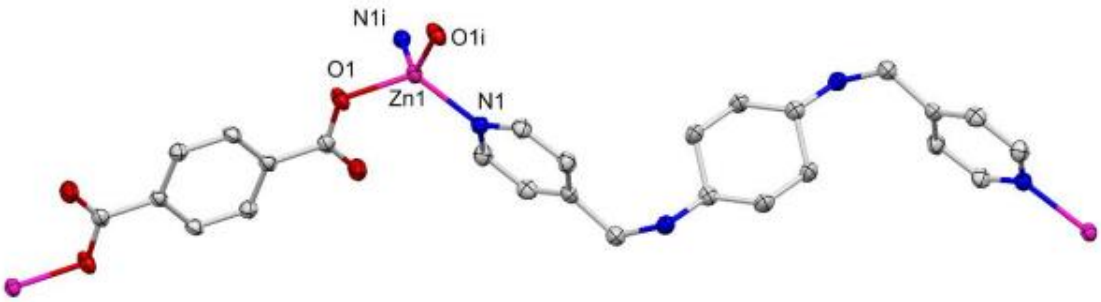

Figure 2.26: Molecular Structure of Zn-MOF: Source (Altaf et al., 2018 Supp. 1S)

This MOF crystalizes in a monoclinic crystal system with space group C2/c, The rest of the cell parameters are given in **Table 2.2.**

Table 2.2 Crystallographic data of Zn-MOF

	Zn-MOF
Cell length a (Å)	18.9102(4)
Cell length b (Å)	6.1743(2) (5)
Cell length c (Å)	20.0362(4)
Cell angle α (°)	90.00
Cell angle beta β (°)	95.453(2
Cell angle gamma γ (°)	90.00
Cell volume (Å^3)	2328.78(10)
Cell formula units Z	4

The 3D structure showing the unit cell of the Zn-MOF is as given in **Figure 2.27**. Each unit cell contains four repeat units of the Zn-MOF.

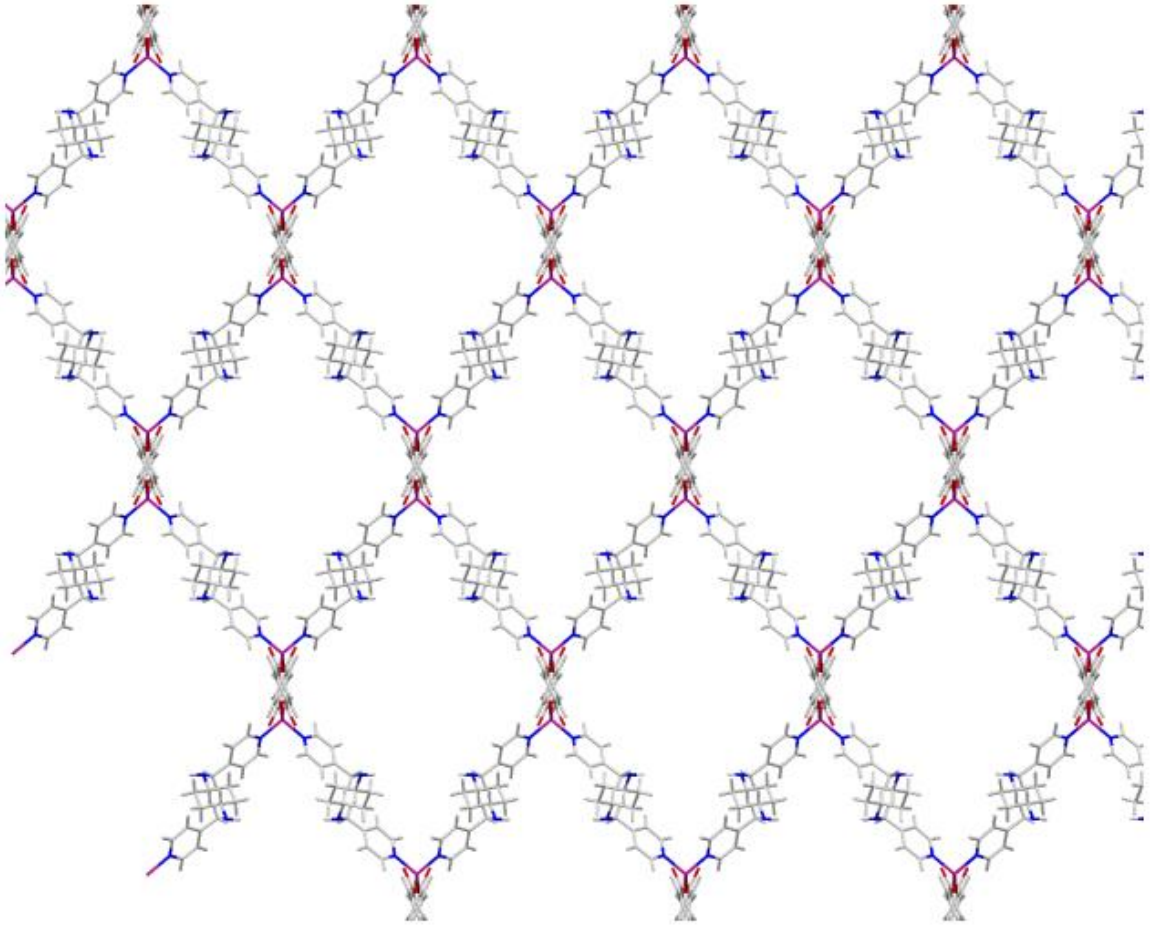

Figure 2.27 3D extended structure of Zn-MOF (Altaf et al., 2018 Supp. 2S).

2.6.7.2 MIL 53

MIL 53 (Fe), is the most common iron-based MOF, where the acronym MIL stands for Materials of Institute Lavoisier, the Institute at which the MIL group of MOFs were first synthesised. MIL 53 was first described as a chromium (Cr^{3+}) material in 2002 (Millange et al., 2002). There are different variants of MIL 53, depending on the metal coordinating centre, MIL 53(Cr), MIL 53(Al), MIL 53(Ga) and MIL 53(Sc) have also been reported. MIL 53(Fe) has major advantages compared with other MOFs, which include chemical stability, the use of iron (a nontoxic and extensively available metal) as well as a green and sustainable manufacturing process.

2.6.7.2.1 Structural description of MIL 53

MIL 53 (Fe) is obtained by a merger between iron (III) cations and 1,4-dicarboxylic acid, to yield a 3D network which contain FeO_6 hexagonal chains and dicarboxylate anions. A series of MIL 53 compounds were deposited into the Cambridge Structural Database (CSD) by Whitfield et al in 2005 (Whitfield et al., 2005). The compounds vary from one another depending on the solvents that were used to synthesise them. The MIL 53 investigated in this

study was synthesised in the presence of N'-N Dimethylformamide, from the reported compounds the deposited ML 53 synthesised in N'-N Dimethylformamide is deposited under Cambridge Crystallographic Data Centre (CCDC) number 258445 Whitfield et al., 2006). The compound was reported as catena-((μ_4-Benzene-1,4-dicarboxylato)-(μ_2-dimethylformamide)-iron(ii)) with chemical formula C_{11} H_{11} Fe N O_5 and molar mass 293.06 g/mol.

In MIL 53, the organic linker, benzene 1,4-dicarboxylate (terephthalate, or BDC) is connected to 4 different metal centres, with each dicarboxylate function bridging a separate pair of metal centres which in turn bridges to another pair of metals where the second dicarboxylate binds in a similar manner (Millange & Walton, 2018). Each metal centre is associated with the oxygens of four different carboxylate groups from four different linkers, which complete the octahedral coordination of the metal as shown in **Figure 2.28.**

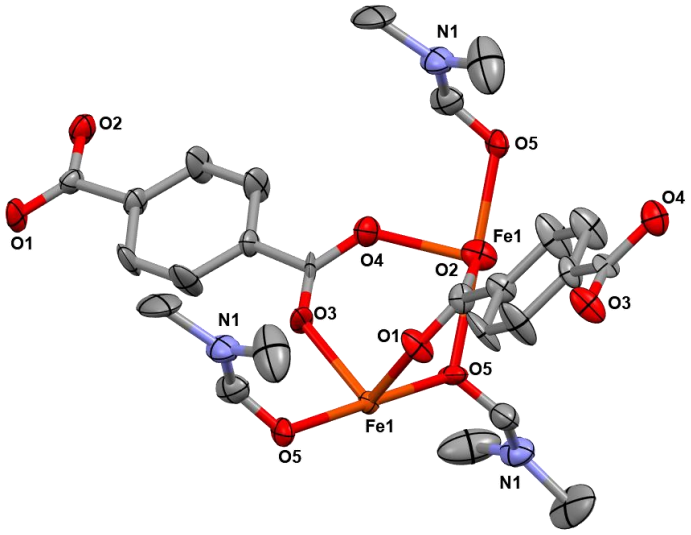

Figure 2.28: Molecular structure of as synthesised MIL 53 (Source cif file 258445) (Whitfield et al., 2006)

This MOF crystalizes in a polyhedral crystal system with space group P n 2_1. The rest of the cell parameters are given in **Table 2.3**.

Table 2.3: Crystallographic data of MIL 53

	MIL 53
Cell length a (Å)	19.4223(15)
Cell length b (Å)	7.3022(5)
Cell length c (Å)	8.8468(7)
Cell angle α (°)	90.00
Cell angle beta β (°)	90.00
Cell angle gamma γ (°)	90.00
Cell volume (Å^3)	1254.70(16)
Cell formula units Z	4

Each metal centre is connected to oxygens from four different carboxylate groups from four different linkers, this in turn completes the octahedral coordination of the metal. The 3D structure of the as-synthesised MIL 53, showing how the organic linker, benzene 1,4-dicarboxylate (bdc) is connected to four different metal centres is shown in the unit cell shown in **Figure 2.29**. The presence of DMF in the MIL 53 before activation is also observed.

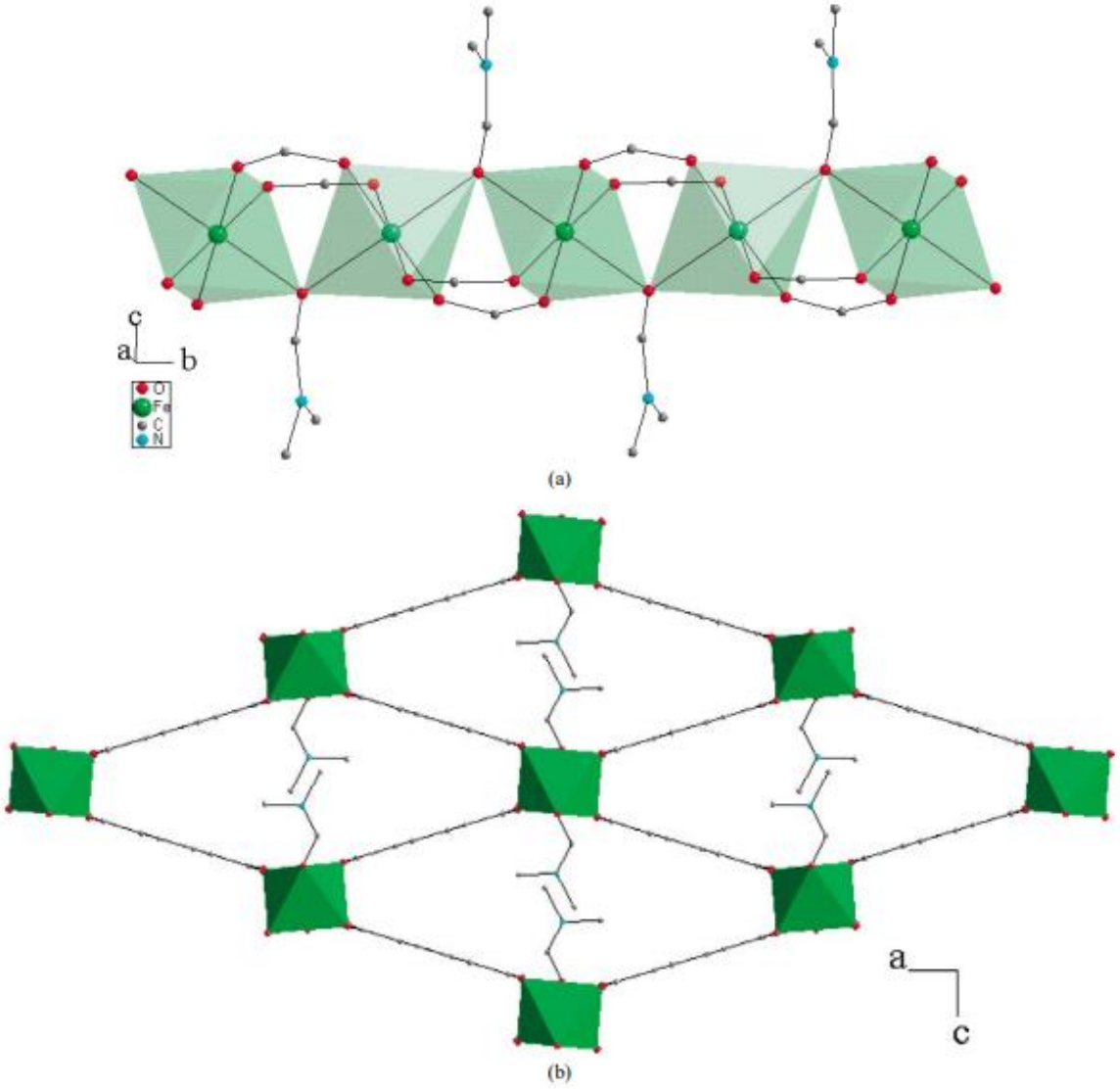

Figure 2.29 (a) Octahedral chain of MIL 53(Fe) (b) Projection of the structure of MIL 53 along the plane (010) (Whitfield et al., 2005)

2.7 CONCLUSION

Improving the overall efficiency of the photoelectrochemical cell remains a big challenge in the quest for developing reliable renewable energy resources. This chapter showed the different types photocatalyst/semiconductor materials that are available for photoelectrocatalytic water splitting. Different materials that have been used as chiral photoelectrodes and the methods for evaluating their effectiveness have been identified, as well as the different electrochemical techniques that can be used in water splitting. The chemistry of Metal Organic Frameworks, their properties, the synthesis methods available as well as the characterization methods were also explored.

Based on the above findings, it has been noted that MOFs have been used in water splitting because of their high porosity, large surface area as well as their ability to have post synthetic modification. Founded on these properties of MOFs and having looked at the advantages of chiral molecules in water splitting, i.e ability to act as spin filters. Further research should look at the application of chiral Metal Organic Frameworks in water splitting.

2.8 REFERENCES

1) Abednatanzi, S., Gohari Derakhshandeh, P., Depauw, H., Coudert, F. X., Vrielinck, H., Van Der Voort, P., & Leus, K. (2019). Mixed-metal metal-organic frameworks. In *Chemical Society Reviews* (Vol. 48, Issue 9, pp. 2535–2565). Royal Society of Chemistry. https://doi.org/10.1039/c8cs00337h
2) Afzali, N., Tangestaninejad, S., Keshavarzi, R., Mirkhani, V., Nematollahi, J., Moghadam, M., Mohammadpoor-Baltork, I., Reimer, M., Olthof, S., Klein, A., & Gimenez, S. (2020). Hierarchical Ti-Based MOF with Embedded RuO2Nanoparticles: A Highly Efficient Photoelectrode for Visible Light Water Oxidation. *ACS Sustainable Chemistry and Engineering*, *8*(50), 18366–18376. https://doi.org/10.1021/acssuschemeng.0c04682
3) Al-Aisaee, N., Alhabradi, M., Yang, X., Alruwaili, M., Rasul, S., & Tahir, A. A. (2023). Fabrication of WO3 /Fe2O3 heterostructure photoanode by PVD for photoelectrochemical applications. *Solar Energy Materials and Solar Cells*, *263*. https://doi.org/10.1016/j.solmat.2023.112561
4) Ali, A., Mangrio, F. A., Chen, X., Dai, Y., Chen, K., Xu, X., Xia, R., & Zhu, L. (2019). Ultrathin MoS2 nanosheets for high-performance photoelectrochemical applications: Via plasmonic coupling with Au nanocrystals. *Nanoscale*, *11*(16), 7813–7824. https://doi.org/10.1039/c8nr10320h
5) Aljammal, N., Jabbour, C., Chaemchuen, S., Juzsakova, T., & Verpoort, F. (2019). Flexibility in metal–organic frameworks: A basic understanding. *Catalysts*, *9*(6):512. https://doi.org/10.3390/catal9060512
6) Altaf, M., Sohail, M., Mansha, M., Iqbal, N., Sher, M., Fazal, A., Ullah, N., & Isab, A. A. (2018). Synthesis, Characterization, and Photoelectrochemical Catalytic Studies of a Water-Stable Zinc-Based Metal–Organic Framework. *ChemSusChem*, *11*(3), 542–546. https://doi.org/10.1002/cssc.201702122
7) Altaf, M., Sohail, M., Mansha, M., Iqbal, N., Sher, M., Fazal, A., Ullah, N., & Isab, A. A. (2018). Synthesis, Characterization, and Photoelectrochemical Catalytic Studies of a Water-Stable Zinc-Based Metal-Organic Framework. *ChemSusChem*, *11*(3 Supporting Information), 542–546.
8) Anantharaj, S., & Noda, S. (2022). How properly are we interpreting the Tafel lines in energy conversion electrocatalysis? *Materials Today Energy*, *29*. https://doi.org/10.1016/j.mtener.2022.101123
9) Appel, A. M., & Helm, M. L. (2014). Determining the overpotential for a molecular electrocatalyst. *ACS Catalysis*, *4*(2), 630–633. https://doi.org/10.1021/cs401013v
10) Aralekallu, S., Sajjan, V. A., Palanna, M., Prabhu C P, K., Hojamberdiev, M., & Sannegowda, L. K. (2020). Ni foam-supported azo linkage cobalt phthalocyanine as

an efficient electrocatalyst for oxygen evolution reaction. *Journal of Power Sources*, *449*. https://doi.org/10.1016/j.jpowsour.2019.227516

11) Ashraf, S., & Wang, B. (2018). *Chirality in Porous Functional Materials*. In Chirality from Molecular Electronic States DOI: 10.5772/intechopen.82288
12) Aziz, A., Ruiz-Salvador, A. R., Hernández, N. C., Calero, S., Hamad, S., & Grau-Crespo, R. (2017). Porphyrin-based metal-organic frameworks for solar fuel synthesis photocatalysis: Band gap tuning: Via iron substitutions. *Journal of Materials Chemistry A*, *5*(23), 11894–11904. https://doi.org/10.1039/c7ta01278k
13) Bedoya-Lora, F. E., Holmes-Gentle, I., & Hankin, A. (2021). Electrochemical techniques for photoelectrode characterisation. In *Current Opinion in Green and Sustainable Chemistry* (Vol. 29). Elsevier B.V. https://doi.org/10.1016/j.cogsc.2021.100463
14) Bhattacharjee, S., Khan, M. I., Li, X., & Zhu, Q. (2018). *Recent Progress in Asymmetric Catalysis and Chromatographic Separation by Chiral Metal – Organic Frameworks*. *Figure 1*. https://doi.org/10.3390/catal8030120
15) Bozoglian, F., Romain, S., Ertem, M. Z., Todorova, T. K., Sens, C., Mola, J., Rodríguez, M., Romero, I., Benet-Buchholz, J., Fontrodona, X., Cramer, C. J., Gagliardi, L., & Llobet, A. (2009). The Ru-Hbpp water oxidation catalyst. *Journal of the American Chemical Society*, *131*(42), 15176–15187. https://doi.org/10.1021/ja9036127
16) Brillet, J., Comuz, M., Formal, F. Le, Yum, J. H., Grätzel, M., & Sivula, K. (2010). Examining architectures of photoanode-photovoltaic tandem cells for solar water splitting. *Journal of Materials Research*, *25*(1), 17–24. https://doi.org/10.1557/jmr.2010.0009
17) Bureekaew, S., Shimomura, S., & Kitagawa, S. (2008). Chemistry and application of flexible porous coordination polymers. *Science and Technology of Advanced Materials*, *9*(1). https://doi.org/10.1088/1468-6996/9/1/014108
18) Carmeli, I., Kumar, K. S., Heifler, O., Carmeli, C., & Naaman, R. (2014). Spin Selectivity in Electron Transfer in Photosystem I. *Angewandte Chemie*, *126*(34), 9099–9104. https://doi.org/10.1002/ange.201404382
19) Chatterjee, S., & Shyamal, S. (2023). Design and advances of semiconductors for photoelectrochemical water-splitting. In *Solar-Driven Green Hydrogen Generation and Storage* (pp. 141–156). Elsevier. https://doi.org/10.1016/B978-0-323-99580-1.00007-8
20) Chen, Q., Fan, G., Fu, H., Li, Z., & Zou, Z. (2018). Tandem photoelectrochemical cells for solar water splitting. In *Advances in Physics: X* (Vol. 3, Issue 1, pp. 863–884). Taylor and Francis Ltd. https://doi.org/10.1080/23746149.2018.1487267

21) Choi, W., Shin, H. C., Kim, J. M., Choi, J. Y., & Yoon, W. S. (2020). Modeling and applications of electrochemical impedance spectroscopy (Eis) for lithium-ion batteries. In *Journal of Electrochemical Science and Technology* (Vol. 11, Issue 1, pp. 1–13). Korean Electrochemical Society. https://doi.org/10.33961/jecst.2019.00528

22) Cichocka, M. O., Liang, Z., Feng, D., Back, S., Siahrostami, S., Wang, X., Samperisi, L., Sun, Y., Xu, H., Hedin, N., Zheng, H., Zou, X., Zhou, H. C., & Huang, Z. (2020). A Porphyrinic Zirconium Metal-Organic Framework for Oxygen Reduction Reaction: Tailoring the Spacing between Active-Sites through Chain-Based Inorganic Building Units. *Journal of the American Chemical Society*, *142*(36), 15386–15395. https://doi.org/10.1021/jacs.0c06329

23) Cox, N., Retegan, M., Neese, F., Pantazis, D. A., Boussac, A., & Lubitz, W. (2014). Electronic structure of the oxygen-evolving complex in photosystem II prior to O-O bond formation. *Science*, *345*(6198). https://doi.org/10.1126/science.1254910

24) Dendisová, M., Jeništová, A., Parchaňská-Kokaislová, A., Matějka, P., Prokopec, V., & Švecová, M. (2018). The use of infrared spectroscopic techniques to characterize nanomaterials and nanostructures: A review. In *Analytica Chimica Acta* (Vol. 1031, pp. 1–14). Elsevier B.V. https://doi.org/10.1016/j.aca.2018.05.046

25) Dutta, A. (2017). Fourier Transform Infrared Spectroscopy. In *Spectroscopic Methods for Nanomaterials Characterization* (Vol. 2, pp. 73–93). Elsevier. https://doi.org/10.1016/B978-0-323-46140-5.00004-2

26) Elgrishi, N., Rountree, K. J., McCarthy, B. D., Rountree, E. S., Eisenhart, T. T., & Dempsey, J. L. (2018). A Practical Beginner's Guide to Cyclic Voltammetry. *Journal of Chemical Education*, *95*(2), 197–206. https://doi.org/10.1021/acs.jchemed.7b00361

27) El-Khouly, M. E., El-Mohsnawy, E., & Fukuzumi, S. (2017). Solar energy conversion: From natural to artificial photosynthesis. *Journal of Photochemistry and Photobiology C: Photochemistry Reviews*, *31*, 36–83. https://doi.org/10.1016/J.JPHOTOCHEMREV.2017.02.001

28) Faraji, M., Yamini, Y., & Salehi, N. (2021). Characterization of magnetic nanomaterials. In *Magnetic Nanomaterials in Analytical Chemistry* (pp. 39–60). Elsevier. https://doi.org/10.1016/B978-0-12-822131-0.00014-5

29) Fareza, A. R., Nugroho, F. A. A., Abdi, F. F., & Fauzia, V. (2022). Nanoscale metal oxides-2D materials heterostructures for photoelectrochemical water splitting—a review. *Journal of Materials Chemistry A*. https://doi.org/10.1039/d1ta10203f

30) Fateeva, A., Chater, P. A., Ireland, C. P., Tahir, A. A., Khimyak, Y. Z., Wiper, P. V., Darwent, J. R., & Rosseinsky, M. J. (2012). A Water-Stable Porphyrin-Based Metal-Organic Framework Active for Visible-Light Photocatalysis. *Angewandte Chemie*, *124*(30), 7558–7562. https://doi.org/10.1002/ange.201202471

31) Feng, D., Wang, K., Wei, Z., Chen, Y.-P., Simon, C. M., Arvapally, R. K., Martin, R. L., Bosch, M., Liu, T.-F., Fordham, S., Yuan, D., Omary, M. A., Haranczyk, M., Smit, B., & Zhou, H.-C. (2018). Metal Organic Frameworks and Ligands for MOF Synthesis. *Strem Chemicals. Inc.* www.strem.com

32) Feng, T., Chen, W., Xue, J., Cao, F., Chen, Z., Ye, J., Xiao, C., & Lu, H. (2023). Spin Polarization of Chiral Amorphous Fe-Ni Electrocatalysts Enabling Efficient Electrochemical Oxygen Evolution. *Advanced Functional Materials*, *33*(27), 1-10. https://doi.org/10.1002/adfm.202215051

33) Freire, D. M., Beeri, D., Pota, K., Johnston, H. M., Palacios, P., Pierce, B. S., Sherman, B. D., & Green, K. N. (2020). Hydrogen peroxide disproportionation with manganese macrocyclic complexes of cyclen and pyclen. *Inorganic Chemistry Frontiers*, *7*(7), 1573–1582. https://doi.org/10.1039/c9qi01509d

34) Fujishima, A., & Honda, K. (1972). Electrochemical photolysis of water at a semiconductor electrode. *Nature*, *238*(5358), 37-38. https://doi.org/10.1038/238037a0

35) Furukawa, H., Cordova, K. E., O'Keeffe, M., & Yaghi, O. M. (2013). The chemistry and applications of metal-organic frameworks. In *Science* (Vol. 341, Issue 6149). https://doi.org/10.1126/science.1230444

36) Garcés-Pineda, F. A., Blasco-Ahicart, M., Nieto-Castro, D., López, N., & Galán-Mascarós, J. R. (2019). Direct magnetic enhancement of electrocatalytic water oxidation in alkaline media. *Nature Energy*, *4*(6), 519–525. https://doi.org/10.1038/s41560-019-0404-4

37) Gazzotti, M., Arnaboldi, S., Grecchi, S., Giovanardi, R., Cannio, M., Pasquali, L., Giacomino, A., Abollino, O., & Fontanesi, C. (2018). Spin-dependent electrochemistry: Enantio-selectivity driven by chiral-induced spin selectivity effect. *Electrochimica Acta*, *286*, 271–278. https://doi.org/10.1016/j.electacta.2018.08.023

38) Gazzotti, M., Stefani, A., Bonechi, M., Giurlani, W., Innocenti, M., & Fontanesi, C. (2020). Influence of Chiral Compounds on the Oxygen Evolution Reaction (OER) in the Water Splitting Process. *Molecules*, *25*(17). https://doi.org/10.3390/molecules25173988

39) Ghosh, K. B., Zhang, W., Tassinari, F., Mastai, Y., Lidor-Shalev, O., Naaman, R., Möllers, P., Nürenberg, D., Zacharias, H., Wei, J., Wierzbinski, E., & Waldeck, D. H. (2019). Controlling Chemical Selectivity in Electrocatalysis with Chiral CuO-Coated Electrodes. *Journal of Physical Chemistry C*, *123*(5), 3024–3031. https://doi.org/10.1021/acs.jpcc.8b12027

40) Ghosh, S., Bloom, B. P., Lu, Y., Lamont, D., & Waldeck, D. H. (2020). Increasing the Efficiency of Water Splitting through Spin Polarization Using Cobalt Oxide Thin Film

Catalysts. *Journal of Physical Chemistry C*, *124*(41), 22610–22618. https://doi.org/10.1021/acs.jpcc.0c07372

41) Gray, H. B. (2009). Powering the planet with solar fuel. *Nature Chem* **1**, 7 . https://doi.org/10.1038/nchem.141

42) Guler, A. C., Antos, J., Masar, M., Urbanek, M., Machovsky, M., & Kuritka, I. (2023). Comprehensive evaluation of photoelectrochemical performance dependence on geometric features of ZnO nanorod electrodes. *Nanoscale Advances*, *5*(11), 3091–3103. https://doi.org/10.1039/d3na00089c

43) Guy, O. J., & Walker, K. A. D. (2016). Graphene Functionalization for Biosensor Applications. *Silicon Carbide Biotechnology: A Biocompatible Semiconductor for Advanced Biomedical Devices and Applications: Second Edition*, 85–141. https://doi.org/10.1016/B978-0-12-802993-0.00004-6

44) Hankin, A., Bedoya-Lora, F. E., Alexander, J. C., Regoutz, A., & Kelsall, G. H. (2019). Flat band potential determination: Avoiding the pitfalls. *Journal of Materials Chemistry A*, *7*(45), 26162–26176. https://doi.org/10.1039/c9ta09569a

45) Harris-Lee, T. R., Marken, F., Bentley, C. L., Zhang, J., & Johnson, A. L. (2023). A chemist's guide to photoelectrode development for water splitting – the importance of molecular precursor design. *EES Catalysis*, *1*(6), 832–873. https://doi.org/10.1039/d3ey00176h

46) Heard, D. M., & Lennox, A. J. J. (2020). Electrode Materials in Modern Organic Electrochemistry. *Angewandte Chemie*, *132*(43), 19026–19044. https://doi.org/10.1002/ange.202005745

47) Hendi, A. H., Osman, A. M., Khan, I., Saleh, T. A., Kandiel, T. A., Qahtan, T. F., & Hossain, M. K. (2020). Visible Light-Driven Photoelectrocatalytic Water Splitting Using Z-Scheme Ag-Decorated MoS2/RGO/NiWO4 Heterostructure. *ACS Omega*, *5*(49), 31644–31656. https://doi.org/10.1021/acsomega.0c03985

48) Hisatomi, T., Kubota, J., & Domen, K. (2014). Recent advances in semiconductors for photocatalytic and photoelectrochemical water splitting. *Chemical Society Reviews*, *43*(22), 7520–7535. https://doi.org/10.1039/c3cs60378d

49) Jafari, T., Moharreri, E., Amin, A. S., Miao, R., Song, W., & Suib, S. L. (2016). Photocatalytic water splitting - The untamed dream: A review of recent advances. *Molecules*, *21*(7). https://doi.org/10.3390/molecules21070900

50) Jaque, P., Marenich, A. V., Cramer, C. J., & Truhlar, D. G. (2007). Computational electrochemistry: The aqueous Ru3+|Ru2+ reduction potential. *Journal of Physical Chemistry C*, *111*(15), 5783–5799. https://doi.org/10.1021/jp066765w

51) Jirkovský, J., Makarova, M., & Krtil, P. (2006). Particle size dependence of oxygen evolution reaction on nanocrystalline RuO2 and Ru0.8Co0.2O2-x. *Electrochemistry Communications*, *8*(9), 1417–1422. https://doi.org/10.1016/j.elecom.2006.06.027
52) Juan Liu, Yang Li, Naiyun Liu, Yuzhi Han, Xing Zhang, Hui Huang, Yeshayahu Lifshitz, Shuit-Tong Lee, Jun Zhong, & Zhenhui Kang. (2015). Metal-free efficient photocatalyst for stable visible water splitting via a two-electron pathway. *Science*, *347*(6225), 970–974.
53) Kohl, S. W., Weiner, L., Schwartsburd, L., Konstantinovski, L., Shimon, L. J. W., David, Y. Ben, Iron, M. A., & Milstein, D. (2009). Consecutive thermal H2 and light-induced O2 evolution from water promoted by a metal complex. *Science*, *324*(5923), 74–77. https://doi.org/10.1126/science.1168600
54) Konstas, K., Osl, T., Yang, Y., Batten, M., Burke, N., Hill, A. J., & Hill, M. R. (2012). Methane storage in metal organic frameworks. *Journal of Materials Chemistry*, *22*(33), 16698–16708. https://doi.org/10.1039/c2jm32719h
55) Kudo, A. (2011). Z-scheme photocatalyst systems for water splitting under visible light irradiation. *MRS Bulletin*, *36*(1), 32–38. https://doi.org/10.1557/mrs.2010.3
56) Kusmierek, E. (2020). A CeO2 semiconductor as a photocatalytic and photoelectrocatalytic material for the remediation of pollutants in industrial wastewater: A review. In *Catalysts* (Vol. 10, Issue 12, pp. 1–54). MDPI. https://doi.org/10.3390/catal10121435
57) Laskowski, F. A. L., Oener, S. Z., Nellist, M. R., Gordon, A. M., Bain, D. C., Fehrs, J. L., & Boettcher, S. W. (2020). Nanoscale semiconductor/catalyst interfaces in photoelectrochemistry. *Nature Materials*, *19*(1), 69–76. https://doi.org/10.1038/s41563-019-0488-z
58) Lazanas, A. C., & Prodromidis, M. I. (2023). Electrochemical Impedance Spectroscopy─A Tutorial. In *ACS Measurement Science Au* (Vol. 3, Issue 3, pp. 162–193). American Chemical Society. https://doi.org/10.1021/acsmeasuresciau.2c00070
59) Lee, Y. R., Kim, J., & Ahn, W. S. (2013). Synthesis of metal-organic frameworks: A mini review. In *Korean Journal of Chemical Engineering* (Vol. 30, Issue 9, pp. 1667–1680). https://doi.org/10.1007/s11814-013-0140-6
60) Li, S., Xu, W., Meng, L., Tian, W., & Li, L. (2022). Recent Progress on Semiconductor Heterojunction-Based Photoanodes for Photoelectrochemical Water Splitting. In *Small Science* (Vol. 2, Issue 5). John Wiley and Sons Inc. https://doi.org/10.1002/smsc.202100112
61) Loera-Serna, S., & Ortiz, E. (2016). Catalytic Applications of Metal-Organic Frameworks. In *Advanced Catalytic Materials - Photocatalysis and Other Current Trends*. InTech. https://doi.org/10.5772/61865

62) López-Lorente, Á. I., & Mizaikoff, B. (2016). Recent advances on the characterization of nanoparticles using infrared spectroscopy. In *TrAC - Trends in Analytical Chemistry* (Vol. 84, pp. 97–106). Elsevier B.V. https://doi.org/10.1016/j.trac.2016.01.012

63) Ma, P., & Wang, D. (2017). The principle of photoelectrochemical water splitting. In *Nanomaterials for Energy Conversion and Storage* (pp. 1–61). www.worldscientific.com

64) Maçaira, J., Andrade, L., & Mendes, A. (2013). Review on nanostructured photoelectrodes for next generation dye-sensitized solar cells. In *Renewable and Sustainable Energy Reviews* (Vol. 27, pp. 334–349). Elsevier Ltd. https://doi.org/10.1016/j.rser.2013.07.011

65) Makuła, P., Pacia, M., & Macyk, W., (2018), How to Correctly Determine the Band Gap Energy of Modified Semiconductor Photocatalysts Based on UV–Vis Spectra, The Journal of Physical Chemistry Letters 9 (23), 6814-6817 DOI: 10.1021/acs.jpclett.8b02892

66) Martinez-Garcia, A., Russell, H. B., Paxton, W., Ravipati, S., Calero-Barney, S., Menon, M., Richter, E., Young, J., Deutsch, T., & Sunkara, M. K. (2018). Unassisted Water Splitting Using a GaSbxP(1−x) Photoanode. *Advanced Energy Materials*, *8*(16). https://doi.org/10.1002/aenm.201703247

67) Masoomi, M. Y., Morsali, A., Dhakshinamoorthy, A., & Garcia, H. (2019). Mixed-Metal MOFs: Unique Opportunities in Metal–Organic Framework (MOF) Functionality and Design. In *Angewandte Chemie - International Edition* (Vol. 58, Issue 43, pp. 15188–15205). Wiley-VCH Verlag. https://doi.org/10.1002/anie.201902229

68) Mayer, M.T., Du, C., Wang, D. (2012). Hematite/Si nanowire dual-absorber system for photoelectrochemical water splitting at low applied potentials. *Journal of the American Chemical Society*. 134(30):12406-12409. DOI: 10.1021/ja3051734. PMID: 22800199.

69) Mei, B. A., Munteshari, O., Lau, J., Dunn, B., & Pilon, L. (2018). Physical Interpretations of Nyquist Plots for EDLC Electrodes and Devices. *Journal of Physical Chemistry C*, *122*(1), 194–206. https://doi.org/10.1021/acs.jpcc.7b10582

70) Meyer, K., Ranocchiari, M., & Van Bokhoven, J. A. (2015). Metal organic frameworks for photo-catalytic water splitting. *Energy and Environmental Science*, *8*(7), 1923–1937. https://doi.org/10.1039/c5ee00161g

71) Millange, F., Serre, C., & Férey, G. (2002). Synthesis, structure determination and properties of MIL-53as and MIL-53ht: The first CrIII hybrid inorganic-organic microporous solids: CrIII(OH)·(O2C-C6H4-CO2)·(HO2C-C6H4-CO2H)x. *Chemical Communications*, *2*(8), 822–823. https://doi.org/10.1039/b201381

72) Mohamed, H. H. (2022). Green processes and sustainable materials for renewable energy production via water splitting. In *Sustainable Materials and Green Processing*

for Energy Conversion (pp. 169–212). Elsevier. https://doi.org/10.1016/B978-0-12-822838-8.00007-7

73) Mohamed, N. M., Bashiri, R., Shahid, M. U., Kait, C. F., & Sufian, S. (2018). Potential Application of Metal-organic frameworks for Photocatalytic Water Splitting. *Journal of Physics: Conference Series*, *1123*(1). https://doi.org/10.1088/1742-6596/1123/1/012055

74) Molnar, C., & Gair, J. (2015). *Concepts of Biology – 1st Canadian Edition. BCcampus. Retrieved from https://opentextbc.ca/biology/* (1st Edition). BCampus.

75) Mondal P.C, Mtangi W., & Fontanesi C. (2018). Chiro-Spintronics : Spin-dependent Electrochemistry and water splitting using chiral molecular films. *Small Molecules* 2 (4) 1700310

76) Mtangi, W. (2012). *Electrical characterization of process, annealing and irradiation induced defects in ZnO* pp11-15.

77) Mtangi, W., Kiran, V., Fontanesi, C., & Naaman, R. (2015). Role of the Electron Spin Polarization in Water Splitting. *Journal of Physical Chemistry Letters*, *6*(24), 4916–4922. https://doi.org/10.1021/acs.jpclett.5b02419

78) Mtangi, W., Tassinari, F., Vankayala, K., Vargas Jentzsch, A., Adelizzi, B., Palmans, A. R. A., Fontanesi, C., Meijer, E. W., & Naaman, R. (2017). Control of Electrons' Spin Eliminates Hydrogen Peroxide Formation during Water Splitting. *Journal of the American Chemical Society*, *139*(7), 2794–2798. https://doi.org/10.1021/jacs.6b12971

79) Nanakoudis, A., (2019). EDX Analysis with SEM: How Does it Work? EDX Analysis with SEM: How Does It Work?

80) Naaman, R., Paltiel, Y., & Waldeck, D. H. (2019). Chiral molecules and the electron spin. *Nature Reviews Chemistry*, *3*(4), 250–260. https://doi.org/10.1038/s41570-019-0087-1

81) Naaman, R., Paltiel, Y., & Waldeck, D. H. (2020). Chiral Induced Spin Selectivity Gives a New Twist on Spin-Control in Chemistry. *Accounts of Chemical Research*, *53*(11), 2659–2667. https://doi.org/10.1021/acs.accounts.0c00485

82) Naaman, R., & Waldeck, D. H. (2012). Chiral-induced spin selectivity effect. *Journal of Physical Chemistry Letters*, *3*(16), 2178–2187. https://doi.org/10.1021/jz300793y

83) Nguyen, P. D., Duong, T. M., & Tran, P. D. (2017). Current progress and challenges in engineering viable artificial leaf for solar water splitting. *Journal of Science: Advanced Materials and Devices*, *2*(4), 399–417. https://doi.org/10.1016/j.jsamd.2017.08.006

84) Nishioka, S., Osterloh, F. E., Wang, X., Mallouk, T. E., & Maeda, K. (2023). Photocatalytic water splitting. *Nature Reviews Methods Primers*, *3*(1), 42. https://doi.org/10.1038/s43586-023-00226-x

85) Nocera, D. G. (2012). The artificial leaf. *Accounts of Chemical Research*, *45*(5), 767–776. https://doi.org/10.1021/ar2003013

86) Obata, K., Van De Krol, R., Schwarze, M., Schomä, R., & Abdi, F. F. (2020). In situ observation of pH change during water splitting in neutral pH conditions: impact of natural convection driven by buoyancy effects †. *5104 | Energy Environ. Sci*, *13*, 5104. https://doi.org/10.1039/d0ee01760d

87) Piccinin, S. (2019). The band structure and optical absorption of hematite (α-Fe2O3): A first-principles GW-BSE study. *Physical Chemistry Chemical Physics*, *21*(6). https://doi.org/10.1039/c8cp07132b

88) Pappalardo, S., & Parisi, M. F. (2008). Ten-membered Rings or Larger with One or More Oxygen Atoms. *Comprehensive Heterocyclic Chemistry III*, *14*, 667–749. https://doi.org/10.1016/B978-008044992-0.01229-3

89) Pereira, C. F., Simoes, M. Q., Tomé, J. P. C., & Paz, F. A. A. (2016). Porphyrin-based metal-organic frameworks as heterogeneous catalysts in oxidation reactions. In *Molecules* (Vol. 21, Issue 10). MDPI AG. https://doi.org/10.3390/molecules21101348

90) Ping, Y., Galli, G., & Goddard, W. A. (2015). Electronic structure of IrO2: The role of the metal d orbitals. *Journal of Physical Chemistry C*, *119*(21), 11570–11577. https://doi.org/10.1021/acs.jpcc.5b00861

91) Prévot, M. S., & Sivula, K. (2013). Photoelectrochemical tandem cells for solar water splitting. *Journal of Physical Chemistry C*, *117*(35), 17879–17893. https://doi.org/10.1021/jp405291g

92) Pullen, S., & Ott, S. (2016). Photochemical Hydrogen Production with Metal–Organic Frameworks. In *Topics in Catalysis* (Vol. 59, Issues 19–20, pp. 1712–1721). Kluwer Academic Publishers. https://doi.org/10.1007/s11244-016-0690-z

93) Remya, V. R., & Kurian, M. (2019). Synthesis and catalytic applications of metal–organic frameworks: a review on recent literature. *International Nano Letters*, *9*(1), 17–29. https://doi.org/10.1007/s40089-018-0255-1

94) Rosenberg, R. A., Abu Haija, M., & Ryan, P. J. (2008). Chiral-selective chemistry induced by spin-polarized secondary electrons from a magnetic substrate. *Physical Review Letters*, *101*(17), 1–4. https://doi.org/10.1103/PhysRevLett.101.178301

95) Rossmeisl, J., Logadottir, A., & Nørskov, J. K. (2005). Electrolysis of water on (oxidized) metal surfaces. *Chemical Physics*, *319*(1–3), 178–184. https://doi.org/10.1016/j.chemphys.2005.05.038

96) Rossmeisl, J., Qu, Z. W., Zhu, H., Kroes, G. J., & Nørskov, J. K. (2007). Electrolysis of water on oxide surfaces. *Journal of Electroanalytical Chemistry*, *607*(1–2), 83–89. https://doi.org/10.1016/j.jelechem.2006.11.008

97) Salcedo-abraira, P., Vilela, S., Babaryk, A., Gregorio, P., Salles, F., Navalón, S., García, H., Horcajada, P., (2021). *Nickel phosphonate MOF as efficient water splitting photocatalyst* HAL Id : hal-03031673 Nickel phosphonate MOF as efficient water splitting photocatalyst.

98) Salvador, P., & Decker, F. (1984). The generation of hydrogen peroxide during water photoelectrolysis at n-titanium dioxide. *The Journal of Physical Chemistry*, *88*(25), 6116–6120. https://doi.org/10.1021/j150669a013

99) Samal, A., & Das, N. (2023). Mini-review on remediation of plastic pollution through photoreforming: progress, possibilities, and challenges. *Environmental Science and Pollution Research*, *30*(35), 83138–83152. https://doi.org/10.1007/s11356-023-28253-x

100) Schumacher, L., Timm, J., & Marschall, R. (2024). Effects of Hydrothermal Etching and Conversion on Photocatalytic Hydrogen Evolution and Overall Water Splitting with Nanoparticulate and Mesoporous TiO_2 and $SrTiO_3$ /TiO_2 Composites. *Journal of Materials Chemistry A*. https://doi.org/10.1039/D4TA03416C

101) Sengupta, K., Chatterjee, S., & Dey, A. (2016). Catalytic H2O2 Disproportionation and Electrocatalytic O2 Reduction by a Functional Mimic of Heme Catalase: Direct Observation of Compound 0 and Compound I in Situ. *ACS Catalysis*, *6*(3), 1382–1388. https://doi.org/10.1021/acscatal.5b02668

102) Sergeev, G. B., & Klabunde, K. J. (2013). Experimental Techniques. In *Nanochemistry* (pp. 75–87). Elsevier. https://doi.org/10.1016/B978-0-444-59397-9.00004-9

103) Serpone, N., & Salinaro, A. (1999). International Union of Pure and Applied Chemistry Organic Chemistry Division Commission on Photochemistry* Terminology, Relative Photonic Efficiencies and Quantum Yields in Heterogeneous Photocatalysis. Part I suggested Protocol† Prepared for publication by Terminology, relative photonic efficiencies and quantum yields in heterogeneous photocatalysis. Part I: Suggested protocol (Technical Report). In *Pure & Appl. Chem* (Vol. 71, Issue 2).

104) Sharmin, E., & Zafar, F. (2016). Introductory Chapter: Metal Organic Frameworks (MOFs). In *Metal-Organic Frameworks*. InTech. https://doi.org/10.5772/64797

105) Sherman, B. D., Sheridan, M. V., Wee, K. R., Marquard, S. L., Wang, D., Alibabaei, L., Ashford, D. L., & Meyer, T. J. (2016). A Dye-Sensitized Photoelectrochemical Tandem Cell for Light Driven Hydrogen Production from Water. *Journal of the American Chemical Society*, *138*(51), 16745–16753. https://doi.org/10.1021/jacs.6b10699

106) Song, F., Li, W., & Sun, Y. (2017). Metal-organic frameworks and their derivatives for photocatalyticwater splitting. *Inorganics*, *5*(3). https://doi.org/10.3390/inorganics5030040

107) Stefani, A., Salzillo, T., Mussini, P. R., Benincori, T., Innocenti, M., Pasquali, L., Jones, A. C., Mishra, S., & Fontanesi, C. (2023). Chiral Recognition: A Spin-Driven Process in Chiral Oligothiophene. A Chiral-Induced Spin Selectivity (CISS) Effect Manifestation. *Advanced Functional Materials* 34, (2308948) 1-11. https://doi.org/10.1002/adfm.202308948

108) Sun, X., Jiang, S., Huang, H., Li, H., Jia, B., & Ma, T. (2022). Solar Energy Catalysis. In *Angewandte Chemie - International Edition* (Vol. 61, Issue 29). John Wiley and Sons Inc. https://doi.org/10.1002/anie.202204880

109) Suntivich, J., May, K. J., Gasteiger, H. A., Goodenough, J. B., & Shao-Horn, Y. (2011). A perovskite oxide optimized for oxygen evolution catalysis from molecular orbital principles. *Science*, *334*(6061), 1383–1385. https://doi.org/10.1126/science.1212858

110) Takanabe, K. (2017). Photocatalytic Water Splitting: Quantitative Approaches toward Photocatalyst by Design. *ACS Catalysis*, *7*(11), 8006–8022. https://doi.org/10.1021/acscatal.7b02662

111) Tariq, S., Ahmad, A., Luque, R., & Kamal, T. (2023). Characterization and theoretical considerations of MOFs. In *Nanomaterial-Based Metal Organic Frameworks for Single Atom Catalysis* (pp. 139–161). Elsevier. https://doi.org/10.1016/B978-0-12-824524-8.00005-0

112) Tee, S. Y., Win, K. Y., Teo, W. S., Koh, L. D., Liu, S., Teng, C. P., & Han, M. Y. (2017). Recent Progress in Energy-Driven Water Splitting. In *Advanced Science* (Vol. 4, Issue 5). https://doi.org/10.1002/advs.201600337

113) Tomar, S., & Singh, V. K. (2021). Review on synthesis and application of mil-53. *Materials Today: Proceedings*, *43*, 3291–3296. https://doi.org/10.1016/j.matpr.2021.02.179

114) Torun, E., Fang, C. M., De Wijs, G. A., & De Groot, R. A. (2013). Role of magnetism in catalysis: RuO2 (110) surface. *Journal of Physical Chemistry C*, *117*(12), 6353–6357. https://doi.org/10.1021/jp4020367

115) van der Heijden, O., Park, S., Vos, R. E., Eggebeen, J. J. J., & Koper, M. T. M. (2024). Tafel Slope Plot as a Tool to Analyze Electrocatalytic Reactions. *ACS Energy Letters*, *9*(4), 1871–1879. https://doi.org/10.1021/acsenergylett.4c00266

116) Vilanova, A., Dias, P., Lopes, T., & Mendes, A. (2024). The route for commercial photoelectrochemical water splitting: a review of large-area devices and

key upscaling challenges. In *Chemical Society Reviews* (Vol. 53, Issue 5, pp. 2388–2434). Royal Society of Chemistry. https://doi.org/10.1039/d1cs01069g

117) Wang, H., & Chu, P. K. (2013). Surface Characterization of Biomaterials. In *Characterization of Biomaterials* (pp. 105–174). Elsevier Inc. https://doi.org/10.1016/B978-0-12-415800-9.00004-8

118) Wang, L., Cao, S., Guo, K., Wu, Z., Ma, Z., & Piao, L. (2019). Simultaneous hydrogen and peroxide production by photocatalytic water splitting. *Cuihua Xuebao/Chinese Journal of Catalysis*, *40*(3), 470–475. https://doi.org/10.1016/s1872-2067(19)63274-2

119) Wang, Z., Li, C., & Domen, K. (2019). Recent developments in heterogeneous photocatalysts for solar-driven overall water splitting. In *Chemical Society Reviews* (Vol. 48, Issue 7, pp. 2109–2125). Royal Society of Chemistry. https://doi.org/10.1039/c8cs00542g

120) Wang, Z., & Wang, Q. (2021). Photocatalytic Z-scheme water splitting. In *Heterostructured Photocatalysts for Solar Energy Conversion* (pp. 131–176). Elsevier. https://doi.org/10.1016/b978-0-12-820072-8.00004-4

121) Whitfield, T. R., Wang, X., Liu, L., & Jacobson, A. J. (2005). Metal-organic frameworks based on iron oxide octahedral chains connected by benzenedicarboxylate dianions. *Solid State Sciences*, *7*(9), 1096–1103. https://doi.org/10.1016/j.solidstatesciences.2005.03.007

122) Xu, Q., Zhang, L., Yu, J., Wageh, S., Al-Ghamdi, A. A., & Jaroniec, M. (2018). Direct Z-scheme photocatalysts: Principles, synthesis, and applications. In *Materials Today* (Vol. 21, Issue 10, pp. 1042–1063). Elsevier B.V. https://doi.org/10.1016/j.mattod.2018.04.008

123) Yamaguchi, K., Yamanaka, S., Isobe, H., Tanaka, K., & Ueyama, N. (2012). Spin hamiltonian models for artificial and native water splitting systems revealed by hybrid DFT calculations. Oxygen activation by high-valent Mn and Ru ions. *International Journal of Quantum Chemistry*, *112*(24), 3849–3866. https://doi.org/10.1002/qua.24270

124) Yang, J. W., Ahn, S. H., & Jang, H. W. (2021). Crucial role of heterostructures in highly advanced water splitting photoelectrodes. In *Current Opinion in Green and Sustainable Chemistry* (Vol. 29). Elsevier B.V. https://doi.org/10.1016/j.cogsc.2021.100454

125) Yang, X., & Baik, M. H. (2008). The mechanism of water oxidation catalysis promoted by [tpyRu(IV)=O] 2L3+: A computational study. *Journal of the American Chemical Society*, *130*(48), 16231–16240. https://doi.org/10.1021/ja8034043

126) Yuan, S., Qin, J. S., Lollar, C. T., & Zhou, H. C. (2018). Stable Metal-Organic Frameworks with Group 4 Metals: Current Status and Trends. *ACS Central Science*, *4*(4), 440–450. https://doi.org/10.1021/acscentsci.8b00073

127) Zhang, H., Liu, J., Xu, T., Ji, W., & Zong, X. (2023). Recent Advances on Small Band Gap Semiconductor Materials (≤2.1 eV) for Solar Water Splitting. In *Catalysts* (Vol. 13, Issue 4). https://doi.org/10.3390/catal13040728

128) Zhang, K., Ma, M., Li, P., Wang, D. H., & Park, J. H. (2016). Water Splitting Progress in Tandem Devices: Moving Photolysis beyond Electrolysis. In *Advanced Energy Materials* (Vol. 6, Issue 15). Wiley-VCH Verlag. https://doi.org/10.1002/aenm.201600602

129) Zhang, Q., Yan, S., Yan, X., & Lv, Y. (2023). Recent advances in metal-organic frameworks: Synthesis, application and toxicity. In *Science of the Total Environment* (Vol. 902). Elsevier B.V. https://doi.org/10.1016/j.scitotenv.2023.165944

130) Zhang, W., Banerjee-Ghosh, K., Tassinari, F., & Naaman, R. (2018). Enhanced Electrochemical Water Splitting with Chiral Molecule-Coated Fe3O4 Nanoparticles. *ACS Energy Letters*, *3*(10), 2308–2313. https://doi.org/10.1021/acsenergylett.8b01454

131) Zhang, W., Liu, F., Hu, Y., Yang, W., Guan, H., Hao, L., & Lu, G. (2020). Pivotal Role of Chirality in Photoelectrocatalytic (PEC) Water Splitting. *Current Chinese Science*, *1*(1), 115–121. https://doi.org/10.2174/2210298101999200819110254

132) Zhang, W., Wang, W., Hu, Y., Guan, H., & Hao, L. (2021). Take a cue from nature: Promoting electrocatalytic watersplitting with a helping hand of hemoglobin. *International Journal of Hydrogen Energy*, *46*(5), 3504–3509. https://doi.org/10.1016/j.ijhydene.2020.10.154

133) Zhao, S. N., Wang, G., Poelman, D., & Van Der Voort, P. (2018). Metal organic frameworks based materials for heterogeneous photocatalysis. *Molecules*, *23*(11), 1–23. https://doi.org/10.3390/molecules23112947

134) Zhao, Y., Wang, C., Han, X., Lang, Z., Zhao, C., Yin, L., Sun, H., Yan, L., Ren, H., & Tan, H. (2022). Two-Dimensional Covalent Heptazine-Based Framework Enables Highly Photocatalytic Performance for Overall Water Splitting. *Advanced Science*, *9*(28). https://doi.org/10.1002/advs.202202417

135) Zhu, P., Slater, P. R., & Kendrick, E. (2022). Insights into architecture, design and manufacture of electrodes for lithium-ion batteries. In *Materials and Design* (Vol. 223). Elsevier Ltd. https://doi.org/10.1016/j.matdes.2022.111208

3 EXPERIMENTAL

3.1 INTRODUCTION TO THE EXPERIMENTAL SECTION

This chapter outlines the general methods used in the synthesis of the metal-organic frameworks (MOFs) used in the study for Iron and Zinc. Procedures for the fabrication of the photoanodes are clearly outlined. Details of the physical characterization, including Fourier Transform Infrared Spectroscopy (FTIR), Thermogravimetric Analysis (TGA), Uv-Vis Spectroscopy, X-ray diffraction Spectroscopy (XRD), scanning electron microscopy (SEM) and inductively coupled plasma optical emission (ICP-OES) are given. The main electrochemical techniques used during water splitting are also listed.

3.2 MATERIALS AND EQUIPMENT

3.2.1 Chemicals

All the chemicals and reagents were analytical grade. N'-N'dimethyl formamide (DMF) with purity ≥99%, anhydrous sodium sulphate (Na_2SO_4) with purity ≥99.0% and zinc nitrate with purity 98% (Zn $(NO_3)_2 \cdot 6H_2O$) were purchased from ACE Chemicals, South Africa and used with no further purification. Titanium (IV) oxide nanoparticles (with purity of ≥99.5% and particle size of 21 nm), Fluorine-doped tin oxide (FTO) coated glass substrates, (with surface resistivity of ~7Ω/sq), absolute ethanol (C_2H_5OH) with purity ≥99.5%, acetone (CH_3COCH_3) purity ≥99%, methanol (CH_3OH) with purity ≥99.5%, Iron (III) chloride ($FeCl_3 \cdot 6H_2O$) purity 97%, cobalt nitrate ($Co(NO_3)_2 \cdot 6H_2O$) with purity 98%, nickel nitrate ($Ni(NO_3)_2 \cdot 6H_2O$) with purity 98%, terephthalic acid H_2BDC (benzene-1,4-dicarboxylic acid) with purity ≥98.0%, 2-aminoterephthalic acid H_2N-BDC (2-aminobenzene-1,4-dicarboxylic acid) with purity 99%, L-cysteine with purity 97%, R (-) camphor sulphonic acid with 98% purity, S (+)camphor sulphonic acid with 99% purity, o-tolidine with purity ≥95%, 4-pyridylcarboxyldehyde with purity of 97%, (1r,4r)-cyclohexane-1,4-diamine with purity ≥98%, triethylamine with purity of ≥ 99%, sodium borohydride ($NaBH_4$) with purity ≥96%, dichloromethane (DCM) with purity of ≥99.5%, Trichloromethane with purity ≥99.5%, Hydrogen Peroxide (H_2O_2) with purity of 35%, 60% Nitric Acid (HNO_3) and 30% Hydrochloric acid (HCl) were bought from Sigma, Germany and used without further treatment. All the aqueous solutions were prepared using deionized water unless stated.

3.2.2 Instrumentation

All the MOFs were synthesized in a Digital oven from Labotec EcoTherm, South Africa. FTIR analysis was carried out using a Thermo Scientific Nicolet 6700 FTIR spectrophotometer whereas PXRD analysis was carried out in a Brucker D2 phaser XRD spectrophotometer. ^{1}H and ^{13}C {1H} spectra for the synthesized linker were attained on a Bruker Ultrashield 500 MHz operating at 500.13 MHz. A UV-1900i Shimadzu Uv-Vis Spectrophotometer, was used for photocatalytic measurements while thermogravimetric analysis was carried out using a TRIOS TGA 550 machine. Surface morphology was investigated using ZEISS field emission scanning electron microscope with an energy dispersive detector. Scanning electron microscope (SEM) images were obtained from a Hitachi SU3800 scanning electron microscope also equipped with an UltimMax Oxford instrument EDS detector. Inductively coupled plasma optical emission (ICP-OES) analysis was performed on a Spectro Arcros instrument. The electrochemical measurements were done using a CHI 608E electrochemical analyzer (USA), while a Sci-Sun 300 (A.M 1.5 G) was used as the solar simulator.

3.2.3 MOF synthesis methods

Solvothermal/hydrothermal methods were used to synthesize the metal-organic frameworks. The first step of the synthesis procedure involves dissolving the organic linkers in DMF by heating and stirring, after which the metal salts were added. The resulting solutions were transferred into a Teflon-lined autoclave and placed in a preheated oven at a specific temperature and time to yield the crystals for the iron-based MOF. In the case of the Zn-MOF, an additional linker was synthesized then dissolved with the terephthalic acid in DMF. Instead of a Teflon lined autoclave, the Zn-MOF was synthesized in loosely capped vials as described by Altaf in 2018. (Altaf et al., 2018). The exact and detailed synthesis methods for the individual MOFs are given in detail in the appropriate chapters.

3.3 CHARACTERIZATION

FTIR characterizations were carried out using a Thermo Scientific Nicolet 6700 FTIR spectrophotometer, with a resolution of 4 and 32 scan times. The analysis was done from 4000 cm^{-1} to 400 cm^{-1} on samples prepared by the KBr method. Each MOF sample was mixed with KBr in a ratio 20:1. The mixture was ground in a mortar and pestle, resulting in a mixture that was used to prepare the pellet. FTIR was used to evaluate the changes in the coordination modes of the carboxylate functional groups to the metal through the significant difference

between the carboxylate stretches. FTIR was also used to identify any shifts due to the introduction of the chiral molecules in the MOF matrix.

PXRD analysis was carried out using a Bruker D2 phaser XRD diffractometer, USA, which uses DIFFRAC-SUITE software for controlling the diffractometer and analyzing the data. The Bruker D2 phaser XRD spectrophotometer uses a copper tube with 1.5418 Angstroms as the X-ray source. X-rays were generated using 30 kV and a current of 10 A. Continuous PSD fast was used as the scan mode, with scan type two theta/theta with detector Lynxeye XET. A scan step of 0.5 second was used, creating 3948 steps and a total time run time of 2180 seconds. The powdered samples were placed on a zero-background sample holder and scanned from 4 to 60, 2 theta positions. The resultant experimental data was plotted using Origin 2023. Calculated data was obtained from Mercury and Match!*. The calculated and experimental data were compared to evaluate the effect of the chiral molecules on the structure and crystallinity of the chiral doped MOFs.

NMR studies ^{1}H and ^{13}C {1H} spectra were acquired using a Bruker Ultrashield 500 MHz operating at 500.13 MHz. All chemical shifts(δ) were recorded in units of ppm. Deuterated chloroform ($CDCl_3$) was used as the internal standard. The ^{13}C NMR data were obtained with 1H broadband decoupling and the spectral conditions were 32 scans, 3.2768 sec acquisition time. The MestReNova NMR data processing software was used to analyse and process all the recorded NMR spectra. All coupling constants (J) were measured in Hertz (Hz).

Thermal Analysis was carried out using a TRIOS TGA 550 machine. Sample was heated from 25 °C to 700 °C using a heating rate of 10 °C/min under dry nitrogen gas purge at 50 ml per minute.

Approximately 3 mg of the samples were placed in an aluminium pan of the TGA followed by thermal analysis. TGA was used to determine the decomposition temperature which in turn determines the thermal stability of the MOFs.

Inductively Coupled Plasma Optical Emission and Elemental Analysis. Inductively coupled plasma optical emission (ICP-OES) analysis was carried out on a Spectro Arcros instrument that was calibrated using known magnesium, manganese, and palladium standards. Samples were microwave-digested in aqua regia (4 mL of 60% HNO_3, 1 mL of 30% HCl) and analyzed directly.

The photocatalytic activity of the MOFs was assessed using a UV-1900i Shimadzu Uv-Vis Spectrophotometer. A 2% MOF solution was made by dissolving the MOFs in ethanol. The sample was then assessed for photocatalytic activity by running a scan from 300 to 500 nm. Tauc plots were used to evaluate the Band gap energy of the photocatalysts.

Chiral recognition was carried out by running cyclic voltammetry on the chiral electrodes from -0.23V to +1.23V (vs Ag/AgCl) using a scan rate of 0.1V/s in 8mM L-Cysteine dissolved in HCl with the pH of the solution maintained at 4.0. using buffer 4 solution. The electrodes for chiral recognition were prepared by drop casting a slurry of 1mg of each MOF dissolved in 1ml of ethanol onto washed FTO. The FTO was then annealed at 100 °C for 15 minutes to harden the layers over the FTO and to excess remove solvent.

Solid State Electrochemistry

Solid-state electrochemistry was used to evaluate the electrochemical behaviour of the MOFs. The glassy carbon electrode-MOF combination (GCE/MOF) served as the working electrode (WE), while a coiled Platinum wire served as counter electrode (CE) and an Ag/AgCl (saturated KCl) electrode served as the reference electrode (RE). The effective cell set-up and GC electrode activation procedure was cross-checked by recording CVs in a solution of 1 mM ferricyanide in 0.1 M KCl.

Surface Morphology was evaluated using:

- ZEISS Field Emission Scanning electron Microscope with an Energy Dispersive Detector.
- Scanning electron microscope (SEM) images were investigated using a Hitachi SU3800 Scanning Electron Microscope equipped with an UltimMax Oxford instrument EDS detector. The samples were placed on a sticky carbon tape and carbon-coated using an Agar-Turbo carbon sputter.

Electrochemical measurements were done using a CHI 608E electrochemical analyzer.

Sci-Sun 300 (A.M 1.5 G) was used as the solar simulator.

Photoelectrochemical cell

Measurements for cyclic voltammetry, linear sweep voltammetry, chronoamperometry and open circuit potential were carried out in an improvised photoelectrochemical cell made up of a 50ml borosilicate beaker and a 3D printed electrode holder. Platinum wire was used as the counter electrode while the Ag/AgCl electrode was used as the reference electrode. A modified Hoffman apparatus was used for the collection of hydrogen gas.

3.4 PREPARATION OF ELECTRODES

The preparation of the electrodes was done according to the methods published by Mtangi et al in 2017 (Mtangi et al., 2017) as well as modifications done by Kawondera et al in 2023 (Kawondera et al., 2023). In detail, the FTO/TiO_2 electrode was prepared first. To accomplish this, a 1% (w/v) TiO_2 nanoparticulate film was deposited on the fluorine-doped tin oxide, FTO (with surface resistivity of ~7 Ω/sq,) coated glass, using the electrophoretic deposition (EPD) technique. A suspension of TiO_2 nanoparticles (NPs) was prepared by dispersing 0.4g TiO_2 NPs in 40 mL of de-ionized water. Before this, the TiO_2 nanoparticle powders were heated at 570 K for 1 hour, then the mixture was stirred for 16 hours to ensure a uniform consistency. Before the nanoparticle deposition, the FTO substrates were washed by boiling them in acetone for 15 minutes, followed by 15 minutes of boiling in ethanol, and then rinsed with de-ionized water. After the final rinsing, the substrates were dried in the air for 15 minutes. Electrophoretic deposition (EPD) was performed with a CHI electrochemical analyser, model 608E, using the Chronopotentiometry mode. During EPD, the suspension was continuously stirred using a magnetic stirrer. After completion of the last cycle, the electrodes were annealed for 2 h at 400K in a hot air oven.

3.4.1 Functionalization FTO/TiO_2 surfaces

Functionalization of FTO/TiO_2 surfaces to obtain the final FTO/TiO_2/MOF photoelectrodes was achieved by drop casting MOF paste onto the FTO/TiO_2 surfaces. 1 mM slurry solutions of the MOFs were made by dissolving the MOFs in ethanol and then carefully depositing 20µL of the MOF solution on the FTO/TiO_2 surface. Before deposition, the MOFs were activated in a hot air oven at 150°C for 1 hour to remove excess DMF. The electrodes were then left to dry under controlled humidity and temperature for three weeks.

3.4.2 Preparation of mixed-metal, metal organic framework photoelectrodes

Preparation of the mixed-metal, metal organic framework photoelectrodes was done by functionalization of FTO/TiO_2 surfaces was achieved by drop casting the mixed metal MOF solutions onto the FTO/TiO_2 surfaces. 1 mM slurry solutions of the mixed metal MOFs were made by dissolving the mixed metal MOFs in ethanol and then carefully depositing 20µL of the mixed metal MOF solution on the FTO/TiO_2 surface. The electrodes were then left to dry under controlled humidity and temperature for a period of three weeks.

3.4.3 Preparation of the tandem device

The tandem device was prepared by electrodepositing α-Fe_2O_3 onto the FTO/TiO_2 surfaces. Electrodeposition was carried out using the same parameters as those used in the electrodeposition of TiO_2 nanoparticles. The electrolyte was made up of 0.25g of α-Fe_2O_3 dissolved in 50 ml of deionized water. The final z -scheme device was obtained by drop casting the MOF solutions onto the FTO/TiO_2/ α-Fe_2 O_3. 1 mM slurry solutions of the MOFs were made by dissolving the MOFs in ethanol and then carefully depositing 20µL of the MOF solution on the FTO/TiO2/ α-Fe_2 O_3 surface. The electrode was then left to dry under controlled humidity and temperature three weeks.

3.5 WATER SPLITTING EXPERIMENTS

Water splitting was performed using the functionalized TiO_2 electrodes. All the measurements were performed versus the Ag/AgCl reference electrode. Na_2SO_4 (0.1 M), was used as the electrolyte with a Platinum wire as the counter electrode. The following tests were carried out:

- Cyclic Voltammetry
- Linear Sweep Voltammetry
- Chronoamperometry.
- Electrochemical Impedance Spectroscopy
- Open Circuit Potential
- Tafel analysis
- Hydrogen peroxide quantification
- Quantification of evolved hydrogen

The full details of the water splitting measurements are given in the relevant sections.

3.6 REFERENCES

1) Altaf, M., Sohail, M., Mansha, M., Iqbal, N., Sher, M., Fazal, A., Ullah, N., & Isab, A. A. (2018). Synthesis, Characterization, and Photoelectrochemical Catalytic Studies of a Water-Stable Zinc-Based Metal–Organic Framework. *ChemSusChem*, *11*(3), 542–546. https://doi.org/10.1002/cssc.201702122
2) Kawondera, R., Bonechi, M., Maccioni, I., Giurlani, W., Salzillo, T., Venuti, E., Mishra, D., Fontanesi, C., Innocenti, M., Mehlana, G., & Mtangi, W. (2023). Chiral “doped” MOFs: an electrochemical and theoretical integrated study. *Frontiers in Chemistry*, *11*. https://doi.org/10.3389/fchem.2023.1215619
3) Mtangi, W., Tassinari, F., Vankayala, K., Vargas Jentzsch, A., Adelizzi, B., Palmans, A. R. A., Fontanesi, C., Meijer, E. W., & Naaman, R. (2017). Control of Electrons’ Spin Eliminates

Hydrogen Peroxide Formation during Water Splitting. *Journal of the American Chemical Society*, *139*(7), 2794–2798. https://doi.org/10.1021/jacs.6b12971

4 PHOTOELECTROCATALYTIC WATER SPLITTING USING CHIRAL DOPED ZN-MOF

4.1 INTRODUCTION

This chapter discusses the synthesis of the zinc-based MOF and its chiral derivatives and their application in photoelectrocatalytic water splitting. Traditionally water splitting has been carried out using noble, rare, very expensive and sometimes toxic elements such as Ruthenium, Iridium and Cadmium, in a bid to reduce the cost of the photoelectrodes a Zinc based photoelectrode was selected. The selected Zn-MOF can be classified as a multivariate metal organic framework (MTV MOF) because it contains more than one linker. Zn-MOF was synthesized using terephthalic acid (H_2BDC or bdc) and N,N'-bis(pyridin-4-ylmethyl)cyclohexane-1,4-diamine (bpcda), that was prepared *in-situ*. The chiral Zn-MOFs were synthesized by incorporating R (-) and S (+) Camphor Sulphonic Acid as well as L Cysteine. The chapter also discusses the synthesis, characterization and application of a novel amine functionalized Zn-MOF, which was synthesized to investigate the effect of the amine linker on the bad gap of the Zn-MOF. The novel Zn-MOF-NH_2 was synthesized through the use of bpcda and NH_2BDC as the linkers. Successful incorporation of the different components of the N,N'-bis(pyridin-4-ylmethyl)cyclohexane-1,4-diamine (bpcda) was evaluated using Nuclear Magnetic Resonance (NMR).

4.2 SYNTHESIS OF ZINC MOF

The Zn-MOF was synthesized from two different linkers to increase the active sites for the water splitting reaction (Altaf et al., 2018). The two linkers used are terephthalic acid (H_2BDC or bdc) purchased from Sigma Aldrich, Germany and used with no further treatment, while the N,N'-bis(pyridin-4-ylmethyl)cyclohexane-1,4-diamine (bpcda), the bpcda was prepared *in-situ.*

4.2.1 The synthesis of the linker N,N'-bis(pyridin-4-ylmethyl)cyclohexane-1,4-diamine (bpcda)

The linker N,N'-bis(pyridin-4-ylmethyl)cyclohexane-1,4-diamine (bpcda) was synthesized according to the method published by Altaf in 2018 (Altaf et al., 2018), with slight modification. **Scheme 4.1** illustrates the method that was used in the preparation of the linker. In detail, 4-pyridylcarboxyldehyde (5g, 46.68 mmol) and (1r,4r)-cyclohexane-1,4-diamine (5.33g, 46.68mmol) was added in ethanol (30 mL). Then, triethylamine (7.08g, 70.02 mmol) was

added drop-wise, the resulting mixture was then refluxed for 4 hours at 80 ° C. After refluxing, the reaction mixture was cooled down to room temperature. Sodium Borohydride ($NaBH_4$) (4.41g, 116.7 mmol) was then added drop-by-drop after which the stirring of the reaction mixture was carried out for 16 hours at room temperature. To quench the extra reducing agent, 10 mL of water was then added to the reaction mixture, then 40 ml of dichloromethane (DCM) was added to separate the organic layer. Repeated extractions using the DCM were carried out and the organic layers were combined. Finally, the product was dried by removing the organic solvent with the aid of anhydrous Na_2SO_4 (Altaf et al., 2018). ^{1}H and ^{13}C Nuclear Magnetic Resonance (NMR) was carried out to confirm the successful synthesis of the linker.

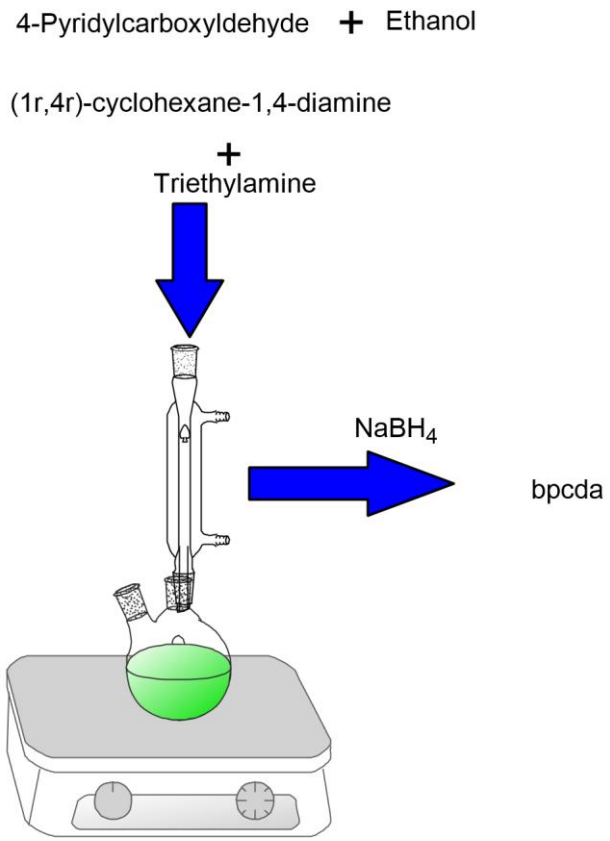

Scheme 4.1: Synthesis of the linker (bpcda)

4.2.2 Synthesis of the metal-organic framework (Zn-MOF)

A mixture of $Zn(NO_3)_2 \cdot 6H_2O$ (0.297 g, 1.0 mmol), N,N'-bis(pyridin-4-ylmethylene)cyclohexane-1,4-diamine (bpcda) (0.297 g, 1.0 mmol), H_2BDC (0.172 g, 1.0 mmol) and mixture of DMF and H_2O (10 mL, v/v: 3/1) was mixed and placed in a glass vial and the vial was loosely capped and then heated at 105 ˚C for three days. White block-shaped crystals were obtained. The crystals were washed using 10ml of DMF, three different times and then dried in a hot air oven

at 80°C for 15 minutes. **Scheme 4.2** shows the steps that were followed in the synthesis of the zinc MOF.

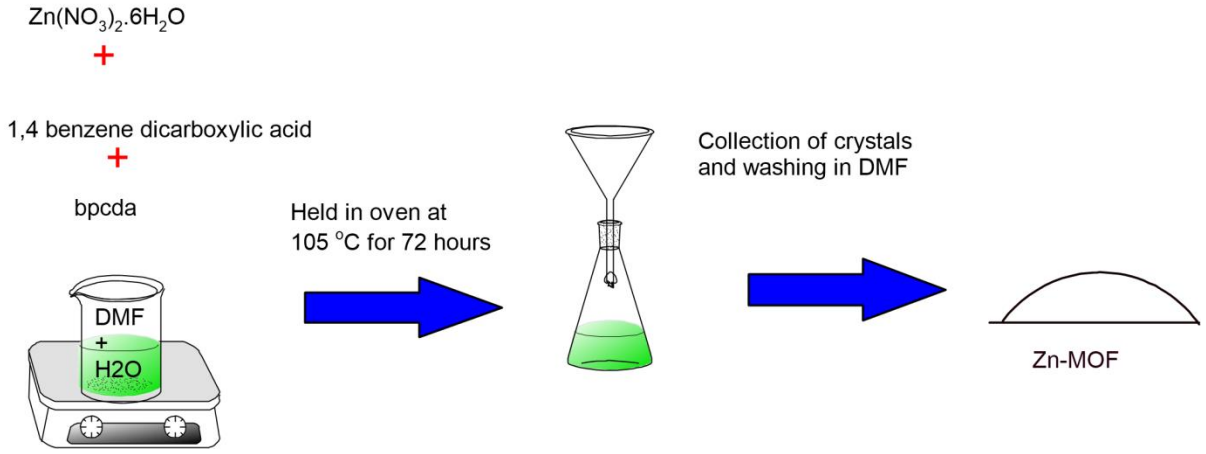

Scheme 4.2. Synthesis of Zn-MOF

4.2.3 Synthesis of Chiral Zn-MOF Derivatives

4.2.3.1 Chiral Zn-MOF-R CSA

A mixture of $Zn(NO_3)_2 \cdot 6H_2O$ (0.297 g, 1.0 mmol), N,N'-bis(pyridin-4-ylmethylene)cyclohexane-1,4-diamine (bpcda) (0.297 g, 1.0 mmol), H_2BDC (0.163 g, 0.95 mmol), R camphor sulphonic Acid (0.0232g) and mixture of DMF and H_2O (10 mL, v/v: 3/1) was mixed and placed in a glass vial and the vial was loosely capped and then heated at 105 ˚C for three days. White block-shaped crystals were obtained. The crystals were washed using 10ml of DMF, three different times eventually dried in a hot air oven at 80°C for 15 minutes.

4.2.3.2 Chiral Zn-MOF-S CSA

A mixture of $Zn(NO_3)_2 \cdot 6H_2O$ (0.297 g, 1.0 mmol), N,N'-bis(pyridin-4-ylmethylene)cyclohexane-1,4-diamine (bpcda) (0.297 g, 1.0 mmol), H_2BDC (0.163 g, 0.95 mmol), S camphor sulphonic Acid (0.0232g) and mixture of DMF and H_2O (10 mL, v/v: 3/1) was mixed and placed in a glass vial and the vial was loosely capped and then heated at 105 ˚C for three days. White block-shaped crystals were obtained. The crystals were washed using 10ml of DMF, three different times and finally dried in a hot air oven at 80°C for 15 minutes.

4.2.3.3 Chiral Zn-MOF-L Cysteine

A mixture of $Zn(NO_3)_2 \cdot 6H_2O$ (0.297 g, 1.0 mmol), N,N'-bis(pyridin-4-ylmethylene)cyclohexane-1,4-diamine (bpcda) (0.297 g, 1.0 mmol), H_2BDC (0.163 g, 0.95 mmol), L Cysteine (0.0121g) and mixture of DMF and H_2O (10 mL, v/v: 3/1) was mixed and placed in a glass vial and the vial was loosely capped and then heated at 105 ˚C for three days. White block-shaped crystals

were obtained. The crystals were then washed using 10ml of DMF three different times and then dried in a hot air oven at 80°C for 15 minutes.

4.2.3.4 Achiral Zn-MOF-NH_2

A mixture of $Zn(NO_3)_2 \cdot 6H_2O$ (0.297 g, 1.0 mmol), N,N'-bis(pyridin-4-ylmethylene)cyclohexane-1,4-diamine (bpcda) (0.297 g, 1.0 mmol), NH_2-H_2BDC (0.181 g, 1.0 mmol) and mixture of DMF and H_2O (10 mL, v/v: 3/1) was mixed and placed in a glass vial and the vial was loosely capped and then heated at 105 ˚C for three days. Slightly green, block-shaped crystals were obtained. The crystals were then washed in 10ml of DMF three different times and then dried in a hot air oven at 80°C for 15 minutes.

4.3 NUCLEAR MAGNETIC RESONANCE

To assess the extent of formation of N,N'-bis(pyridin-4-ylmethylene)cyclohexane-1,4-diamine (bpcda), NMR studies were conducted. The procedure for carrying out the NMR studies is as described in Section 3.3. The linker, bpcda was successfully synthesized as witnessed by the ^1H and ^{13} C NMR.

4.3.1 ^1H NMR

The ^{1} H chemical shifts are summarized as shown in **Table 4.1**.

Table 4.1: ^1H chemical shifts (ppm) of the bpcda in $CDCl_3$

Functional group	**4-pyridine C-H**	**Aliphatic CH_2**	**Amine N-H**	**Cyclohexane CH_2**
shifts (ppm)	8.55, 7.35	3.75	2.0	1.6

The ^{1} H NMR spectrum of the linker (bpcda) (shown in Appendix A) displays aromatic protons in the region from 8.55 ppm to 7.35 ppm, these can be attributed to the C-H groups that are present in 4-pyridine. Methylene group (CH_2) was observed by chemical shifts at 3.75 ppm and at 1.6 ppm, the source of CH_2 was assigned to the aliphatic and cyclohexane groups respectively. The chemical shift at 2.0 ppm was assigned to the amine group (NH). The presence of the ^{1} H NMR signals of these spectra are similar to the predicted NMR signal for ^1H. The prediction was done using Chemdraw and the output file shown in Appendix A. The ^{1} H NMR spectrum of the linker (bpcda) is shown in Appendix A.

4.3.2 Carbon-13 NMR

The ^{13} C chemical shifts are summarized as shown in **Table 4.2**.

Table 4.2: ^{13} C chemical shifts (ppm) of the Zn-MOF in $CDCl_3$

Functional Group	**Pyridine**	**Cyclohexane**	**CH_2**
Shift (ppm)	150.07, 122.86	56.18, 30.68	50.20

The ^{13}C chemical shifts of Zn MOF are summarized in **Table 4.2**. In the ^{13}C {H} NMR spectrum of bpcda, chemical shifts were observed at 150.07 ppm and 122.86 and these were attributed to the presence of the pyridine group, while the chemical shifts at 56.18 and 30.63 ppm were due to the presence of the cyclohexane. The presence of chemical shift at 50.20 ppm is due to the existence of an aliphatic group (CH_2). The ^{13}C {H} NMR spectrum of the complex exhibited the expected number of carbon signals. The ^{13}C {H} NMR spectrum of the linker (bpcda) is also shown in Appendix A.

The appearance of chemical shifts for N-H (Amine), C=O (Carbonyl), Cyclohexyl, -CH_2- (Methylene) and Pyridyl groups of both ligands (4-Pyridylcarboxyldehyde and (1r,4r)-cyclohexane-1,4-diamine) in ^{1}H and ^{13}C NMR spectra is a confirmation that the linker: N,N'-bis(pyridin-4-ylmethyl)cyclohexane-1,4-diamine (bpcda) was successfully synthesized (Altaf et al., 2018).

4.4 CHEMICAL ELEMENTAL ANALYSIS OF ZN MOF

4.4.1 Energy Dispersive Spectroscopy (EDS)

Chemical elemental analysis was carried out using Energy Dispersive Spectroscopy (EDS) of the Zn-MOF as well as its different derivatives. From EDS spectra, the chemical composition of the MOFs expressed as a percentage can be evaluated.

Table 4.3: Elemental Analysis of Zn-MOF and Zn-MOF derivatives

MOF	Zn (%w/w)	O (%w/w)	C (%w/w)	N (%w/w)	S (%w/w)
Zn-MOF	31.1	35.5	30.1	3.7	-
Zn-MOF - NH_2	23.4	35.1	47.5	3.9	-
Zn-MOF R-CSA	22.0	30.5	41.5	3.4	2.6
Zn-MOF S-CSA	26.4	28.5	39.8	4.2	1.1
Zn-MOF -L Cysteine	25.9	33.3	35.2	4.1	1.5

Table 4.3, shows a summary of the composition of the Zn-MOF and its derivatives. In the Zn-MOF structures, the zinc is observed in all the MOFs. In the chiral doped MOFs Zn-MOF L-Cysteine, Zn-MOF R-CSA and Zn-MOF S-CSA, the EDS analysis indicates the presence of the element sulphur. The sulphur detected is present in cysteine and camphor sulphonic acid, and the presence of the sulphur in the chiral derivatives of the Zn-MOF, are confirmation that the MOFs were successfully “chiralized.” Figure 4.1, shows the EDS spectra of Zn-MOF and its derivatives.

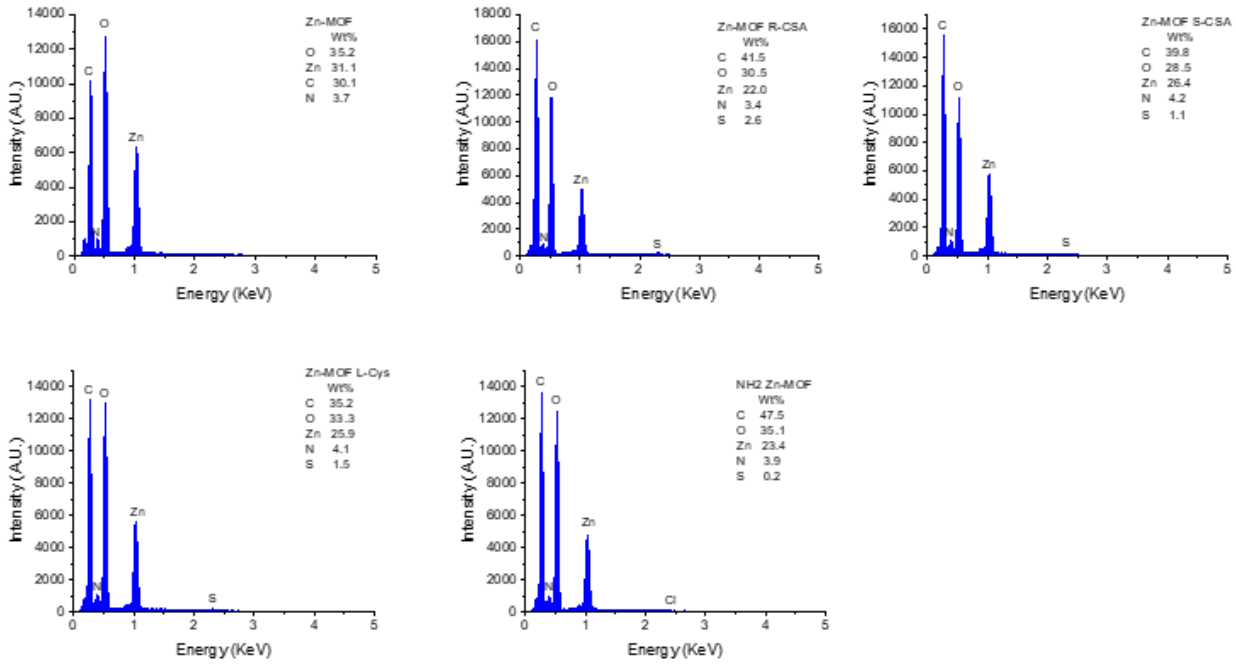

Figure 4.1: EDS spectra of the Zn-MOF and its derivatives

4.5 FUNCTIONAL GROUPS

4.5.1 Zn-MOF FTIR

The IR spectra of the Zn[(bdc)(bpdca)]$_n$ **(Figure 4.2)** shows the characteristic band that is due to the carboxylic functional group in the 1300 to 1000 cm^{-1} range. In the fingerprint region, the peak observed at 534 cm^{-1} is attributed to the Zn-O bond, while the peaks that are observed at 887 cm^{-1}, and 1091 cm^{-1}, are attributed to a N-H wag and a C-N stretch, respectively. A strong, sharp peak is observed at 1220 cm^{-1} and this peak can be attributed to the C-N stretching due to an aromatic amine, while the sharp peak observed at 1349 cm^{-1} can be attributed to the O-H bending of an alcohol.

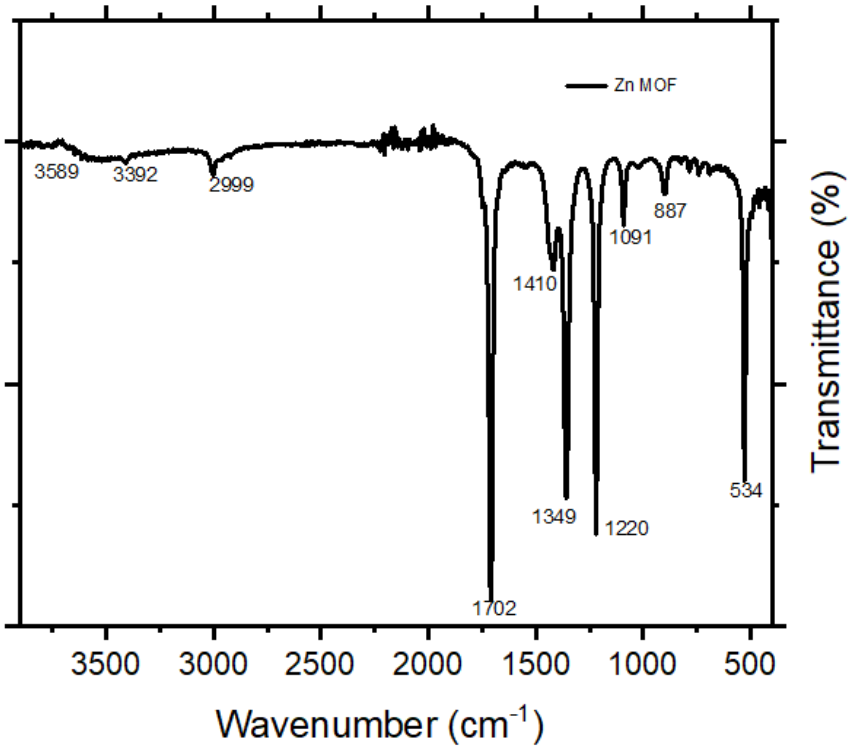

Figure 4.2: Zn-MOF FTIR Spectrum

At 1410 cm^{-1} a medium peak was observed, and this can be attributed to the presence of C-H bending of a methyl group. A strong and very sharp peak is observed at 1702 cm^{-1}, this peak is attributed to C=O cm^{-1} stretching due to cyclohexane, the weak peak observed at 2999 cm^{-1} can be attributed to C-H stretching in an alkane group. The weak peak at 3392 cm^{-1} can be attributed to the stretching of N-H present in a secondary amine. The presence of functional groups attributed to cyclohexane, primary amines as well as the Zn-O bond greatly point to the successful formation of the Zn-MOF.

4.5.2 FTIR of the derivatives of the Zn-MOF

FTIR measurements were also carried out for Zn-MOF derivatives.

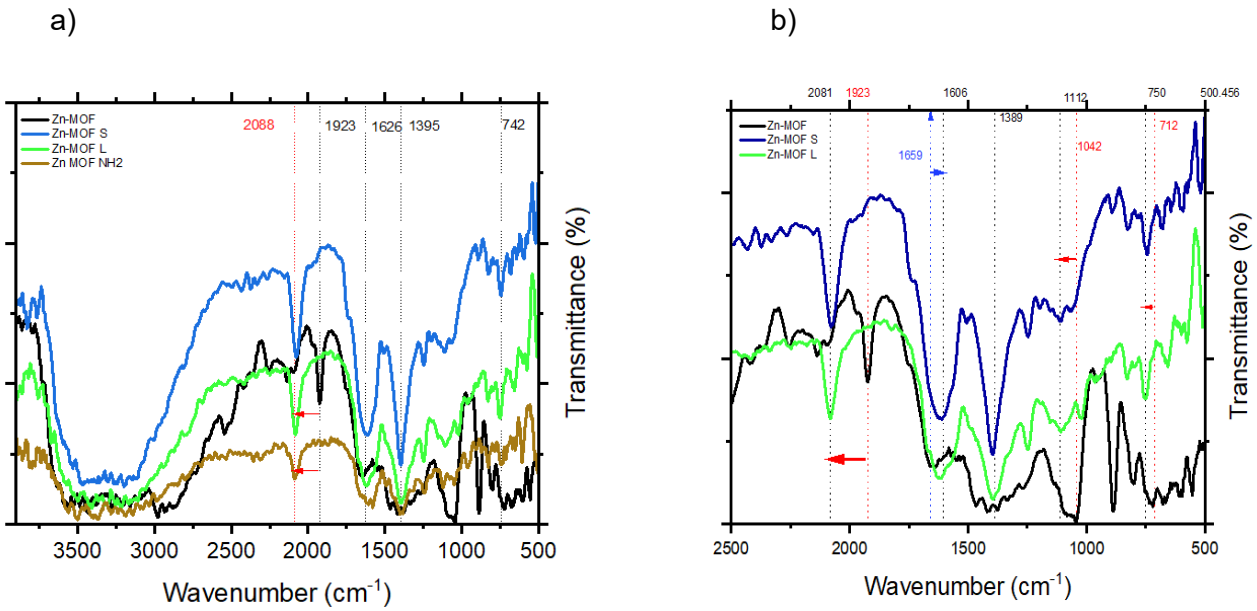

Figure 4.3 FTIR spectra showing comparison between (a) Zn-MOF and the Zn-MOF derivatives (b) Zn-MOF and the chiral derivatives

Figure 4.3, shows a comparison of the FTIR spectra between Zn MOF and its derivatives. In **Figure 4.3 (a**), an apparent red shift has occurred in all the derivatives, from 1923 cm^{-1} in the parent Zn-MOF (black line) to 2088 cm^{-1} in the derivatives. This shift can be attributed to the bond weakening in N-H is due to the hydrogen bonds formed between the chiral linkers and the linker N,N'-bis(pyridin-4-methyl)cyclohexane-1,4-diamine (Kawondera et al., 2023). Zn-MOF-NH_2 and Zn-MOF-L Cysteine show a peak between 3300 cm^{-1}, and 3400 cm^{-1} , which can be attributed to N-H stretching. In **Figure 4.3(b)**, a number of redshifts are observed from 1042cm^{-1} to 1112 cm^{-1} and at 712 cm^{-1} to 750cm^{-1} all showing formation of new hydrogen bonds between the chiral moieties and the Zinc salt. Interestingly, when comparing the Zn-MOF spectra (black line) and the chiral derivatives, the peak observed at 1659 cm^{-1} in Zn-MOF, has undergone a blue shift and can now be observed at 1606cm^{-1} in Zn MOF S-CSA and Zn MOF L Cysteine indicating that the C-H bonds in the Zn-MOF has been strengthened in the chiral derivatives.

4.6 POWDER X-RAY DIFFRACTION

4.6.1 Zn-MOF PXRD

To investigate the crystalline nature of the Zn-MOFs, PXRD measurements were carried out according to the methods described in Chapter 3.3. All the PXRD patterns were drawn using Origin 2023 and a comparison was made versus the calculated PXRD profile of the Zn-MOF as shown in **Figure 4.4.**

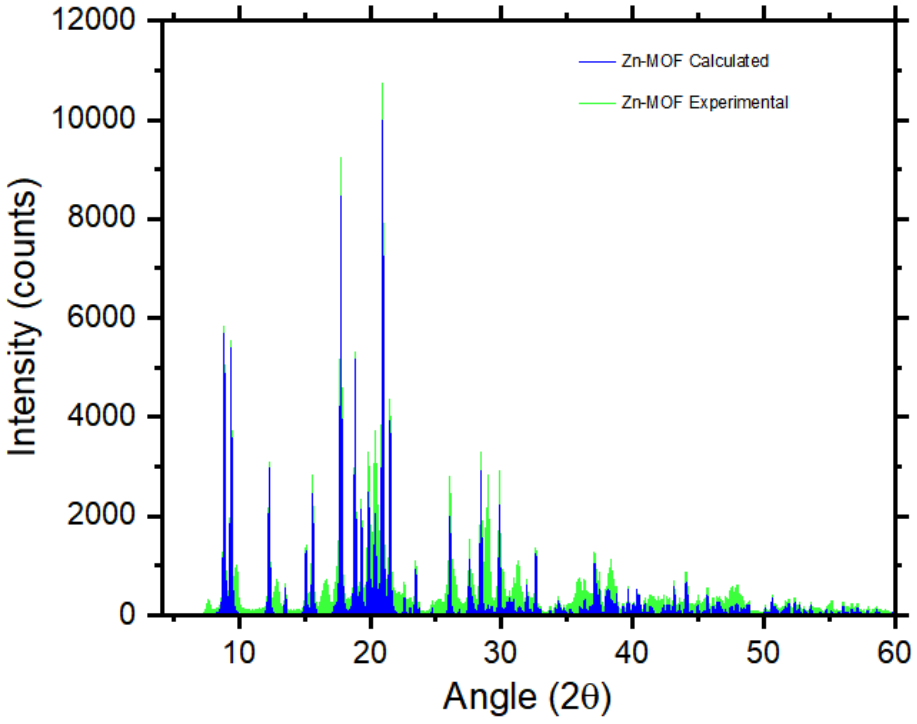

Figure 4.4: PXRD pattern of synthesized Zn-MOF vs Calculated PXRD spectrum of Zn-MOF

The peaks observed in the PXRD pattern **Figure 4.4** of the synthesized Zn-MOF (green phase) are similar to those observed in the calculated (simulated) PXRD spectrum (blue phase) of the Zn-MOF with slight deviations which can be attributed to unreacted $Zn(NO_3)_2$ $.6H_2O$.

In detail, a doublet can be identified at 8.25 and 9.23° in both patterns, similarities are also observed at 16.65, 17.68. 20.44, 21.73, 26.19, 30.07, 31.78, 34.3, 36.37, 37.42, 39.05, 42.21, 46.14, 48,04 and 48.61°. These observations lead to the conclusion that the Zn-MOF, was successfully synthesized.

4.6.2 PXRD for the Zn-MOF chiral derivatives

In the PXRD patterns of the Zn-MOF chiral derivatives, shown in **Figure 4.5**, all the peaks observed in the Zn-MOF, are observed in chiral derivatives, with Zn-MOF R CSA showing exhibiting poor crystallinity compared to the other chiral MOFs. In all the chiral Zn-MOFs, there is a noticeable absence of peaks beyond 40 (2θ), position, the chiral MOFs contain three different linkers and this will ultimately affect their crystallinity. The presence of dopants affects the mean atomic scattering of a given site. The introduction of the chiral dopants can be observed by the changes in the 2θ positions of some of the peaks mainly to the left. A shift to lower 2 theta values indicate an increase in the unit cell volume the incorporation of the larger linker, reduces the unit cell volume.

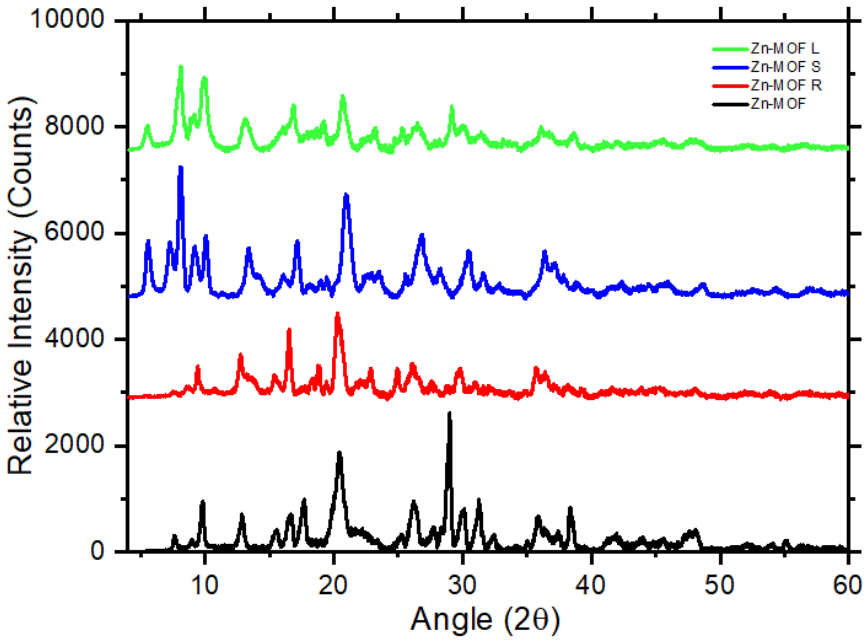

Figure 4.5: PXRD pattern of the chiral derivatives of Zn-MOFs

From the EDS results in section 4.4.1, it was observed that the sulphur from the chiral dopants has been successfully incorporated. Based on this observation it can also be assumed that the chiral linkers (Camphor Sulphonic Acid and L-Cysteine), were incorporated into the MOF matrix.

4.6.3 Zn-MOF-NH_2 PXRD

PXRD analysis was also carried out for the Zn-MOF-NH_2, and the PXRD pattern of Zn-MOF-NH_2, is shown in **Figure 4.6**.

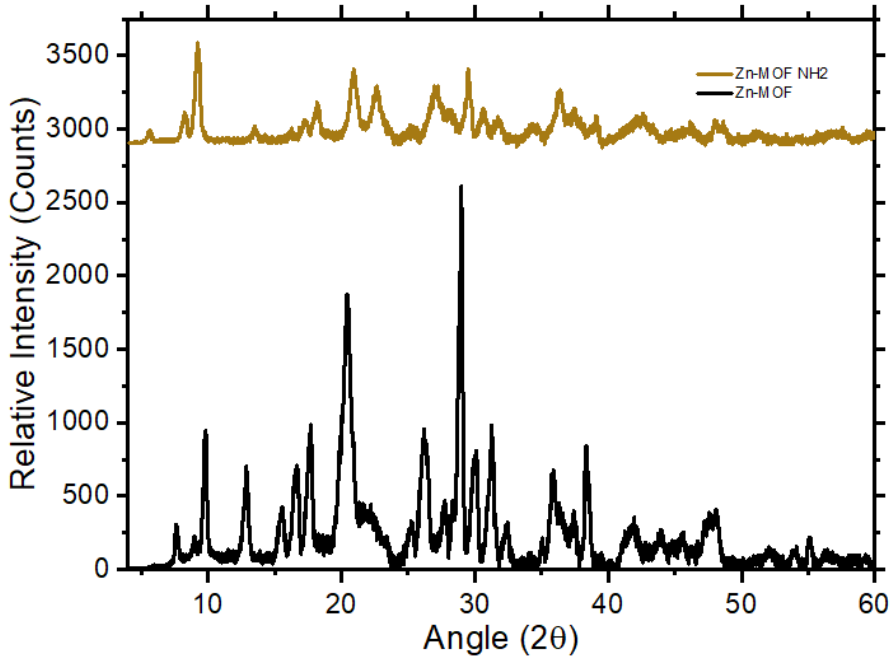

Figure 4.6: PXRD pattern of Zn-MOF-NH_2

The PXRD pattern of Zn-MOF and Zn-MOF-NH_2 is almost similar as the two MOFs are isostructural; they have the same structure. However, when comparing the positions of the first peaks, there is a shift to the left in the first peak. In Zn-MOF, the first peak was observed at 8.25° while in the Zn-MOF-NH_2, the first peak is observed at 7.11°. The shift can be attributed to the incorporation of the larger linker (amino terephthalic acid) into the crystal structure (Bitzer et al., 2021)

4.7 Photocatalytic Activity

In order to evaluate the effectiveness of the Zn-MOF and its derivatives as photocatalysts, Uv-Vis measurements were carried out. In Uv-Vis spectroscopy, when a solution is irradiated, an electron from a lower set orbital is promoted into the upper set orbital. In transition metals, this

happens when the electrons move onto the partially filled 3d orbitals. The synthesized MOFs exhibited very distinct colours, the Zn-MOF and the chiral Zn-MOFs were all white in colour while the Zn-MOF-NH_2 was slightly green.

a) b)

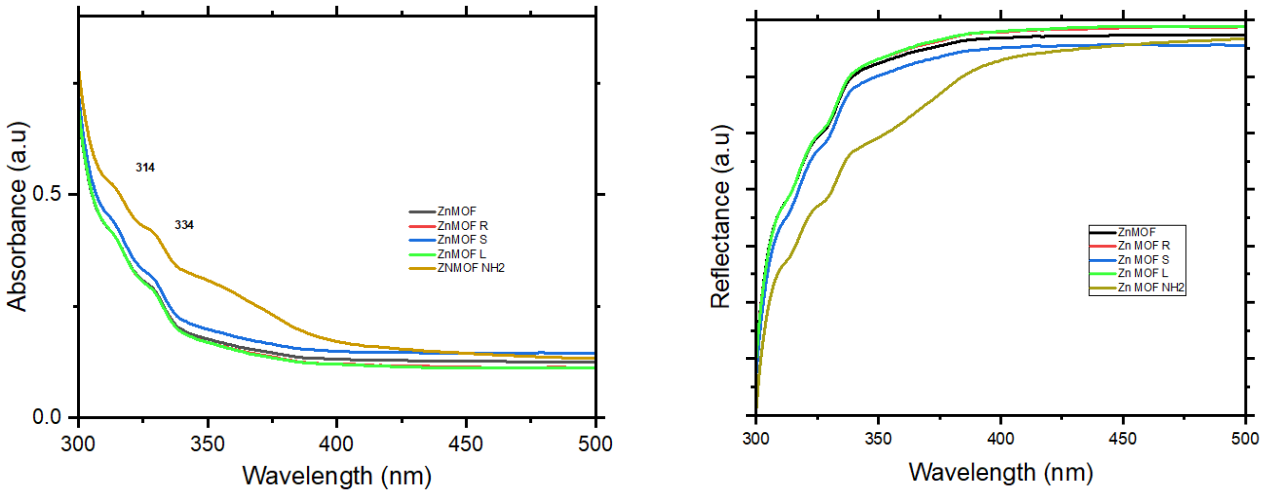

Figure 4.7 a) Uv-Vis Absorption Spectra for Zn-MOF and derivatives b) Diffuse Reflectance Spectra for Zn-MOF and derivatives.

In the Zn-MOF, the absorption spectra shown in **Figure 4.7 (a),** are almost identical with the only difference being the intensity of the absorbance with Zn-MOF-NH_2 exhibiting the greatest absorbance. **Figure 4.7 (b),** shows the diffuse reflectance spectra (DRS) of the Zn-MOF and its derivatives. DRS is used quantitatively to measure the colour and intensity of reflected light, it gives the light reflectance and absorbance of materials (Tran et al., 2023). From **Figure 4.7 (b),** Zn-MOF-NH_2 has the least reflectance, suggesting that it has better light harvesting properties. From the physical appearance of the MOFs, all the Zn MOFs are white in colour except the Zn-MOF-NH_2 which is slightly green in colour. The green colour Zn-MOF-NH_2 can be attributed to the presence of the amino terephthalic acid, suggesting that the addition of amino group, enhances the light harvesting capabilities of MOFs. Peaks are observed at 314nm, 335nm and the absorption edge falls at 370nm. There are multiple HOMO/LUMO levels due to multiple absorption bands, and these can be attributed to the presence of two different ligands (Altaf et al., 2018). Zinc contains a completely filled 3d orbital, it has no partially filled 3d orbital where the excited electron can transition to as such the absorbance of the Zn-MOF is low in the visible range, with the exception of Zn-MOF-NH_2. To better

elucidate the band gap energies of the Zn-MOFs, Tauc plots were plotted. The Tauc plots are used to estimate the band gap energy of the MOFs. Tauc plots are drawn using the equation:

$$(\alpha h\nu)^n = (h\nu - E_g) \qquad \text{Equation 4.1}$$

Where h is Planck's constant, (6.63x 10^{-34} J/s)

v is the speed of light (3.0 x 10^8 m/s)

α is the absorption coefficient

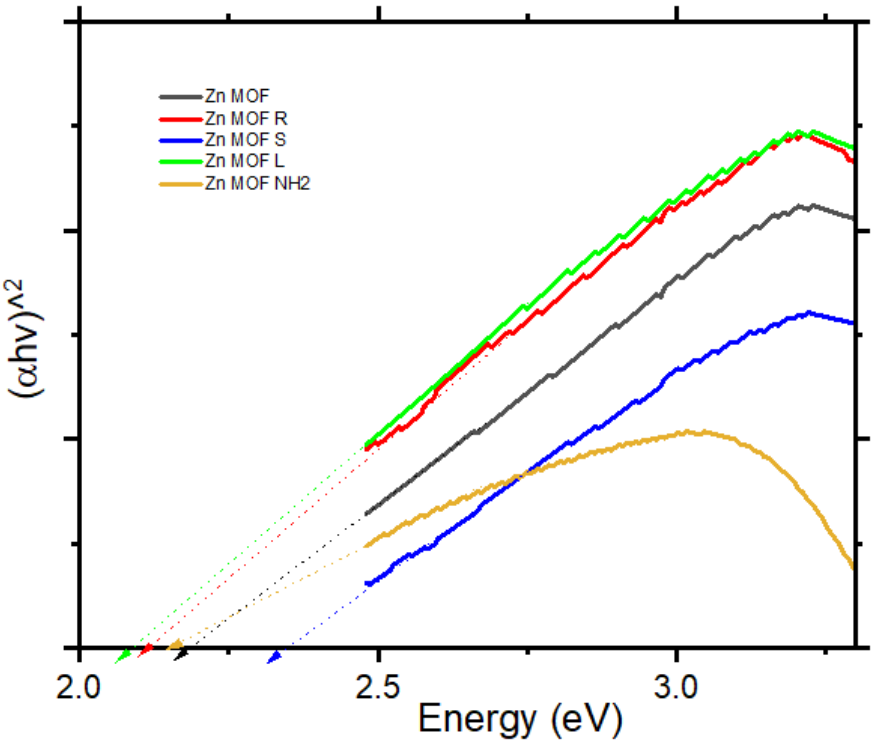

Figure 4.8 Tauc Plots for Zn-MOF and its derivatives

From **Figure 4.8**, the band gap energies were observed to be 2.17, 2.11, 2.32, 2.07 and 2.15 eV for Zn-MOF, Zn-MOF-R CSA, Zn-MOF-S CSA, Zn-MOF L Cysteine and Zn-MOF-NH_2 respectively. Reduction of band gap energies was observed for the Zn-MOF doped with L Cysteine, Zn-MOF-R CSA as well as Zn-MOF-NH_2.

For Zn-MOF-NH_2 the Uv-Vis spectrum produced had larger absorbances in the visible region (300 and 450nm) than those exhibited by Zn-MOF and this implies that the Zn-MOF-NH_2 would be a better photocatalyst for water splitting. The use of 2-aminoterephthalic acid as a substitute linker for terepthalic acid introduces new properties in the final MOF produced. In this case,

the Zn-MOF-NH_2 becomes more active in visible range compared to the original Zn-MOF. According to Nasalevich and co-workers, the addition of 2- aminoterephthalic acid improves the light harvesting properties of a MOF. The 2-aminoterephthalic acid provides a lone pair of nitrogen for the interaction with the π*- orbitals of the benzene ring, donating electron density to the antibonding orbitals. This results in a new HOMO level that brings arbsorption to the visible range (Nasalevich et al., 2014).

4.8 THERMAL STABILITY

To evaluate the thermal stability of the Zn-MOF, TGA measurements were carried out. The thermogravimetric curve of the Zn-MOF shown in **Figure 4.9** shows the usual three stage thermogram.

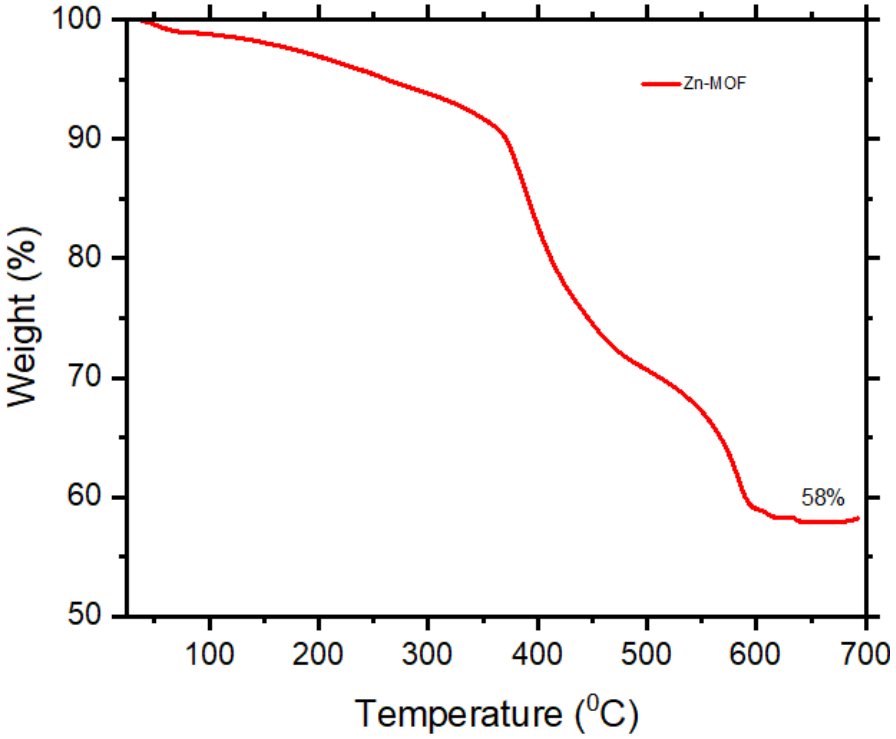

Figure 4.9 Thermogravimetric curve for Zn-MOF

The initial decomposition before 100°C can be attributed to the loss of the occluded water molecules. Weight loss recorded between 100°C and 366°C corresponds to the liberation of the DMF molecules (Tshuma et al., 2020), while the decomposition of the framework occurred after 366°C. The Zn-MOF experienced a weight loss of 42%. The Zn-MOF exhibited high thermal stability and as such can be utilized in water splitting.

4.9 CHIRAL RECOGNITION

Chiral recognition is a chemical interaction, in which a given chiral molecule recognizes a particular stereoisomer (Pappalardo & Parisi, 2008). It is the ability to discriminate between enantiomers by which a given chiral molecule recognizes a particular stereoisomer. Chiral molecules tend to create totally different effects on many processes such as biological processes in nature. In general, just one out of a pair of enantiomers produces the characteristic effect and the other either has no effect or has a totally different (and sometimes toxic) effect due to the pair interaction energy of the two (Stefani et al., 2023). In this study cyclic voltammetry was used to differentiate the chiral MOFs.

The electrodes for chiral recognition were prepared by depositing a MOF paste on the surface of the FTO substrate. Before depositing the MOF paste onto the FTO substrates, the FTO substrates were washed by boiling them in acetone for 15 minutes, followed by 15 minutes of boiling in ethanol, and then rinsed with de-ionized water. After rinsing, the substrates were dried in air for 15 minutes. After the deposition of the paste, the electrodes were annealed for 2 hours at 80°C in an oven to remove excess solvent. Cyclic voltammetry was carried out on the chiral electrodes from -0.23V to +1.23V (vs Ag/AgCl) using a scan rate of 0.1V/s in 8mM L Cysteine dissolved in HCl with the pH of the solution maintained at 4.0 using the pH 4 buffer solution.

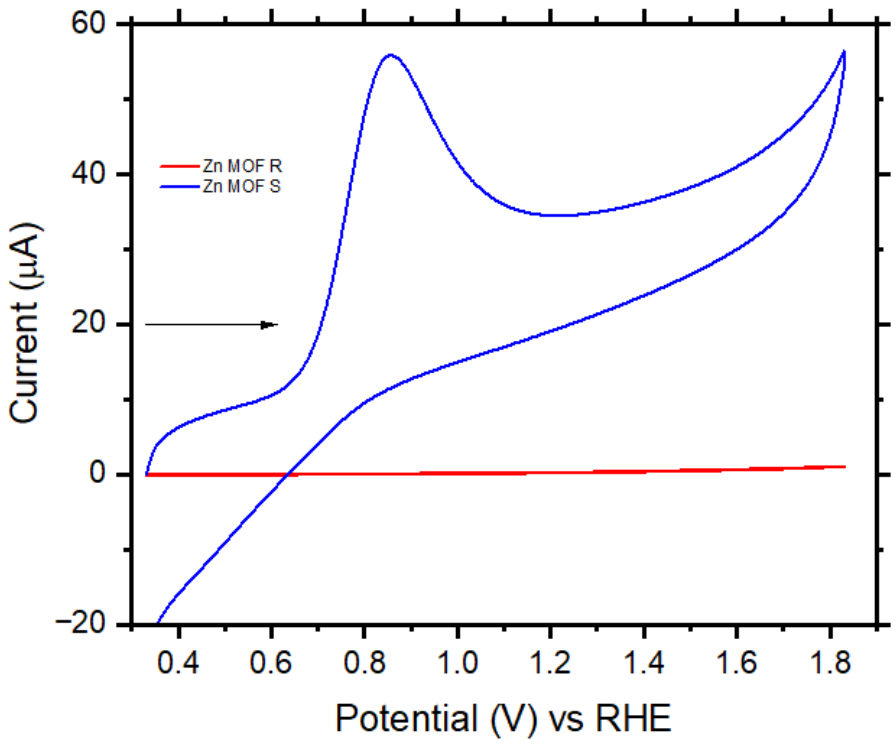

Figure 4.10: A comparison of CVs produced by Zn-MOF vs chiral Zn-MOF photoelectrodes in 8mM L-Cysteine at a scan rate of 0.1V/s

Figure 4.10, shows the cyclic voltammograms obtained during chiral recognition. In the measurements, a marked difference between the interactions of the R CSA and S CSA molecules was observed. Zn-MOF R CSA had no identifiable oxidation or reduction peaks, while Zn-MOF S CSA had peak separation (ΔE) of 0.1V. From the molecular structures of the chiral linkers, L Cysteine can also be called R Cysteine, hence Zn-MOF R CSA, whose chirality was induced by the R Camphor Sulphonic Acid shows no ΔE at all and this can be attributed to the molecular recognition that occurred between the R CSA MOFs and the L Cysteine. In contrary, Zn-MOF S-CSA, whose chirality was induced using S Camphor Sulphonic Acid molecule, shows very high ΔE showing no interaction between it and the L-Cysteine. **Table 4.4** below shows a summary of the ΔE values obtained during the cyclic voltammetry measurements.

Table 4.4: ΔE values obtained during chiral recognition of the chiral electrodes

Photoelectrode	**ΔE (V)**
Zn-MOF	0.118
Zn-MOF R-CSA	-
Zn-MOF S-CSA	0.1

Based on the cyclic voltammograms obtained it was concluded that chirality was successfully induced.

4.10 SOLID STATE ELECTROCHEMISTRY

Solid-state cyclic voltammetry was carried out to evaluate the electrochemical behaviour of the Zn-MOF and its derivatives. The solid-state electrochemistry was carried out, using a three-electrode system in which the glassy carbon electrode coated with the graphite and MOF mixture (GCE/MOF) served as the working electrode (WE), a coiled Platinum wire and an Ag/AgCl (saturated KCl) electrode was used as the counter electrode (CE) and reference electrode (RE), respectively. The graphite powder and MOF mixture, mixed in equal proportions was deposited onto the glassy carbon electrode (GCE). Before the surface modification, the glassy carbon, working electrode was polished using 0.05 μm alumina slurries on a polishing cloth; then it was cleaned carefully, and sonicated for 10 min in milliQ water to clean the surface and remove any polishing residue before being dried. The effective cell set-up and glass carbon electrode activation procedure was cross-checked by recording CVs in a solution of 1 mM ferricyanide in 0.1 M KCl.

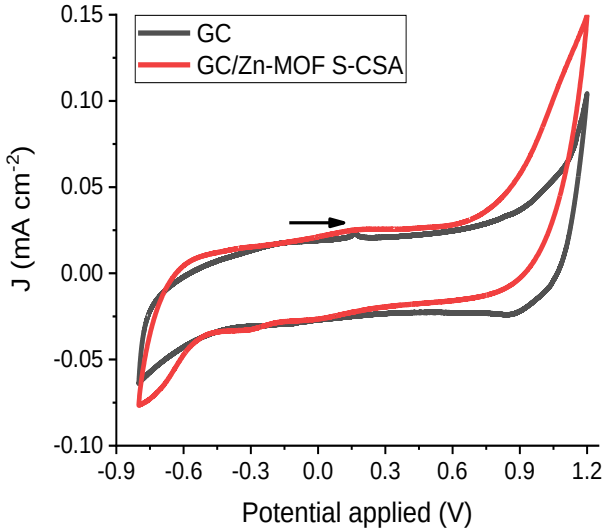

Figure 4.11: Cyclic Voltammetry curve in aqueous 0.1 M Potassium Chloride (KCl), of GC/ Zn-MOF S CSA (Working Electrode) vs Ag/AgCl/KCl_{sat} (Reference Electrode) at a scan rate 0.01V s^{-1}.

Figure 4.11 shows CV curves recorded for Zn-MOF S CSA. The black solid line is the control CV recorded using the graphite powder only, i.e. the "blank" baseline. It was observed that a prominent capacitive contribution, in the -0.7 to 1.0 V potential range yields a regular "rectangular box" CV pattern, as depicted in **Figures 4.11**. The red solid line, shows a peak in the CV recorded after mixing the graphite powder with the chiral MOF (Zn-MOF S CSA).
The electrochemistry of the zinc-based MOFs is characterized by the absence of reversible (or quasi-reversible) oxidation/reduction current signal, as it can be seen from the CVs shown in **Figure 4.11**. Based on this, zinc-based MOFs appear promising materials, to be used in amperometric sensors, because of very low faradaic currents and large volume/surface ratio. On the other hand, the absence of any faradaic current is a direct proof of the electrochemical stability of the "doping" chiral compounds, cysteine and camphor sulphonic acid. The rest of the CV curves for the other zinc-based MOFs are shown in Appendix B.

4.11 SURFACE MORPHOLOGY

4.11.1 Scanning Electron Microscopy (SEM)

Scanning electron microscopy (SEM), was used to investigate the surface morphology of the Zn-MOF. The Zn-MOF exhibits a lamellar morphology, (a pile of flakes, arranged in sheets), while Zn-MOF R-CSA and Zn-MOF S-CSA show the typical lamellar structure of Zn-MOF in a

different way. The lamellar structure is less visible in Zn-MOF L Cysteine and Zn-MOF-NH_2, in which the MOF particles appear clumped, the presence of nitrogen in the structures of L-Cysteine and Amino-terephthalic acid, the linkers in the Zn-MOF L Cysteine and Zn-MOF-NH_2 respectively could have attributed to the change in the surface morphology. The secondary electron, SEM images of the Zn-MOF and its derivatives (all at the same magnitude) are given in **Figure 4.12.**

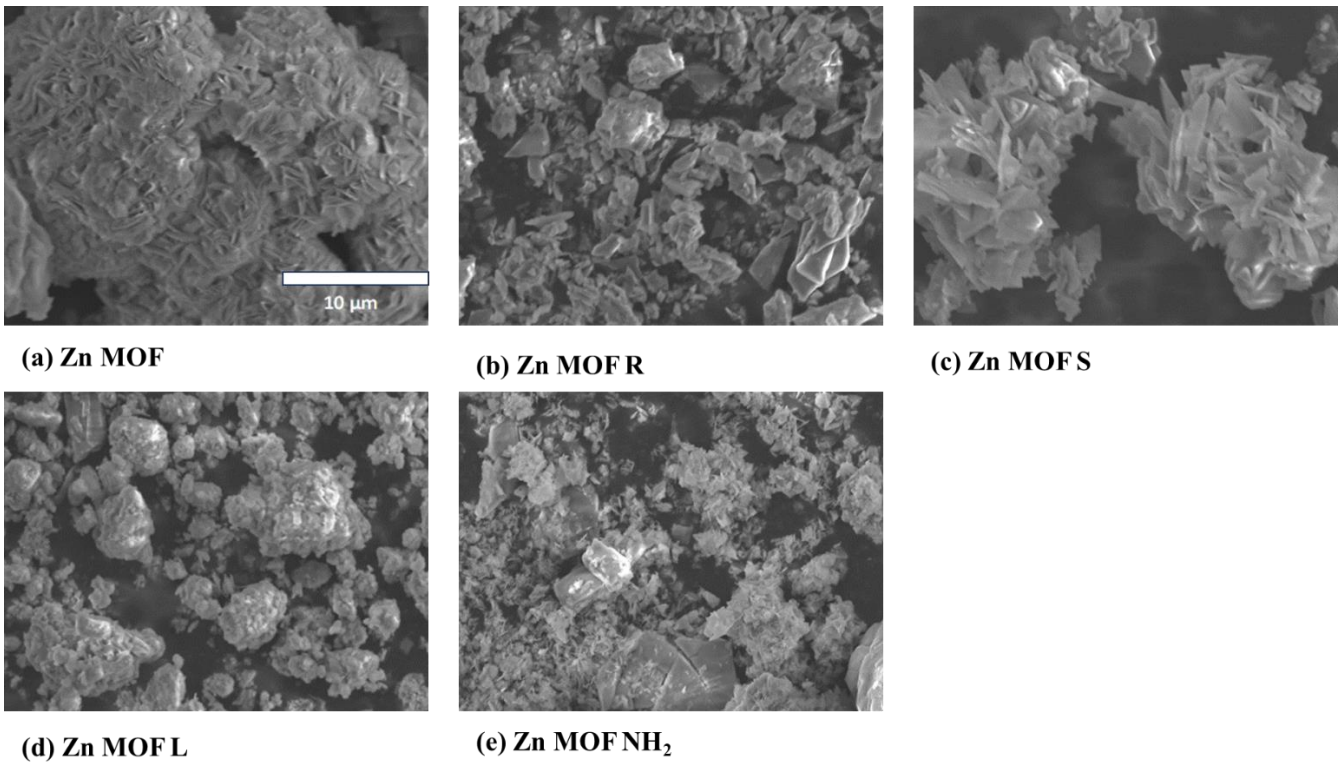

Figure 4.12: SE SEM images of Zn-MOF and derivatives

4.11.2 Field Emission Scanning Electron Microscopy (FESEM)

To consolidate the findings from SEM-EDS, Field Emission Scanning Electron Microscopy (FESEM) was also carried out on Zn-MOF and the Zn-MOF doped with R (-) Camphor Sulphonic acid. From the FESEM images, the lamellar structure of the Zn based MOFs is greatly magnified as shown by the flakes.

a) b)

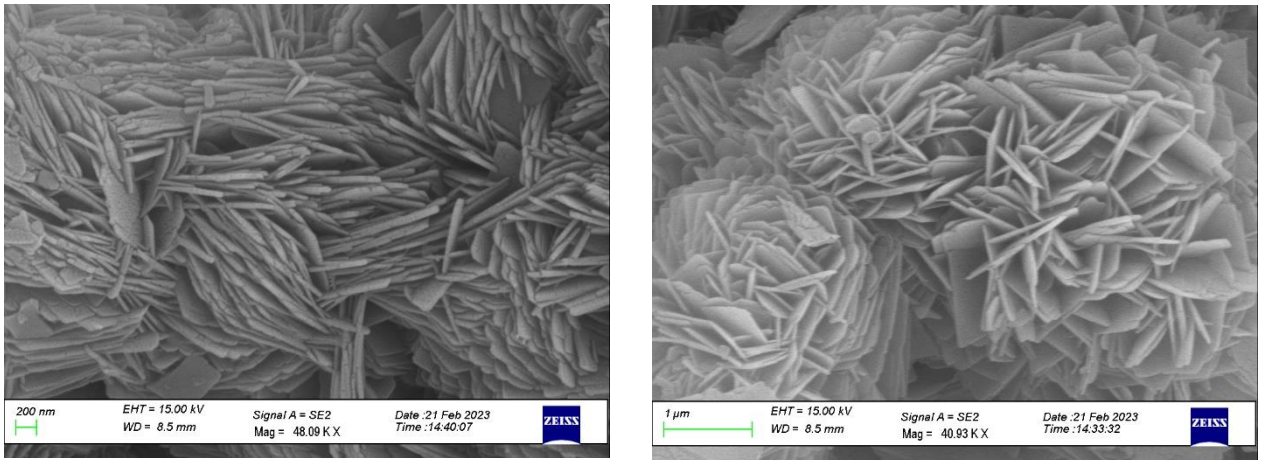

Figure 4.13: FESEM Images for Zn-MOF at different magnifications

In the FESEM images of Zn-MOF shown in **Figure 4.13 (a) and (b)**, the surface morphology is significantly magnified and the previously identified pile of flakes (section 4.11.1) is amplified to show the flakes arranged in a manner that would resemble flower petals, which possesses exposed edges. The flower petal morphology offers a larger surface area as well as abundant active edge sites for the water splitting reaction.

a) b)

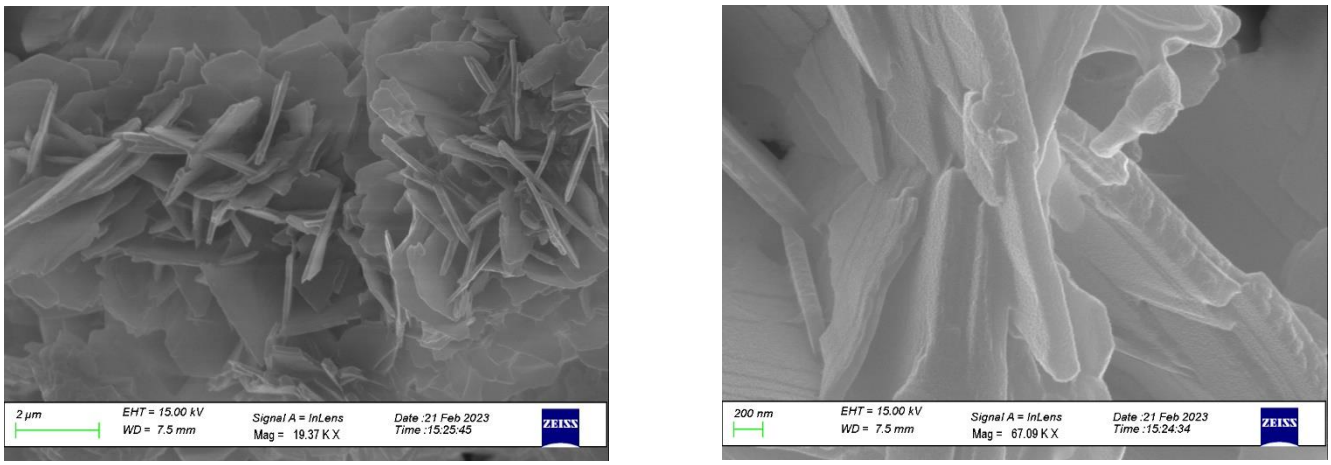

Figure 4.14: FESEM Images for Zn-MOF-R CSA at different magnifications.

In the FESEM images of Zn-MOF- R-CSA, shown in **Figure 4.14** the layered structure with the flower petal arrangement with exposed edges is repeated again. In **Figure 4.14 (b)** with greater magnification shows the surface of the petals with a rugged surface, implying a large surface area for the reaction. The availability of the exposed edges again offers a more active sites for the water splitting reaction.

4.12 PREPARATION OF ELECTRODES

The preparation of the electrodes was done according to the methods published by Mtangi et al in 2017 (Mtangi et al., 2017) as well as modifications done by Kawondera et al in 2023 (Kawondera et al., 2023). In detail, the FTO/TiO_2 electrode was prepared first. TiO_2 nanoparticulate films were deposited on fluorine-doped tin oxide, FTO (surface resistivity of ~7 Ω/sq,) coated glass, using the electrophoretic deposition (EPD) technique. A suspension of TiO_2 nanoparticles (NPs) was prepared by dispersing 0.4g TiO_2 NPs in 40 mL of de-ionized water. Before this, the TiO_2 nanoparticle powders were heated at 570 K for 1 hour, then the mixture was stirred for 16 hours to ensure homogeneity. Prior to nanoparticle deposition, the FTO substrates were washed by boiling them in acetone for 15 minutes, followed by 15 minutes of boiling in ethanol, and finally rinsed with de-ionized water. After rinsing, the substrates were dried in the air for 15 minutes. Electrophoretic deposition (EPD) was performed with a CHI electrochemical analyser, model 600E, using the Chronopotentiometry mode. During EPD, the suspension was continuously stirred using a magnetic stirrer. After completion of the last cycle, the electrodes were annealed for 2 h at 400K.

4.12.1 Functionalization FTO/TiO_2 surfaces

Functionalization of FTO/TiO_2 surfaces to yield the final FTO/TiO_2/MOF photoelectrodes was achieved by drop casting MOF solutions onto the FTO/TiO_2 surfaces. 1 mM slurry solutions of the MOFs were made by dissolving the MOFs in ethanol and then carefully depositing 20µL of the MOF solution on the FTO/TiO_2 surface. Before deposition, the MOFs were activated in a hot air oven at 150°C for 1 hour to remove excess DMF. The electrodes were then left to dry under controlled humidity and temperature for a period of three weeks.

4.13 WATER SPLITTING MEASUREMENTS

Water splitting experiments were performed using the functionalized TiO_2 electrodes. All the measurements were performed versus the Ag/AgCl reference electrode, 0.1 M Na_2SO_4 was used as the electrolyte with a platinum wire as the counter electrode. The potentials were converted from Ag/AgCl to Reversible Hydrogen Electrode (RHE) using the equation:

$$E = E_{ref} + 0.059 * pH + 0.1976 \qquad \text{Equation 4.2}$$

Where E Potential versus the RHE

E_{ref} Potential versus the reference electrode (Ag/AgCl)

pH Electrolyte pH (the working pH was 6.5)

4.13.1 Photo response measurements

To evaluate the photo response of the photoelectrodes, linear sweep voltammetry was carried out from -0.2V to +0.8V vs Ag/AgCl using a scan rate of 0.01 V/s under illumination with light intensity 100mW/cm^2 chopping light ON/OFF at 10s intervals.

a)

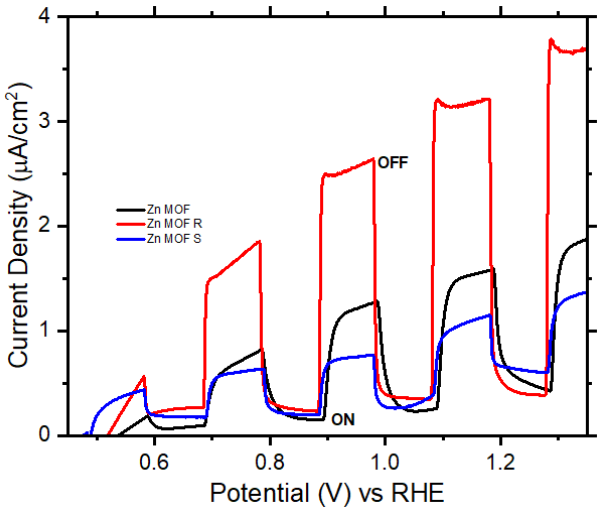

b)

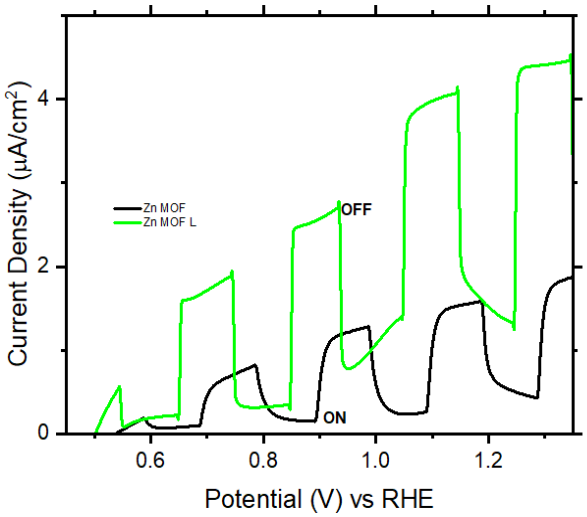

c)

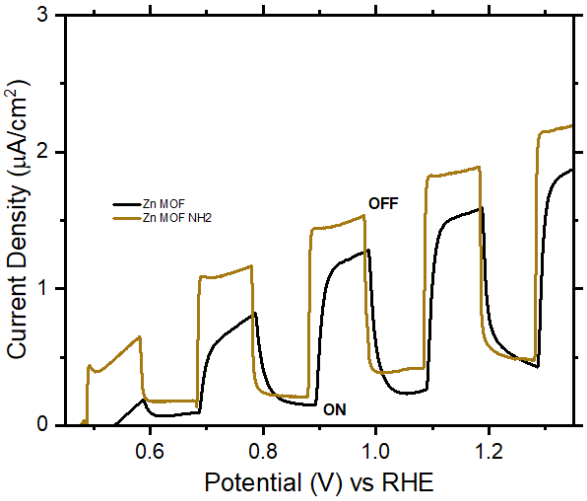

Figure 4.15: Photo response measurements for a) Zn-MOF vs Zn-MOF R CSA and Zn-MOF S CSA b) Zn-MOF vs Zn-MOF L c) Zn-MOF vs Zn-MOF-NH_2 in 0.1M Na_2SO_4 at 0.01V/s scan rate

---

From the **Figures 4.15 (a), (b),** and **(c)** it can be noticed that once the light was switched on, there was a spike in the current density generated, but once the light source was turned off, the current density instantaneously disappears, this is an affirmation of the UV-Vis results in

section 4.6 confirming that the synthesized MOFs are photocatalytic in nature (Altaf et al., 2018; Seenivasan et al., 2022).

4.13.2 Cyclic Voltammetry

Cyclic Voltammetry from was carried out by sweeping potential from -0.35V to +1.35V (vs Ag/AgCl) with a positive initial polarity using a scan rate of 0.1V/s.

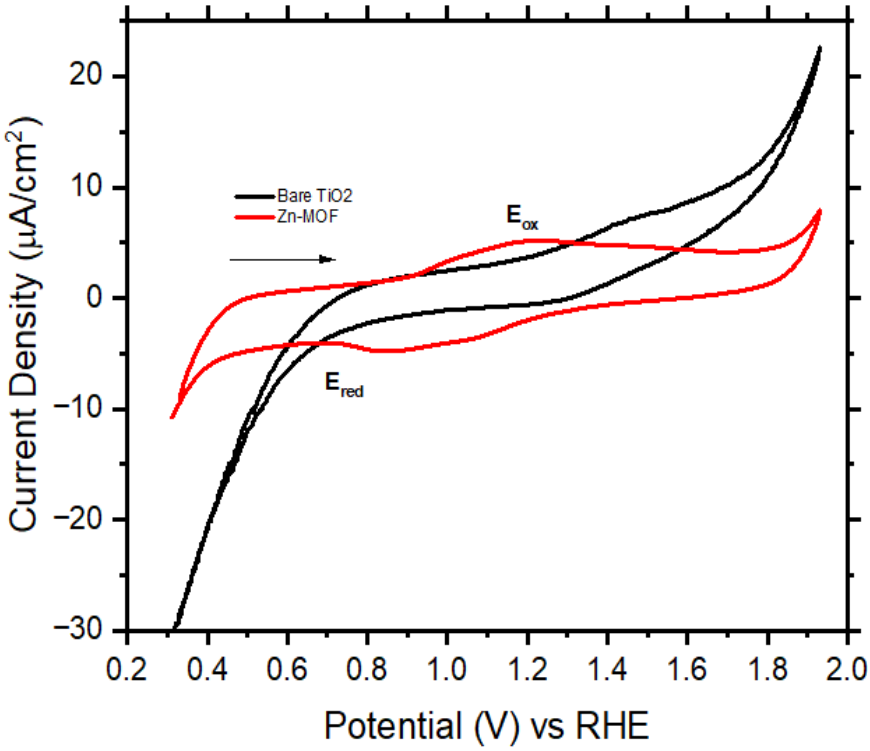

Figure 4.16: CV curves in 0.1M Na_2SO_4 of Zn-MOF vs Bare TiO_2 at 0.1V/s

In the CV curve of the Zn-MOF (red line) in **Figure 4.16**, a weak anodic (forward scan) current peak at about +1.192V is observed, while a weak cathodic peak is observed at +1.033V in the backward scan to give a formal reduction potential of 1.11V. The black line shown in **Figure 4.16** is the CV of Bare TiO_2 nanoparticles and it was used as the control in all the CV measurements. The area produced in the forward as well as the backward current which is related to the charge exchanged during the potential scan is nearly similar and this suggests that the chemistry of the redox processes underlying current peaks in the CVs are reversible (Gazzotti et al., 2018), meaning that there is no kinetic barrier or coupled chemical reaction

The observed peaks are consistent with peaks reported for ZnO nanoparticles at the same scan rate (0.1V/s) (Pradeeswari et al., 2019).

Similar measurements were also carried out for the chiral doped Zn-MOFs.

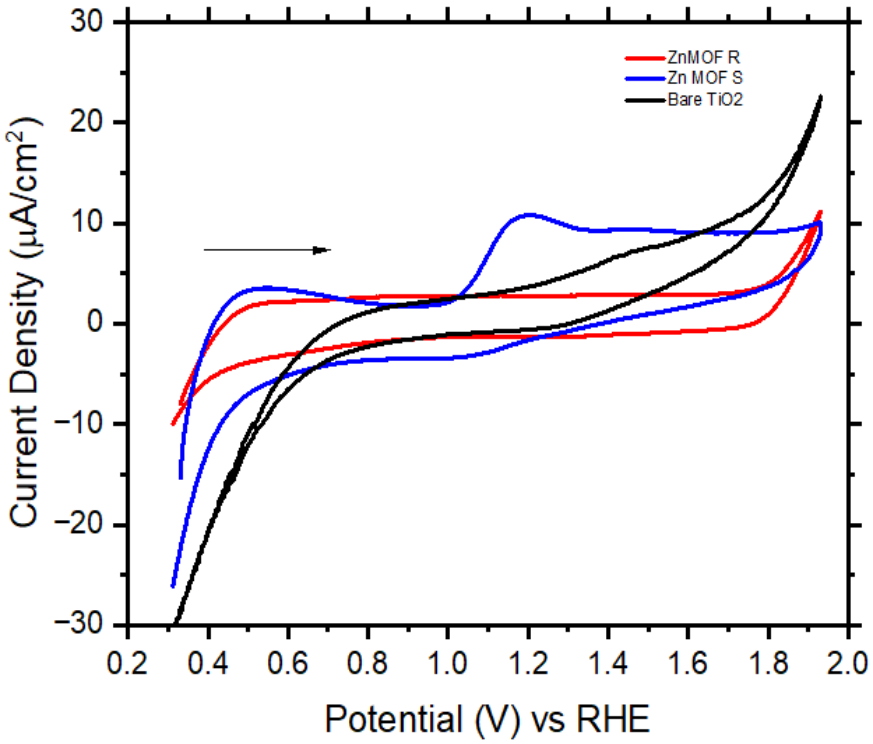

Figure 4.17: CV curves in 0.1M Na_2SO_4 of Zn-MOF R-CSA (red curve) and Zn-MOF S-CSA (blue curve) vs Bare TiO_2 at 0.1V/s

---

In a comparison of the CV curves of the Zn-MOF R-CSA vs Zn-MOF S-CSA, (**Figure 4.17**), there are no peaks (both forward scan and backward scan). This is in agreement with the solid-state electrochemistry witnessed in section 4.10, indicating that the Zn-MOF R-CSA does not have any reduction or oxidation reactions taking place in the voltage window. The Zn-MOF S-CSA shows an anodic peak at + 1.19V and a cathodic peak at +1.04V to give a formal reduction potential of 1.12V which is almost similar to the formal reduction potential for the Zn MOF. In Zn-MOF S-CSA, the area under the anodic peak is not equal to the area in the cathodic peak and this can be classified as a quasi-reversible reaction, there exists some kinetic barrier (Gazzotti et al., 2018). The CV curves obtained from Zn-MOF L and Zn-MOF-NH_2 could not be superimposed on the Bare TiO_2 curve in the same voltage window and they are shown in **Figure 4.18**. In the Zn-MOF L Cysteine and Zn-MOF-NH_2, the presence of the additional amino groups in these two MOFs, did not only change their surface morphology,

but their electrochemical properties, from this observation The Zn-MOF L and Zn-MOF-NH_2 become difficult to reduce.

a) b)

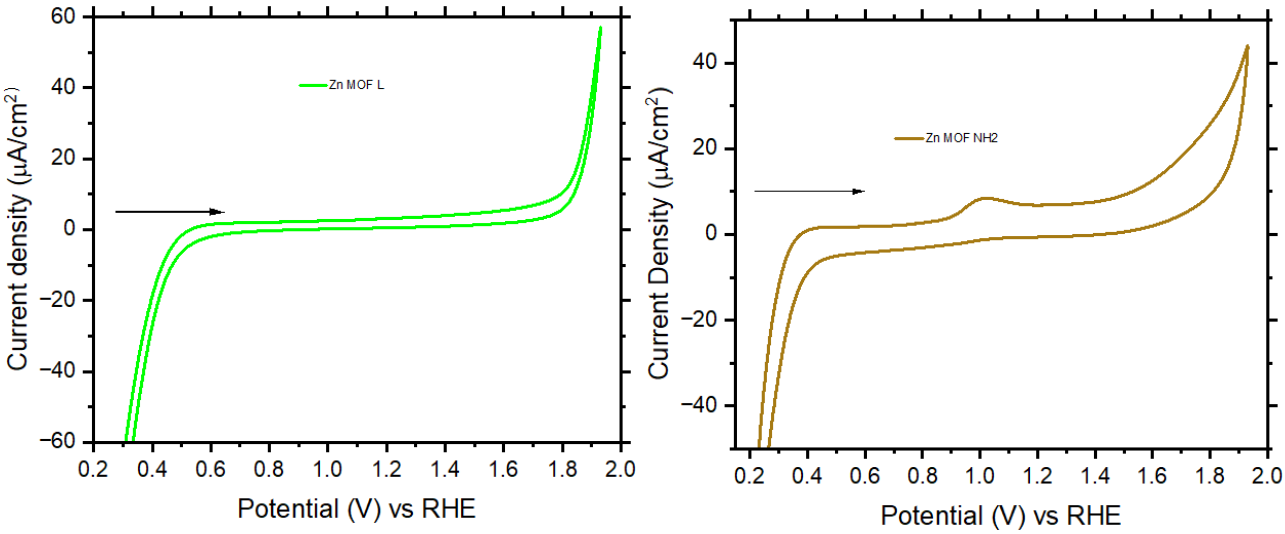

Figure 4.18: CV curves in 0.1M Na_2SO_4 of: a) Zn-MOF L and b) Zn-MOF-NH_2 at 0.1V/s

The CV for Zn-MOF-NH_2 shows an anodic peak at +1.02V but with no cathodic peak, therefore it can be classified as an irreversible reaction.

4.13.3 Oxygen Evolution Reaction

In order to determine the OER efficiency of the fabricated photoanodes, Linear Sweep Voltammetry from 0.0 V to +1.4 V (vs Ag/AgCl) using a scan rate of 0.01 V/s under illumination and under darkness was carried out.

The OER curves were plotted and are shown in **Figure 4.19**. From the OER curves of the Zn-MOF and the Zn-MOF R CSA and S CSA, the Zn-MOF doped with R camphor sulphonic Acid showed an onset potential of +1.72V compared to +1.79V exhibited by the achiral Zn-MOF while the Zn-MOF doped with S camphor Sulphonic Acid has a large onset potential of +1.88V as shown in **Figure 4.19 (a)**. In the OER curves for Zn-MOF doped with L Cysteine, the onset potential was observed at +1.75V compared to the +1.79V vs RHE as shown in **Figure 4.19 (b)**. In the chiral Zn-MOF R and Zn-MOF L a reduction in onset potential was evidenced whereas the onset potential in the chiral Zn MOF S CSA was larger.

a) b)

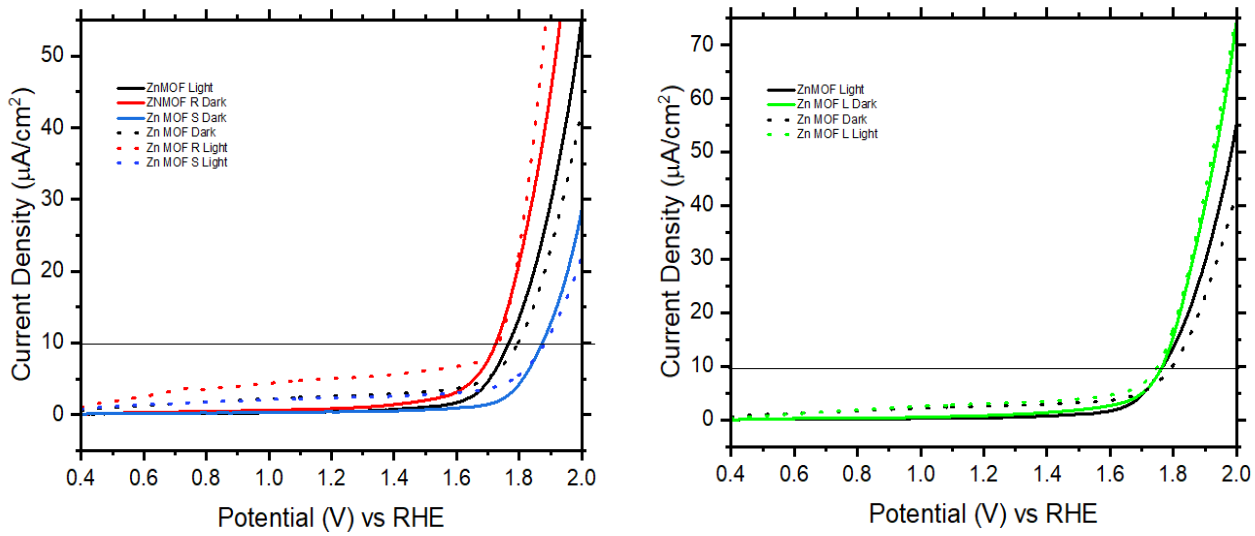

Figure 4.19: Comparison of Zn-MOF and a) chiral Zn-MOF R-CSA and Zn-MOF S-CSA OER Linear Sweep Voltametry b) chiral Zn-MOF L OER Linear Sweep Voltametry in 0.1M Na_2SO_4 at 0.01V/s scan rate

---

In the chiral photolelctrodes, (Zn-MOF R CSA and Zn-MOF L), the reduction in the onset potential can be attributed to the action of the chiral moieities that ensured that only electrons spinning on one direction were selectively transmitted thereby reducing production of hydrogen peroxide (Bhartiya et al., 2022).

When the photoelectrode fabricated from the novel Zn-MOF-NH_2 was used in the OER measurements, a remarkable reduction in the onset potential was noticed with the onset potential shifting to +1.50V vs RHE compared to the +1.79V exhibited by the achiral Zn-MOF (**Figure 4.20**). The ability of the Zn-MOF-NH_2 to reduce the OER potential can be attributed to its better light harvesting properties as shown in the Uv-DRS measurements.

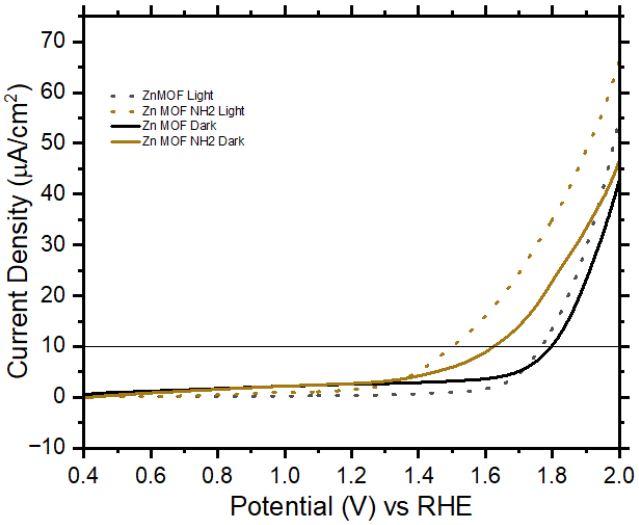

Figure 4.20: Zn-MOF-NH_2 OER Linear Sweep Voltametry in 0.1M Na_2SO_4 at 0.01V/s scan rate

4.13.4 Chronoamperometry

Chronoamperometry at +1.0 V under illumination with light of intensity 100 mW/cm^2 chopping light ON/OFF at 10s intervals was carried out for transient photocurrent density measurements for Zn-MOF and the chiral doped Zn-MOFs. Swift and reproducible photocurrent for all the samples were observed, with pure Zn-MOF exhibiting the lowest (black line), while Zn-MOF R-CSA produced the highest photocurrent density **(Figure 4.21).** Moreover, the transient curve showed that the photocurrents were slowly reduced to zero when the light source was off. However, the bulk of the current decays very rapidly as expected, and the slowly decaying component, which is a very small fraction of the total, could come from various processes, such as slow collection of trapped electrons or slow oxidation of water at some of the catalytic sites in the electrode film. This slow component is observed with all samples.

a) b)

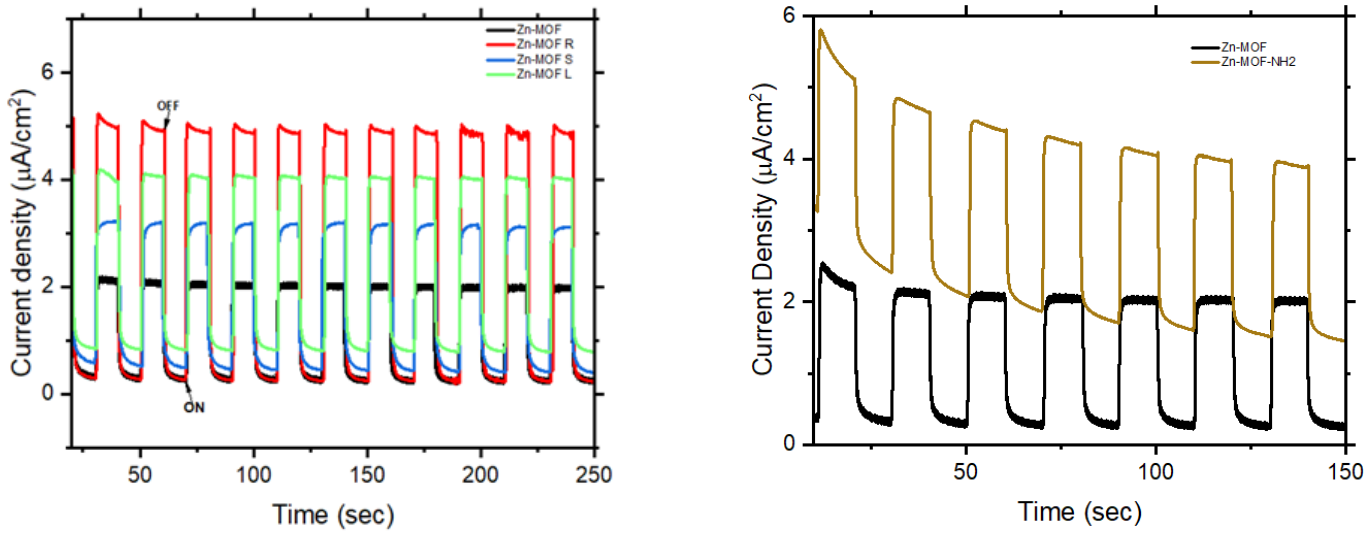

Figure 4.21: Transient PEC measurements at +1.0V for (a) Zn-MOF (black line), Zn-MOF R-CSA (red line), Zn-MOF S-CSA (red line) and Zn-MOF L (green line) (b) Zn-MOF vs Zn-MOF-NH_2 in 0.1M Na_2SO_4

4.13.5 Electrode stability

Electrode stability was evaluated by running chronoamperometry measurements at +1.0V for 300 s under light intensity of 100 mW/cm^2.

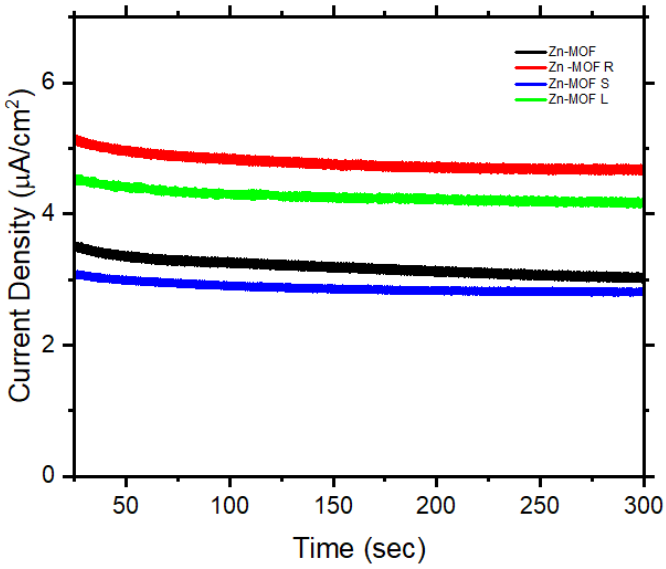

Figure 4.22: Photoelectrode stability of Zn-MOFs

From the stability tests carried out it was observed that all the photoelectrodes were able to generate the same amount of current density that they had generated during the chronoamperometry tests as reported in section 4.13.4. The stability measurements were carried out after approximately 100 cycles and the results obtained are shown in **Figure 4.22**. A slight decrease in the current density was observed for all the photoelectrodes and this can be attributed to the build-up of oxygen on the surface of the photoelectrode as well as depletion of the active sites on the photoelectrode surface (Altaf et al., 2018).

4.13.6 Electrochemical Impedance Spectroscopy

4.13.6.1 Mott Schottky

Mott-Schottky analysis was carried out to determine the electronic properties of the fabricated photoelectrodes. The measurements were performed by sweeping voltages from 0.75V to -0.5V using an AC Voltage with an amplitude of 5mV and frequency of 1000Hz. The Mott Schottky measurements were carried out under illumination and under darkness.

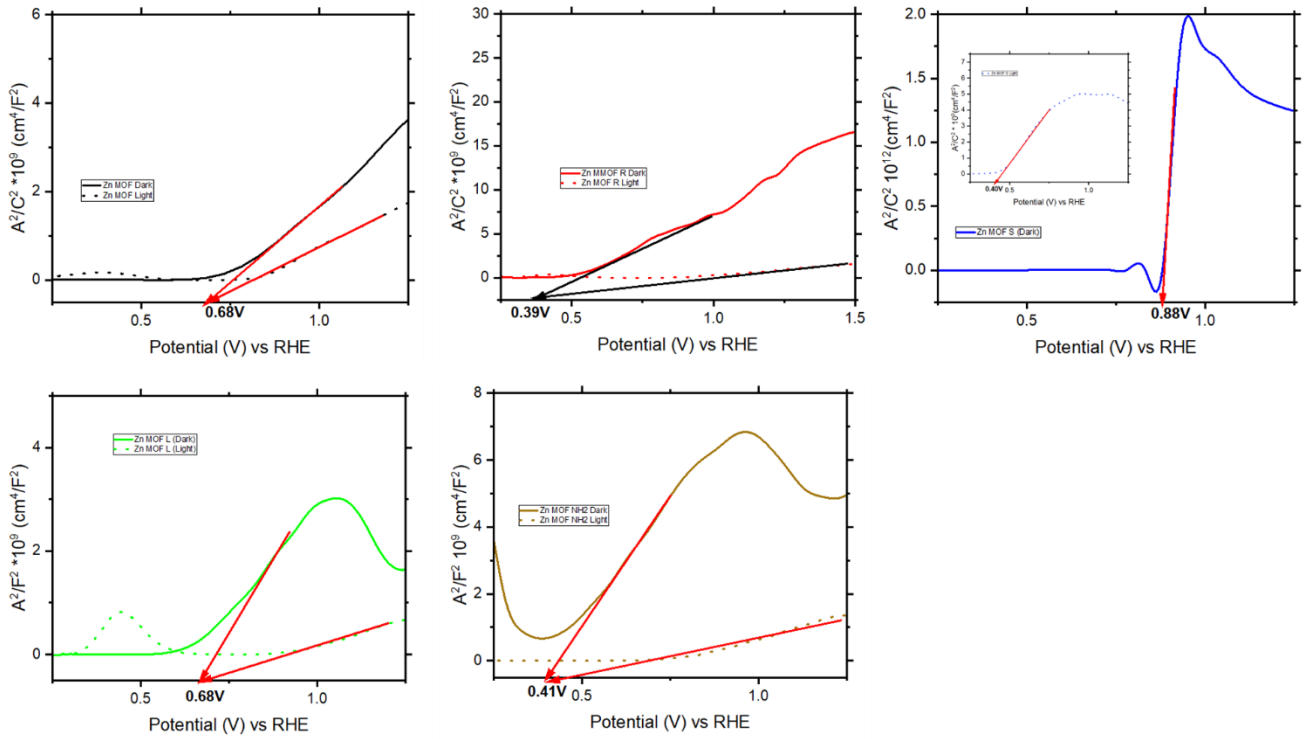

Figure 4.23: Mott Schottky plots for the Zn-based MOFs

The flat band potentials obtained for each photoelectrode for measurements carried out under darkness and under illumination are summarized in **Table 4.5**:

Table 4.5: Flat band Potentials of Zn- MOF and its derivatives

Electrode	**V_{bi} Darkness (V) vs RHE**	**V_{bi} illumination(V) vs RHE**
Zn-MOF	0.68	0.68
Zn-MOF R-CSA	0.39	0.39
Zn-MOF S-CSA	0.4	0.88
Zn-MOF L Cysteine	0.68	0.68
Zn-MOF-NH_2	0.41	0.41

The flat band potentials versus the RHE are almost similar in most cases, both under darkness and under illumination for the same electrode. This indicates that the electronic properties of the TiO_2 are not affected by molecular modification for each class of molecules used (Mtangi et al., 2017). The flat band potential occurs when the surface potential is equal to zero.

In the Mott Schottky plot for Zn-MOF doped with S Camphor Sulphonic Acid, it is interesting to note that there was a remarkable difference in the capacitance produced, to the extent that the plots could not be drawn on the same axis. The capacitance produced under darkness was relatively large when compared to that produced under illumination. Additionally, a positive gradient of the Mott Schottky plot shows the n-type nature of a semiconductor, while a negative gradient is typical of a p-type semiconductor (Kusmierek, 2020) based on this statement, we can conclude that the synthesised Zn-MOF and its derivatives are n-type semiconductors/photocatalysts.

4.13.6.2 Nyquist Plots

To evaluate the charge transfer kinetics, Nyquist plots were used. The Nyquist measurements were carried out by varying frequency between 1MHz and 0.1Hz, with an initial potential of 0V and an amplitude of 5mV. The measurements were carried out under darkness and under illumination.

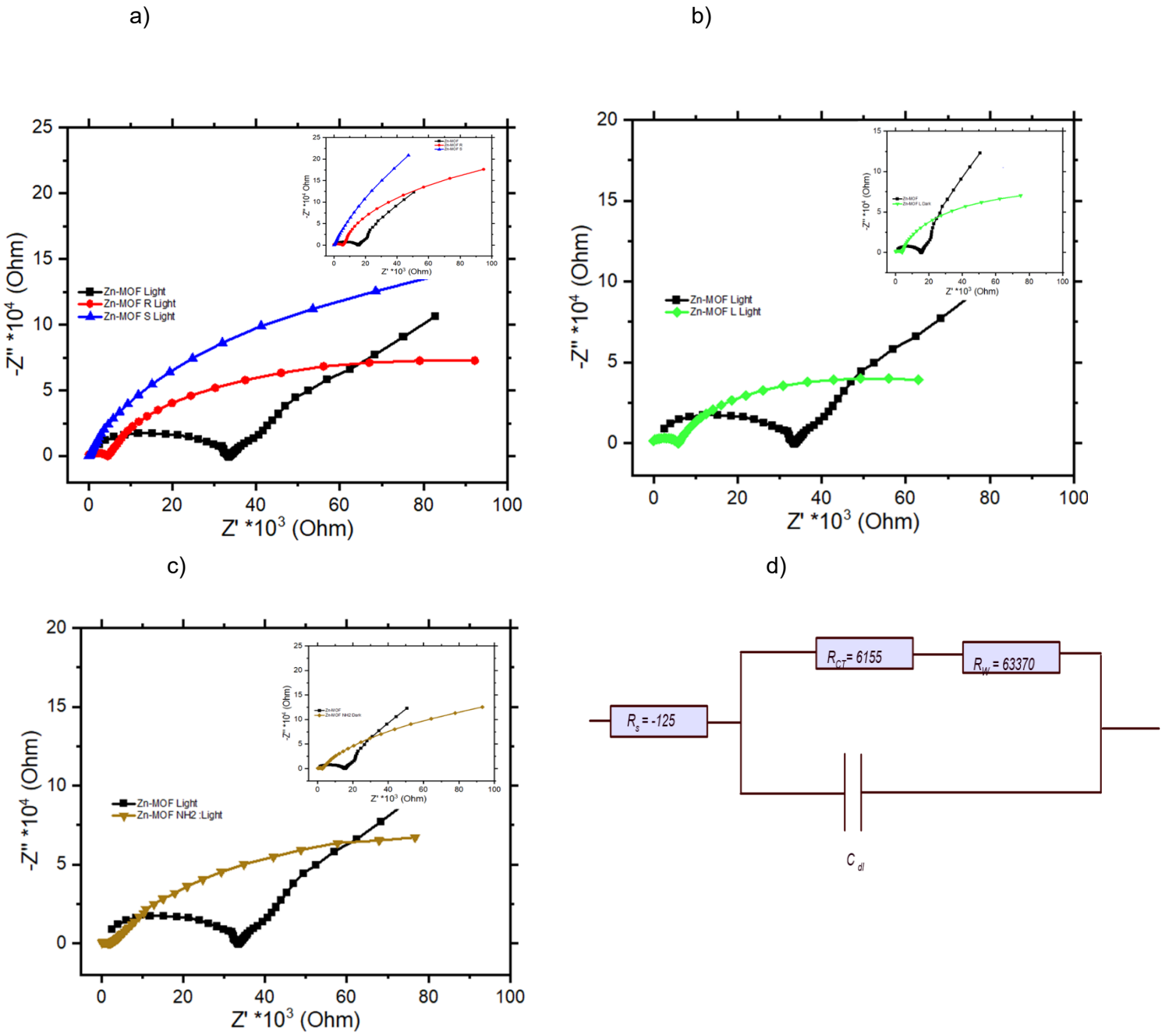

Figure 4.24: Nyquist Plots of the Zn-MOF based photoelectrodes a) Zn-MOF vs Zn-MOF R-CSA (red curves) vs Zn-MOF S-CSA (blue curve) b) Zn-MOF vs Zn-MOF L Cysteine (green curve) c) Zn-MOF vs Zn-MOF-NH_2 (brown curve) d) Equivalent circuit for Zn-MOF L

The EIS spectra reveal the charge transfer kinetics in the photocatalysts. As shown in **Figure 4.24**, the semicircle diameters of the R-CSA and S-CSA doped Zn MOFs are much smaller than that of Zn-MOF, which indicates a more favourable interfacial charge transfer process between photocatalyst and electrolyte in chiral Zn-MOF R-CSA and Zn-MOF S-CSA

photocatalysts than the achiral one (Feng et al., 2023). The same can be observed for the Zn-MOF doped with the L Cysteine, as well as the Zn-MOF-NH_2 where the first semicircle diameter is observed to be considerably smaller compared to that of the pristine Zn-MOF. The first semicircle can be attributed to the capacitance of the bulk space charge region/Helmholtz layer, while the large semicircle can be attributed to charge tunnelling (Seenivasan et al., 2022). The equivalent circuit for Zn-MOF doped with L-cysteine was fitted using the values obtained from the Nyquist plots. In the equivalent circuit, the R_s refers to the electrolyte resistance, R_{ct}, is the charge transfer frequency while R_w is the Warburg resistance and these values are obtained from the respective Nyquist plot.

4.13.6.3 Bode Plots

To further investigate the electronic properties of the photoelectrodes, Bode plots were used. The measurements were carried out by varying frequency between 1MHz and 0.1Hz, with an initial potential of 0V and an amplitude of 5mV and a graph of Log frequency vs -phase angle was plotted as shown in **Figure 4.25.** Measurements were carried out under darkness and under illumination to evaluate the photoelectrodes' sensitivity to light.

a)

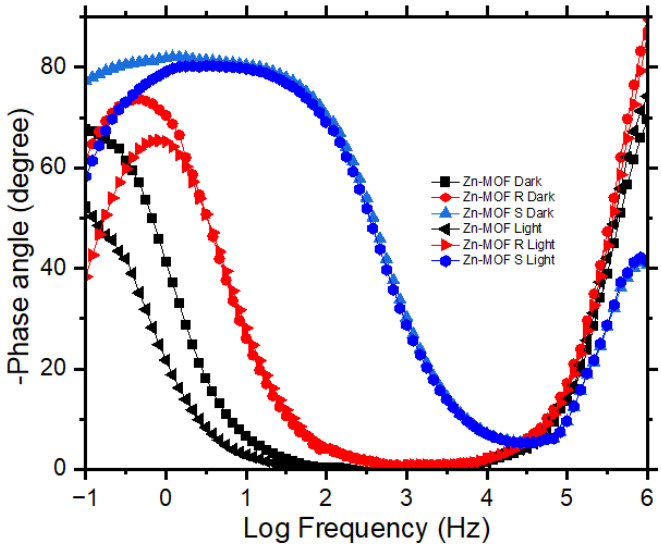

b)

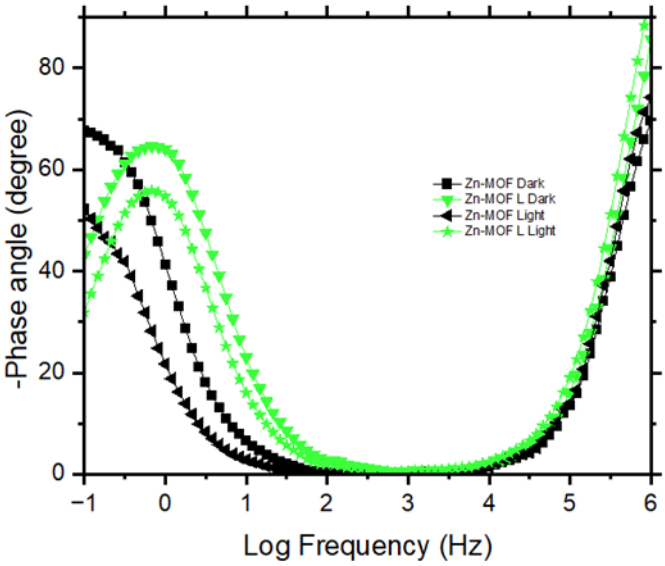

c)

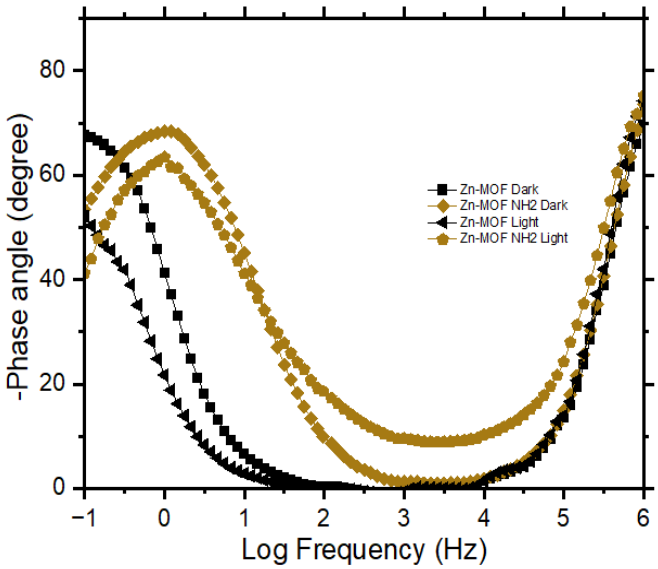

Figure 4.25: Bode Plots of the Zn-MOF based photoelectrodes a) Zn-MOF vs Zn-MOF R-CSA (red curves) vs Zn-MOF S-CSA (blue curve) b) Zn-MOF vs Zn-MOF L Cysteine (green curve) c) Zn-MOF vs Zn-MOF-NH_2 (brown curve)

From the Bode Plots it can be observed that the photoelectrode/electrolyte system showed phase angles below -90°, which is synonymous with non-ideal capacitive behaviour (Digdaya et al., 2016). In all the bode plots an apparent shift towards the high frequencies is observed. The shift towards the higher frequencies can be described according to the charge transfer process taking place in the bulk electrolyte, while the charge transfer taking place in the low frequency in the pristine Zn-MOF can be attributed electron transfer on the electrode surface (Toledo et al., 2017).

4.13.7 Activity of the electrodes

The activity of the photoelectrodes was assessed by measuring the open circuit potential (OCP) in the dark and under illumination at zero current. Open circuit potential values were obtained for all electrodes indicating that an equilibrium of the electrode/electrolyte system exists. The equilibrium is between formation of metal oxide and/or metal hydroxide onto the photoelectrode surface and the reduction of water molecules during the equation

$4H_2O + 4e^- \leftrightarrow 4OH^- + 2H_2$ (Zerdoumi et al., 2019).

a) b)

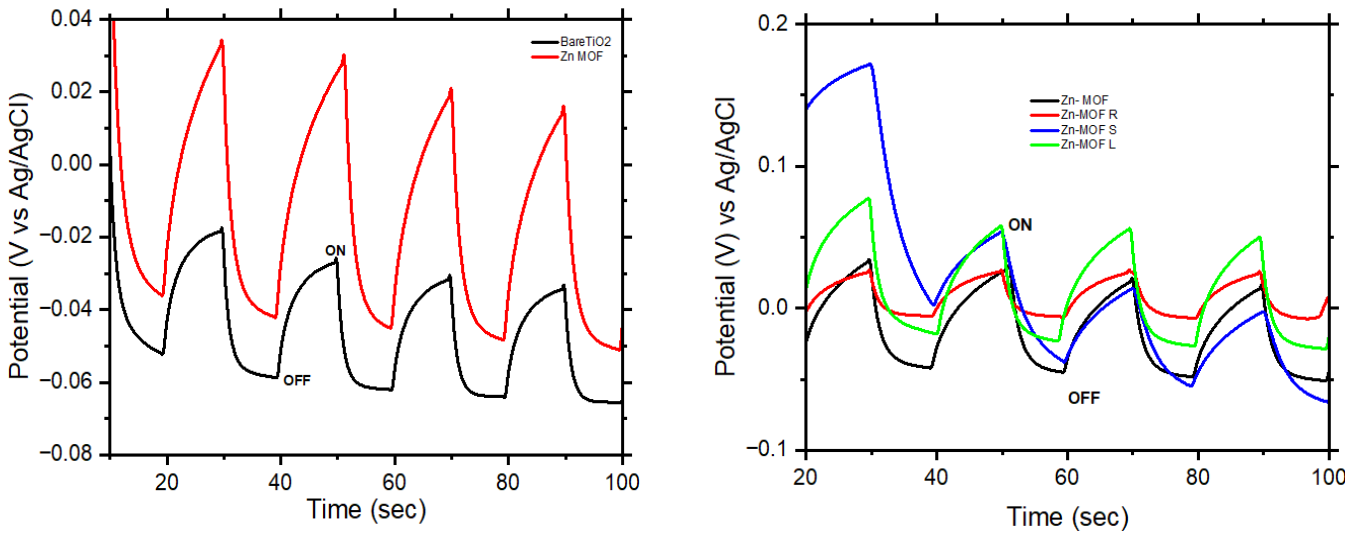

Figure 4.26: OCP Curves for a) Bare TiO_2 vs Zn-MOF b) A comparison of OCP curves for chiral Zn-MOFs

OCP curves obtained from the measurements are illustrated in **Figure 4.26**. In the curves above, it can be observed that in the dark, there is a quasi-steady state current flow, however, on illumination, there is a transient photocurrent spike followed by decay to a quasi-steady state. The changes in the spikes in dark current and photocurrents are associated with capacitance charging of the surface (Hankin et al., 2019).

For n-type semiconductors/photocatalysts, the OCP without illumination is predominantly less negative. When the electrode is illuminated, the potential becomes more negative (Ji et al., 2017). This is because when the semiconductor is illuminated electrons get excited and they are released onto the surface of the photoelectrode, making it more negative (Hankin et al., 2019) and the higher the negative shift, the better the photoactivity of the photoelectrode. OCP evaluates the tendency of an electrode to take part in electrochemical corrosion reaction with the electrolyte and can be used to measure the nobility of the photoelectrodes. A high OCP value indicates a driving force for water oxidation and it determines the difference between the hole quasi-Fermi-level of the semiconductor heterojunction and the redox potential of the electrolyte (Ye et al., 2019).

The OCP values obtained for the synthesized MOFs are: +0.064V, +0.033V, +0.053V and +0.083V for Zn MOF, Zn MOF R CSA, Zn MOF S CSA and Zn MOF L, respectively, while the Zn MOF NH_2 had an OCP value of +0.057V. From the OCP curves shown (**Figure 4.26**) and the positive slope from the Mott Schottky plots it can be concluded that the fabricated Zn-MOF based photoelectrodes are n-type photoelectrodes.

4.13.8 Overpotential

The overpotential was evaluated by running a Tafel plot from -1.5V to +1.5V (vs Ag/AgCl) at a scan rate of 0.01V/s. Tafel plots are used in a bid to unravel the reaction kinetics as well as the oxygen evolution reaction mechanism. Tafel plots are also used to evaluate the catalytic properties of various photocatalysts that may be under study (Aralekallu et al., 2020). The Tafel slope can be used to deduce and explain the rate-determining step which provides information on the sensitivity of the current response to a given voltage. When the catalyst has a large current density and a smaller Tafel slope, it is regarded as a good OER catalyst. The Tafel slope was obtained according to the Tafel equation (E = A + B *log j), where E, j, and B correspond to potential, current density, and Tafel slope, respectively (Cardoso et al., 2015). To investigate the kinetics of chiral catalysts during OER the overpotential was determined.

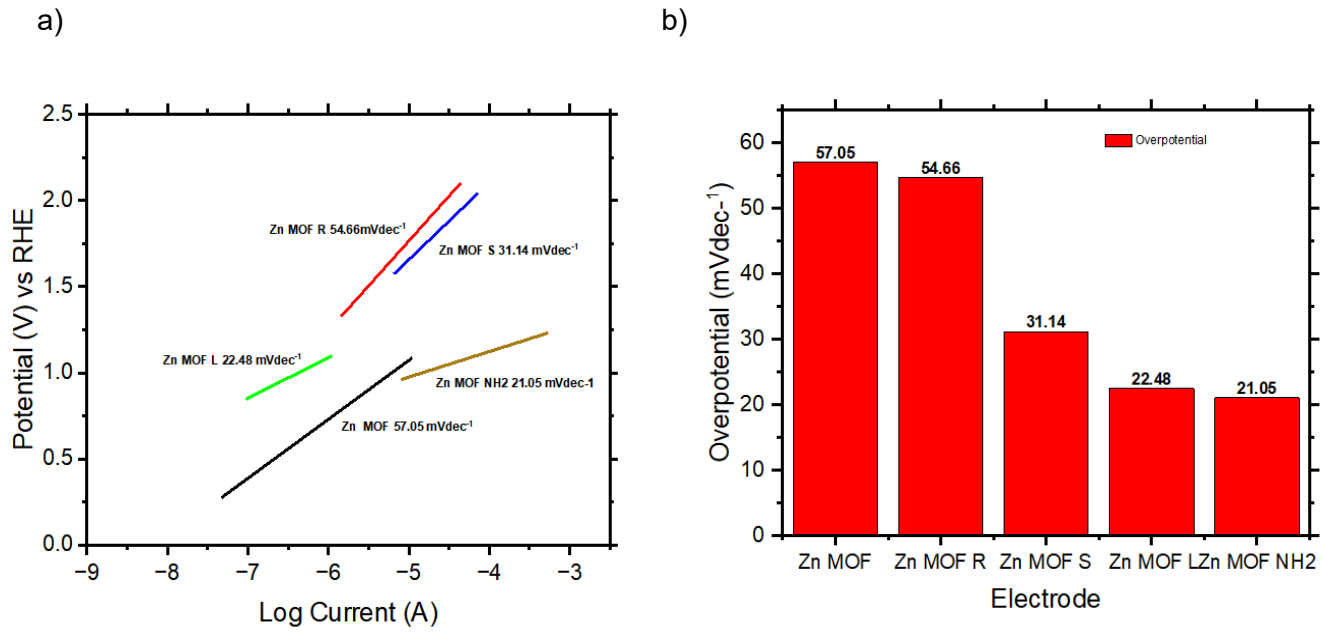

Figure 4.27: a) Tafel plot of Zn-MOF derivatives showing overpotential in $mVdec^{-1}$ b) Comparison of the overpotentials produced by Zn-MOF and its derivatives

As shown in **Figure 4.27,** the chiral doped photocatalysts displayed lower overpotentials of 54.44 $mVdec^{-1}$, 32.14 $mVdec^{-1}$ and 22.48$mVdec^{-1}$ for Zn-MOF R CSA, Zn-MOF S CSA and Zn-MOF L respectively compared to the 57.05$mVdec^{-1}$ produced by the achiral Zn-MOF, suggesting a more favourable intermediate kinetic process in the chiral doped photocatalysts (Feng et al., 2023). Of interest is the low overpotential exhibited by the Zn-MOF-NH_2 of 21.05$mVdec^{-1}$ implying that the amine functionalised Zn-MOF is a potential photocatalyst for water splitting.

4.13.9 Hydrogen Peroxide quantification

For the Zn-MOF, there was the Zn-MOF, Zn-MOF doped with R-Camphor Sulphonic Acid, S-Camphor Sulphonic Acid, Camphor Sulphonic Acid, L Cysteine and amine functionalized Zn-MOF-NH_2.

Electrochemistry, using the chronoamperometry mode was performed with a 0.1 M Na_2SO_4 aqueous solution as the electrolyte and an Ag/AgCl (saturated KCl) reference electrode. A potential (+1.23V versus the Ag/AgCl) was chosen and applied to the bare TiO_2 electrode so that hydrogen and oxygen were evolved on the Platinum wire (counter electrode) and fabricated photoelectrodes (working electrode), respectively. Bubbles were observed on both the Platinum wire and the photoelectrode (TiO_2/MOF electrode) during the electrochemical

measurements. Chronoamperometry measurements were conducted for 40 minutes. The presence of hydrogen peroxide was verified in a colorimetric test titration experiment of the used electrolyte, with o-tolidine as a redox indicator. In the colorimetric measurements, 2.0 mL of an o-tolidine solution prepared according to the Ellms-Hauser method (Ellms A X & Hauser, 1913) were added to 10 mL of the electrolyte solution obtained from the photoelectrochemical cell and left to react for 40 minutes. The sample was then analyzed using a Uv-vis spectrophotometer, to determine the presence of hydrogen peroxide and the spectra given in **Figure 4.28** were obtained.

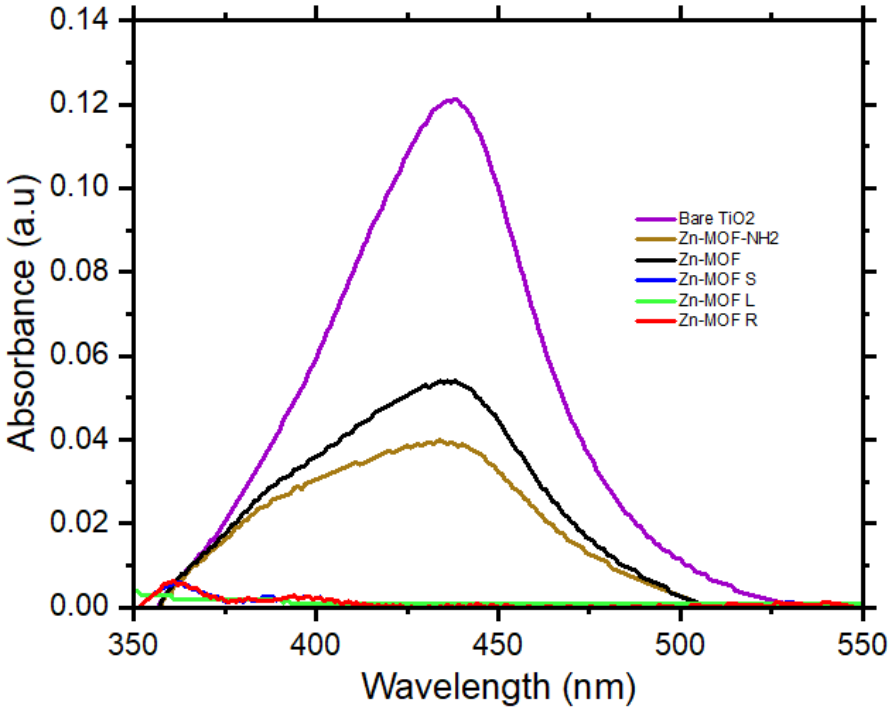

Figure 4.28: Uv-vis spectra from titration of electrolyte used with the respective electrodes.

From **Figure 4.28** it can be noticed that the electrolyte obtained from the photoelectrochemical cell that used chiral photoelectrodes (Zn-MOF R-CSA, Zn-MOF S-CSA and Zn-MOF L Cysteine) have no hydrogen peroxide formed, whereas the electrolyte from the photoelectrochemical cell containing the achiral photoelectrodes produced a peak at 436nm. When the o-tolidine is added to the electrolyte from achiral photoelectrodes, a yellow colour is formed. This is due to the oxidative reaction between the o-tolidine and the H_2O_2 present in the achiral electrolyte (Zhang et al., 2018). In the case of Zn-MOF-NH_2, a peak at 436nm was observed, this because in as much as it was treated, its treatment did not include chiral moieties as such there was no spin filtration in the electrons hence the production of the

hydrogen peroxide. The amount of hydrogen peroxide formed was evaluated using calibration curve given in Appendix C and the following were obtained.

Table 4.6: Quantity of hydrogen peroxide present in electrolyte from Zn-MOF based electrodes

Electrode	Absorbance	Hydrogen Peroxide(M)
Bare TiO_2	0.1215	0.242
Zn-MOF	0.054	-
Zn-MOF-NH_2	0.040	-
Zn-MOF R-CSA	0.017	-
Zn-MOF S-CSA	0.017	-
Zn-MOF L Cysteine	0.001	-

4.13.10 Hydrogen Quantification

To measure the hydrogen produced, a modified Hoffman apparatus was fabricated. Hydrogen was collected for only one photoelectrode (Zn-MOF R-CSA). Hydrogen produced was quantified by running chronoamperometry at +1.23V for 90 minutes in the modified Hoffman apparatus which was made airtight to ensure accuracy of the measurements. The amount of hydrogen collected over 90 minutes is as shown in **Figure 4.29.**

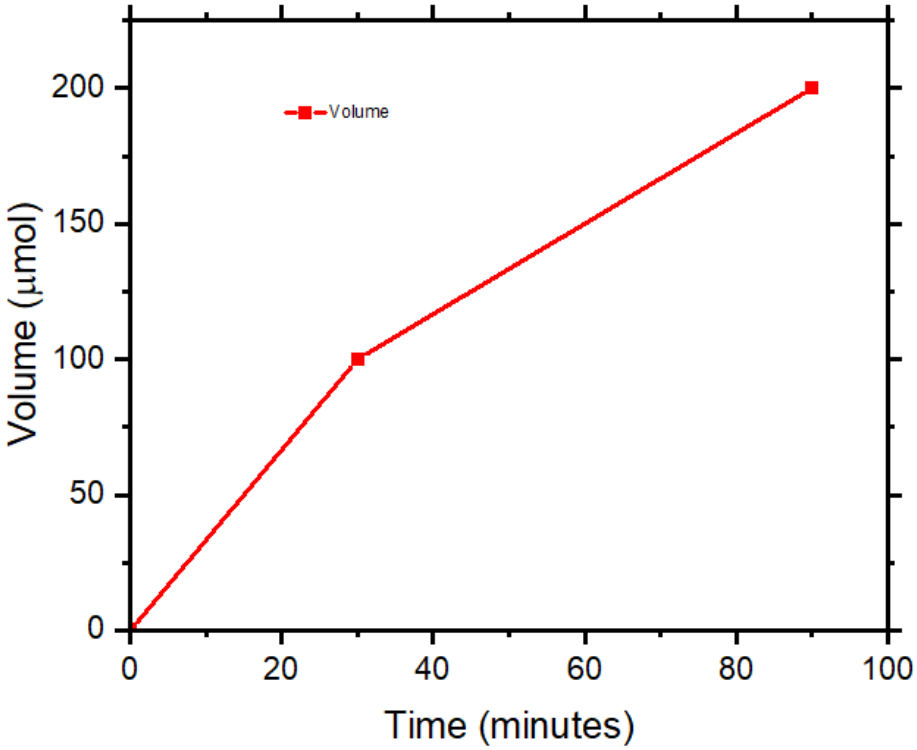

Figure 4.29: Amount of hydrogen formed after 90 minutes from Zn-MOF R- CSA

During the production of hydrogen, a lot of oxygen bubbles could be observed accumulating on the photoanode, as the oxygen bubbles increased a noticeable decrease in the photocurrents recorded during the chronoamperometry was observed. Higher current densities were restored when the cell was shaken.

4.14 WATER SPLITTING MECHANISM ON THE CHIRAL ZN-MOF PHOTOELECTRODE

During the water splitting process, hydrogen is formed at the cathode (Counter Electrode), while oxygen is formed at the anode (Working Electrode) through a process involving the net transfer of four electrons. **Figure 4.30** shows the processes taking place in the chiral PEC. The anodic process often referred to as the oxygen evolution reaction (OER), has previously been identified as greatly influencing the overpotential for the water splitting reaction (S. Ghosh et al., 2020).

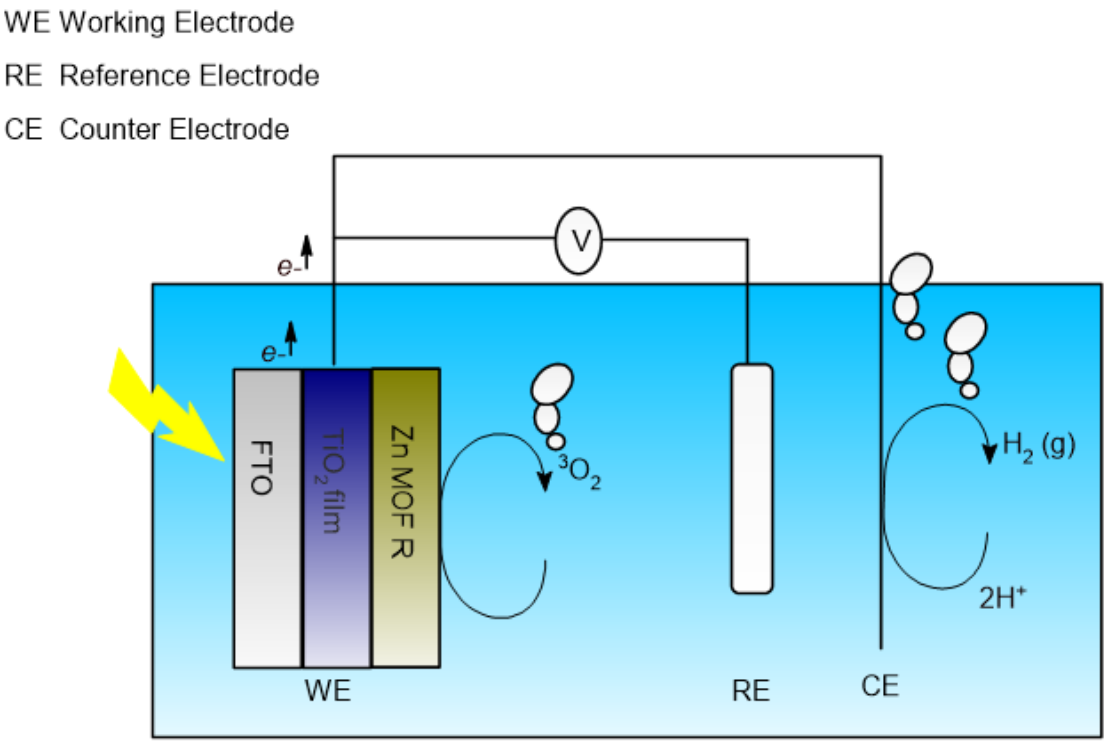

Figure 4.30: Chiral PEC

Ground state oxygen exists in a triplet state, ($^3\Sigma_gO_2$) other researchers have theorized that the 'sluggishness' arises from spin constraints that exist in the elementary reaction steps for its formation (K. B. Ghosh et al., 2019). Spin constraints are not usually included in the design of water splitting cell as such by-products such as hydrogen peroxide are often produced. The formation of hydrogen peroxide and superoxides have also been known to decrease the stability of the anode (Seabold & Choi, 2011) which in turn negatively affects the photocatalyst's performance. The ability of a photocatalyst to minimize side reactions while improving the production of triplet oxygen ($^3\Sigma_gO_2$) is important as this improves the overall efficiency of the PEC. When the chiral photoelectrodes are used in water splitting, their main purpose is to filter the spin of the generated electrons resulting in the promotion formation of ($^3\Sigma_gO_2$) over hydrogen peroxide (Bhartiya et al., 2022; S. Ghosh et al., 2020; Mtangi et al., 2017; Vadakkayil et al., 2023; Zhang et al., 2018, 2021) .

From the results from the water splitting measurements, there is evidence that the TiO_2 and MOF heterojunctions produce significant photogenerated electro-hole pairs with facile charge transfer to suppress their recombination. Results from section 4.13.9, show that there is clear evidence that chiral molecules are important in hindering the formation of hydrogen peroxide. The water splitting was carried out at pH 6.5, the near neutral pH was chosen to minimise

problems associated with corrosion at highly acidic or highly alkaline conditions. When the electrons are transferred from OH^-/H_2O to the chiral photoanode, the chiral molecules perform spin filtering and this results in electrons that have one spin state being transmitted. In turn, this ensures that the resulting OH* radical are also left with only one spin state (Zhang et al., 2018).

The parallel aligned OH* will interact with the triplet state to form triplet oxygen ($^3\Sigma_gO_2$) according to **scheme 4.3**.

$$H_2O\,(l) + M* \rightarrow MOH* + H^+ + e^- \qquad \text{Equation 4.3}$$

$$OHM* \rightarrow MO* + H^+\,e^- \qquad \text{Equation 4.4}$$

$$H_2O\,(l) + MO* \rightarrow MOOH* + H^+ + e^- \qquad \text{Equation 4.5}$$

$$MOOH* \rightarrow M* + {}^3\Sigma_g O_2 + H^+ + e^- \qquad \text{Equation 4.6}$$

To give the overall reaction

$$2H_2O\,(l) \rightarrow O_2 4H^+ + 4e^- \qquad \text{Equation 4.7}$$

Scheme 4.3 . Proposed water splitting mechanism in the chiral PEC

In which

M∗ represents the active site on the MOF photocatalyst,

(l) refers to the liquid phase,

(g) refers to the gas phase and

MOH*, MO*, and MOOH* represent the species adsorbed on the active sites

Generally, the OER process can proceed via a four-electron pathway to form oxygen molecules while the two-electron pathway to give H_2O_2 during water oxidation is rarely involved (Feng et al., 2023). The H_2O_2 will not be produced on a triplet potential surface as it is spin forbidden (Zhang et al., 2018).

Therefore, it can be concluded that the mechanism illustrated in **scheme 4.3** is responsible for the water splitting in the chiral Zn-MOFs. The processes taking place on the chiral photoelectrodes can be illustrated by **Figure 4.31**, where it is observed that in TiO_2 the electrons produced under illumination are not spin filtered but due to their interaction with the

chiral Zn-MOF R the electrons become spin filtered creating a triplet surface and this results in better water splitting activity than that of the achiral Zn-MOF.

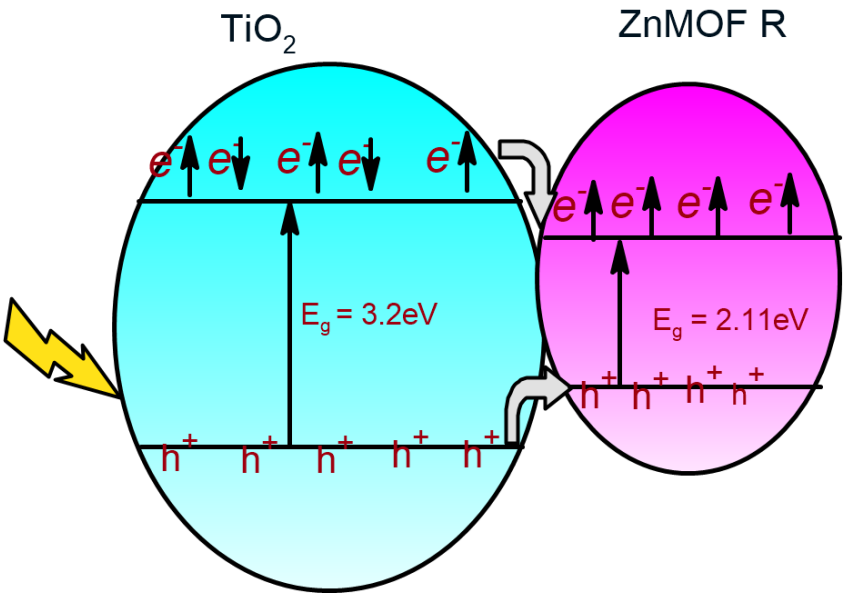

Figure 4.31: Energy diagram for Zn-MOF R-CSA

4.15 CONCLUSION

The Zn-MOF based multivariate MOF has been successfully synthesised and characterised. Uv-vis measurements revealed that the zinc-based MOFs are photoactive and can therefore be used as photocatalysts. TGA showed that the MOF is thermally stable while SEM revealed the lamellar structure of the Zn-MOF. In water splitting measurements, OER was successfully carried out with Zn- MOF R CSA performing better than the other chiral doped MOFs in OER evolution and in chronoamperometry. In Tafel plots, remarkable reduction in overpotential was witnessed in all the chiral MOFs. Moreover, the n-type nature of the photoelectrodes was confirmed, first by the slope of the Mott Schottky plots and then by the Open Circuit Potential curves. The reduction in hydrogen peroxide formed by the chiral Zn-MOFs is proof that the inclusion of the chiral molecules results in the inhibition of the production of H_2O_2 thereby making the chiral PEC more efficient. The Zn-MOF-NH_2 also exhibits superior water splitting characteristics and it offers a new possibility for doping it with chiral molecules resulting in a photocatalyst in which the band gap is solely in the visible spectrum.

4.16 REFERENCES

1) Altaf, M., Sohail, M., Mansha, M., Iqbal, N., Sher, M., Fazal, A., Ullah, N., & Isab, A. A. (2018). Synthesis, Characterization, and Photoelectrochemical Catalytic Studies of a Water-Stable Zinc-Based Metal–Organic Framework. *ChemSusChem*, *11*(3), 542–546. https://doi.org/10.1002/cssc.201702122
2) Aralekallu, S., Sajjan, V. A., Palanna, M., Prabhu C P, K., Hojamberdiev, M., & Sannegowda, L. K. (2020). Ni foam-supported azo linkage cobalt phthalocyanine as an efficient electrocatalyst for oxygen evolution reaction. *Journal of Power Sources*, *449*. https://doi.org/10.1016/j.jpowsour.2019.227516
3) Bhartiya, P. K., Srivastava, M., & Mishra, D. (2022). Chiral-induced enhanced electrocatalytic behaviour of cysteine coated bifunctional Au–Ni bilayer thin film device for water splitting application. *International Journal of Hydrogen Energy*, *47*(100), 42160–42170. https://doi.org/10.1016/j.ijhydene.2021.08.219
4) Bitzer, J., Teubnerová, M., & Kleist, W. (2021). Increasing the Complexity in the MIL-53 Structure: The Combination of the Mixed-Metal and the Mixed-Linker Concepts. *Chemistry - A European Journal*, *27*(5). https://doi.org/10.1002/chem.202003304
5) Cardoso, D. S. P., Amaral, L., Santos, D. M. F., Šljukić, B., Sequeira, C. A. C., Macciò, D., & Saccone, A. (2015). Enhancement of hydrogen evolution in alkaline water electrolysis by using nickel-rare earth alloys. *International Journal of Hydrogen Energy*, *40*(12), 4295–4302. https://doi.org/10.1016/j.ijhydene.2015.01.174
6) Digdaya, I. A., Rodriguez, P. P., Ma, M., Adhyaksa, G. W. P., Garnett, E. C., Smets, A. H. M., & Smith, W. A. (2016). Engineering the kinetics and interfacial energetics of Ni/Ni-Mo catalyzed amorphous silicon carbide photocathodes in alkaline media. *Journal of Materials Chemistry A*, *4*(18), 6842–6852. https://doi.org/10.1039/c5ta09435f
7) Ellms, J.W., & Hauser, S.J. (1913). Ortho-Tolidine as a Reagent for the Colorimetric Estimation of Small Quantities of Free Chlorine. *Journal of Industrial and Engineering Chemistry, 5*, 915-917. https://doi.org/10.1021/ie50059a012
8) Feng, T., Chen, W., Xue, J., Cao, F., Chen, Z., Ye, J., Xiao, C., & Lu, H. (2023). Spin Polarization of Chiral Amorphous Fe-Ni Electrocatalysts Enabling Efficient Electrochemical Oxygen Evolution. *Advanced Functional Materials*, *33*(27), 1-10. https://doi.org/10.1002/adfm.202215051
9) Gazzotti, M., Arnaboldi, S., Grecchi, S., Giovanardi, R., Cannio, M., Pasquali, L., Giacomino, A., Abollino, O., & Fontanesi, C. (2018). Spin-dependent electrochemistry: Enantio-selectivity driven by chiral-induced spin selectivity effect. *Electrochimica Acta*, *286*, 271–278. https://doi.org/10.1016/j.electacta.2018.08.023

10) Ghosh, K. B., Zhang, W., Tassinari, F., Mastai, Y., Lidor-Shalev, O., Naaman, R., Möllers, P., Nürenberg, D., Zacharias, H., Wei, J., Wierzbinski, E., & Waldeck, D. H. (2019). Controlling Chemical Selectivity in Electrocatalysis with Chiral CuO-Coated Electrodes. *Journal of Physical Chemistry C*, *123*(5), 3024–3031. https://doi.org/10.1021/acs.jpcc.8b12027
11) Ghosh, S., Bloom, B. P., Lu, Y., Lamont, D., & Waldeck, D. H. (2020). Increasing the Efficiency of Water Splitting through Spin Polarization Using Cobalt Oxide Thin Film Catalysts. *Journal of Physical Chemistry C*, *124*(41), 22610–22618. https://doi.org/10.1021/acs.jpcc.0c07372
12) Hankin, A., Bedoya-Lora, F. E., Alexander, J. C., Regoutz, A., & Kelsall, G. H. (2019). Flat band potential determination: Avoiding the pitfalls. *Journal of Materials Chemistry A*, *7*(45), 26162–26176. https://doi.org/10.1039/c9ta09569a
13) Ji, X., Ma, M., Ge, R., Ren, X., Wang, H., Liu, J., Liu, Z., Asiri, A. M., & Sun, X. (2017). WO3 Nanoarray: An Efficient Electrochemical Oxygen Evolution Catalyst Electrode Operating in Alkaline Solution. *Inorganic Chemistry*, *56*(24), 14743–14746. https://doi.org/10.1021/acs.inorgchem.7b02552
14) Kawondera, R., Bonechi, M., Maccioni, I., Giurlani, W., Salzillo, T., Venuti, E., Mishra, D., Fontanesi, C., Innocenti, M., Mehlana, G., & Mtangi, W. (2023). Chiral “doped” MOFs: an electrochemical and theoretical integrated study. *Frontiers in Chemistry*, *11*. https://doi.org/10.3389/fchem.2023.1215619
15) Kusmierek, E. (2020). A CeO2 semiconductor as a photocatalytic and photoelectrocatalytic material for the remediation of pollutants in industrial wastewater: A review. In *Catalysts* (Vol. 10, Issue 12, pp. 1–54). MDPI. https://doi.org/10.3390/catal10121435
16) Mtangi, W., Tassinari, F., Vankayala, K., Vargas Jentzsch, A., Adelizzi, B., Palmans, A. R. A., Fontanesi, C., Meijer, E. W., & Naaman, R. (2017). Control of Electrons’ Spin Eliminates Hydrogen Peroxide Formation during Water Splitting. *Journal of the American Chemical Society*, *139*(7), 2794–2798. https://doi.org/10.1021/jacs.6b12971
17) Muhammad Altaf, Manzar Sohail, Muhammad Mansha, Naseer Iqbal, Muhammad Sher, Atif Fazal, Nisar Ullah, & Anvarhusein A. Isab. (2017). *CCDC 1452209 Experimental Crystal Structure Determination, 2018*.
18) Nasalevich, M. A., Van Der Veen, M., Kapteijn, F., & Gascon, J. (2014). Metal-organic frameworks as heterogeneous photocatalysts: Advantages and challenges. *CrystEngComm*, *16*(23), 4919–4926. https://doi.org/10.1039/c4ce00032c
19) Pappalardo, S., & Parisi, M. F. (2008). Ten-membered Rings or Larger with One or More Oxygen Atoms. *Comprehensive Heterocyclic Chemistry III*, *14*, 667–749. https://doi.org/10.1016/B978-008044992-0.01229-3

20) Pradeeswari, K., Venkatesan, A., Pandi, P., Karthik, K., Hari Krishna, K. V., & Mohan Kumar, R. (2019). Study on the electrochemical performance of ZnO nanoparticles synthesized via non-aqueous sol-gel route for supercapacitor applications. *Materials Research Express*, *6*(10). https://doi.org/10.1088/2053-1591/ab3cae

21) Seabold, J. A., & Choi, K. S. (2011). Effect of a cobalt-based oxygen evolution catalyst on the stability and the selectivity of photo-oxidation reactions of a WO3 photoanode. *Chemistry of Materials*, *23*(5), 1105–1112. https://doi.org/10.1021/cm1019469

22) Seenivasan, S., Moon, H., & Kim, D. H. (2022). Multilayer Strategy for Photoelectrochemical Hydrogen Generation: New Electrode Architecture that Alleviates Multiple Bottlenecks. *Nano-Micro Letters*, *14*(1). https://doi.org/10.1007/s40820-022-00822-8

23) Stefani, A., Salzillo, T., Mussini, P. R., Benincori, T., Innocenti, M., Pasquali, L., Jones, A. C., Mishra, S., & Fontanesi, C. (2023). Chiral Recognition: A Spin-Driven Process in Chiral Oligothiophene. A Chiral-Induced Spin Selectivity (CISS) Effect Manifestation. *Advanced Functional Materials* 34, (2308948) 1-11. https://doi.org/10.1002/adfm.202308948

24) Toledo, R. P., Dias, C. E. S., Huanca, D. R., & Salcedo, W. J. (2017). Electrochemical impedance study of fresh and passivated macroporous silicon for sensors. *2017 32nd Symposium on Microelectronics Technology and Devices (SBMicro)*, 1–4. https://doi.org/10.1109/SBMicro.2017.8113011

25) Tran, D. P. H., Pham, M. T., Nguyen, T. H., Wang, Y. F., & You, S. J. (2023). Photocatalytic membrane reactors (PMRs) for hydrogen production. In *Current Developments in Biotechnology and Bioengineering: Membrane Technology for Sustainable Water and Energy Management* (pp. 19–42). Elsevier. https://doi.org/10.1016/B978-0-443-19180-0.00022-5

26) Tshuma, P., Makhubela, B. C. E., Bingwa, N., & Mehlana, G. (2020). Palladium(II) Immobilized on Metal-Organic Frameworks for Catalytic Conversion of Carbon Dioxide to Formate. *Inorganic Chemistry*, *59*(10), 6717–6728. https://doi.org/10.1021/acs.inorgchem.9b03654

27) Vadakkayil, A., Clever, C., Kunzler, K. N., Tan, S., Bloom, B. P., & Waldeck, D. H. (2023). Chiral electrocatalysts eclipse water splitting metrics through spin control. *Nature Communications*, *14*(1). https://doi.org/10.1038/s41467-023-36703-w

28) Ye, K. H., Li, H., Huang, D., Xiao, S., Qiu, W., Li, M., Hu, Y., Mai, W., Ji, H., & Yang, S. (2019). Enhancing photoelectrochemical water splitting by combining work function tuning and heterojunction engineering. *Nature Communications*, *10*(1). https://doi.org/10.1038/s41467-019-11586-y

29) Zerdoumi, R., Rößner, L., & Armbrüster, M. (2019). Addressing the Stability of Bulk Electrode Materials in the Electrochemical Methanol Oxidation. *Journal of The Electrochemical Society*, *166*(14), F1079–F1087. https://doi.org/10.1149/2.0631914jes

30) Zhang, W., Banerjee-Ghosh, K., Tassinari, F., & Naaman, R. (2018). Enhanced Electrochemical Water Splitting with Chiral Molecule-Coated Fe3O4 Nanoparticles. *ACS Energy Letters*, *3*(10), 2308–2313. https://doi.org/10.1021/acsenergylett.8b01454

31) Zhang, W., Wang, W., Hu, Y., Guan, H., & Hao, L. (2021). Take a cue from nature: Promoting electrocatalytic water splitting with a helping hand of hemoglobin. *International Journal of Hydrogen Energy*, *46*(5), 3504–3509. https://doi.org/10.1016/j.ijhydene.2020.10.154

5 APPLICATION OF IRON BASED CHIRAL METAL ORGANIC FRAMEWORKS IN PHOTOELECTROCATALYTIC WATER SPLITTING

5.1 INTRODUCTION

This chapter discusses the synthesis and application of MIL 53 (Fe), an iron-based Metal-Organic Framework, synthesis of the chiral derivatives as well as their application in photoelectrocatalytic water splitting. MIL 53 (Fe), is the most common iron-based MOF, where the acronym MIL stands for Materials of Institute Lavoisier, the Institute at which the MIL group of MOFs were first synthesised. MIL 53 was first described as a chromium (Cr^{3+}) material in 2002 (Millange et al., 2002). There are different variants of MIL 53, depending on the metal coordinating centre, MIL 53(Cr), MIL 53(Al), MIL 53(Ga) and MIL 53(Sc) have also been reported. MIL 53(Fe) has major advantages compared with other MOFs, which include chemical stability, the use of iron (a nontoxic and extensively available metal) as well as a green and sustainable manufacturing process. In the following text MIL 53 is used to refer to MIL 53(Fe).

The MIL 53 was synthesized using terephthalic acid (H_2BDC), a commercially available linker. The MIL 53 was chiral doped using R (-) and S (+) Camphor Sulphonic Acid as well as L Cysteine. An achiral form, MIL 53-NH_2 was also synthesized, prior to this study MIL 53-NH_2, was the best modification made to the MIL 53. Fourier Transform Infrared (FTIR) Spectroscopy was used to evaluate the functional groups that are present in the MOFs. To evaluate the crystallinity of the MOFs, powder X-ray diffraction (PXRD) was used, while Thermogravimetric Analysis (TGA) was used to assess the thermal stability. Cyclic Voltammetry (CV) was carried out to explore the electrochemical behaviour of the MOFs, as well as assessing the chirality the chiral MOFs. Scanning Electron Microscopy coupled with Energy Dispersive Spectroscopy (SEM-EDS) as well as Field Emission Scanning Electron Microscopy (FESEM) were employed to evaluate the surface morphology of the MOFs. The electrochemical properties were assessed using different electrochemical techniques which include linear sweep voltammetry, chronoamperometry as well as electrochemical impedance spectroscopy.

5.2 SYNTHESIS OF MIL 53 AND ITS DERIVATIVES

5.2.1 Synthesis of MIL 53

A mixture of $FeCl_3 \cdot 6H_2O$ (1.35 g) and H_2BDC (0.83 g) were dissolved in 25 mL dimethylformamide (DMF). The resulting mixture was then transferred into a Teflon-lined hydrothermal autoclave and then heated up at 150 °C for 6 hours. A yellow solid was extricated and refluxed with DMF for 15 hours. After which the mixture was filtered and the solid was washed three times using 10 ml of ethanol (C_2H_5OH), and subsequently dried at 80 °C for 15 minutes (Whitfield et al., 2005). **Scheme 5.1** depicts the preparation steps used to obtain MIL-53(Fe).

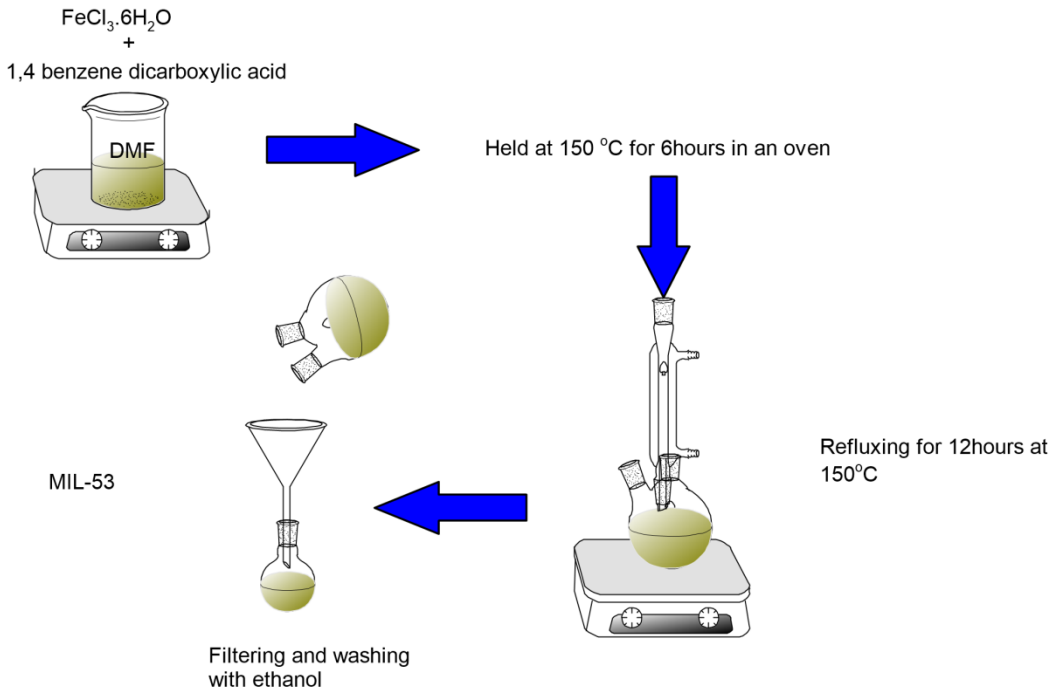

Scheme 5.1: Synthesis of MIL-53 (Fe)

5.2.2 Synthesis of chiral MIL 53 derivatives

5.2.2.1 Synthesis of MIL 53 doped with R (-) Camphor Sulphonic Acid

A mixture of 1.35 g of $FeCl_3 \cdot 6H_2O$, 0.788 g of H_2BDC and 0.06g R (-) camphor sulphonic acid were dissolved in 25 mL of DMF. The resulting mixture was then transferred into a teflon-lined hydrothermal autoclave and heated up at 150°C for 6 hours. The yellow solid was extricated and refluxed in DMF for 15 hours. After filtering the solid was washed with 10ml of C_2H_5OH, three different times and subsequently dried at 80° C in a hot air oven for 15 minutes.

5.2.2.2 Synthesis of MIL 53 doped with S (+) Camphor Sulphonic Acid

A mixture of 1.35 g of $FeCl_3 \cdot 6H_2O$, 0.788 g of H_2BDC and 0.06g S (+) camphor sulphonic acid were dissolved in 25 mL of DMF. The resulting mixture was then transferred into a teflon-lined hydrothermal autoclave and heated up at 150 °C for 6 hours. The yellow solid was extracted and refluxed in DMF for 15 hours. After filtering the solid was washed with 10ml of C_2H_5OH, three different times and subsequently dried at 80 °C in a hot air oven for 15 minutes.

5.2.2.3 Synthesis of MIL 53 doped with L-Cysteine

A mixture of 1.35 g of $FeCl_3 \cdot 6H_2O$, 0.788 g of H_2BDC and 0.04g L-Cysteine were dissolved in 25 mL of DMF. The mixture was then transferred into a teflon-lined hydrothermal autoclave and heated up at 150 °C for 6 hours. A yellow solid was isolated and refluxed in DMF for 15 hours. The resulting mixture was then filtered, the resulting solid was washed with 10ml of C_2H_5OH, three different times and subsequently dried at 80 °C in a hot air oven for 15 minutes.

5.2.2.4 Synthesis of MIL 53 NH_2

A mixture of 1.35 g of $FeCl_3 \cdot 6H_2O$, 0.788 g of H_2BDC and 0.90 g amino terephthalic acid (NH_2-BDC) were dissolved in 25 mL DMF. The mixture was then transferred into a teflon-lined hydrothermal autoclave and heated up at 150 °C for 6 hours. The resulting brown solid was isolated and refluxed in DMF for 15 hours. After filtering the solid was washed with 10ml C_2H_5OH, three different times (3 × 10 mL), and subsequently dried at 80 °C in a hot air oven for 15 minutes.

5.3 CHEMICAL ELEMENTAL ANALYSIS

Chemical elemental analysis was carried out using Energy Dispersive Spectroscopy (EDS) of for MIL 53 and its derivatives.

5.3.1 Chemical Elemental Analysis of MIL 53

Table 5.1: Elemental analysis of MIL 53 and its derivatives

MOF	Fe (%w/w)	O (%w/w)	C (%w/w)	Cl (%w/w)	N (%w/w)	S (%w/w)
MIL 53	4.4	22.8	68.7	0.7	3.4	-
MIL 53- NH_2	6.5	24.1	59.9	2.5	7.0	-
MIL 53- RCSA	8.5	27.0	58.1	2.5	3.7	0.2
MIL 53-SCSA	7.7	22.9	59.8	6.3	3.2	0.2
MIL 53-LCys	7.1	24.1	65.2	2.0	1.4	0.3

In the MIL 53 structures, the presence of iron is detected. In the chiral variations MIL53 L-Cysteine, MIL53 R-CSA, MIL53 S-CSA, EDS analysis shows the presence of sulphur which is a component of cysteine and camphor sulfonic acid doping molecules. **Table 5.1** shows a summary of the elemental analysis of MIL 53 and its derivatives. The nitrogen recorded is due to the presence of DMF molecules occupying the pores within the MIL 53 structure and this molecule is removed during activation of the MOFs. The different EDS spectra of MIL 53 and its derivatives are shown in **Figure 5.1**.

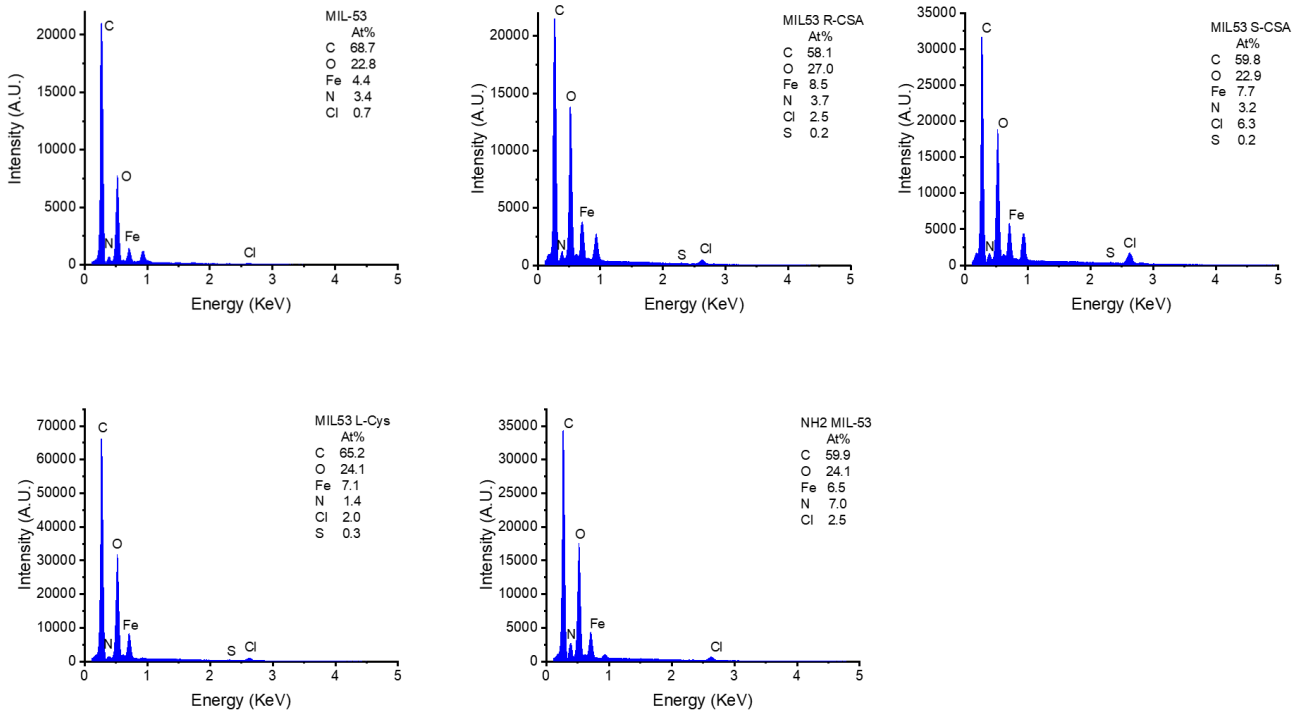

Figure 5.1: EDS spectra of the MIL 53 and its derivatives

5.4 FUNCTIONAL GROUPS

The functional groups present in the synthesized metal-organic frameworks, were evaluated though FTIR measurements. The exact methods have been described in Chapter 3, Section 3.3.

5.4.1 MIL 53 FTIR

Figure 5.2, shows the Infrared (IR) spectrum of the reference MIL 53(Fe). The spectrum of MIL 53 shows the characteristic absorption peaks of MIL 53(Fe) which were observed at 1660, 1596, 1390, 752, and at 551 cm^{-1}. These values are similar to those reported in the literature for iron-based MOFs (Banerjee et al., 2012; López et al., 2021) In detail, the peak detected at 1660 cm^{-1} is assigned to the carboxylic C=O bonds stretching vibration confirming the absence of free ligand in the synthesized MIL 53(Fe) sample. The free ligand MIL 53(Fe) precursor H_2BDC shows the carboxylic C=O stretching at about 1660 cm^{-1}, there is a decrease in energy, and this confirms the interaction of the ligand with the iron of the network (Li et al., 2018). There are two intense peaks characterizing the IR spectrum at 1596 and 1390 cm^{-1} and these correspond to the asymmetric and symmetric vibrations of the C-O of the two carboxyl groups of the H_2BDC ligand, respectively.

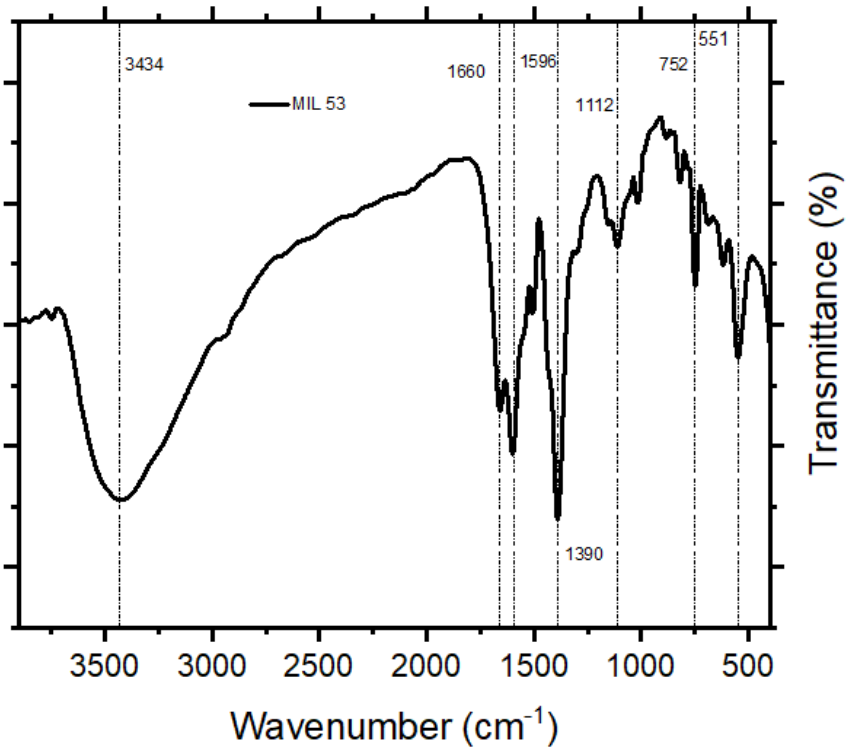

Figure 5.2: FTIR Spectrum of MIL 53

There is an intense and sharp peak at 752 cm^{-1}, this can be assigned to the aromatic C-H bending of the benzene ring. These results show that there is a dicarboxylate linker within frameworks. The bands in the fingerprint region, between 700–400 cm^{-1}, are ascribed to the stretching vibration of Fe–O, confirming the formation of a Fe-oxo bond between the Fe (III) and the carboxylic group of BDC ligand (Li et al., 2018).

5.4.2 FTIR for MIL 53 derivatives

Figure 5.3, shows the IR spectra of the reference MIL 53 (black line), **Figure 5.3(a)**, shows a comparison of MIL -53 with the chiral derivatives of MIL 53, those synthesized by including chiral linkers while **Figure 5.3 (b)** is a comparison between MIL 53 and MIL 53-NH_2. MOFs synthesized with chiral ligands, L-Cysteine and R-CSA; all show the same peaks as described above with the confirmation of the Fe-O bond formation by the peak at 527 cm^{-1}. However, a new peak is observed at 2048 cm^{-1} in MIL 53 L-Cysteine and MIL 53 R while absent from MIL 53. The formation of this peak can be attributed to the presence of C=S which is not present in MIL 53.

a) b)

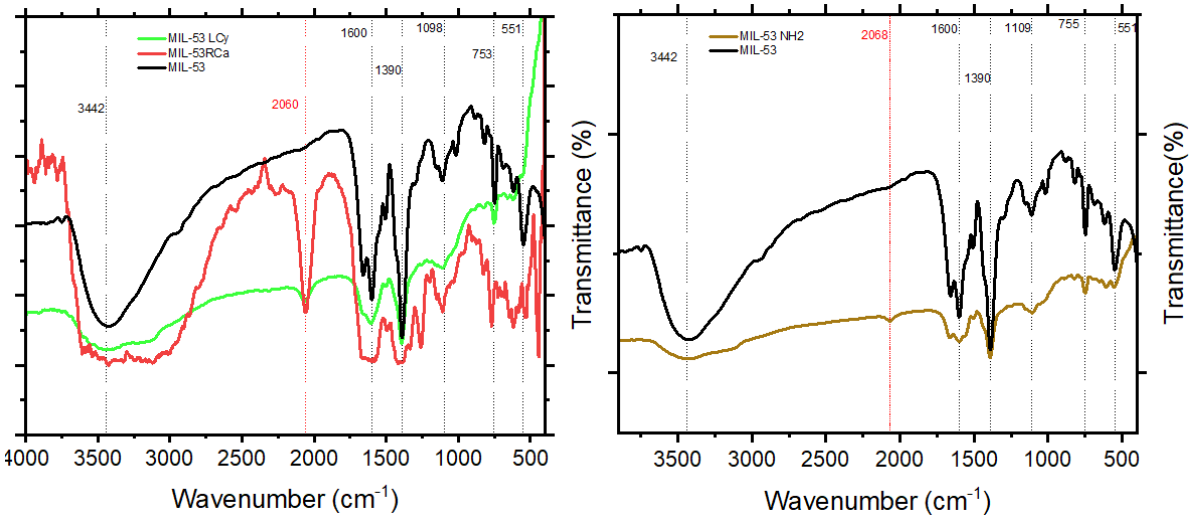

Figure 5.3 a) FTIR Spectra comparing MIL 53 and chiral MIL 53 derivatives

b) FTIR Spectra comparing MIL 53 and MIL 53-NH_2

MIL 53-NH_2 shows the same spectral pattern however, it has more features in the range 3300-3500 cm^{-1} which can be attributed to the N-H stretching of the amino group of the amino-terephthalic acid used for its synthesis. The presence of the amino group on the benzene ring of the terephthalic acid shifts the C-H bending peak from 753 cm^{-1} of the MIL 53 to higher energy at 755 cm^{-1}.

5.5 Powder X-Ray Diffraction

To investigate the crystallinity of the MIL 53 and its derivatives, PXRD measurements were carried out according to the methods described in Chapter 3.3. The PXRD pattern obtained for the achiral MIL 53 was drawn using Origin 2023 and a comparison was made versus the calculated PXRD profile of the MIL 53 as shown in **Figure 5.4**. The calculated PXRD pattern was evaluated using Mercury.

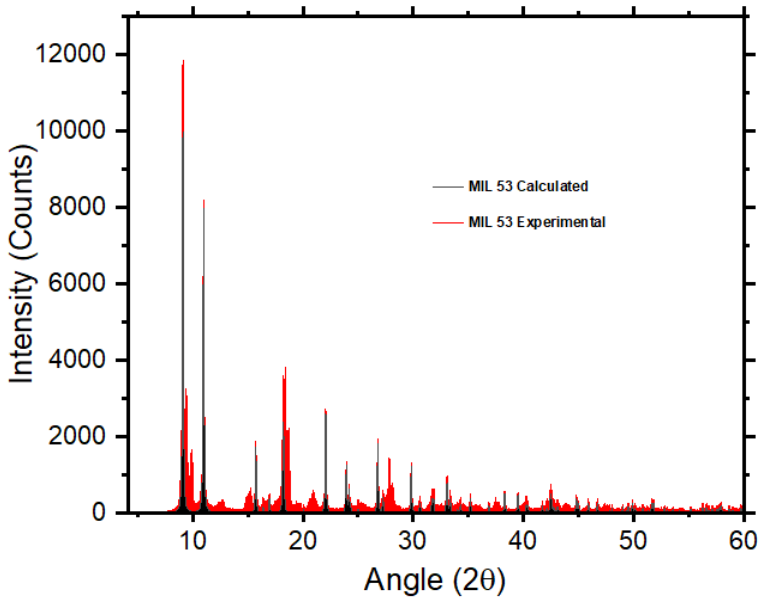

Figure 5.4: PXRD pattern of synthesized MIL 53

In the PXRD pattern shown in **Figure 5.4**, the doublets at 2θ 9.29° and 9.69° which are synonymous with MIL 53 as reported previously (Banerjee et al., 2012; Abdollahi et al., 2022). Peaks were also observed at 12.7, 18.31, 25.04 and 27.76° which are consistent with previously reported (Chaturvedi et al., 2019). The absence of peaks at 38 and 55° which are synonymous with α-Fe_2O_3 shows that the synthesized MIL 53 was free from the α-Fe_2O_3. The peaks observed at 9.29 and 18.31° have higher intensity and clarity, showing that the structure of MIL 53 is highly crystalline.

Further analysis of the results was also carried out using Match!*, the MIL 53 sample the observed peaks are consistent with CIF file 96-156-4912, which is MIL 53 (Fe) as shown in Appendix D. Match!* has the ability of identifying the phases present and the phases present are as shown in **Figure 5.5**. In **Figure 5.5** there is an unidentified phase which can be attributed to the unreacted ferric chloride as well as the DMF, in agreement with the chlorine and nitrogen observed during EDS.

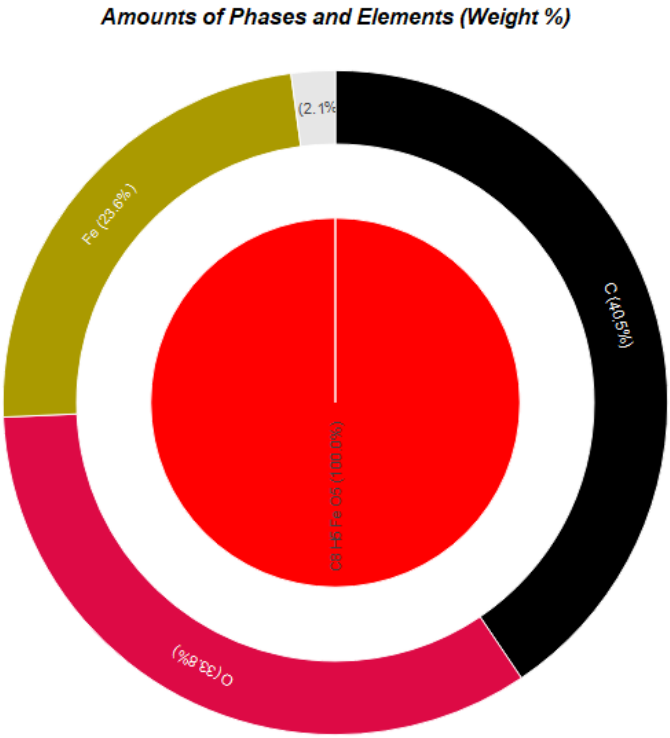

Figure 5.5: Phases present in the as synthesised MIL 53

5.5.1 PXRD for chiral MIL 53

The PXRD patterns for the chiral derivatives are shown in **Figure 5.6**. The PXRD pattern of the MIL 53 is similar to that of MIL 53 R-CSA and MIL 53 S CSA, from this observation, we can infer that that Camphor Sulphonic Acid does not destroy or alter in a significant way the MOF framework. In contrast, the PXRD pattern for MIL 53 doped with L-Cysteine is different from that of the as-synthesised MIL 53, suggesting that the inclusion of the L-Cysteine in the pores induced some structural transformation to the MOF framework.

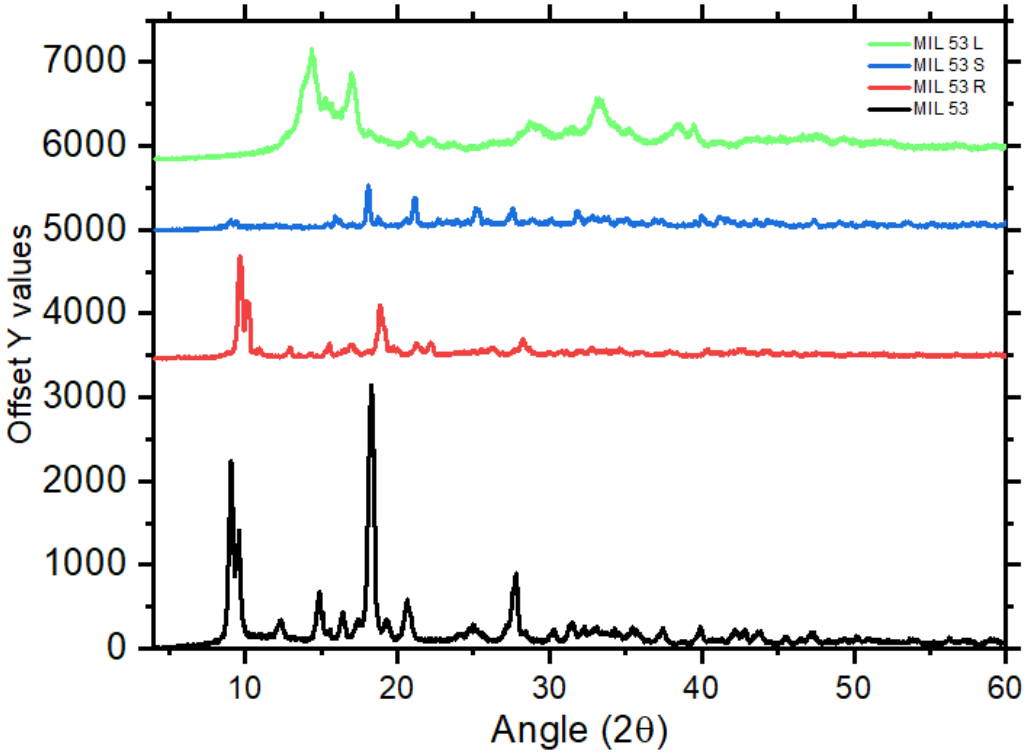

Figure 5.6: PXRD pattern of chiral derivatives of MIL 53

For the chiral derivatives doped with CSA, the peaks consistent with MIL 53 are observed at 9.29 and at 18.31° showing that the structure of MIL 53 was maintained. MIL 53 and MIL53 R-CSA synthesized appear to be a mixture of dehydrated form, as for the presence of the diffraction peak at about 12.7 °, and of the hydrated form, for matching the peak at 19 °.

5.5.2 PXRD for MIL 53-NH_2

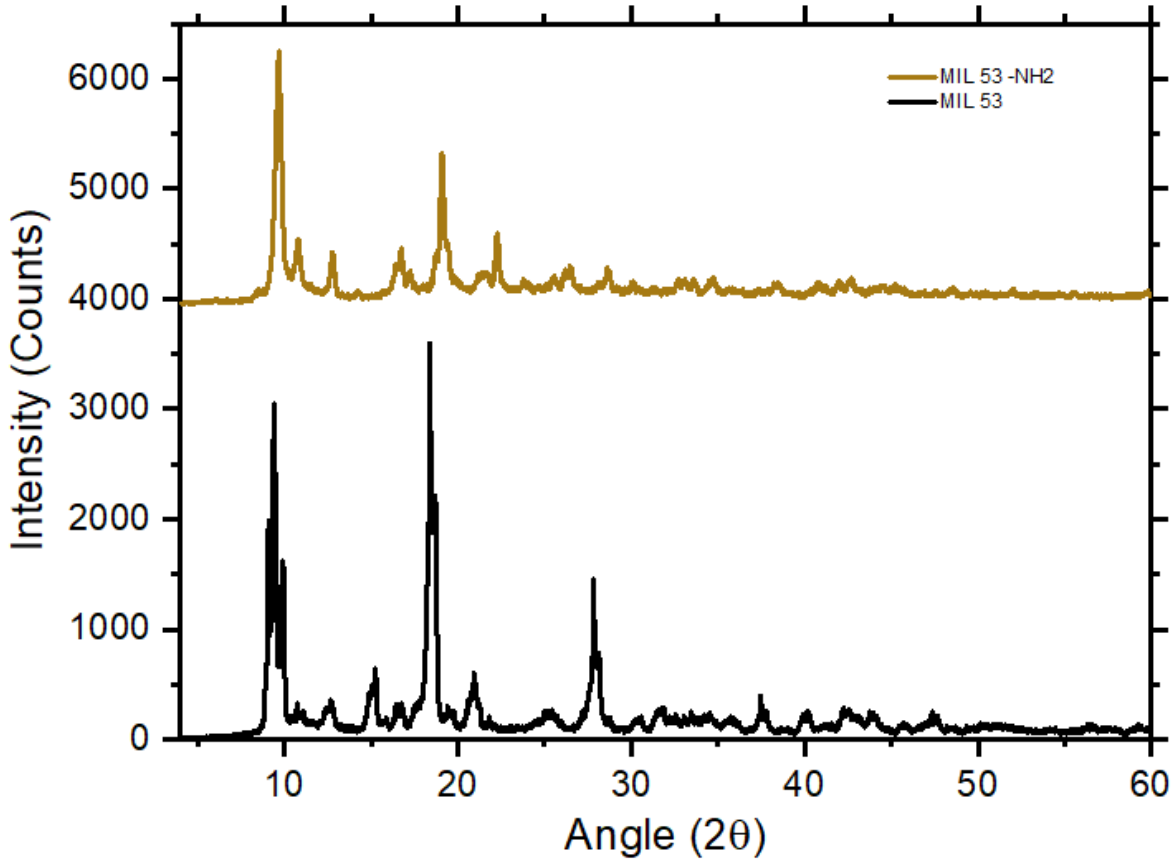

Figure 5.7: PXRD pattern of MIL 53-NH_2

Figure 5.7 shows the PXRD pattern for MIL 53-NH_2, in the PXRD profile of MIL 53-NH_2, The PXRD pattern for MIL 53 NH2 is similar to that of the parent MIL 53, because the two are isostructural, their structures are the same. The observed peaks are consistent with observations from previous data (Sun et al., 2015).

5.6 PHOTOCATALYTIC ACTIVITY

The photocatalytic activity of the MOFs was assessed using a UV-1900i Shimadzu Uv-Vis Spectrophotometer. A 2% MOF paste was made by dissolving the MOFs in ethanol. The sample was then assessed for photocatalytic activity by running a scan from 300 to 500 nm.

In Uv-Vis spectroscopy, when a solution is irradiated, an electron from a lower set orbital is promoted into the upper set orbital. In transition metals, this happens when the electrons move onto the partially filled 3d orbitals. The synthesized MOFs exhibited very distinct colours, with the MIL 53 based MOFs all being brown in colour with the tone for MIL 53-NH_2 being darker.

5.6.1 MIL 53 Uv-Vis

The Uv-Vis measurements, produced the spectra given in **Figures 5.8 a) and b)** where **Figure 5.8 a)** is the Uv-Vis absorption spectra for MIL 53 and its derivatives and **Figure 5.8 b)** Diffuse Reflectance of MIL 53 and its derivatives In **Figure 5.8 (a**), the black line that represents MIL 53, there is a slight peak at 314 nm and another at 330 nm The first peak can be attributed π to π* in C=C due to sp^2 hybridization while the peak at 330 nm can be attributed to ligand-to-metal charge transfer (LMCT) of O (II) →Fe (III) due to the presence of a lone pair of electrons on the oxygen atom (López et al., 2021).

a) b)

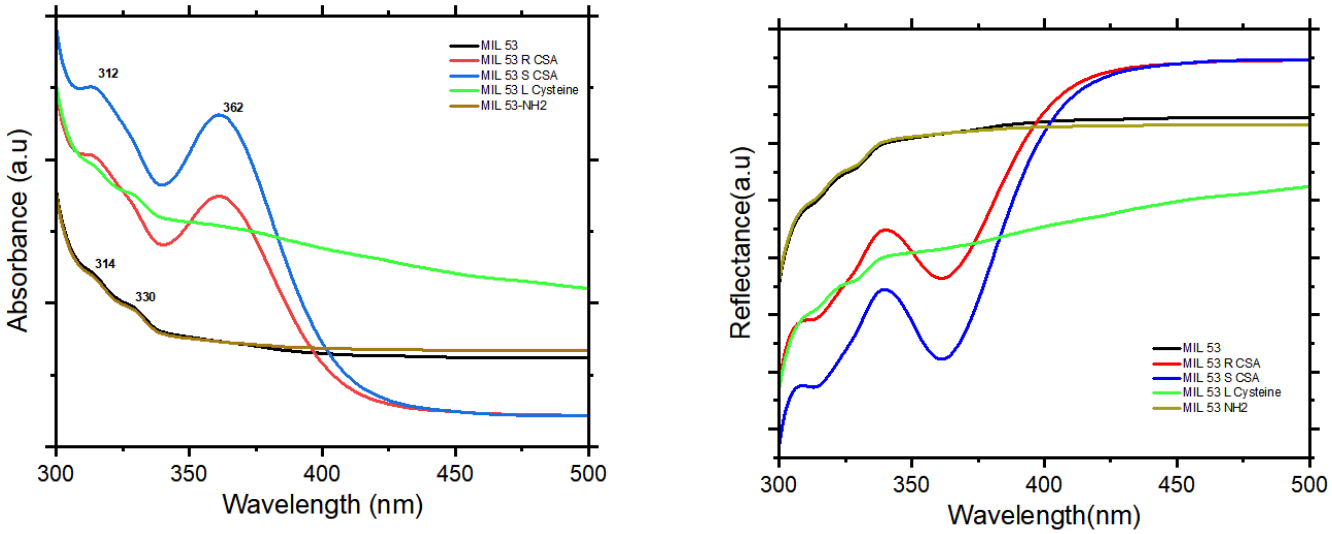

Figure 5.8 a) Uv-Vis absorption Spectra for MIL 53 and its derivatives. b) Diffuse Reflectance of MIL 53 and its derivatives

For the MIL 53 CSA derivatives, the peaks observed in MIL 53 are now pronounced at 312 nm and at 362 nm. The peak at 312 nm can be attributed to π to π* in C=C due to sp^2 hybridization as has been alluded to in the MIL 53. The peak at 362 nm is attributed to ligand-to-metal charge transfer (LMCT) of O (II) →Fe(III) due to presence of multiple lone pairs of electrons (Najafidoust et al., 2022).

Figure 5.8 (b), shows the diffuse reflectance spectra (DRS) of the MIL 53 and its derivatives. DRS quantitatively measures the colour and intensity of reflected light by different materials (Tran et al., 2023). From **Figure 5.8 (b),** it can be observed that the optical properties of the

MOFs vary. The main absorption edge for the different MOFs were evaluated as shown in Appendix E and are tabulated in **Table 5.2**.

The band gap energies, were evaluated using equation 5.1.

$$E_{g=\frac{1240}{\lambda}}$$ Equation 5.1

Table 5.2: Band gaps of MIL 53 and its derivatives

MOF	End of Band Gap	E_g (eV)
MIL 53	411	3.01
MIL 53-NH_2	395	3.14
MIL 53 RCSA	480	2.58
MIL 53 S CSA	480	2.58
MIL 53 L Cysteine	489	2.54

The calculated value for the MIL 53 is similar to that reported by previous researchers (Najafidoust et al., 2022). In comparison, the chiral MOFs have lower band gap energies compared to the MIL 53. The chiral MOFs exhibit lower band gaps than the original MOF with the chiral MOFs, being active in the near visible region. The reduction in the band gap energy can be attributed to the structural defects that took place during the formation of the of the chiral MOFs. The lowering of the band gap is essential in improving the photocatalytic performance of the MOFs.

5.7 THERMAL STABILITY

Thermogravimetric analysis of the MIL 53 was carried out to evaluate its thermal stability. In thermogravimetric analysis, the MIL 53 shows a three-stage weight loss as shown in **Figure 5.9**.

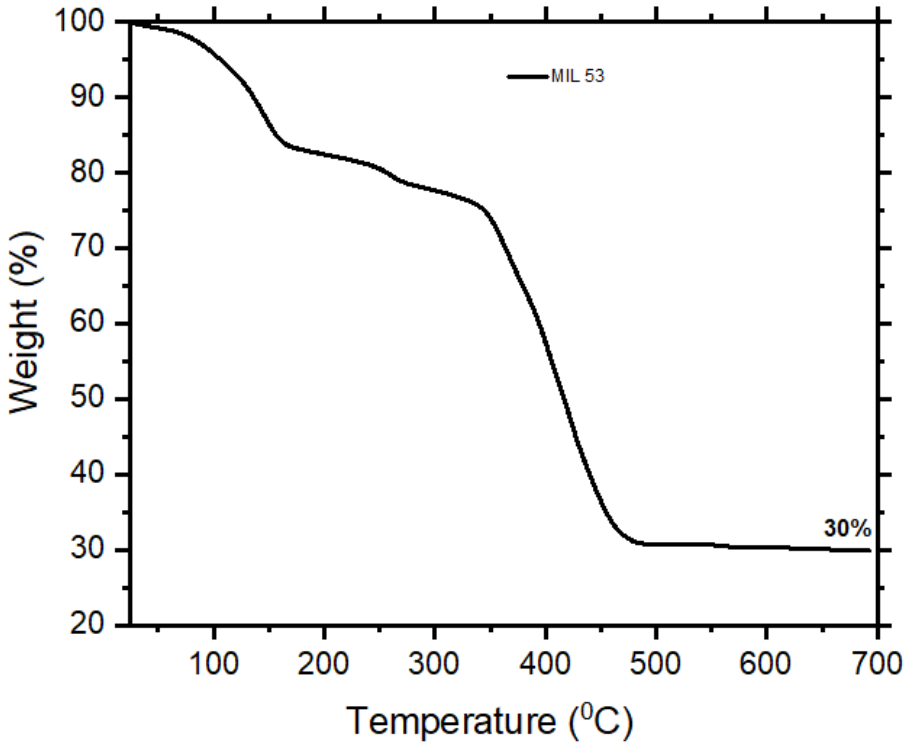

Figure 5.9: Thermogravimetric curve for MIL 53

The initial weight loss that occurs between 50°C and 165°C with weight loss of 16.3%, this corresponds to the loss of water and DMF molecule respectively. Further degradation around 300°C can be attributed to the breakdown of the bdc linker. The sharp decrease between 348 °C and 466 °C can be attributed to the loss of carbon, while stabilization was achieved around 500 °C (Banerjee et al., 2012). The final residue of 30% is in agreement with previously published results for thermal stability of MIL 53 (López et al., 2021).

5.8 CHIRAL RECOGNITION

The use of chiral metal electrodes coated with chiral molecules for chiral recognition has been used because they display enantiospecific interactions (Metzger et al., 2020). Chiral recognition is a chemical interaction, in which a given chiral molecule recognizes a particular stereoisomer (Pappalardo & Parisi, 2008). The enantio-specificity displayed when

the chiral surface and the redox electrolyte come into contact can be explained by the lock and key model.

In this study cyclic voltammetry was used to differentiate the chiral MOFs. Cyclic voltammetry was carried out on the chiral electrodes from -0.23V to +1.23V (vs Ag/AgCl) using a scan rate of 0.1V/s in 8mM L-Cysteine dissolved in HCl with the pH of the solution maintained at 4.0 using the pH 4 buffer solution.

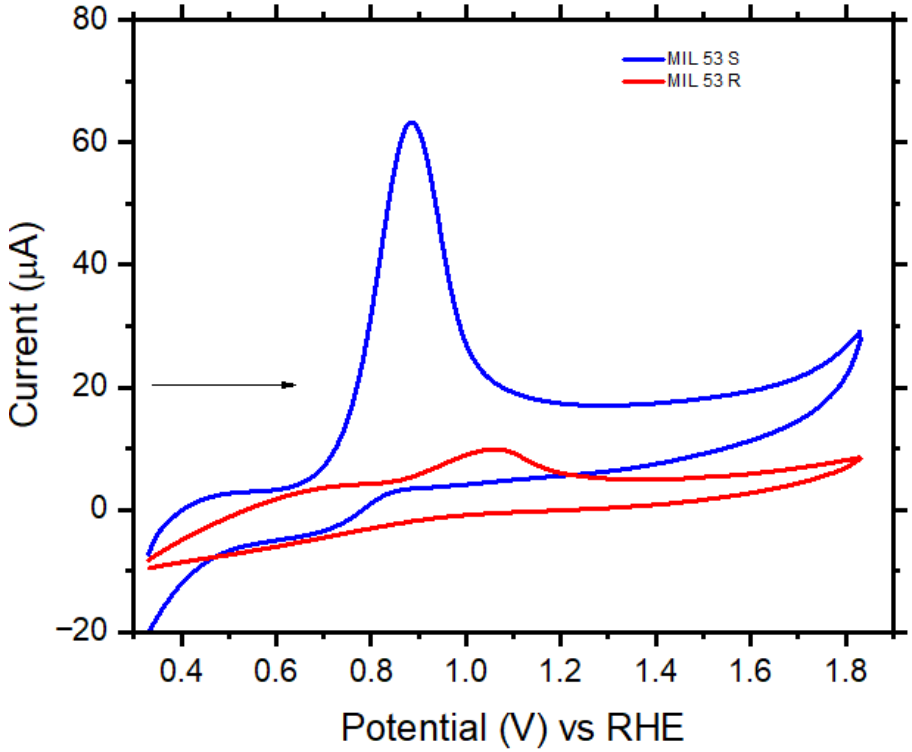

Figure 5.10: A comparison of CVs of produced by MIL 53 vs chiral MIL 53 photoelectrodes in 8mM L-Cysteine

Figure 5.10, shows the cyclic voltammograms obtained during chiral recognition. In the measurements, there is a remarkable difference between the interactions of the R and S doped molecules. In MIL 53 R CSA and MIL 53 S CSA showed remarkable differences with ΔE 0.186V for MIL 53 S CSA, while no ΔE was observed for MIL 53 R CSA. From the molecular structures of the chiral linkers L cysteine can also be called R Cysteine, MIL 53 R, shows no ΔE at all and this can be attributed to the molecular recognition that occurred between the R CSA MOFs and the L Cysteine. In contrary, S-CSA molecules, showed very high ΔE showing no interaction between them and the L Cysteine. **Table 5.3** shows a summary of the ΔE values obtained during the cyclic voltammetry measurements.

Table 5.3: ΔE values obtained during chiral recognition of the chiral electrodes

Photoelectrode	ΔE (V)
MIL 53	0.1926
MIL 53 R CSA	-
MIL 53 S CSA	0.186

Based on the cyclic voltammograms obtained we can conclude that chirality was successfully induced.

5.9 SOLID STATE CYCLIC ELECTROCHEMISTRY

Solid-state electrochemistry was carried out to evaluate the electrochemical behaviour of the MIL 53 and its derivatives. The solid-state electrochemistry was carried out, using a three-electrode system the glassy carbon electrode coated with the graphite and MOF mixture (GCE/MOF) served as the working electrode (WE), a coiled Platinum wire and an Ag/AgCl (saturated KCl) electrode was used as the counter electrode (CE) and reference electrode (RE), respectively. A graphite powder and MOF mixture, mixed in equal proportions was deposited onto the glassy carbon electrode (GCE). Before the surface modification, the glassy carbon, working electrode was polished using 0.05 μm alumina slurries on a polishing cloth; then it was cleaned carefully, and sonicated for 10 min in milliQ water to clean the surface and remove any polishing residue before being dried. The effective cell set-up and glass carbon electrode activation procedure was cross-checked by recording CVs in a solution of 1 mM ferricyanide in 0.1 M KCl.

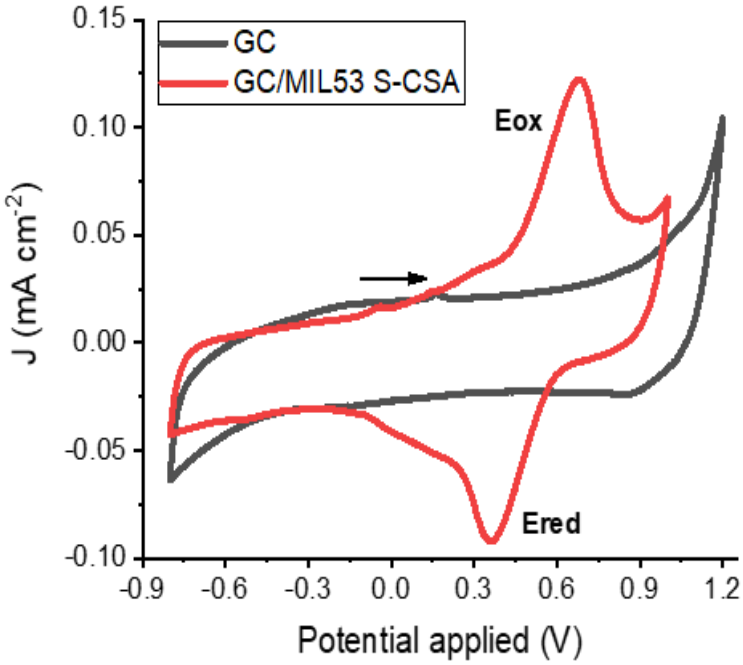

Figure 5.11: Cyclic Voltammetry curve in aqueous 0.1 M Potassium Chloride (KCl), of GC/ MIL 53 S CSA (Working Electrode) vs Ag/AgCl/KCl_{sat} (Reference Electrode) at a scan rate 0.01V s^{-1}.

Figures 5.11 show CV curves recorded for MIL53 S CSA. The black solid line is the control CV recorded using the graphite powder only and it serves as the. the "blank" baseline. It must be noted that a prominent capacitive contribution, in the -0.7 to 1.0 V potential range produces a regular "rectangular box" CV pattern, as depicted in **Figures 5.11**. The red solid curves in **Figure 5.11.**

are the CVs recorded after mixing the graphite powder with the chiral MOF. The CV of the MIL53 S CSA MOF features two redox peaks (labelled as E_{ox} and E_{red} in **Figures 5.11** centred at about 0.5 V. This suggests that the redox process underlying the presence of the two current peaks in **Figure 5.11** can be assigned to the Fe(III)/Fe(II) redox couple. The peak-to-peak separation is about 0.3 V, which is relatively large, such a potential difference is due to the solid-state nature of the electroactive system

In addition, the overall MOF framework is based on organic molecules which are well known to behave more closely to a dielectric than to a conductive material, this further hinders the Fe (III)/Fe(II) charge transfer kinetics. Appendix F shows the CV curves obtained for the remaining four iron-based MOFs. **Table 5.4** summarizes the electrochemical results.

Table 5.4: Electrochemical results for MIL 53.

Compound	Oxidation (V)	Reduction (V)	Difference
MIL53	0.682	0.366	0.316
MIL53 S-CSA	0.676	0.363	0.313
MIL53 R-CSA	0.608	0.418	0.190
MIL53 NH_2	0.592	0.408	0.184
MIL53 L Cysteine	0.805	0.198	0.607

The chiral dopants affect the electrochemical behaviour by both shifting the redox peak potential and CV pattern. Camphor sulphonic acid derivatives cause an overall shift of the peak potential to slightly more positive values, featuring a pronounced quasi-reversible behaviour. Current peaks are definitively much more symmetric. However, the ΔE values are relatively larger than 0.59V, implying that the redox processes taking place a non-Nernstian and, in this case, there was electrochemical irreversibility between electrolyte and electrode (Elgrishi et al, 2018). A rather unusual result is obtained in the case of cysteine, where a much broader shoulder is present. This is can be attributed to the overlap of two/three separate peaks present, suggesting the existence of two/three different species formed between iron and cysteine (cysteine contains three functional groups that are able to bind iron, i.e. the thio, amino and carboxylic acid moieties).

5.10 SURFACE MORPHOLOGY

5.10.1 Scanning Electron Microscopy (SEM)

Scanning electron microscope (SEM) images were investigated to evaluate the surface morphology of the MIL 53 and its derivatives.

Figures 5.12, shows SEM images of iron-based MOFs (MIL 53) from the secondary electrons (all at the same magnification). MIL 53 shows a regular morphology with uniform hexagonal bipyramid particles similar to those reported in literature (Zhang 2017). The SEM images indicate that the material synthesized consists of well-defined rods of varying sizes with a smooth surface, sharp edge, and multiple cracks/fractures (López et al., 2021). The MIL 53 chiral derivatives show similar structures to that of the MIL 53. In addition, in the chiral derivatives, smaller bulky irregular fragments are also observed and these can be attributed to the presence of the chiral motifs.

In the MIL 53-NH_2 there is a completely different surface morphology. The particles in MIL53-NH_2 are organized in a spherical way.

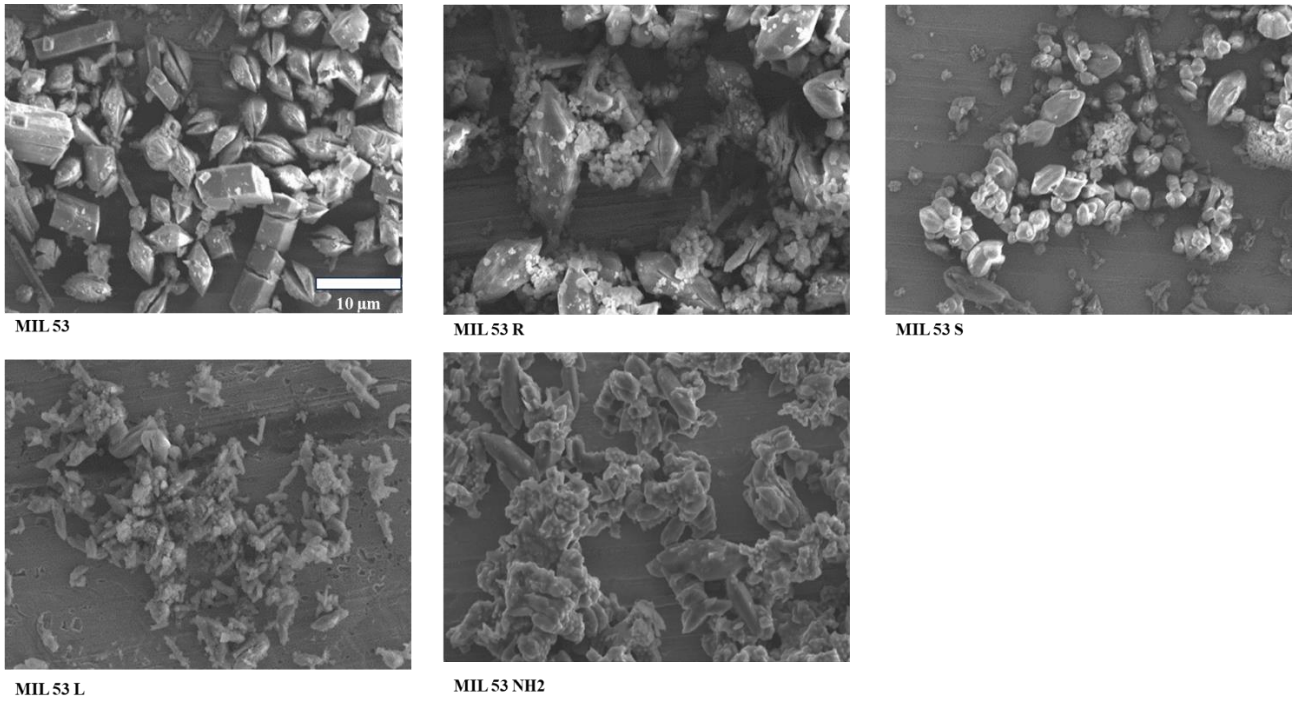

Figure 5.12: SEM Images for MIL 53 and its derivatives.

5.10.2 Field Emission Scanning Electron Microscopy (FESEM)

To consolidate the findings from SEM-EDS, Field Emission Scanning Electron Microscopy (FESEM) was also carried out on MIL 53 only. From the FESEM images, shown in **Figure 5.13**, the rod like, hexagonal crystals are highly amplified, confirming the crystalline nature of MIL 53. In the FESEM images of MIL 53, **(Figure 5.13 a)),** single crystalline grains of the MIL53 are clearly visible showing their polyhedral configurations while a magnified image in **Figure 5.13 b)** shows the single crystal clearly. The uniformity in the shape of the crystals, suggests the crystals are due to MIL 53. One iron-based MOF that closely resembles the MIL

53, the MIL 88 forms microrods that are either sharp and pointy spindle or diamond shaped, with many faces that resemble an octahedral (Ma et al, 2013: L Wang et al, 2015), based on this observation, the crystals in the sample are due to MIL 53 only.

a) b)

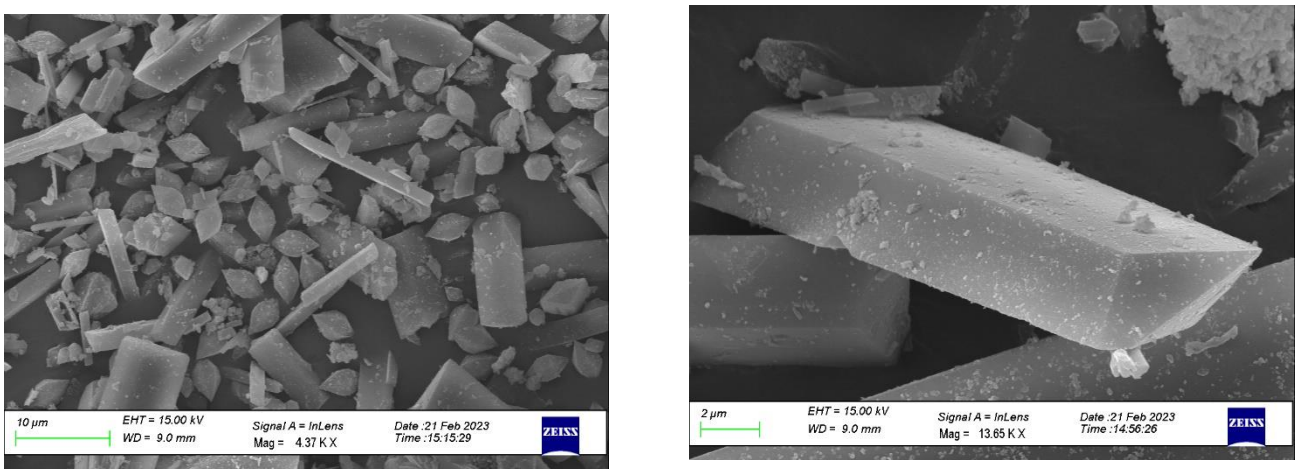

Figure 5.13: FESEM Images of MIL 53

5.11 PREPARATION OF ELECTRODES

The preparation of the electrodes was done according to the methods published by Mtangi et al in 2017 (Mtangi et al., 2017) as well as modifications done by Kawondera et al in 2023 (Kawondera et al., 2023). In detail, the FTO/TiO_2 electrode was prepared first. TiO_2 nanoparticulate films were deposited on fluorine-doped tin oxide, FTO (surface resistivity of ~7 Ω/sq,) coated glass, using the electrophoretic deposition (EPD) technique. A suspension of TiO_2 nanoparticles (NPs) was prepared by dispersing 0.4g TiO_2 NPs in 40 mL of de-ionized water. Before this, the TiO_2 nanoparticle powders were heated at 570 K for 1 hour, then the mixture was stirred for 16 hours to ensure homogeneity. Before nanoparticle deposition, the FTO substrates were washed by boiling them in acetone for 15 minutes, followed by 15 minutes of boiling in ethanol, and finally rinsed with de-ionized water. After rinsing, the substrates were dried in the air for 15 minutes. Electrophoretic deposition (EPD) was performed with a CHI electrochemical analyser, model 608E, using the Chronopotentiometry mode. During EPD, the suspension was continuously stirred using a magnetic stirrer. After completion of the last cycle, the electrodes were annealed for 2 hours at 400K.

5.11.1 Functionalization FTO/TiO_2 surfaces

Functionalization of FTO/TiO_2 surfaces to yield the final FTO/TiO_2/MOF photoelectrodes was achieved by drop casting MOF solutions onto the FTO/TiO_2 surfaces. 1 mM slurry solutions of the MOFs were made by dissolving the MOFs in ethanol and then carefully depositing 20µL of the MOF solution on the FTO/TiO_2 surface. Before deposition, the MOFs were activated in a hot air oven at 150 °C for 1 hour to remove excess DMF. The electrodes were then left to dry under controlled humidity and temperature for a period of three weeks.

5.12 WATER SPLITTING MEASUREMENTS

Water splitting experiments were performed using the functionalized TiO_2 electrodes. All the measurements were performed versus the Ag/AgCl reference electrode, 0.1 M Na_2SO_4 was used as the electrolyte with a Platinum wire as the counter electrode. The potentials were converted from Ag/AgCl to Reversible Hydrogen Electrode (RHE) using the equation:

$$E = E_{ref} + 0.059 * pH + 0.1976 \qquad \text{Equation 5.2}$$

Where E Potential versus the RHE

E_{ref} Potential versus the reference electrode (Ag/AgCl)

pH Electrolyte pH (the working pH was 6.5)

5.12.1 Photo response Measurement

To evaluate and confirm the photocatalytic activity of the MIL 53 and its derivatives, Linear Sweep Voltammetry in which the light at 100mW/cm^2 was chopped ON/OFF at 10s was carried out. The obtained voltammograms are given in **Figure 5.14.**

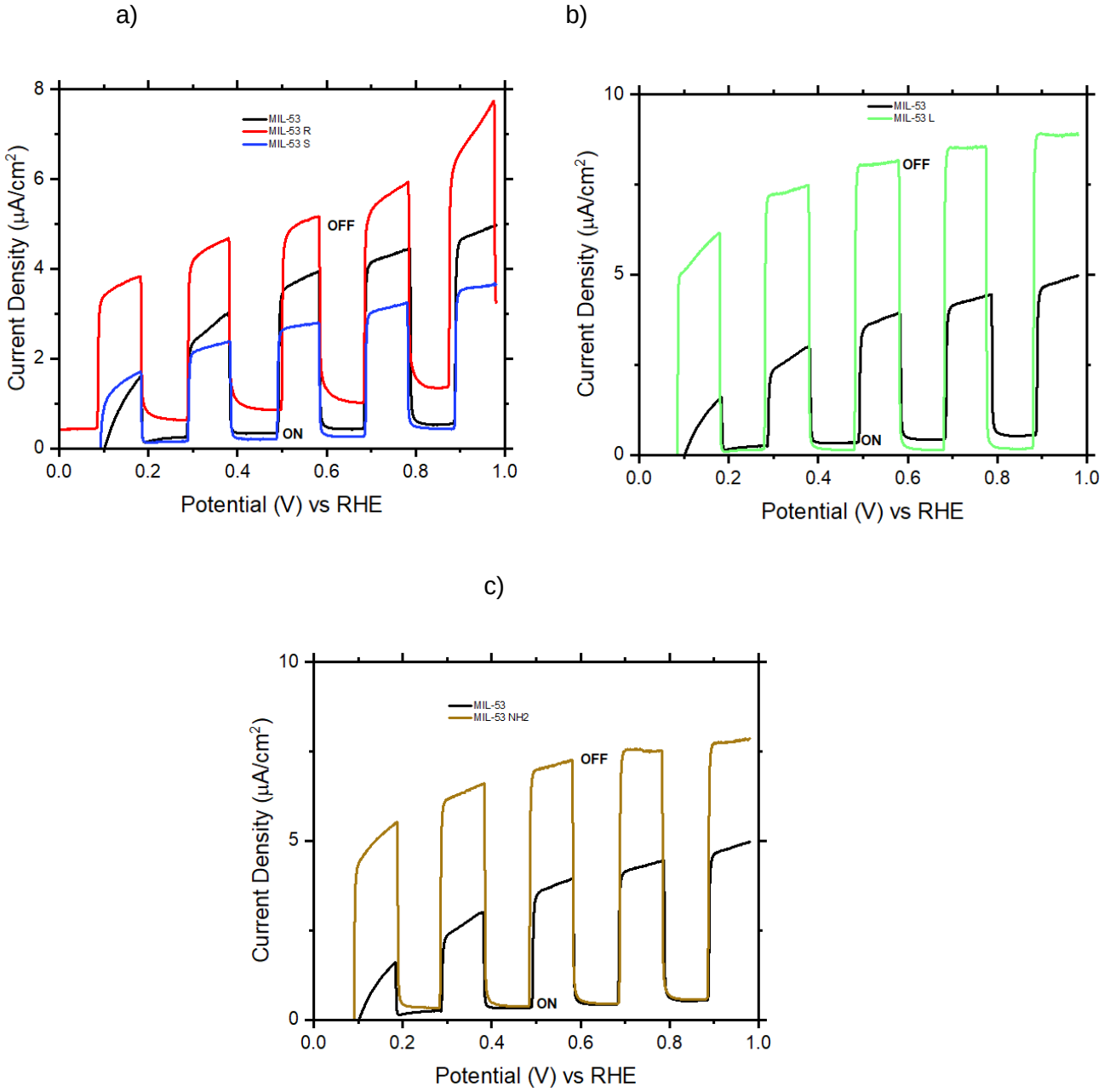

Figure 5.14: Photo response measurements for a) MIL 53 vs MIL 53 R-CSA and MIL 53 S-CSA b) MIL 53 vs MIL 53 L c) MIL 53 vs MIL 53-NH_2 in 0.1M Na_2SO_4 at 0.01V/s scan rate

All the MIL 53 derivatives showed a response to the illumination as witnessed by the sudden spikes in current densities, when the light is switched on and the abrupt manner in which the current densities disappear when the light is switched off. The chiral doped molecules, particularly MIL 53 doped with R Camphor Sulphonic Acid and the MIL 53 doped with L-Cysteine showed the greatest photocurrent densities suggesting that they are able to sustain electron hole separation longer when illuminated by light during photoelectrochemical water splitting. The chiral photoelectrodes produced greater than the MIL 53-NH_2, showing an improvement to the existing MIL 53. In all the voltammograms a smooth peak is observed and this can be attributed to the absence of crystalline defects, when crystalline defects are present in a photocatalyst, very sharp photocurrent spikes which decay to a constant value are observed (Krysa et al., 2015).

5.12.2 Cyclic Voltammetry

Cyclic Voltammetry from -0.35V to +1.35V (vs Ag/AgCl) with a positive initial polarity using a scan rate of 0.1V/s.

5.12.2.1 MIL 53

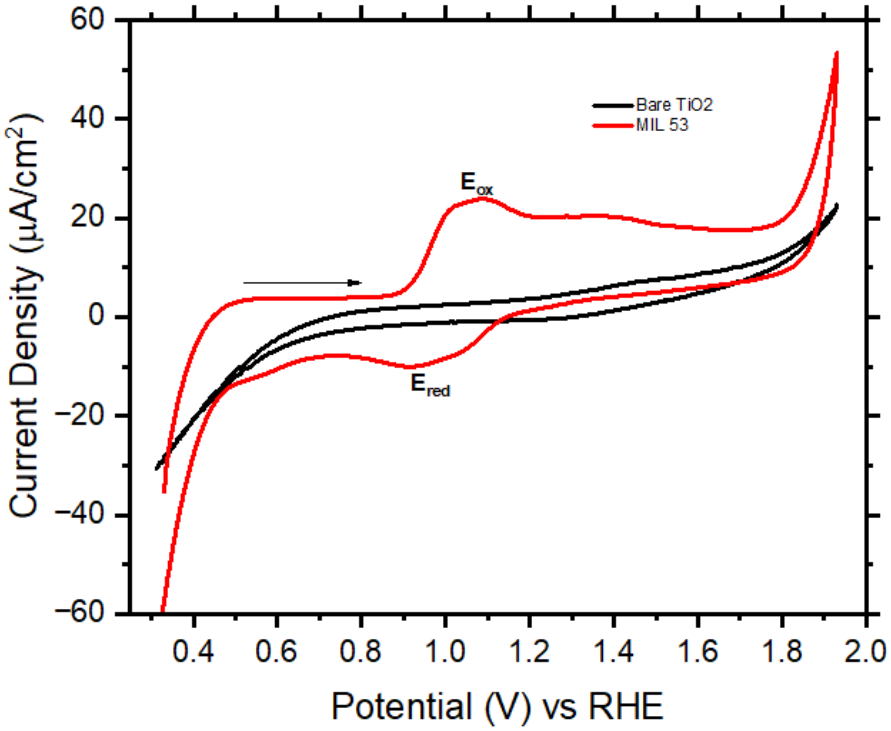

Figure 5.15: CV curves in 0.1M Na_2SO_4 of MIL 53 vs Bare TiO_2 at 0.1V/s

In the CV curve of MIL 53 (red line) in **Figure 5.15**, a strong anodic (forward scan) current peak is observed at 1.08V is, while a strong cathodic peak is observed at +0.94V in the backward scan to give a formal reduction potential of +1.01V. The presence of the anodic and cathodic peaks, suggests that the redox process taking place in **Figure 5.15** can be assigned to the Fe(III)/Fe(II) redox couple. The black line shown in **Figure 5.15** is the CV of Bare TiO_2 nanoparticles and it was used as the control in all the CV measurements. The area of the forward and backward current which is related to the charge exchanged during the potential scan is nearly similar suggesting that the chemistry of the redox processes responsible for the current peaks in the CVs are reversible (Gazzotti et al., 2018), implying that there is no kinetic barrier or coupled chemical reaction. The steepness of the CV curve after the anodic peak suggests intense water splitting taking place.

5.12.2.2 Comparison of chiral MIL 53 derivatives

Similar measurements were also carried out for the chiral doped MIL 53. In a comparison of the CV curves of the MIL 53 R vs MIL 53 S CSA, (**Figure 5.16**), clear anodic and cathodic peaks can be observed (both forward scan and backward scan).

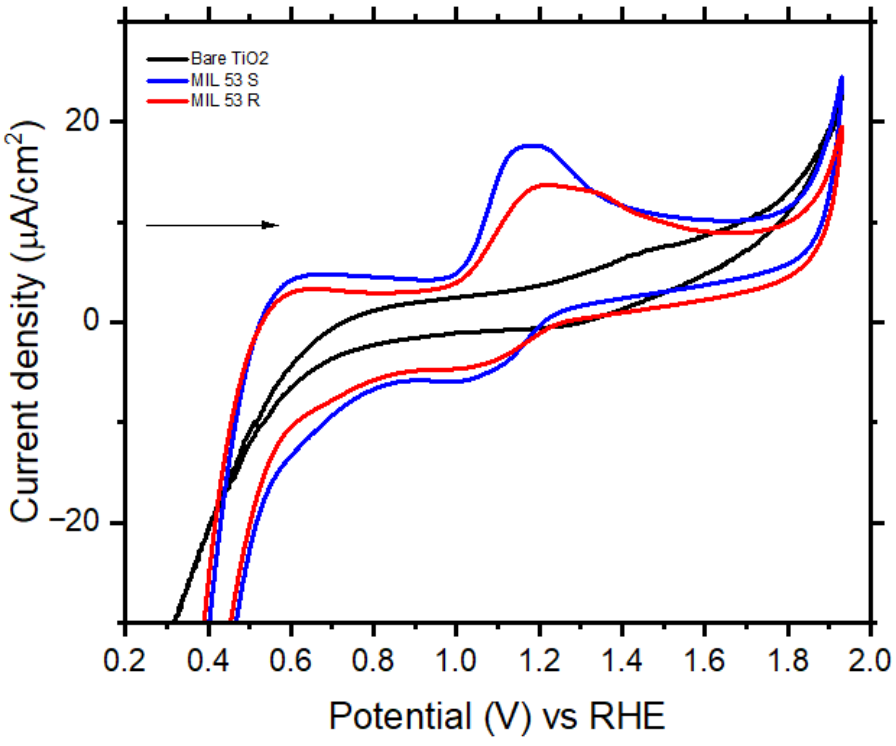

Figure 5.16:Comparison of CV curves of MIL 53 R CSA vs MIL 53 S CSA in 0.1M Na_2SO_4 at 0.1V/s

The observed results are in agreement with the solid-state electrochemistry witnessed in section 5.7. The MIL 53 R-CSA shows an anodic peak at + 1.22V and a cathodic peak at +1.05V to give a formal reduction potential of 1.14V while MIL 53 S CSA has anodic peak at $_{+}$1.17V and a cathodic peak at 1.04V again with a formal reduction potential of 1.11V. In the chiral MOFs there has been a shift to the right, of the both the anodic and cathodic peaks, to make way for the incorporation of the chiral molecules. The two peaks observed are can be attributed to the Fe (III)/Fe(II) redox couple. The area under the anodic peak is not equal to the area in the cathodic peak and this can be classified as a quasi-reversible reaction, there exists some kinetic barrier (Gazzotti et al., 2018). The CV curves obtained from MIL 53 L and MIL 53-NH_2 could not be superimposed on the Bare TiO_2 curve in the same voltage window and they are shown in **Figure 5.17**.

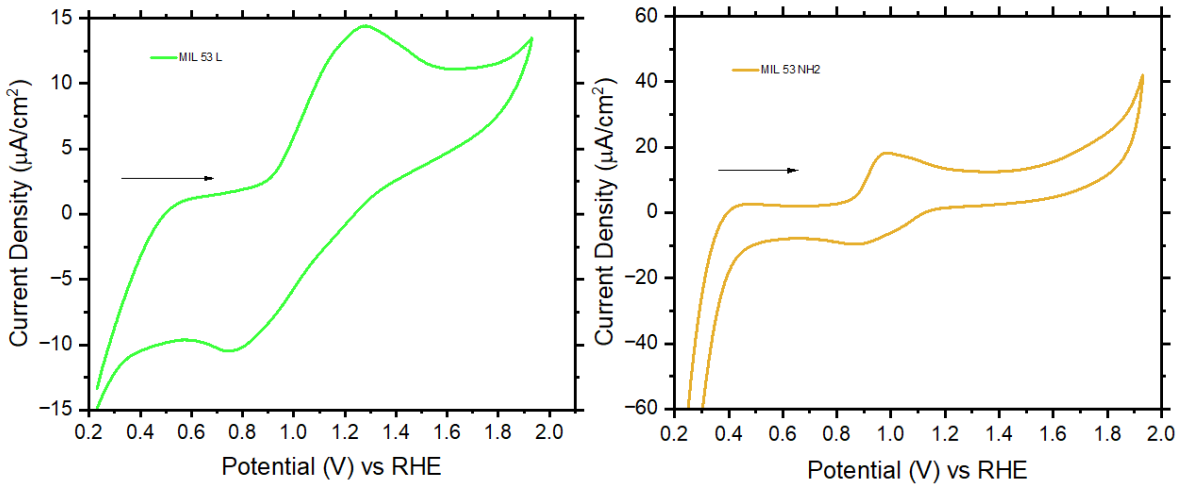

Figure 5.17: CV curves in 0.1M Na_2SO_4 of MIL 53 L Cysteine and MIL 53-NH_2 at 0.1V/s

When compared with the other chiral MOFs, the CV curve for MIL 53 doped with L-Cysteine shows two anodic peaks at +0.53V and +1.27V and a cathodic peak at +0.78V. The CV curve for MIL 53 L suggests multi electron redox process and this can be attributed to the existence of two or three different species formed between iron and cysteine (cysteine features three functional groups able to bind iron, i.e. the thio, amino and carboxylic acid moieties).

In the MIL 53-NH_2 CV curve, an anodic peak is observed at +0.98V and a cathodic peak at +0.88V. Here, when compared with the CV curve for MIL 53, a shift of both peaks to the left (more negative values) is observed, implying that the MIL 53-NH_2 is difficult to reduce compare to MIL 53.

5.12.3 Linear Sweep Voltammetry

To determine the OER performance of the fabricated photoanodes, Linear Sweep Voltammetry from 0.0 V to +1.4 V (vs Ag/AgCl) using a scan rate of 0.01 V/s under illumination and under darkness was carried out.

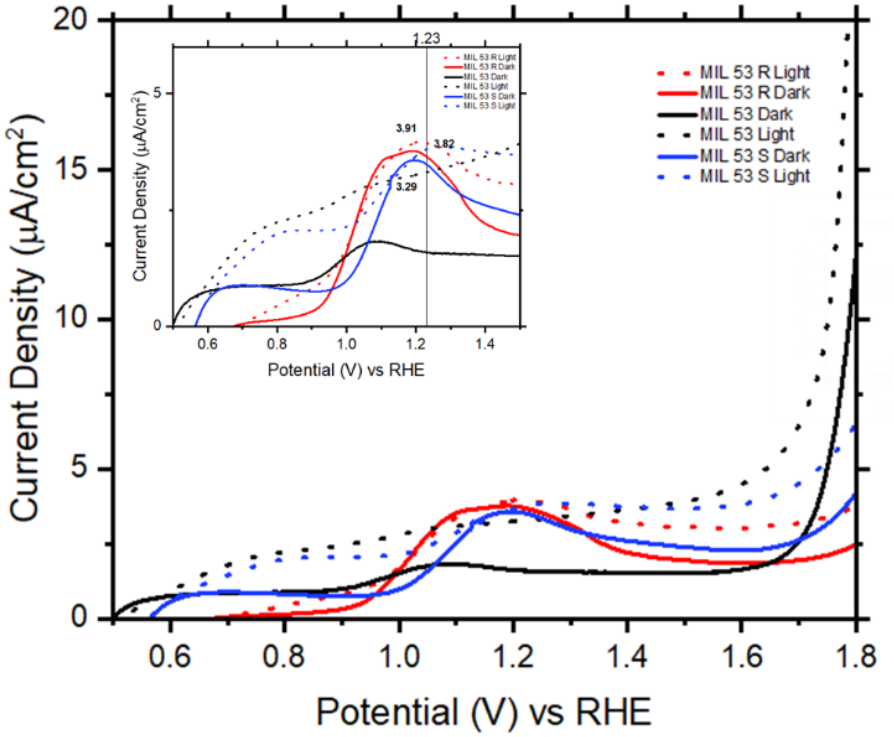

Figure 5.18: Comparison of MIL 53 (black line) and chiral MIL 53-R (red line) and MIL 53-S (blue line) OER Linear Sweep Voltametry in 0.1M Na_2SO_4 at 0.01V/s scan rate. Insert: Zoomed LSV at +1.23V

In the linear sweep voltammetry of MIL 53 and its chiral derivatives (**Figure 5.18**), the steep gradient as the potential was approaching +1.23V show that rigorous water splitting was taking place, especially in the chiral derivatives. To determine the performance of the photoelectrodes at +1.23V vs the RHE, current densities were noted. It was observed that under illumination, MIL 53 R produces highest current density of 3.91 μA/cm^2 against 3.82 μA/cm^2 for MIL 53 S while the achiral MIL 53 produced 3.29 μA/cm^2.

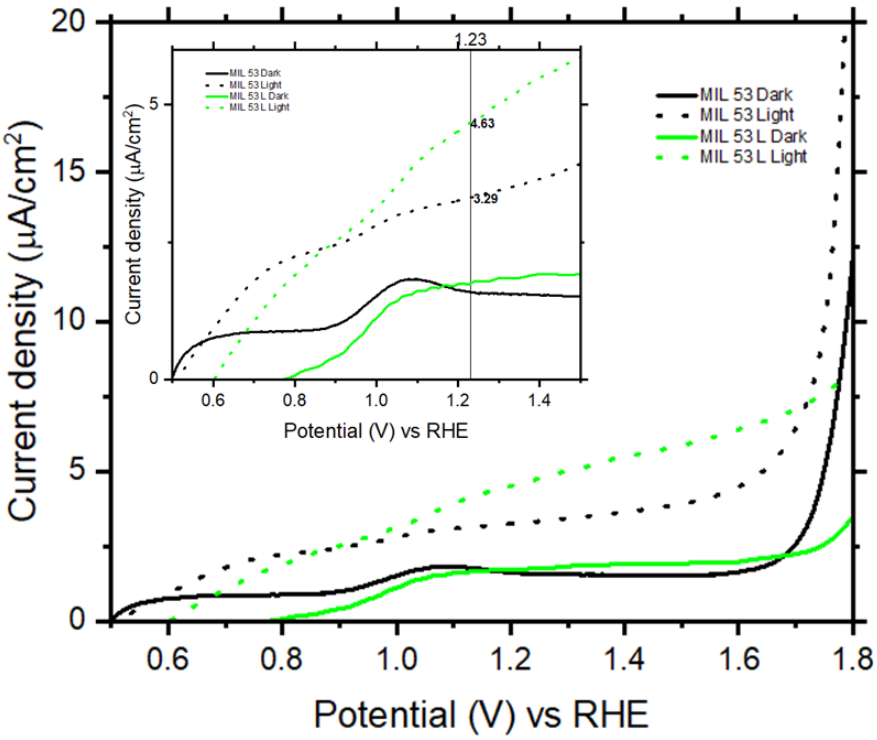

Figure 5.19 Chiral MIL 53 L Cysteine OER Linear Sweep Voltametry in 0.1M Na_2SO_4 at 0.01V/s scan rate

In the OER, linear sweep voltammetry curve of MIL 53 doped with L cysteine (**Figure 5.19**), under illumination shows a remarkable amount of photocurrent density of 4.63 μA/cm^2 at +1.23V. The current density exhibited by the MIL 53 L is the highest produced by the MIL 53 based photoelectrodes implying that MIL 53 doped with L cysteine has the best charge transfer properties

5.12.4 Chronoamperometry

Chronoamperometry at +1.0 V under illumination with light of intensity 100mW/cm^2 chopping light ON/OFF at 10s intervals was carried out for transient photocurrent density measurements for MIL 53 and its derivatives. From the curves shown in **Figure 5.20,** it can be noted that a swift and reproducible photocurrent densities are produced for all the photoelectrodes. On close inspection, it can be observed that in the transient curve the photocurrents slowly reduced to zero when the light source was off with, the bulk of the current decays occurring very rapidly as expected. However, there is a slowly decaying component, which is a very small fraction of the total, could come from various processes, such as slow collection of

trapped electrons or slow oxidation of water at some of the catalytic sites in the electrode film (Afzali et al., 2020). This slow component is observed with all samples.

A comparison of the chronoamperometry curves of MIL 53 R CSA and MIL 53 S CSA **(Figure 5.20 a)),** show that the photocurrent density increased from 5.5 µA/cm^2 produced by the parent MOF (MIL 53 shown in black line) to 9.0 and 8.0 µA/cm^2 for the MOFs doped with the R- (-), S- (+) camphor sulphonic acid respectively. The MIL 53 doped with L Cysteine produced a current density of 10.0 µA/cm^2, which is almost two-fold that produced by the achiral MIL 53. The above observations, supported by **Figure 5.20** show that the MIL 53 doped with L-cysteine has the best photocurrent density suggesting that it has better electron hole separation compared to the other chiral doped MOFs compared to the other chiral doped MOFs.

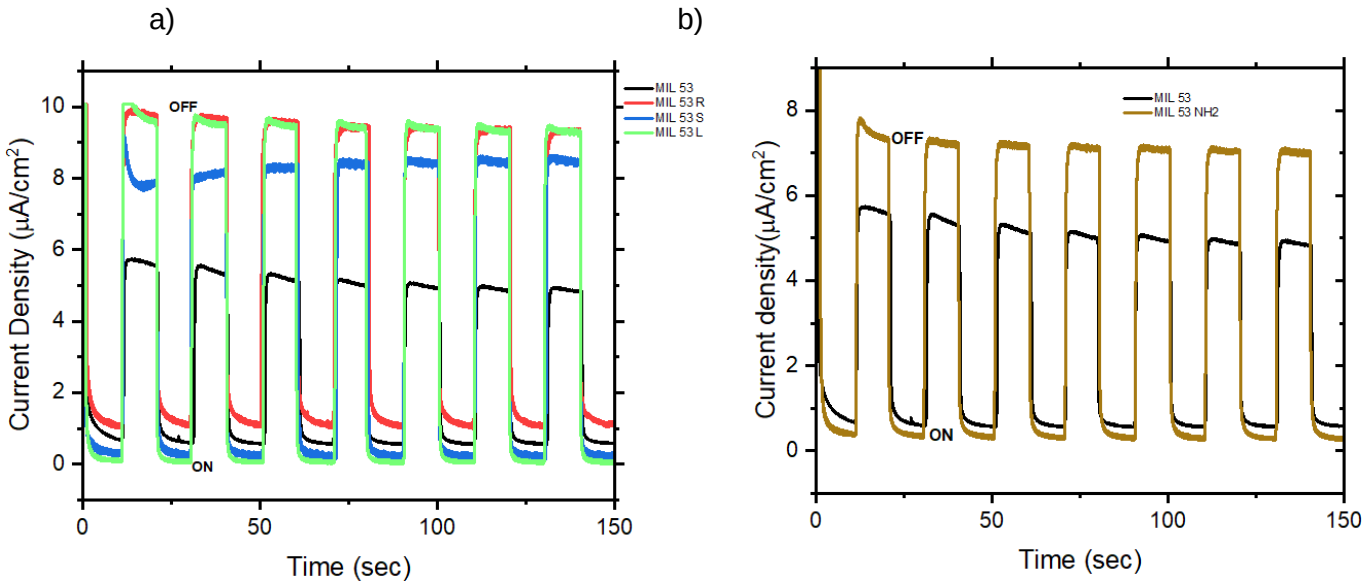

Figure 5.20:Chronoamperometry curves at +1.0 V for a) MIL 53 (black line), MIL 53 R CSA(red) and MIL 53 S(blue line) and MIL 53 L Cysteine (green line) b) MIL 53 and MIL 53-NH_2 under illumination with light of intensity 100mW/cm^2 chopping light ON/OFF at 10s intervals in 0.1M Na_2SO_4 at 0.01V/s scan rate

In comparison the MIL 53-NH_2 produced lower photocurrent densities than all the chiral MOFs, though its performance was better than the original MIL 53. From the above graphs, it can be concluded that the inclusion of the chiral motifs into the MOF framework greatly improves the photocurrent densities. This can be attributed to the spin filtering that takes place when electrons pass through a chiral molecule. The spin filtering has the ability to maximise the

triplet oxygen that is produced while minimising the formation of hydrogen peroxide (Zhang et al., 2018).

5.1.1.1 Comparison of self-assembly time

A comparison of the results obtained using photoelectrodes that had been different self-assembly times was also carried out **Figure 5.21,** was obtained.

a) b)

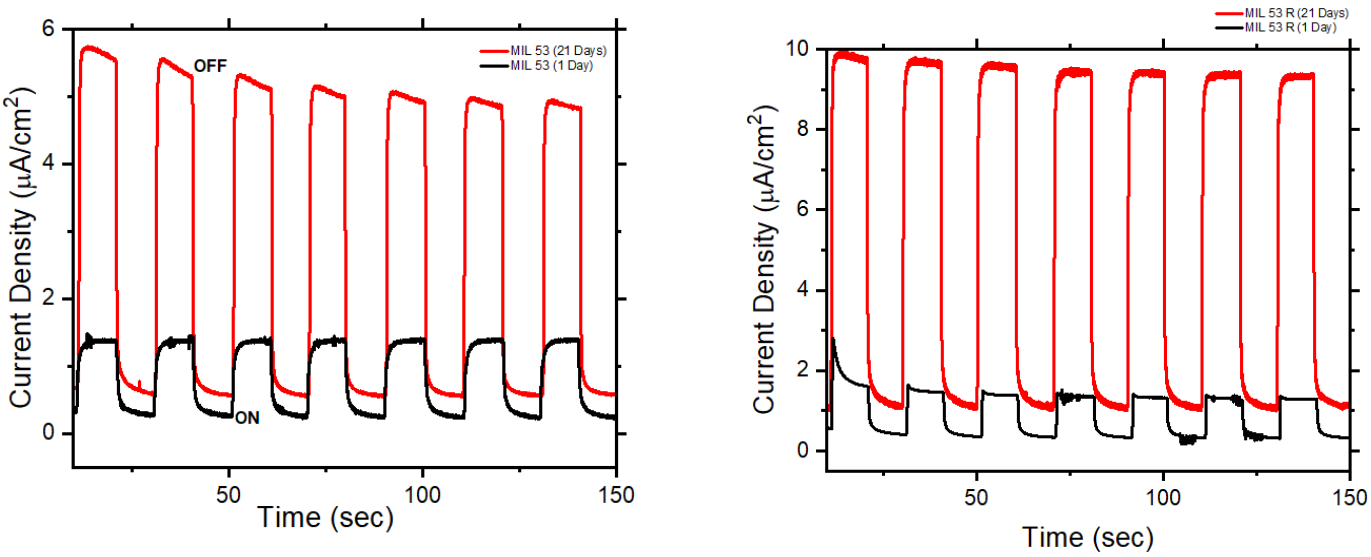

Figure 5.21: Comparison of chronoamperometry curves for (a) MIL 53 (b) MIL 53 R CSA in 0.1M Na_2SO_4 at 0.01V/s scan rate for different incubation times.

From **Figure 5.21**, it is observed that the photocurrents produced increased fourfold, when the period allowed for self-assembly was increased from 1 day to 21 days, therefore the period allowed for self-assembly affects the performance of the photoelectrodes. The increased incubation time, ensured that the self-assembly reaction reached completion compared to when the incubation period was shorter.

5.12.5 Photoelectrode Stability

To evaluate practical utility of the photoelectrochemical catalysts, the stability is a key factor. Different electrochemical techniques such as chronoamperometry and cyclic voltammetry and linear sweel voltammetry can be used to evaluate the reusability of the photoelectrodes. For the MIL 53 based photoelectrodes, Linear Sweep Voltammetry from 0.0 V to +1.4 V (vs Ag/AgCl) using a scan rate of 0.01 V/s was used to evaluate their stability.

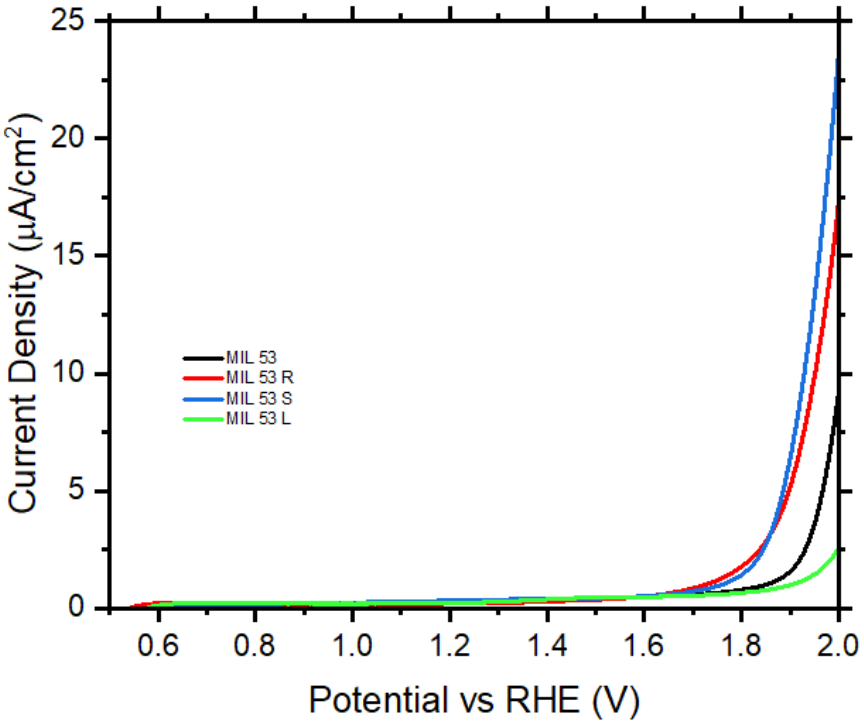

Figure 5.22: LSV curves for the MIL 53 based photoelectrodes in 0.1M Na_2SO_4 at 0.01V/s scan rate

The stability measurements were carried out after approximately 100 cycles of continuous use. The results produced (**Figure 5.22**) show that the peaks observed at +1.23V had somewhat disappeared showing that the reactivity of the species adsorbed on the FTO surface had reduced, however clear onset potentials are clearly visible showing the reusability of the photoelectrodes over extended periods.

5.12.6 Electrochemical Impedance Spectroscopy

5.12.6.1 Mott Schottky

The electronic properties of the fabricated photoelectrodes were characterized using Mott-Schottky measurements. The flat band potential of each modified electrode was determined by fitting the lower linear part of the data to **Equation 5.3**.

$$\frac{1}{C^2} = \frac{2}{\varepsilon\varepsilon_o q N_D}\left(E - V_{bi} - \frac{kT}{q}\right) \qquad \text{Equation 5.3}$$

where C is the capacitance, N_D is the net doping density, which can be calculated from the gradient, E is the applied potential, and V_{bi} is the flat band potential. The flat band potential is

the potential at which there is inversion between cathodic and anodic photocurrents and this occurs when band bending occurs (Hankin et al., 2019) and it occurs when the surface potential is equal to zero. The flat band potential was obtained as an intercept to the horizontal axis as shown in **Figure 5.23**.

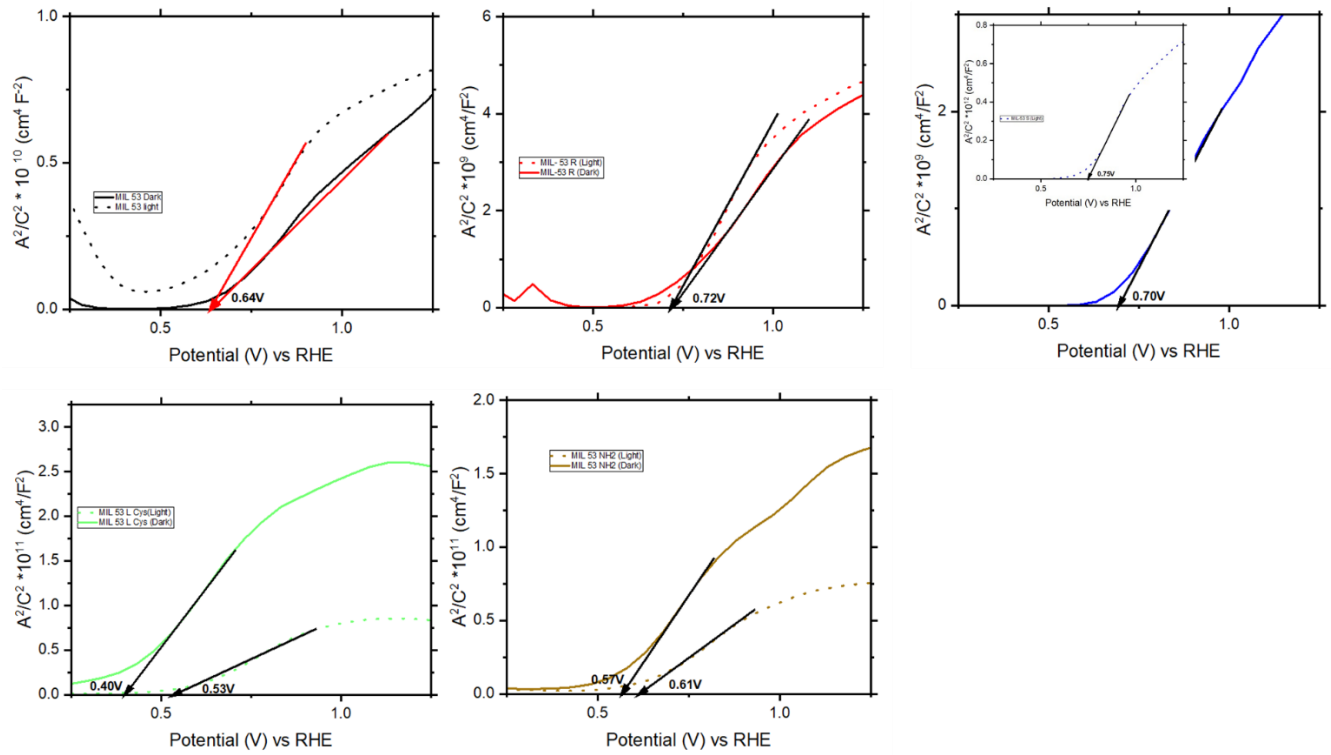

Figure 5.23: Mott Schottky plots for MIL 53 and chiral doped MIL 53 derivatives in 0.1M Na_2SO_4

The flat band potentials obtained for each photoelectrode for measurements carried out under darkness and under illumination are summarized in **Table 5.5**.

Table 5.5: Flat band potentials for MIL 53 based chiral photoelectrodes

Photoelectrode	Vb dark (V)	Vb illumination (V)
MIL 53	0.64	0.64
MIL 53 R CSA	0.72	0.72
MIL 53 S CSA	0.70	0.75
MIL 53 L Cysteine	0.40	0.53
MIL 53 NH_2	0.57	0.61

The flat band potentials versus the RHE are almost similar in most cases, both under darkness and under illumination for the same electrode. This indicates that the electronic properties of the TiO_2 are not affected by molecular modification for each type of molecules used (Mtangi et al., 2017).

In the Mott Schottky plot for MIL 53 doped with S camphor Sulphonic Acid, it is interesting to note that there was a remarkable difference in the capacitance produced, to the extent that the plots could not be drawn on the same axis. The capacitance produced under light was relatively large when compared to that produced under darkness. A similar observation was noted in Chapter 4 for the Zn MOF doped with S camphor sulphonic acid, however then it was noted that under darkness that is when the large capacitance was observed. In order to understand this phenomenon, a systematic review was carried out and was observed that camphor sulphonic acid in its achiral form has often been used in the fabrication of supercapacitors (Awata et al., 2020). Supercapacitors are electrochemical energy storage devices that work by adsorbing ions from the electrolyte onto their surface area.

The slope of a Mott Schottky plot shows the nature of the photocatalyst, , a positive gradient alludes to the n-type nature of a semiconductor, while a negative gradient is indicative of a p-type semiconductor (Kusmierek, 2020). All the plots in **Figure 5.23**, have positive gradients, therefore it can be concluded that the synthesised MIL 53 and its derivatives are n-type semiconductors/photocatalysts.

5.12.6.2 Nyquist Plots

In order to evaluate the charge transfer kinetics, Nyquist plots were used. The Nyquist measurements were carried out by varying frequency between 1MHz and 0.1Hz, with an initial potential of 0V and an amplitude of 5mV. Measurements were carried out under darkness and under illumination to assess the light sensitivity of the photoelectrodes.

a) b)

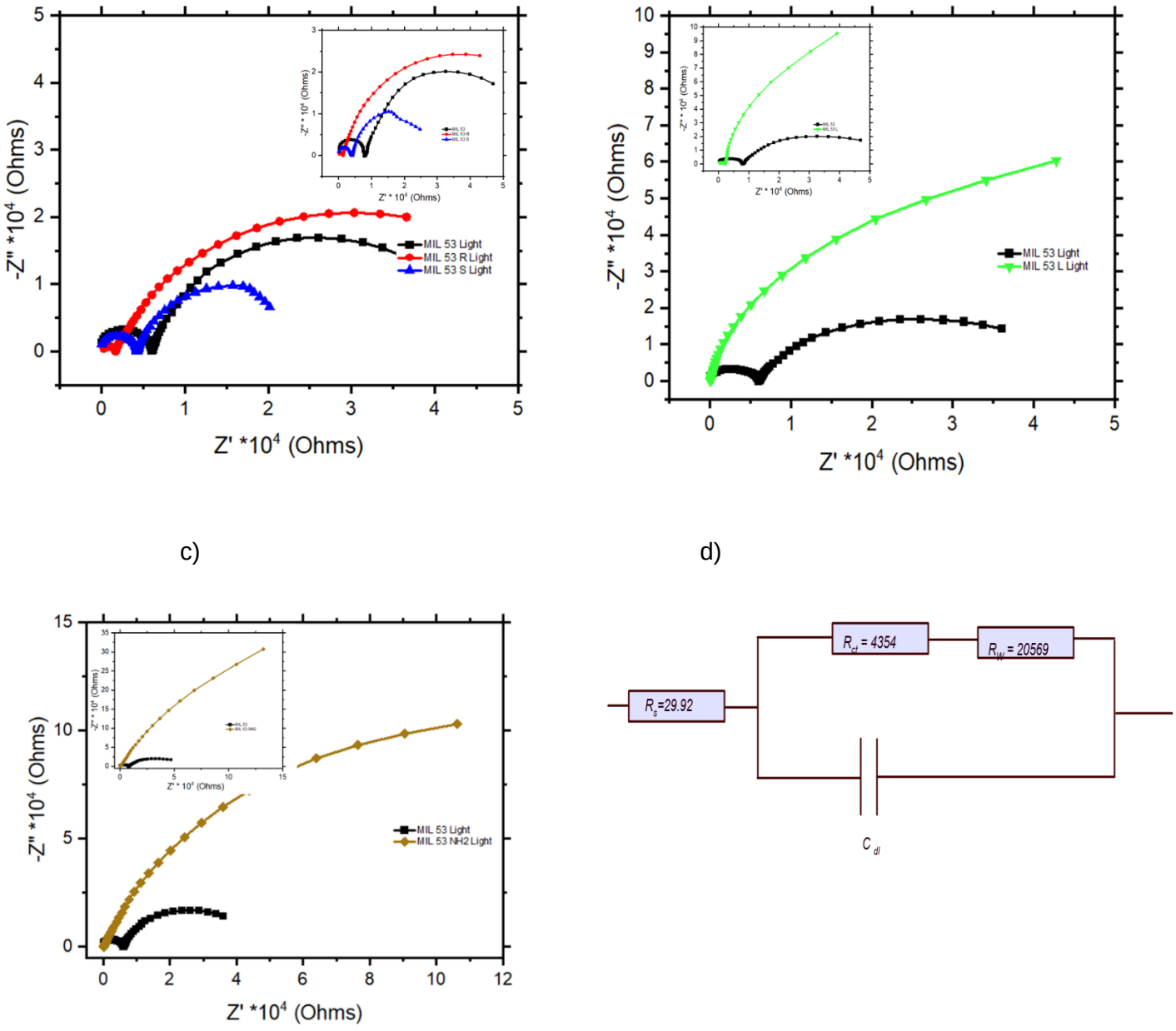

c) d)

Figure 5.24: Nyquist plots for MIL 53 and its chiral derivatives a) MIL 53 vs MIL 53 R-CSA (red curves) vs MIL 53 S-CSA (blue curve) b) MIL 53 vs MIL 53 L Cysteine (green curve) c) MIL 53 vs MIL 53-NH_2 (brown curve) d) Equivalent circuit for MIL 53 S-CSA

Nyquist plots are used to reveal the charge transfer kinetics in the photocatalysts. As shown in **Figure 5.24**, a small semicircle is observed in the high frequency regions for the chiral photoelectrodes (MIL 53 R-CSA, MIL 53 S-CSA and MIL 53 L Cysteine) and this shows the contribution from the space-charge layer of TiO_2, while the large semi-circle is due to the contribution of the MOF photocatalysts (Digdaya et al., 2016) . From the observation in **Figure 5.24** it can be concluded that in the camphor sulphonic acid doped MOFs, the stabilising effect of the TiO_2 layer is felt. When comparing the measurements carried out under darkness and under illumination, the Nyquist plots for measurements under illumination have smaller semicircle diameters, indicating faster charge transfer kinetics under illumination than under darkness (Feng et al., 2023). The equivalent circuit was fitted for MIL 53 S-CSA, the values of the R_s (electrolyte resistance), R_{ct} (charge transfer resistance) and Warburg resistance were obtained from the Nyquist plot for MIL 53 S-CSA.

5.12.6.3 Bode Plots

To further investigate the electronic properties of the photoelectrodes, Bode plots were used. The measurements were carried out by varying frequency between 1MHz and 0.1Hz, with an initial potential of 0V and an amplitude of 5mV and a graph of Log frequency vs negative phase angle was plotted as shown in **Figure 5.25.**

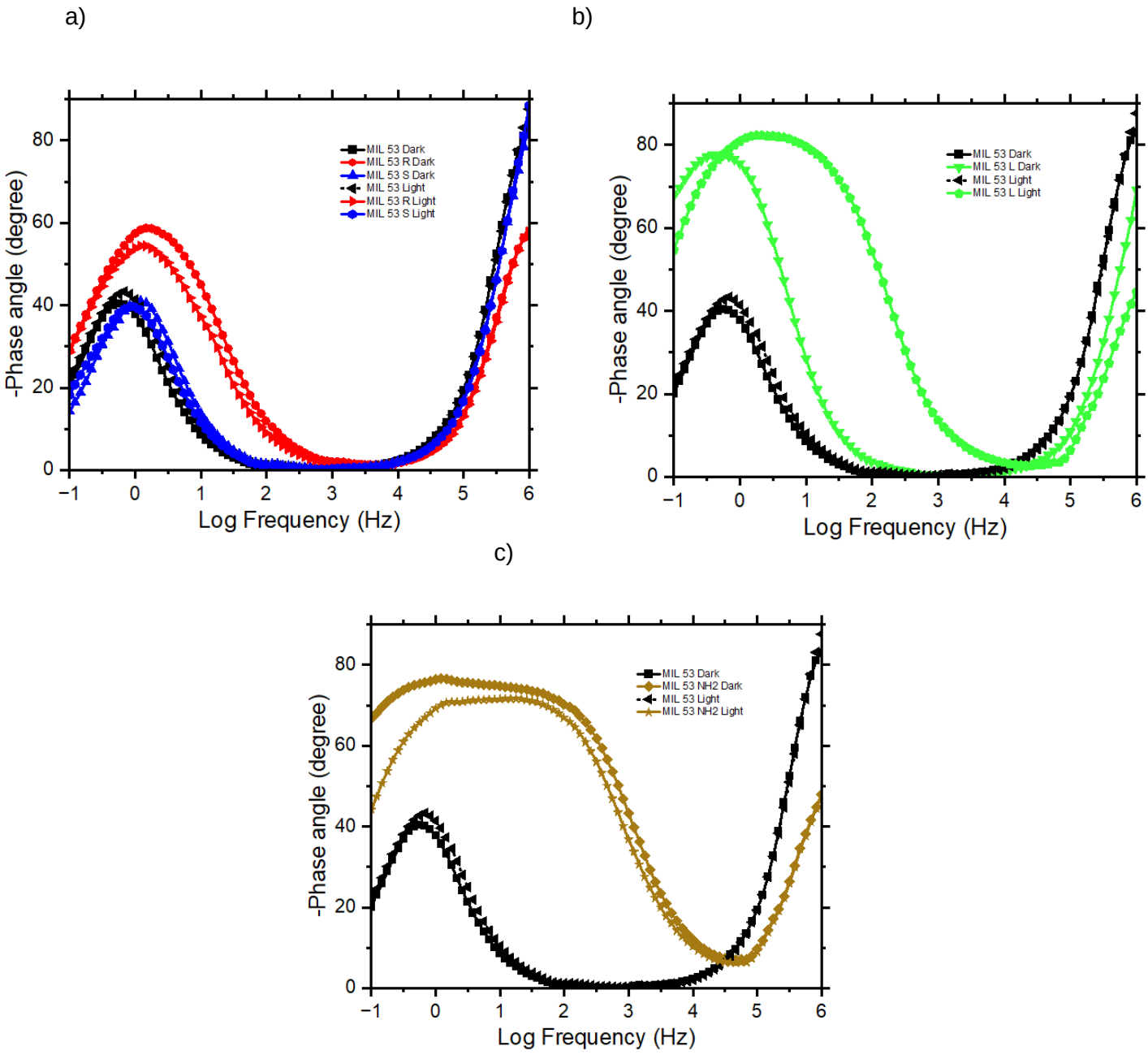

Figure 5.25: Bode Plots of the MIL 53 based photoelectrodes a) MIL 53 vs MIL 53 RCSA (red curves) vs MIL 53 S CSA (blue curve) b) MIL 53 vs MIL 53 L Cysteine (green curve) c) MIL 53 vs MIL 53 (brown curve)

The Bode Plots showed that the photoelectrode/electrolyte system produces phase angles below -90°, which is showing non-ideal capacitive behaviour (Digdaya et al., 2016). In comparison with the pristine MIL 53, there is shift towards the higher frequencies and this can be attributed to charge transfer processes in electrode/electrolyte boundaries (Toledo et al., 2017; Wierzbicka et al., 2024) whereas the pristine MIL 53 is undergoing diffusion-controlled processes.

5.12.7 Activity of the photoelectrodes

The activity of the fabricated photoelectrodes was characterized by measuring the open circuit potential, OCP in the dark and under illumination at zero current. All the electrodes gave OCP curves (**Figure 5.26**), meaning that an equilibrium was reached between the electrolyte and the electrodes. During water splitting, when the semiconductor comes into contact with the electrolyte, the Fermi level of the semiconductor is adjusted to the Fermi level of the electrolyte.

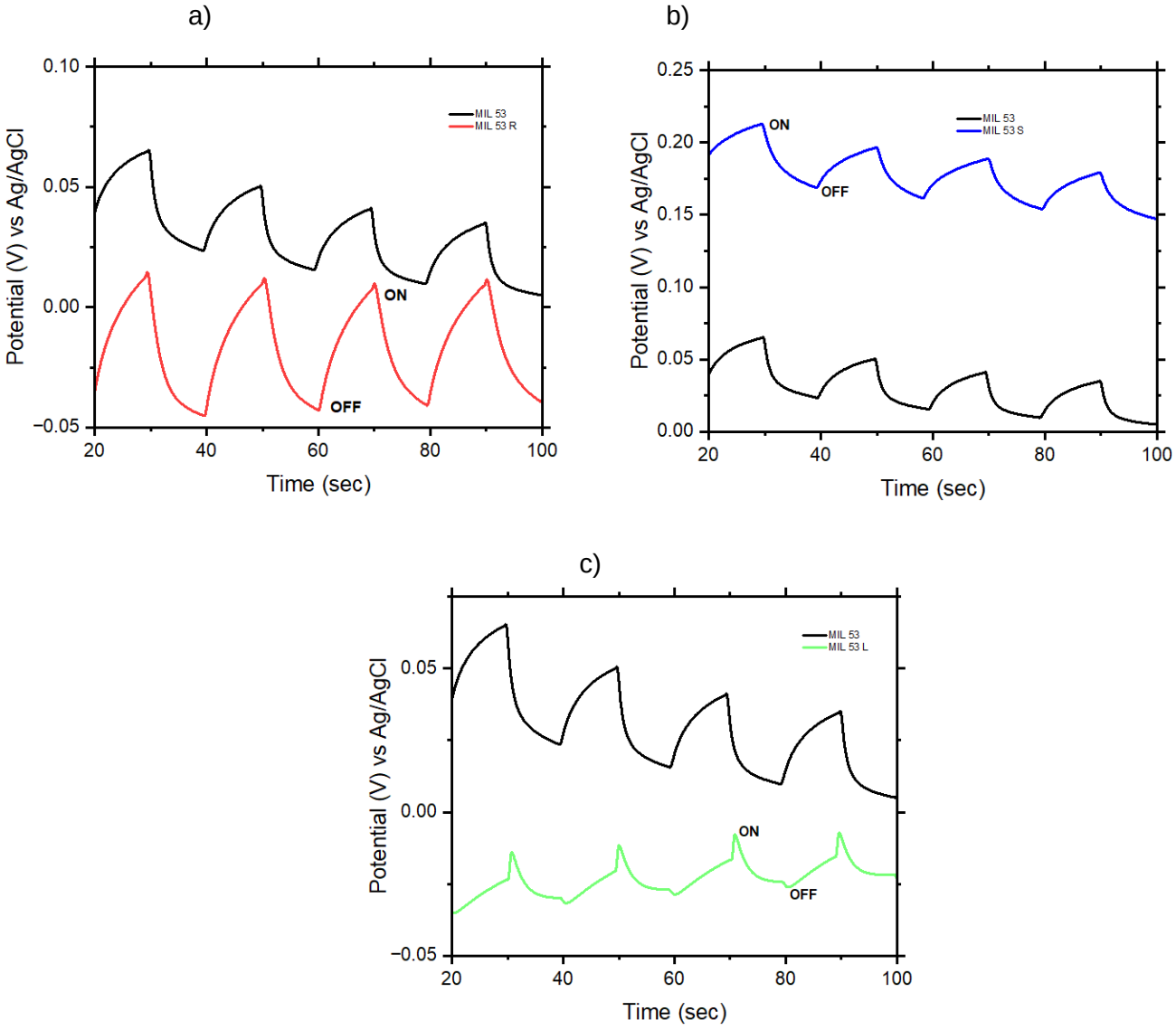

Figure 5.26: OCP Curves for a) MIL 53 vs MIL 53 R CSA b) MIL 53 vs MIL 53 S CSA c) MIL 53 vs MIL 53 L in 0.1M Na_2SO_4 at 0.01V/s scan rate.

From the Mott-Schottky measurements in section 5.12.6 all the MOFs were concluded to be n-type semiconductors because of the positive slope of the Mott Schottky plots. For n-type

semiconductors, the Fermi level is close to its conduction band minimum (CBM) and higher than the electrochemical potential of the electrolyte. Thus, the majority carrier of electrons will flow from the semiconductor to the electrolyte after contact until the Fermi level of the semiconductor and the electrochemical potential of the electrolyte are aligned (Ma & Wang, 2017). In n-type semiconductors, the OCP without illumination is predominantly less negative which becomes more negative when illuminated. The difference in potential upon illumination is an indication of the extent of the photoactivity of the electrode

5.12.8 Overpotential

The overpotential was determined by carrying out a Tafel analysis from -1.5V to +1.5V at a scan rate of 0.01V/s. Tafel plots are also used to understand the reaction kinetics as well as the OER mechanism. Tafel plots are also used to compare the catalytic properties of various photocatalysts that may be under study (Aralekallu et al., 2020)

The Tafel plots from the analysis are given in **Figure 5.27**. Overpotential is defined as the difference between the equilibrium potential for a given reaction and the potential at which the catalyst operates at a specific current under specific conditions (Appel & Helm, 2014).

As shown in section 2.6.1.1, results from theoretical and experimental studies have demonstrated the dependence of the overpotential on the magnetic properties of the anode material.

a) b)

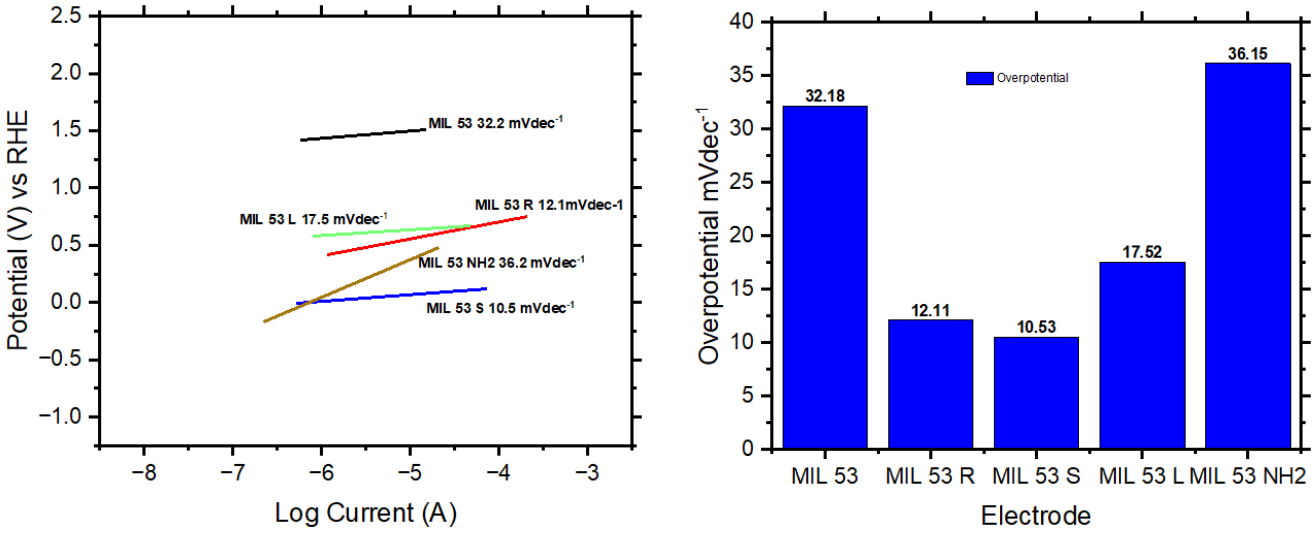

Figure 5.27: a) Tafel plot of MIL 53 derivatives showing overpotential in $mVdec^{-1}$ b) Comparison of the overpotentials exhibited by MIL 53 and its derivatives.

In **Figure 5.27**, the overpotential values recorded are remarkably low and this can be attributed to the ferromagnetic nature of the MIL 53 as it possesses an iron metal centre, Further reduction of the overpotential is also observed int the chiral MOFs indicating that chiral motifs are also responsible for the reduction of overpotential. When the overpotential is reduced, then the additional energy needed for the reaction to take place has been reduced, meaning that the OER reaction can now occur easily.

5.12.9 Hydrogen Peroxide Quantification

To evaluate the ability of the chiral photoelectrodes in the reduction of hydrogen peroxide formation, electrochemistry using the chronoamperometry mode was performed with a 0.1 M Na_2SO_4 aqueous solution as the electrolyte and an Ag/AgCl (saturated KCl) reference electrode. A potential (+1.23V versus the Ag/AgCl) was chosen and applied to the bare TiO_2 electrode so that hydrogen and oxygen were evolved on the Platinum wire (counter electrode) and the fabricated photoelectrodes (working electrodes), respectively. Bubbles were observed on both the Platinum wire and the photoelectrode (TiO_2/MOF electrode) during the electrochemical measurements. Chronoamperometry measurements were conducted for 40 minutes. The presence of hydrogen peroxide was confirmed using a colorimetric test titration experiment of the used electrolyte, with o-tolidine as a redox indicator. In the colorimetric measurements, 2.0 mL of an o-tolidine solution prepared according to the Ellms-Hauser method (Ellms A X & Hauser, 1913) were added to 10 mL of the electrolyte solution obtained from the photoelectrochemical cell and left to react for 40 minutes. The sample was then

analyzed using a Uv-vis spectrophotometer, to determine the presence of hydrogen peroxide and the spectra given in **Figure 5.28** were obtained.

For the MIL 53, there was the MIL 53, MIL 53 doped with R-Camphor Sulphonic Acid, S-Camphor Sulphonic Acid, Camphor Sulphonic Acid, L Cysteine and amine functionalized MIL 53 -NH_2.

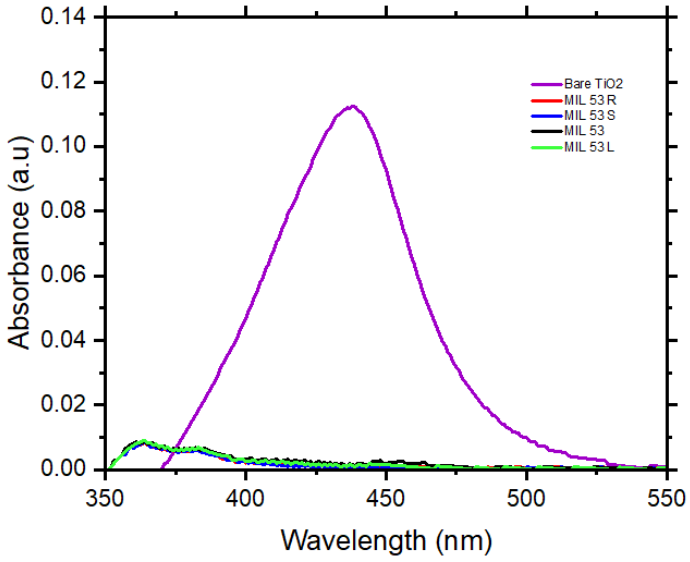

Figure 5.28: Uv-vis spectra from titration of electrolyte used with the respective electrodes.

From **Figure 5.28** it can be noticed that the electrolyte obtained from the photoelectrochemical cell that used chiral photoelectrodes (MIL 53 R CSA, MIL 53 S CSA and MIL 53 L) have no hydrogen peroxide formed, whereas the electrolyte from the photoelectrochemical cell containing the achiral photoelectrodes produced a peak at 436nm. Due to the oxidative reaction between the o-tolidine and the H_2O_2 present in the achiral electrolyte (Zhang et al., 2018), when o-tolidine is added to the electrolyte from achiral photoelectrodes, a yellow colour is formed. In the case of MIL 53, a weak peak is observed at 436nm was observed this is because the MIL 53 is iron based and has assumed ferromagnetic properties in which the CISS effect states that spin filtering is also observed in ferromagnetic materials. The amount of hydrogen peroxide present was quantified using the calibration curve given in chapter 4, Appendix C and the amounts of H_2O_2 present are as shown in **Table 5.6**.

Table 5.6: Quantity of hydrogen peroxide present in electrolyte from Zn-MOF based electrodes

Electrode	Absorbance at 436 nm	Hydrogen Peroxide(M)
Bare TiO_2	0.1215	0.242
MIL 53	-	-
MIL 53-R	-	-
MIL 53-S	-	-
MIL 53 L	-	-

5.12.10 Hydrogen collection

To measure the hydrogen produced, a modified Hoffman apparatus was fabricated. Hydrogen produced was quantified by running chronoamperometry at +1.23V for 90 minutes in the modified Hoffman apparatus which was made airtight to ensure accuracy of the measurements. The hydrogen was collected for MIL 53 R and the volume obtained after 90 minutes as shown in **Figure 5.29**.

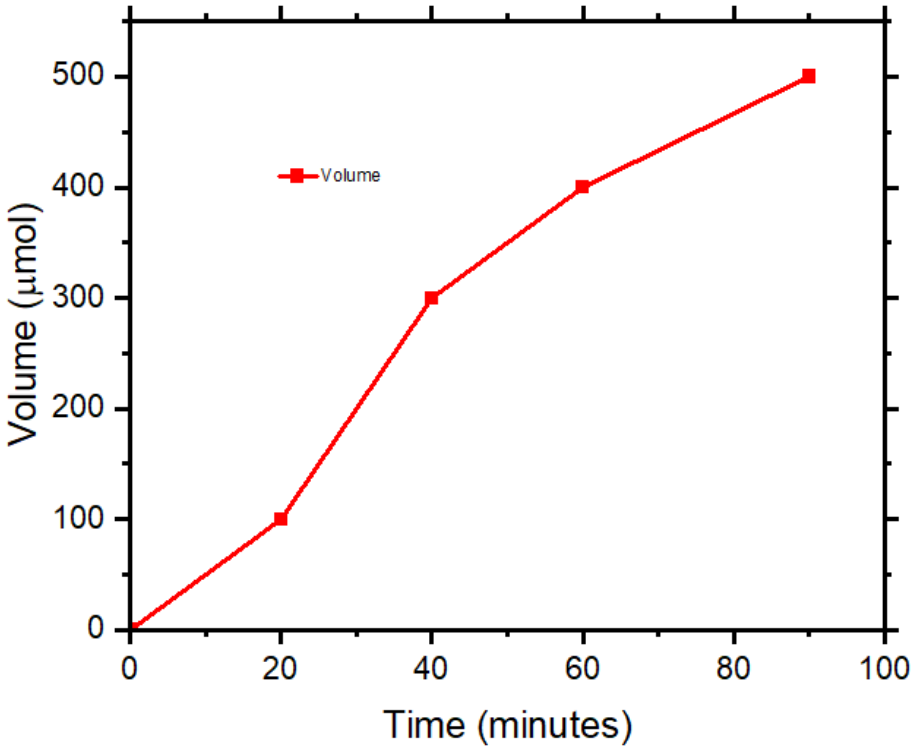

Figure 5.29: Amount of hydrogen produced after 90 minutes by MIL 53 R CSA

5.13 COMPARISON OF THE PERFORMANCE OF THE METAL COORDINATING CENTRES

5.13.1 Photocatalytic Activity

A comparison of the metal centres was also done, where the Uv-Vis spectra for MIL 53 R CSA was compared to that of Zn-MOF R-CSA. The same was done for the S-CSA derivatives of both MOFs.

a) b)

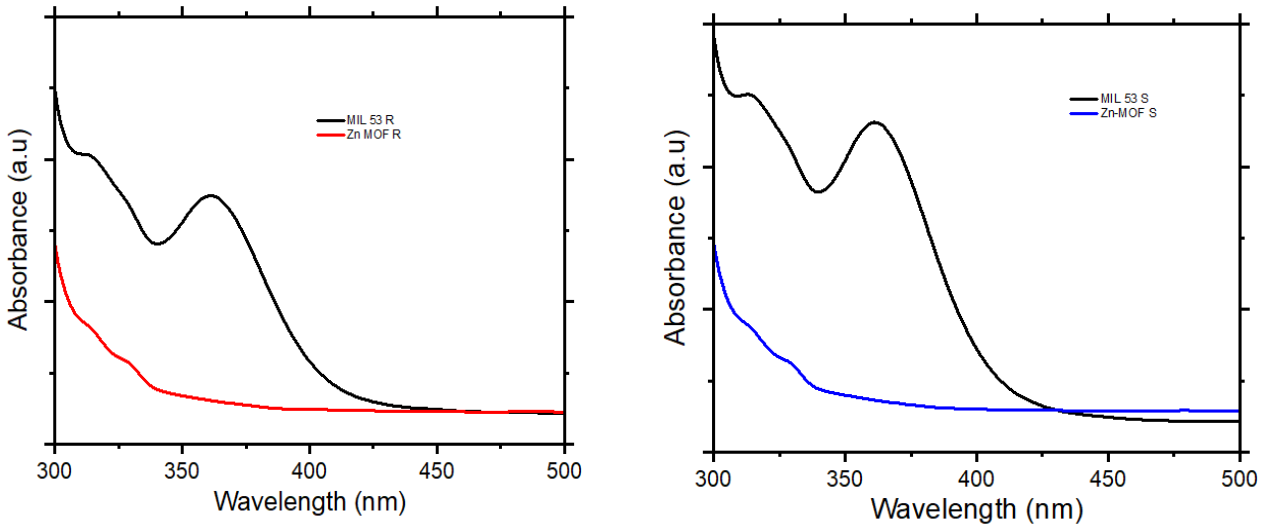

Figure 5.30 : Uv-Vis absorption spectra for a) MIL 53 R CSA vs Zn-MOF R CSA b) MIL 53 S CSA vs Zn-MOF S CSA

From **Figures 5.30a) and 5.30b)**, it can be noticed that the MIL 53 chiral derivatives had higher absorbances in the visible range compared to their Zn-MOF counterparts. This observation can be attributed to the fact that iron, a transition metal has a partially filled 3d orbital which makes it possible for pi-pi transitions. The presence of the partially filled 3d orbital in the iron is also responsible for the colour exhibited by the iron compounds, while zinc compounds are mostly white. The colour exhibited by the iron compounds is responsible for their photocatalytic activity in the visible range of the spectrum. Iron also has multiple oxidation states, compared to zinc which only has one oxidation state. These observations will also play a great role in explaining the water splitting properties of the respective metals.

5.13.2 Chronoamperometry

The results obtained from chronoamperometry of photoelectrodes incubated over 21 days were compared. The current densities obtained by the two MOFs in their chiral derivatives was carried out and **Figure 5.31,** was obtained.

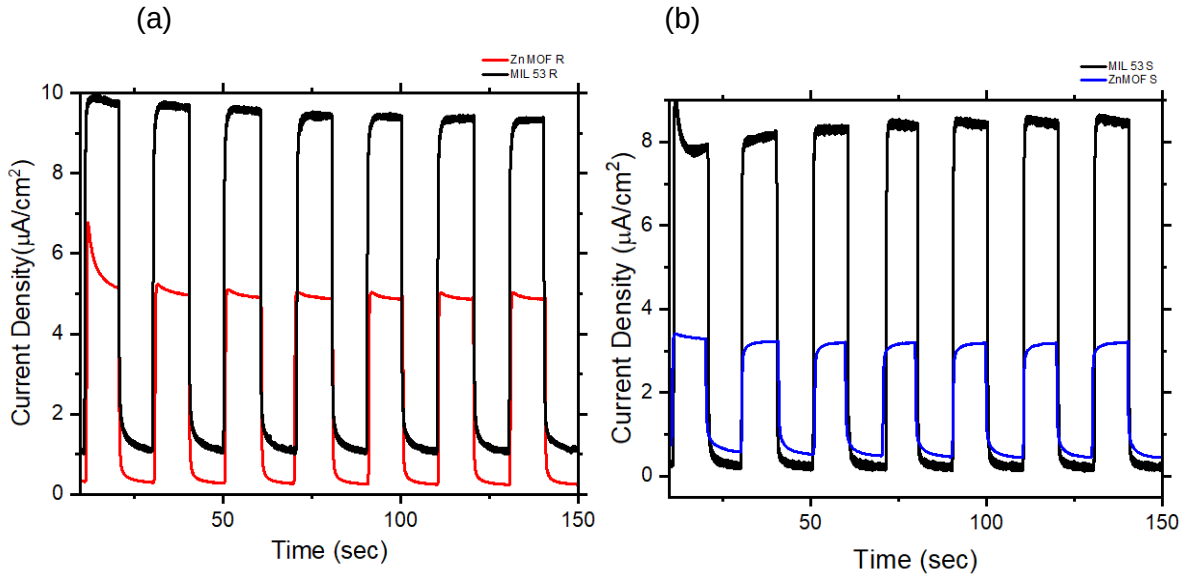

Figure 5.31: Comparison of (a) MIL 53 R-CSA and Zn MOF R-CSA (b) MIL 53 S-CSA and Zn MOF S-CSA in 0.1M Na_2SO_4 at 0.01V/s scan rate

The results above suggest that MIL 53 with an iron centre produces more photocurrents compared to the Zn(bdc)(bpcda) with a zinc metal centre. The iron metal is better in separating the electron hole pairs longer than the zinc-based MOF. This may be attributed to ferromagnetic nature of Iron. According to the CISS effect an electron passing through a chiral molecule, or a ferromagnetic material becomes spin polarized (Naaman & Waldeck, 2012) that is when electrons passing through a magnetic material, they become spin filtered with electrons spinning in one direction only transmitted. This allows for the formation triplet oxygen and minimises formation of a by-product (hydrogen peroxide) (K. B. Ghosh et al., 2019; S. Ghosh et al., 2020; Zhang et al., 2018, 2020). With the preferential production of triplet oxygen, the production of hydrogen is favoured and this results in the large current densities exhibited by the iron based photoelectrodes.

The crystalline nature of the photocatalyst used in fabricating the photoelectrodes greatly affects how they perform. When the photocatalyst is crystalline in nature, enhanced charge separation is achieved as the electrons and holes can move freely without being trapped or combined (Nishioka et al., 2023; Takanabe, 2017). When comparing the crystallinity of the iron and zinc-based MOFs, it was observed that the iron-based MOFs are more crystalline

hence the larger current densities in the MIL 53 can be attributed to the enhanced charge separation that is present in the crystalline Iron based MOFs.

5.13.3 Overpotential

A graph comparing the overpotential for MIL 53 and Zn-MOF was also plotted and the results are shown in **Figure 5.32**. From the plot it can be observed that MIL 53 and MIL 53 based photoelectrodes have lower overpotentials compared to Zn-MOF and Zn-MOF based photoelectrodes.

The reduction in overpotential in the iron-based electrodes, can be attributed to the ferromagnetic properties of the Iron centre in the MIL 53. From section 2.2.6.1, it has noted that the overpotential of a material is greatly influenced by its ferromagnetic properties (Torun et al., 2013).

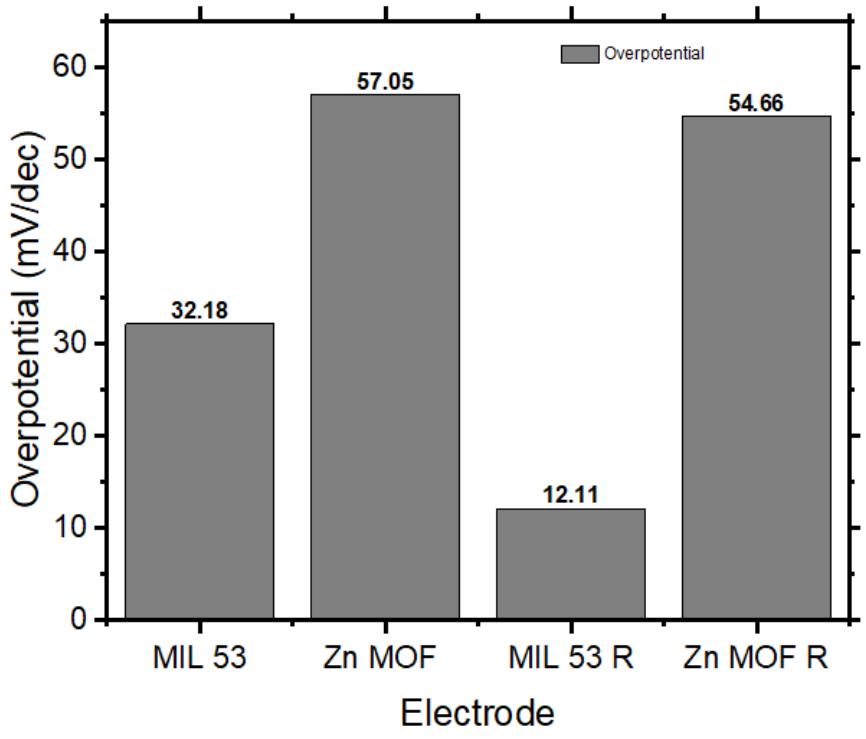

Figure 5.32: Comparison of overpotential values

The observations made by Heard and Lennox also support this position where it was noted that electrodes made from traditionally ferromagnetic material such Iron, Nickel, Cobalt and Stainless Steel exhibited lower overpotentials of 0.41V, 0.61V, 0.39V and 0.28V, respectively,

compared to 1.11V, 0.80V and 1.5 V exhibited by Platinum, Lead and Boron Doped Diamond, respectively (Heard & Lennox, 2020). The ability of ferromagnetic based photoelectrodes to produce lower overpotentials can also be attributed to the CISS effect. In the CISS effect, the electrons become spin polarised as they are transmitted through the material (Naaman & Waldeck, 2012).

5.13.4 Charge transfer kinetics

A comparison of the charge transfer kinetics between MIL 53 and Zn-MOF (**Figure 5.33 a)**) and MIL 53 S CSA vs Zn-MOF S CSA (**Figure 5.33 b)**) under darkness and under illumination was carried out. In the comparison of the pristine MOFs, MIL 53 under both darkness and illumination exhibits smaller semicircle diameters in both the high and low frequency regions when compared to the Zn-MOF, implying the charge transfer kinetics are higher in the MIL 53 than in the Zn-MOF (Feng et al., 2023).

a) b)

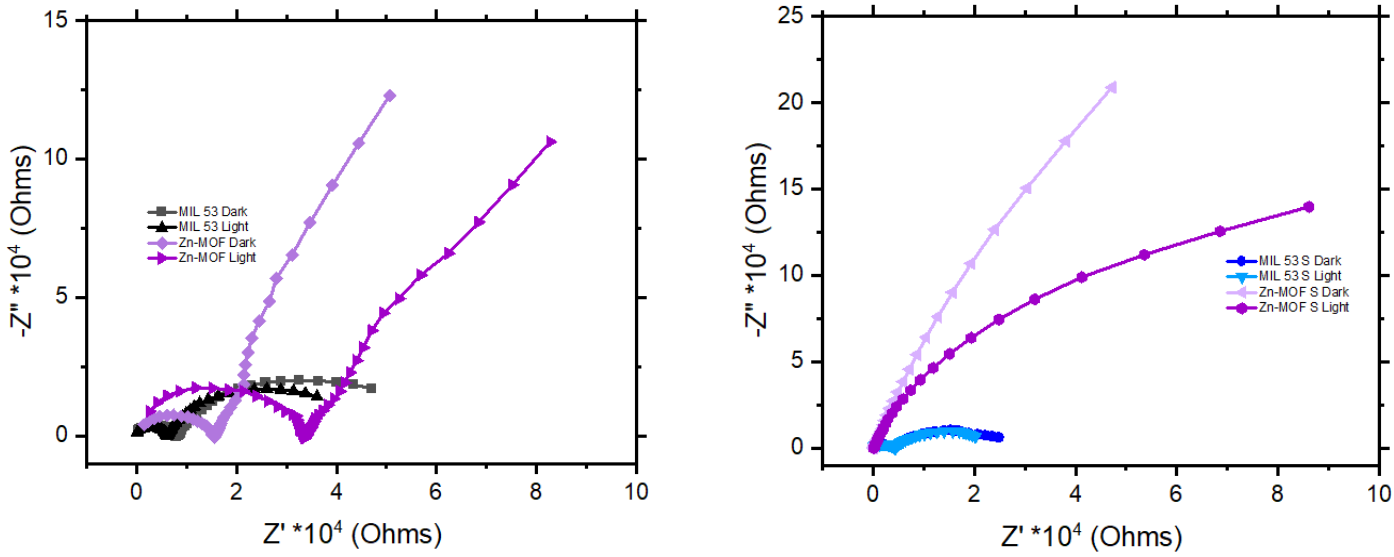

Figure 5.33 :a) Nyquist plots for comparing MIL 53 vs Zn-MOF under darkness and under illumination b) Nyquist plots for comparing MIL 53 S CSA vs Zn-MOF S CSA under darkness and under illumination

In the comparison of the S CSA doped MIL 53 and Zn-MOF under darkness and under illumination, the Zn-MOF S CSA does not show the two semicircle curves as shown by the MIL 53 S CSA. The Zn-MOF S CSA curve is one large semicircle, which is relatively larger

than that of the MIL 53 S CSA implying that the charge transfer kinetics are slower in the zinc-based MOF (Feng et al., 2023).

5.14 WATER SPLITTING MECHANISM

The use of chiral iron-based metal organic frameworks has further proven the concept of the CISS effect where the electrons passing through a chiral molecule are spin polarised on a triplet surface to form triplet oxygen and because the formation of hydrogen peroxide is spin forbidden, it is not formed (Zhang et al., 2018). The observed photocurrents for MIL 53 and its derivatives are remarkably larger than those exhibited by Zn MOF and its derivatives under the same conditions. This observation is also in agreement with the CISS effect which also states that spin filtering is also observed when electrons are transmitted through a ferromagnetic material (Naaman et al., 2020).

When the chiral photoelectrode is irradiated with sufficient energy, electrons are emitted onto the surface, as we have earlier determined that all the photoelectrodes in the study are n-type, therefore they emit electrons when irradiated with the proper energy. The emitted electrons are spin polarised by the chiral MOF layer before being transmitted to the counter electrode as illustrated in **Figure 5.34**.

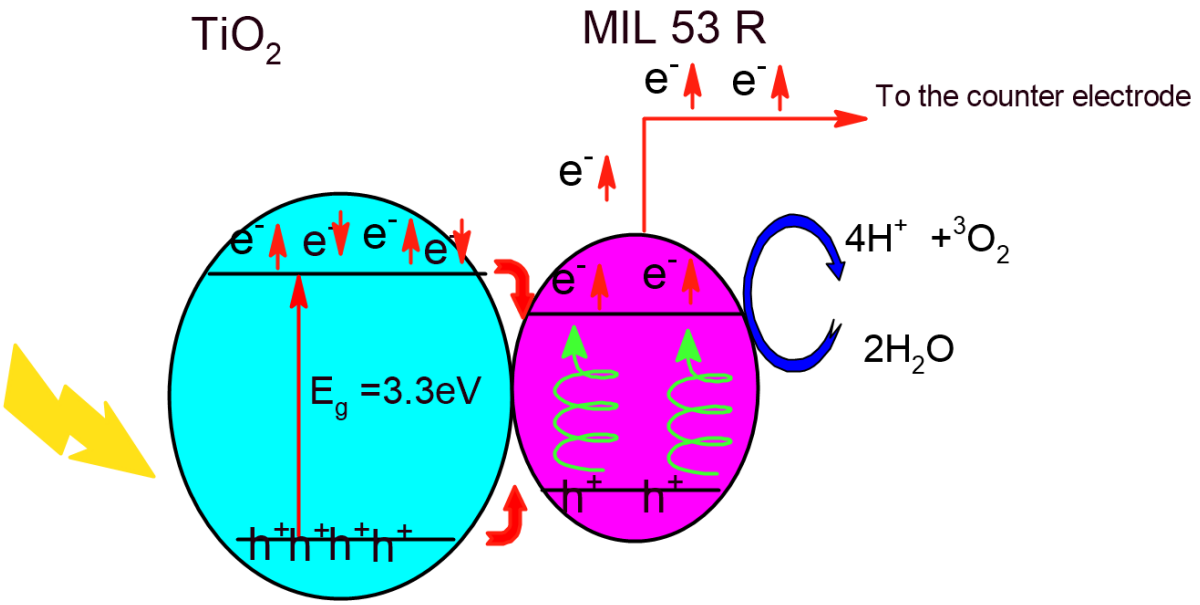

Figure 5.34: MIL 53 R CSA energy diagram

Only electrons spinning in one direction are transmitted to the platinum counter electrode where the protons are reduced to give Hydrogen gas. From OCP measurements as well as the Mott-Schottky, it was determined that the chiral doped MIL 53 photoelectrodes are n-type in nature, the same as the Zn-MOF based photoelectrodes discussed in chapter 4. Based on this observation, the OER evolution mechanism proposed in section 4.20 in which a four-electron system is employed also applies to the photoelectrochemical water splitting using chiral doped MIL 53 photoelectrodes.

5.15 CONCLUSION

Chiral Iron based MOFs of the MIL 53 category were successfully synthesised and characterized. In PXRD, they exhibited high crystallinity while exhibiting excellent light absorption properties in the visible range. Thermal stability of the MOF was confirmed via TGA, while surface morphology was confirmed by SEM and FESEM. EDS confirmed the incorporation of the chiral molecules into the MOF framework. In water splitting measurements, the chiral doped variants of MIL 53 produced greater current densities compared to the achiral MOF and this can be attributed to the spin filtering that takes in the chiral photosystem which allows only electrons that are spinning in one direction to go through. Tafel plots indicated a significant reduction in overpotential in the chiral doped MOFs. Significant reduction of hydrogen peroxide was noticed when the spectrophotometric titration was carried out. The interesting behaviour exhibited by MOFs doped by S (+) Camphor Sulphonic Acid in Mott Schottky measurements open up other research pathways in energy storage using chiral MOFs. A comparison between the electrochemical behaviour of Zn-MOF and its derivatives and the MIL 53 and its derivatives, show that MIL 53 is a better photocatalyst than Zn-MOF, this behaviour can be attributed to (i) the fact that Iron is a transition metal with a partially filled 3d orbital and (ii) Iron is ferromagnetic in nature which means that it can easily spin filter electrons passing through it according to the CISS effect. The interesting observations made in the study then led to the modification of the Zn-MOF as outlined in Chapter 6.

5.16 REFERENCES

1) Abdollahi, B., Salari, D., & Zarei, M. (2022). Synthesis and characterization of magnetic Fe3O4@SiO2-MIL-53(Fe) metal-organic framework and its application for efficient removal of arsenate from surface and groundwater. *Journal of Environmental Chemical Engineering*, *10*(2). https://doi.org/10.1016/j.jece.2022.107144
2) Afzali, N., Tangestaninejad, S., Keshavarzi, R., Mirkhani, V., Nematollahi, J., Moghadam, M., Mohammadpoor-Baltork, I., Reimer, M., Olthof, S., Klein, A., & Gimenez, S. (2020). Hierarchical Ti-Based MOF with Embedded RuO2Nanoparticles: A Highly Efficient Photoelectrode for Visible Light Water Oxidation. *ACS Sustainable Chemistry and Engineering*, *8*(50), 18366–18376. https://doi.org/10.1021/acssuschemeng.0c04682
3) Appel, A. M., & Helm, M. L. (2014). Determining the overpotential for a molecular electrocatalyst. *ACS Catalysis*, *4*(2), 630–633. https://doi.org/10.1021/cs401013v
4) Aralekallu, S., Sajjan, V. A., Palanna, M., Prabhu C P, K., Hojamberdiev, M., & Sannegowda, L. K. (2020). Ni foam-supported azo linkage cobalt phthalocyanine as an efficient electrocatalyst for oxygen evolution reaction. *Journal of Power Sources*, *449*. https://doi.org/10.1016/j.jpowsour.2019.227516
5) Awata, R., Shehab, M., El Tahan, A., Soliman, M., & Ebrahim, S. (2020). High performance supercapacitor based on camphor sulfonic acid doped polyaniline/multiwall carbon nanotubes nanocomposite. *Electrochimica Acta*, *347*. https://doi.org/10.1016/j.electacta.2020.136229
6) Banerjee, A., Gokhale, R., Bhatnagar, S., Jog, J., Bhardwaj, M., Lefez, B., Hannoyer, B., & Ogale, S. (2012). MOF derived porous carbon-Fe 3O 4 nanocomposite as a high performance, recyclable environmental superadsorbent. *Journal of Materials Chemistry*, *22*(37), 19694–19699. https://doi.org/10.1039/c2jm33798c
7) Chaturvedi, G., Kaur, A., & Kansal, S. K. (2019). CdS-Decorated MIL-53(Fe) Microrods with Enhanced Visible Light Photocatalytic Performance for the Degradation of Ketorolac Tromethamine and Mechanism Insight. *Journal of Physical Chemistry C*, *123*(27), 16857–16867. https://doi.org/10.1021/acs.jpcc.9b04312
8) Digdaya, I. A., Rodriguez, P. P., Ma, M., Adhyaksa, G. W. P., Garnett, E. C., Smets, A. H. M., & Smith, W. A. (2016). Engineering the kinetics and interfacial energetics of Ni/Ni-Mo catalyzed amorphous silicon carbide photocathodes in alkaline media. *Journal of Materials Chemistry A*, *4*(18), 6842–6852. https://doi.org/10.1039/c5ta09435f

9) Elgrishi, N., Rountree, K. J., McCarthy, B. D., Rountree, E. S., Eisenhart, T. T., & Dempsey, J. L. (2018). A Practical Beginner's Guide to Cyclic Voltammetry. *Journal of Chemical Education*, *95*(2), 197–206. https://doi.org/10.1021/acs.jchemed.7b00361
10) Ellms, J.W., & Hauser, S.J. (1913). Ortho-Tolidine as a Reagent for the Colorimetric Estimation of Small Quantities of Free Chlorine. *Journal of Industrial and Engineering Chemistry, 5*, 915-917. https://doi.org/10.1021/ie50059a012
11) Feng, T., Chen, W., Xue, J., Cao, F., Chen, Z., Ye, J., Xiao, C., & Lu, H. (2023). Spin Polarization of Chiral Amorphous Fe-Ni Electrocatalysts Enabling Efficient Electrochemical Oxygen Evolution. *Advanced Functional Materials*, *33*(27), 1-10. https://doi.org/10.1002/adfm.202215051
12) Gazzotti, M., Arnaboldi, S., Grecchi, S., Giovanardi, R., Cannio, M., Pasquali, L., Giacomino, A., Abollino, O., & Fontanesi, C. (2018). Spin-dependent electrochemistry: Enantio-selectivity driven by chiral-induced spin selectivity effect. *Electrochimica Acta*, *286*, 271–278. https://doi.org/10.1016/j.electacta.2018.08.023
13) Ghosh, K. B., Zhang, W., Tassinari, F., Mastai, Y., Lidor-Shalev, O., Naaman, R., Möllers, P., Nürenberg, D., Zacharias, H., Wei, J., Wierzbinski, E., & Waldeck, D. H. (2019). Controlling Chemical Selectivity in Electrocatalysis with Chiral CuO-Coated Electrodes. *Journal of Physical Chemistry C*, *123*(5), 3024–3031. https://doi.org/10.1021/acs.jpcc.8b12027
14) Ghosh, S., Bloom, B. P., Lu, Y., Lamont, D., & Waldeck, D. H. (2020). Increasing the Efficiency of Water Splitting through Spin Polarization Using Cobalt Oxide Thin Film Catalysts. *Journal of Physical Chemistry C*, *124*(41), 22610–22618. https://doi.org/10.1021/acs.jpcc.0c07372
15) Hankin, A., Bedoya-Lora, F. E., Alexander, J. C., Regoutz, A., & Kelsall, G. H. (2019). Flat band potential determination: Avoiding the pitfalls. *Journal of Materials Chemistry A*, *7*(45), 26162–26176. https://doi.org/10.1039/c9ta09569a
16) Heard, D. M., & Lennox, A. J. J. (2020). Electrode Materials in Modern Organic Electrochemistry. *Angewandte Chemie*, *132*(43), 19026–19044. https://doi.org/10.1002/ange.202005745
17) Kawondera, R., Bonechi, M., Maccioni, I., Giurlani, W., Salzillo, T., Venuti, E., Mishra, D., Fontanesi, C., Innocenti, M., Mehlana, G., & Mtangi, W. (2023). Chiral "doped" MOFs: an electrochemical and theoretical integrated study. *Frontiers in Chemistry*, *11*. https://doi.org/10.3389/fchem.2023.1215619
18) Krysa, J., Zlamal, M., Kment, S., Brunclikova, M., & Hubicka, Z. (2015). Tio2and Fe2O3 films for photoelectrochemical water splitting. *Molecules*, *20*(1), 1046–1058. https://doi.org/10.3390/molecules20011046

19) Kusmierek, E. (2020). A CeO2 semiconductor as a photocatalytic and photoelectrocatalytic material for the remediation of pollutants in industrial wastewater: A review. In *Catalysts* (Vol. 10, Issue 12, pp. 1–54). MDPI. https://doi.org/10.3390/catal10121435
20) Li, R., Chen, Z., Cai, M., Huang, J., Chen, P., Liu, G., & Lv, W. (2018). Improvement of Sulfamethazine photodegradation by Fe (III) assisted MIL-53(Fe)/percarbonate system. *Applied Surface Science*, *457*, 726–734. https://doi.org/10.1016/j.apsusc.2018.06.294
21) López, J., Chávez, A. M., Rey, A., & Álvarez, P. M. (2021). Insights into the stability and activity of mil-53(Fe) in solar photocatalytic oxidation processes in water. *Catalysts*, *11*(4). https://doi.org/10.3390/catal11040448
22) Ma, M., Betard, A., Weber, I., Fischer R.A., & Meltzer-Nolte N. (2013). Iron-based Metal-Organic Framework MIL 88B: High quality microwave synthesis and solvent-induced lattice “breathing”. *Crystal Growth and Design* 13(6) 2286-2291 https://doi.org/10.1021/cg301738p
23) Ma, P., & Wang, D. (2017). The principle of photoelectrochemical water splitting. In *Nanomaterials for Energy Conversion and Storage* (pp. 1–61). www.worldscientific.com
24) Metzger, T. S., Mishra, S., Bloom, B. P., Goren, N., Neubauer, A., Shmul, G., Wei, J., Yochelis, S., Tassinari, F., Fontanesi, C., Waldeck, D. H., Paltiel, Y., & Naaman, R. (2020). The Electron Spin as a Chiral Reagent. *Angewandte Chemie*, *132*(4), 1670–1675. https://doi.org/10.1002/ange.201911400
25) Millange, F., Serre, C., & Férey, G. (2002). Synthesis, structure determination and properties of MIL-53as and MIL-53ht: The first CrIII hybrid inorganic-organic microporous solids: CrIII(OH)·(O2C-C6H4-CO2)·(HO2C-C6H4-CO2H)x. *Chemical Communications*, *2*(8), 822–823. https://doi.org/10.1039/b201381a
26) Millange, F., & Walton, R. I. (2018). MIL-53 and its Isoreticular Analogues: a Review of the Chemistry and Structure of a Prototypical Flexible Metal-Organic Framework. In *Israel Journal of Chemistry* (Vol. 58, Issue 9, pp. 1019–1035). Wiley-VCH Verlag. https://doi.org/10.1002/ijch.201800084
27) Mtangi, W., Tassinari, F., Vankayala, K., Vargas Jentzsch, A., Adelizzi, B., Palmans, A. R. A., Fontanesi, C., Meijer, E. W., & Naaman, R. (2017). Control of Electrons’ Spin Eliminates Hydrogen Peroxide Formation during Water Splitting. *Journal of the American Chemical Society*, *139*(7), 2794–2798. https://doi.org/10.1021/jacs.6b12971

28) Naaman, R., Paltiel, Y., & Waldeck, D. H. (2020). Chiral Induced Spin Selectivity Gives a New Twist on Spin-Control in Chemistry. *Accounts of Chemical Research*. https://doi.org/10.1021/acs.accounts.0c00485

29) Naaman, R., & Waldeck, D. H. (2012). Chiral-induced spin selectivity effect. *Journal of Physical Chemistry Letters*, *3*(16), 2178–2187. https://doi.org/10.1021/jz300793y

30) Najafidoust, A., Abdollahi, B., Sarani, M., Darroudi, M., & Vala, A. M. (2022). MIL-(53) Fe metal-organic framework (MOF)-based Ag2CrO4 hetrostructure with enhanced solar-light degradation of organic dyes. *Optical Materials*, *125*. https://doi.org/10.1016/j.optmat.2022.112108

31) Nishioka, S., Osterloh, F. E., Wang, X., Mallouk, T. E., & Maeda, K. (2023). Photocatalytic water splitting. *Nature Reviews Methods Primers*, *3*(1), 42. https://doi.org/10.1038/s43586-023-00226-x

32) Pappalardo, S., & Parisi, M. F. (2008). Ten-membered Rings or Larger with One or More Oxygen Atoms. *Comprehensive Heterocyclic Chemistry III*, *14*, 667–749. https://doi.org/10.1016/B978-008044992-0.01229-3

33) Sun, Q., Liu, M., Li, K., Zuo, Y., Han, Y., Wang, J., Song, C., Zhang, G., & Guo, X. (2015). Facile synthesis of Fe-containing metal-organic frameworks as highly efficient catalysts for degradation of phenol at neutral pH and ambient temperature. *CrystEngComm*, *17*(37), 7160–7168. https://doi.org/10.1039/c5ce01375e

34) Takanabe, K. (2017). Photocatalytic Water Splitting: Quantitative Approaches toward Photocatalyst by Design. *ACS Catalysis*, *7*(11), 8006–8022. https://doi.org/10.1021/acscatal.7b02662

35) Toledo, R. P., Dias, C. E. S., Huanca, D. R., & Salcedo, W. J. (2017). Electrochemical impedance study of fresh and passivated macroporous silicon for sensors. *2017 32nd Symposium on Microelectronics Technology and Devices (SBMicro)*, 1–4. https://doi.org/10.1109/SBMicro.2017.8113011

36) Torun, E., Fang, C. M., De Wijs, G. A., & De Groot, R. A. (2013). Role of magnetism in catalysis: RuO2 (110) surface. *Journal of Physical Chemistry C*, *117*(12), 6353–6357. https://doi.org/10.1021/jp4020367

37) Tran, D. P. H., Pham, M. T., Nguyen, T. H., Wang, Y. F., & You, S. J. (2023). Photocatalytic membrane reactors (PMRs) for hydrogen production. In *Current Developments in Biotechnology and Bioengineering: Membrane Technology for Sustainable Water and Energy Management* (pp. 19–42). Elsevier. https://doi.org/10.1016/B978-0-443-19180-0.00022-5

38) Wang, L., Zhang, Y., Li, X., Xie, Y., He, J., Yu, J.,& Song Y. (2015). The MIL 88A-derivedFe3O4 carbon Hierarchical nanocomposites for electrochemical sensing. Scientific Reports 5 (14341) https://doi.org.1038/srep14341

39) Whitfield, T.R., Wang, X., Liu, L., & Jacobson, A.J. (2006). *CCDC 258445: Experimental Crystal Structure Determination*.

40) Whitfield, T. R., Wang, X., Liu, L., & Jacobson, A. J. (2005). Metal-organic frameworks based on iron oxide octahedral chains connected by benzenedicarboxylate dianions. *Solid State Sciences*, *7*(9), 1096–1103. https://doi.org/10.1016/j.solidstatesciences.2005.03.007

41) Wierzbicka, E., Szaniawska-Białas, E., Schultz, T., Basilio, A. O., Siemiaszko, D., Ray, K., Koch, N., Pinna, N., & Polański, M. (2024). Long-Term Stability of Light-Induced Ti3+ Defects in TiO2 Nanotubes for Amplified Photoelectrochemical Water Splitting. *ChemSusChem*, *17*(5). https://doi.org/10.1002/cssc.202301614

42) Zhang, W., Banerjee-Ghosh, K., Tassinari, F., & Naaman, R. (2018). Enhanced Electrochemical Water Splitting with Chiral Molecule-Coated Fe3O4 Nanoparticles. *ACS Energy Letters*, *3*(10), 2308–2313. https://doi.org/10.1021/acsenergylett.8b01454

43) Zhang, W., Liu, F., Hu, Y., Yang, W., Guan, H., Hao, L., & Lu, G. (2020). Pivotal Role of Chirality in Photoelectrocatalytic (PEC) Water Splitting. *Current Chinese Science*, *1*(1), 115–121. https://doi.org/10.2174/2210298101999200819110254

6 FABRICATION AND CHARACTERIZATION OF FERROMAGNETIC BASED PHOTOELECTRODES

6.1 INTRODUCTION

To address the low current densities produced by the Zn-MOF based photoelectrodes, adjustments were carried out by i) incorporating ferromagnetic metal ions (Nickel and Cobalt) into the Zn-MOF structure, thereby creating Mixed-Metal, Metal Organic frameworks and ii) fabrication of a tandem device incorporating Iron oxide nanoparticles (hematite, (α-Fe_2O_3)). In both cases the introduction of the ferromagnetic materials was done in agreement with the CISS effect which also states that the spin control noticed in chiral molecules is also observed in ferromagnetic materials. One advantage offered by metal organic frameworks is that they offer post synthesis modification. Post synthetic modification of MOFs makes it possible to create new and activate existing catalytic sites. Post synthesis modification has been used to change the metal node in a process called transmetalation as well as exchanging or activating the organic linker. The ability of MOFs to undergo transmetalation makes them versatile. Transmetalation is achieved by soaking the MOF of interest with the metal salt in an appropriate solvent for an extended period of time.

A tandem cell junction is made up of two light absorbing species which target different parts of the solar spectrum to generate voltage necessary for water splitting. The tandem device was prepared by electrodepositing α-Fe_2O_3 nanoparticles onto the FTO/TiO_2 surfaces and the drop casting the MOF paste onto the FTO/TiO_2/α-Fe_2O_3. The α-Fe_2O_3 nanoparticles were synthesized according to the method detailed in 6.3.2.

This chapter gives details on the synthesis, physical characterization and application of Mixed-Metal, Metal Organic Frameworks in photoelectrocatalytic water splitting as well as the fabrication and application of the tandem device in photoelectrocatalytic water splitting.

6.2 APPLICATION OF MIXED-METAL, METAL ORGANIC FRAMEWORKS IN WATER SPLITTING

6.2.1 Introduction

Mixed-metal-organic frameworks (MM-MOFs), are metal organic frameworks in which two or more types of metal ions are periodically arrayed throughout the framework and this endows them with an extra degree of structural diversity and a variety of advanced applications (T. Zhang et al., 2019).

MM-MOFs have attracted a great consideration in photoelectrochemical water splitting because, i) the introduction of two metal ions results in cooperative interaction between the metal ions which assists in the reduction of the optical band gap for the desired reaction, ii) incorporation of photoactive or metal-containing organic linker makes the frameworks visible light active and improves the properties compared to the homometallic MOFs, iii) presence of two metal ions assists in reducing the recombination of photo-generated electrons and holes, as one of the metal ions acts as an electron sink and helps in transferring electrons to the protons for the generation of molecular hydrogen (Jaryal et al., 2022). In this study the introduction of ferromagnetic metal ions in the framework introduces spin filtering of the transmitted electrons as stipulated by the CISS effect.

Strategies for MM-MOF synthesis are broadly classified into i) one-pot synthesis, in which the MM-MOFs are synthesized by directly reacting the appropriate mixture of metal precursors with the organic linker and ii) post synthetic modification, in which there is partial replacement of metal ions in the homometallic MOFs with another metal ion in a method called transmetalation. Both strategies involve the use of different metal salts as metal precursors, and suitable organic linkers that react to form the bi- or tri-metallic MOFs.

In transmetalation, the homometallic MOF is either immersed in a solution of other metal ions or the homometallic MOF and the metal ions of interest are soaked in a suitable solvent. During transmetalation, the metal-exchange process occurs at a significant rate provided there is a well-established reversibility of the metal–ligand bonds (Masoomi et al., 2019) Transmetalation is behind the construction of MOFs with more crystallinity i.e transmetalation has been attributed to the increase in crystallinity of MOFs (Jaryal et al., 2022; Masoomi et al., 2019)

The metals for use in the transmetalation, Cobalt and Nickel were selected because they possess properties that are similar to those of iron. The similarities in properties of iron, cobalt and nickel have led to the three elements being referred to as the iron triad (Petrucci et al., 2011). The iron triad elements possess ferromagnetism that is comparable to that of gadolinium and neodymium, their excellent ferromagnetic properties can be attributed to the presence of unpaired electrons that they possess (Petrucci et al., 2011). The presence of a

variable oxidation states makes the elements in the iron triad suitable for use as catalysts. According to the CISS effect, spin selectivity can also be achieved when electrons pass through a ferromagnetic material (Naaman, Paltiel, et al., 2019; Naaman & Waldeck, 2012; Waldeck et al., 2021) hence the Cobalt and Nickel were selected and used in the synthesis of the mixed-metal MOFs.

6.2.2 Synthesis of Mixed-Metal, Metal Organic Frameworks

6.2.2.1 Zn-MOF

In the synthesis Zn-MOF based Mixed-metal, metal organic frameworks, 0.1 moles of Zn MOF were mixed with 0.1moles of either Cobalt (II) Nitrate Hexahydrate or Nickel (II) Nitrate Hexahydrate, (Co $(NO_3)_2 \cdot 6H_2O$) or (Ni $(NO_3)_2 \cdot 6H_2O$)) and dissolved in 20 ml of methanol and held for 24 hours at room temperature. After 24 hours the mixture was filtered, washed in excess methanol and dried in a hot air oven at 80 °C for 15 minutes. **Scheme 6.1** depicts the preparation steps for the mixed-metal MOFs.

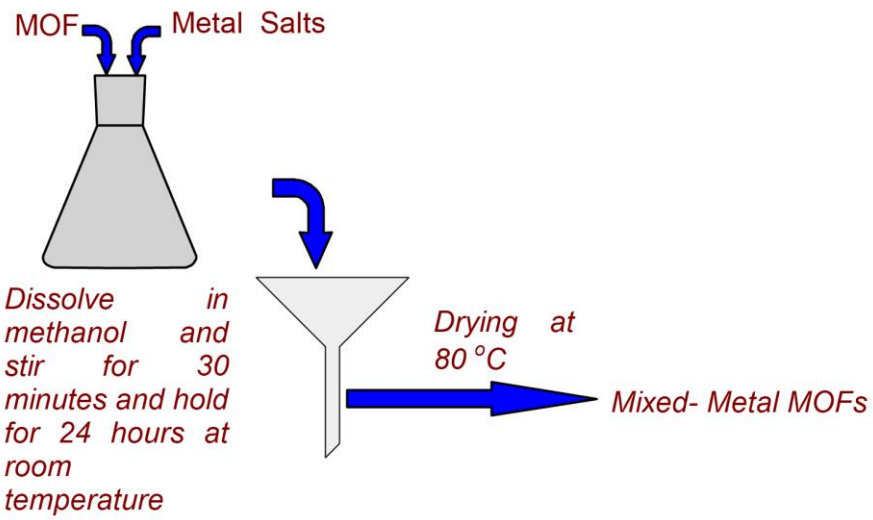

Scheme 6.1: Synthesis of Mixed-Metal, Metal Organic Frameworks

6.2.3 Characterization

6.2.3.1 Photocatalytic activity

The photocatalytic activity of the Mixed metal MOFs was assessed using a UV-1900i Shimadzu Uv-Vis Spectrophotometer. A 2% MOF solution was made by dissolving the MM-MOFs in ethanol. The sample was then assessed for photocatalytic activity by running a scan from 300 to 800 nm.

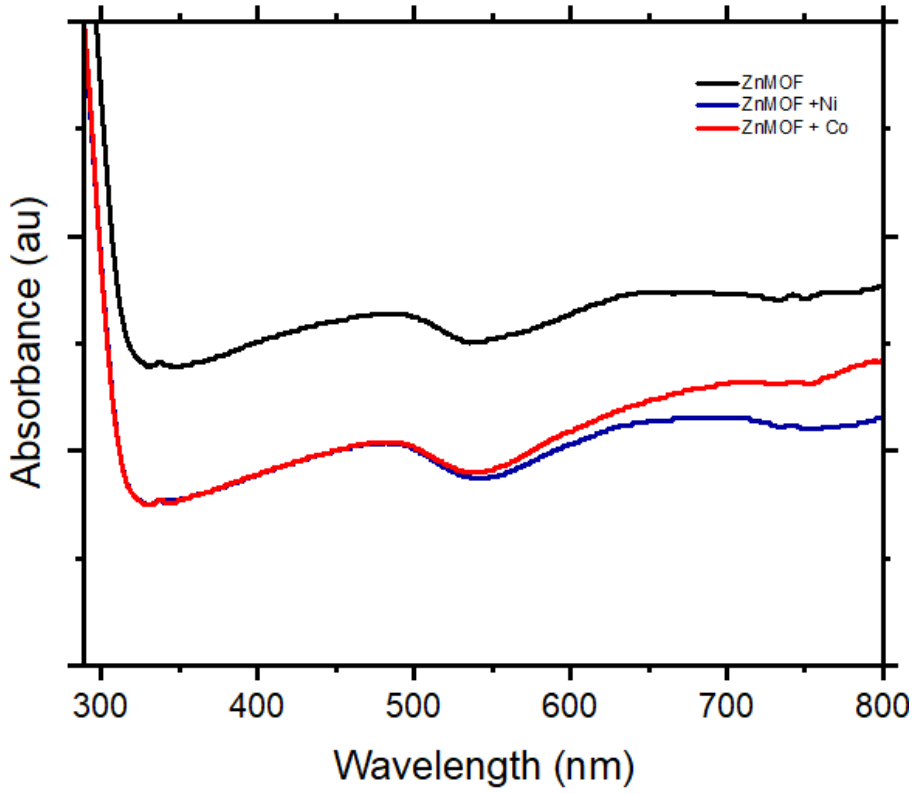

Figure 6.1: Uv-Vis Spectra of the mixed metal-Metal Organic frameworks

The ability of the synthesized mixed-metal MOFs to absorb energy in the ultra-violet and visible regions ensures that they can be applied as photocatalysts. In Uv-vis measurements both MM-MOFs are able to absorb wavelengths, in a wide range of wavelengths that span from ultra-violet to the near infrared and this is proof that they are applicable as photocatalysts (Altaf et al., 2018).

6.2.3.2 Crystallinity

PXRD analysis was carried out to evaluate the effect of the metal ions on the phases present, phase composition as well as crystallinity of the mixed metal MOFs. The PXRD analysis was carried out using a Brucker D2 phaser PXRD diffractometer, USA, which uses DIFFRAC-SUITE software for controlling the instrument and analyzing the data. The Brucker D2 phaser PXRD diffractometer uses a copper tube with 1.5418 Angstroms as the X-ray source. X-rays were generated using 30 kV and a current of 10 Amperes. The scan mode was continuous PSD fast with scan type two theta/theta with detector Lynxeye XET. The scan step was 0.5 second with 3948 steps and the total time was 2180 seconds. Powdered samples were placed on a zero-background sample holder and scanned from 4 to 60, 2 theta positions.

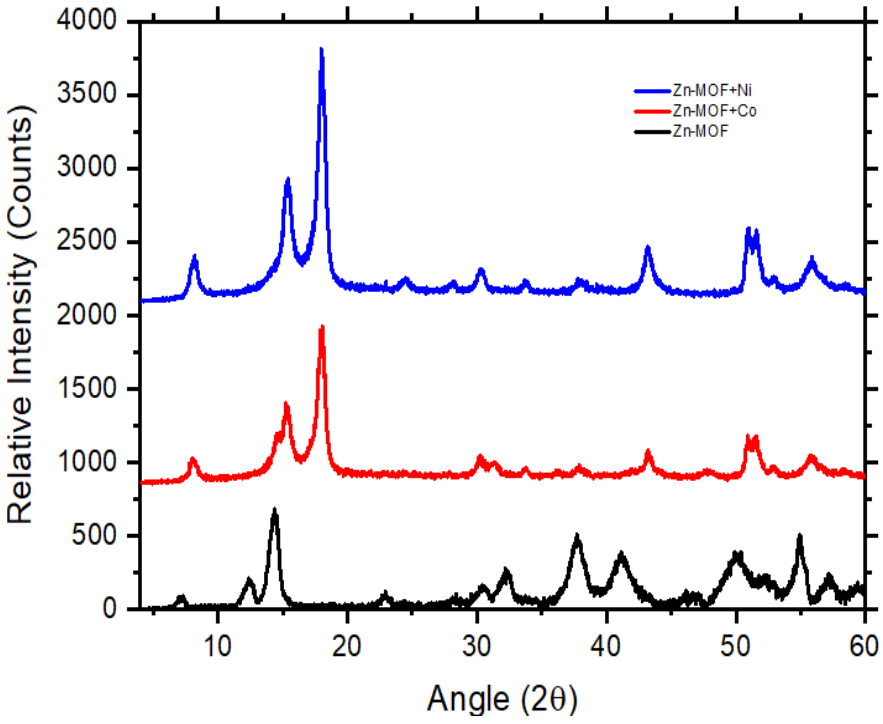

Figure 6.2: PXRD Pattern showing a comparison between (a) MIL 53 and the Mixed Metal MIL 53 (b) Zn-MOF and the Mixed Metal Zn-MOFs

A comparison of the PXRD analysis of Zn-MOF and the mixed metal MOFs, it can be observed that during the transmetalation, the general MOF structure was maintained, while the non-crystalline phase present in the Zn-MOF, disappeared from the Zn-MOF +Ni and the Zn-MOF+ Co. The observed increase in crystallinity is in agreement with the observations made by Jaryal et al (Jaryal et al., 2022). In the mixed-metal MOFs an apparent shift in the 2 theta positions to the right can be noticed, for example the peak at 8.9° in Zn-MOF can be observed at 11.13° and 11.03° in Zn-MOF +Co and Zn-MOF + Ni respectively. The shifts to the right can be attributed to either lattice strain or crystalline size shrinking.

6.2.3.3 Inductively coupled Plasma- optical emission spectroscopy

Inductively Coupled Plasma was carried out to the detect and quantify the ferromagnetic metals that had been incorporated during transmetalation. The inductively coupled plasma optical emission (ICP-OES) analysis was performed on a Spectro Arcros instrument that was calibrated using known magnesium, manganese, and palladium standards. Samples were microwave-digested in aqua regia (4 mL of 60% HNO_3, 1 mL of 30% HCl) and analysed directly. Inductively Coupled Plasma Optical Emission (ICP-OES).

The results from ICP-OES show that in the as-synthesised Zn-MOF, the ferromagnetic metals (Ni^{2+} and Co^{2+}) are absent as expected, however, in the mixed-metal MOFs the presence of ferromagnetic metals is witnessed. In Zn-MOF + Co, 4.23 m/m of Cobalt was incorporated into the framework, while 2.33 m/m of Nickel was incorporated in the Zn-MOF +Ni over the same period of time. When comparing the composition of the MM-MOFs, it can be observed the content of Cobalt ions is almost double the content of Nickel ions suggesting that the Cobalt was more readily incorporated into the matrix compared to the nickel.

Table 6.1: ICP-OES results for the Zn-MOF Mixed-Metal MOFs

	Ni	**Co**	**Zn**
Sample	%m/m	%m/m	%m/m
Zn-MOF	< 0.01	<0.01	10.8
Zn-MOF + Co	<0.01	4.23	16.3
Zn-MOF + Ni	2.33	<0.01	14.6

6.2.4 Preparation of electrodes

Preparation of the mixed-metal, metal organic framework photoelectrodes was done by functionalization of FTO/TiO_2 surfaces and was achieved by drop casting the mixed-metal MOF solutions onto the FTO/TiO_2 surfaces. The FTO/TiO_2 were fabricated according to the method described in section 4.12. Solutions of 1 mM slurry of the mixed metal MOFs were prepared by dissolving the mixed-metal MOFs in ethanol and then carefully depositing 20µL of the mixed-metal MOF solution on the FTO/TiO_2 surface. The electrodes were then left to dry under controlled humidity for a period of three weeks.

6.2.5 Water Splitting experiments

Water splitting was performed using the mixed-metal functionalized TiO_2 electrodes. All the measurements were performed versus the Ag/AgCl reference electrode. A 0.1 M Na_2SO_4 was used as the electrolyte with a Platinum wire as the counter electrode. The potentials were converted from Ag/AgCl to Reversible Hydrogen Electrode (RHE) using the equation:

$$E = E_{ref} + 0.059 * pH + 0.1976 \qquad \text{Equation 6.1}$$

Where E Potential versus the RHE

E_{ref} Potential versus the reference electrode (Ag/AgCl)

pH Electrolyte pH (the working pH was 6.5)

6.2.5.1 Photo response Measurement

To evaluate and confirm the photocatalytic nature of the mixed-metal MOFs, Linear Sweep Voltammetry in which the light at 100mW/cm^2 was chopped ON/OFF at 10s was carried out. The obtained voltammograms are given in **Figure 6.3.** LSV measurements in which the light is chopped ON/OFF at periodic intervals is a measure of the photocatalytic activity of the photoelectrodes (Bedoya-Lora et al., 2021).

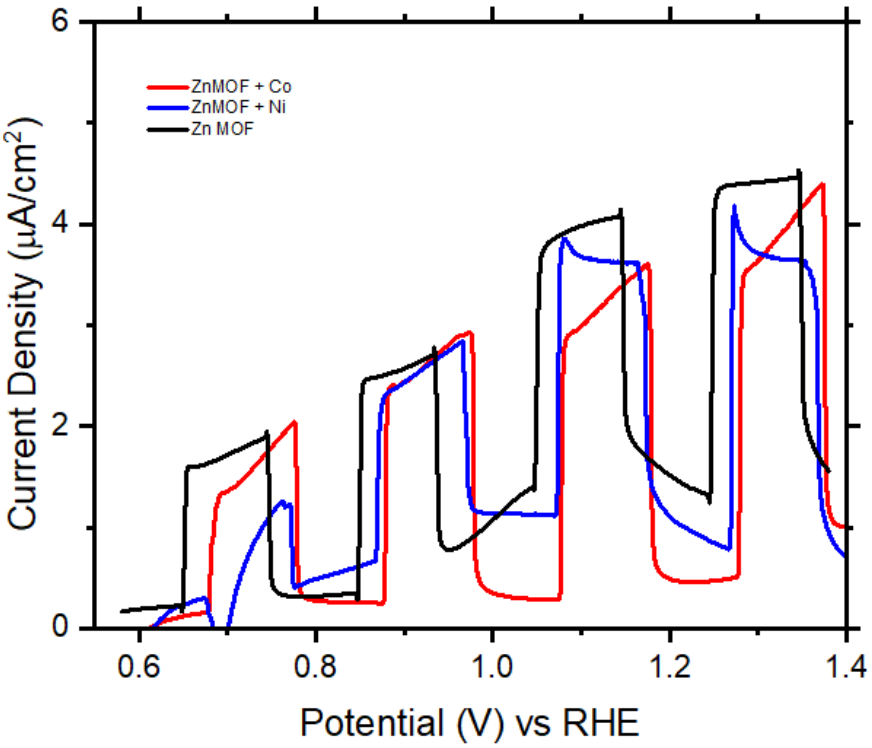

Figure 6.3: Photo response measurements for (a) Zn-MOF vs Zn-MOF + Co (red line) and Zn-MOF + Ni (blue line) in 0.1M Na_2SO_4 at 0.01V/s scan rate.

From the **Figures 6.3** it can be observed that there was a spike in the current density generated once the light was switched on, however, once the light source was turned off, the current density disappeared immediately. This confirms the photocatalytic activity of the mixed-metal MOF photoelectrodes as an increase in the current density when the light was increased show that the mixed-metal MOF photoelectrodes were responding to the light (Altaf et al., 2018; Seenivasan et al., 2022).

6.2.5.2 OER Measurements

Linear Sweep Voltammetry from 0.0 V to +1.3 V (vs Ag/AgCl) using a scan rate of 0.01 V/s under illumination and under darkness.

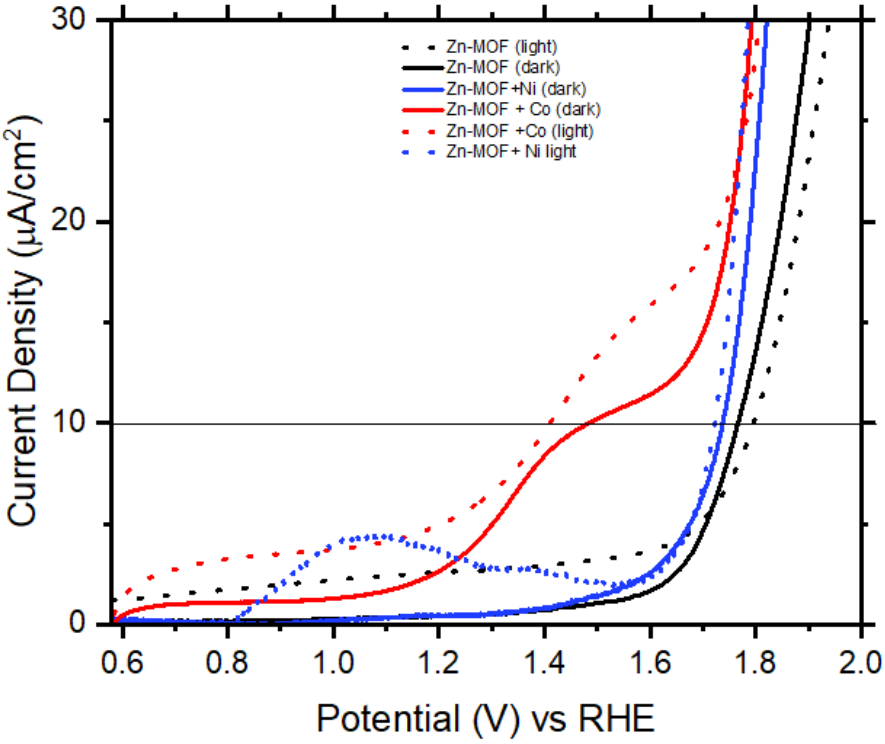

Figure 6.4: OER graphs showing comparison between the mixed metal Zn-MOFs, Zn-MOF +Co (red line), Zn-MOF +Ni (blue line) vs Zn-MOF (black line)

In the OER curves of the mixed metal MOFs an apparent reduction in the OER voltage, is witnessed in the Zn-MOF + Co (+1.42V), Zn-MOF +Ni (+1.72) vs Zn-MOF (+1.77). In comparison with the parent Zn-MOF, the Mixed metal, MOFs produced higher photocurrent densities *circa* +1.23V, they also exhibited lower overpotentials. Under illumination, both mixed-metal MOFs produce current densities of around 5 $*10^{-6}$ A, around +1.23V vs the RHE.

The response shown by the Zn-MOF+ Ni under illumination i.e the peak visible around +1.15V can be attributed to the presence of the Ni-OH bond undergoing oxidation from Ni^{2+} to Ni^{3+} (J. Zhang et al., 2021; Zhu et al., 2019). The observation of the characteristic Ni-OH bond is also confirmation that the mixed-metal MOFs were successfully synthesised.

To further investigate this observation chronoamperometry measurement were carried out.

6.2.5.3 Chronoamperometry

Chronoamperometry at +1.0V under illumination with light of intensity 100mW/cm^2 chopping light ON/OFF at 10s intervals was carried out for transient photocurrent density measurements for the MM-MOFs. From the curves shown in **Figure 6.5,** it can be noted that a swift and reproducible photocurrent densities are produced for all the photoelectrodes.

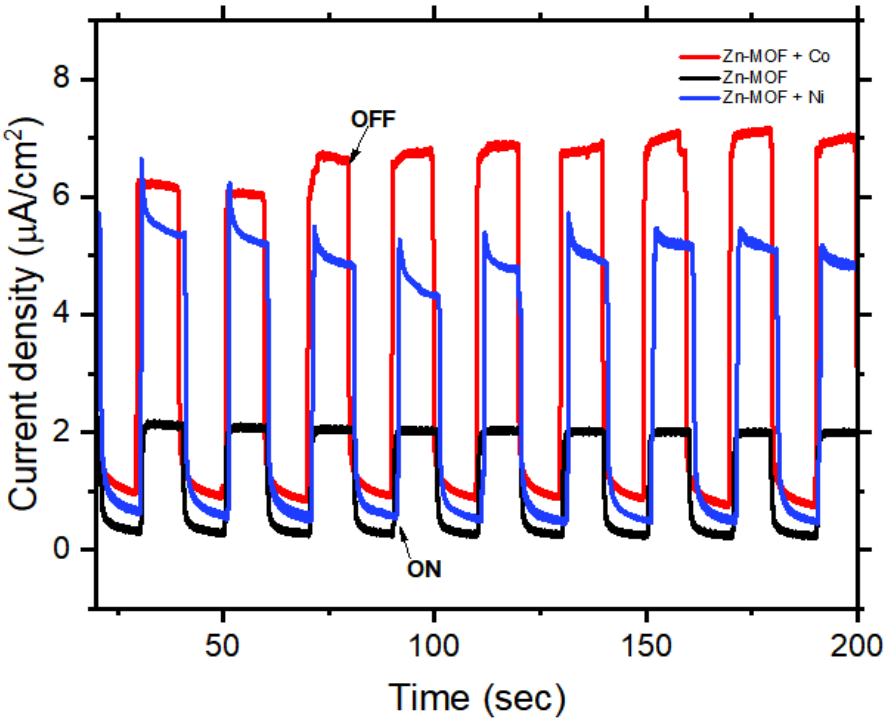

Figure 6.5 Chronoamperometry at +1.0 V under illumination with light of intensity 100mW/cm^2 chopping light ON/OFF at 10s intervals of Zn-MOF (Black line), Zn-MOF +Ni (blue line) and Zn-MOF + Co (red line).

From the trends observed in **Figure 6.5**, both forms of mixed metal MOFs exhibited increased current densities compared to the as synthesised MOFs. In the Zn-MOF+ Co the current densities tripled while the Zn-MOF+ Ni, they doubled. In the curve of the Zn-MOF + Ni a sharp spike is observed when the light is turned on, which gradually decreases, the sudden spike of current is due to the flooding of the electrons produced when the light is switched on, onto the surface of the photoelectrode, however, because the current density was levelling off, suggesting recombination of the holes and electrons generated (Xiao et al., 2021).

6.2.5.4 Electrochemical Impedance Spectroscopy

6.2.5.4.1 Mott Schottky measurements

Mott-Schottky analysis was carried out to determine the electronic properties of the fabricated photoelectrodes. The measurements were performed by sweeping voltages from 0.75V to -0.5V using an AC Voltage with an amplitude of 5mV and frequency of 1000Hz. Measurements were carried out under illumination and under darkness.

a) b)

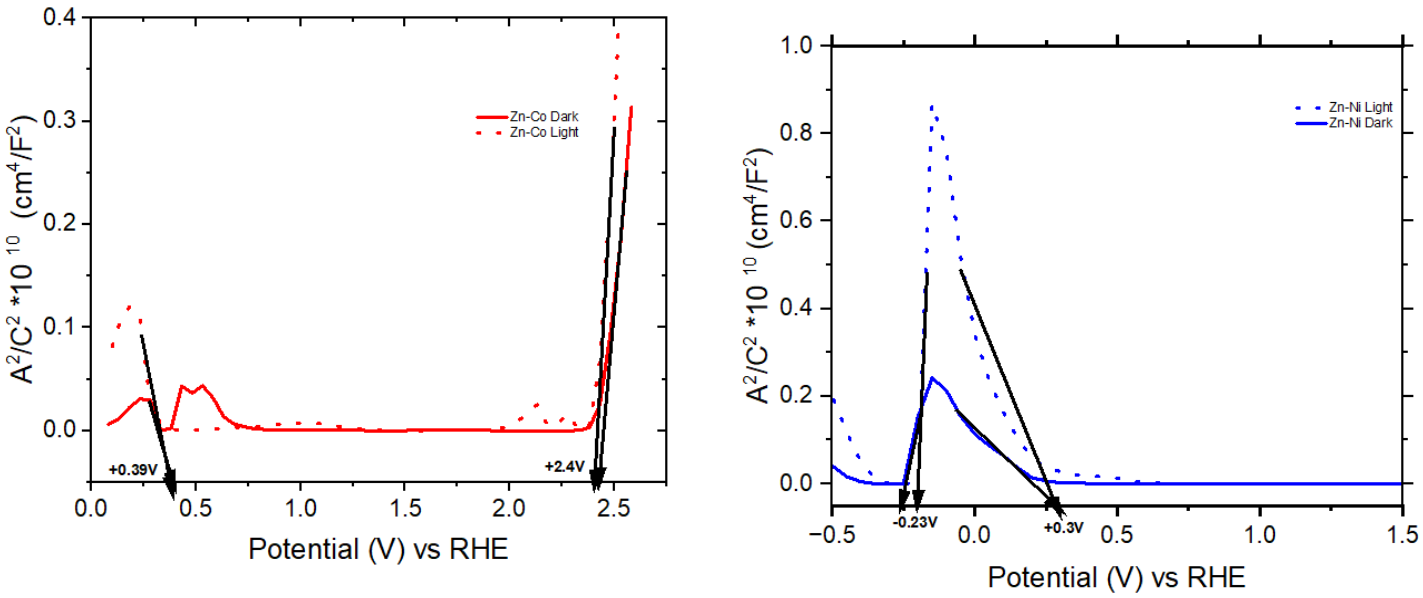

Figure 6.6: a) The Mott Schottky plots for Zn-MOF+ Co under illumination and under darkness b) The Mott Schottky plots for Zn-MOF+ Ni under illumination and under darkness

---

The plots for the Mott-Schottky measurements from the mixed-metal MOFs shown in **Figure 6.6**, each mixed-metal MOF produced two flat band potentials, in each case the material exhibited both n-type and p-type properties as witnessed by the positive gradient (n- type) and negative gradient (p-type) as described by Kusmierek (Kusmierek, 2020). The oxides of Nickel (NiO) and Cobalt (Co_3O_4) are intrinsically p-type semiconductors (Iacomi et al., 2011), while Zinc oxides are intrinsically n-type semiconductors. The presence of both n-type peaks and p-types in the Mott-Schottky plots indicate that the Nickel and Cobalt was successfully incorporated into the Zn-MOF framework.

6.2.5.4.2 Nyquist Plots

To evaluate the charge transfer kinetics, Nyquist plots were used. The Nyquist measurements were carried out by varying frequency between 1MHz and 0.1Hz, with an initial potential of 0V and an amplitude of 5mV.

a) b)

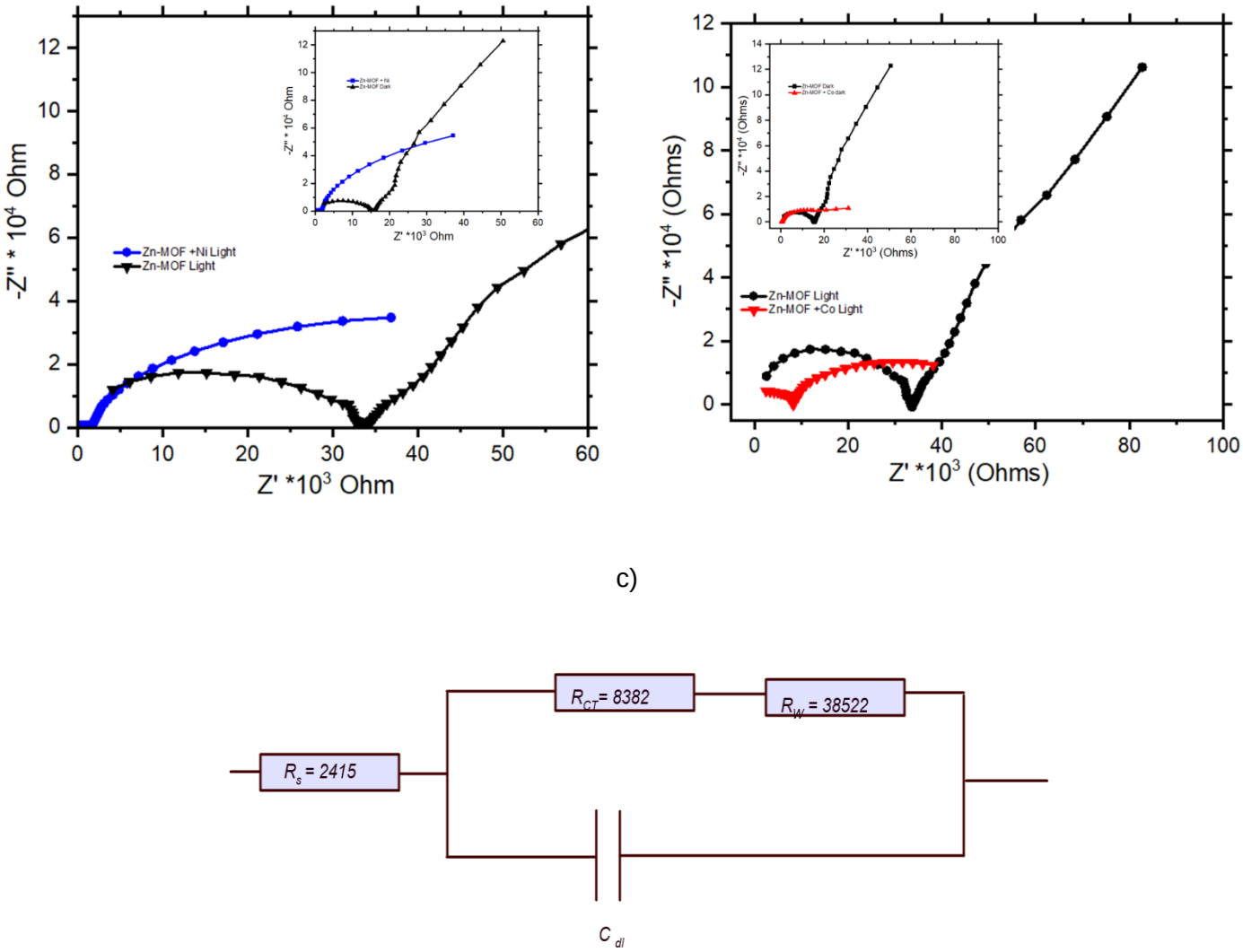

c)

Figure 6.7: a) Nyquist plots for Zn-MOF (black curve) Zn-MOF + Ni b) Zn-MOF + Co c) Equivalent circuit for Zn-MOF + Co

---

The charge transfer kinetics of the photocatalysts are investigated using EIS spectra. In **Figure 6.7 (a) and (b)**, the semicircle diameter for photoelectrodes containing the mixed-metal MOFs is very small compared to that of the as-synthesised Zn-MOF, this indicates a more favourable interfacial charge transfer process between photocatalyst and electrolyte in chiral the Zn-MOF+ Co and Zn-MOF+ Ni than the as-synthesised Zn-MOFs (Feng et al., 2023; Zahra et al., 2020). The change in charge transfer kinetics as witnessed by the Nyquist plots also point to the fact that the inclusion of ferromagnetic materials in the MOF matrix improves the overall water splitting efficiency as predicted by the CISS effect. **Figure 6.7 c)** shows the equivalent circuit for the Zn-MOF + Co.

6.2.5.4.3 Bode plots

To further investigate the electronic properties of the photoelectrodes, bode plots were used. The measurements were carried out under darkness and under illumination. In the measurements, the frequency was varied between 1MHz and 0.1Hz, with an initial potential of 0V and an amplitude of 5mV and a graph of Log frequency vs -phase angle was plotted as shown in **Figure 6.8**.

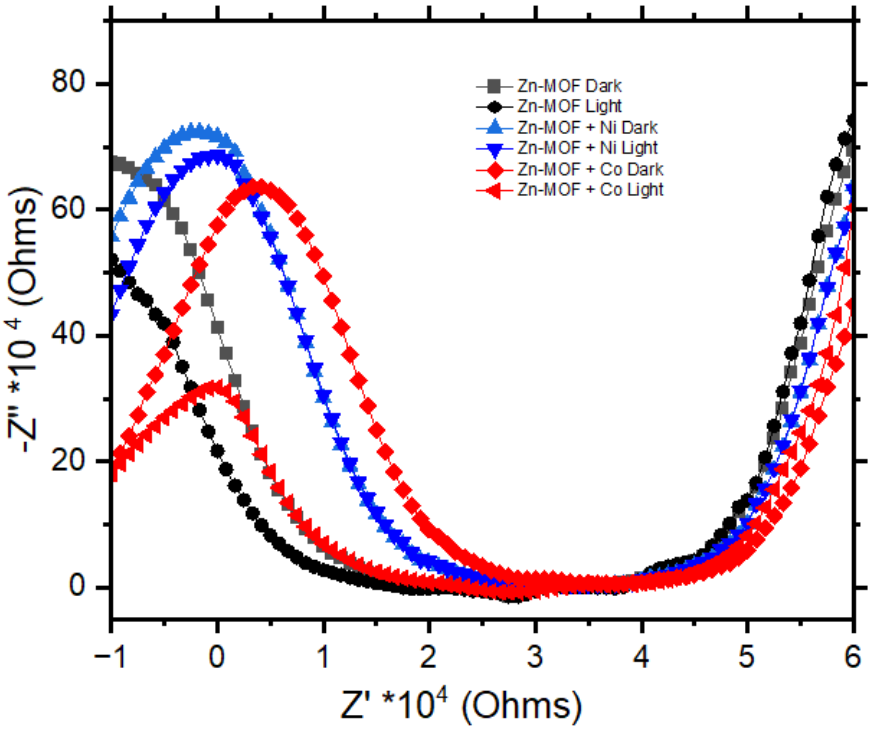

Figure 6.8: Bode plots for Zn-MOF (black curve), Zn-MOF + Co (red curve) and Zn-MOF + Ni (blue curve).

From the Bode Plots shown in **Figure 6.8** it can be observed that the photoelectrode/electrolyte system showed phase angles below -90°, which is synonymous with non-ideal capacitive behaviour (Digdaya et al., 2016). In comparison with the as-synthesised Zn-MOF, there is a shift towards the higher frequencies and this can be attributed to charge transfer processes taking place in electrode/electrolyte boundaries (Toledo et al., 2017; Wierzbicka et al., 2024) whereas the as-synthesised Zn-MOF is prone to diffusion-controlled processes.

6.2.5.5 Activity of the photoelectrodes

To evaluate the activity of the photoelectrodes, open circuit potential (OCP) in the dark and under illumination at zero current were carried out. Both MM-MOF based photoelectrodes produced an OCP curve, indicating that an equilibrium was reached between the electrolyte and the device (Bedoya-Lora et al., 2021).

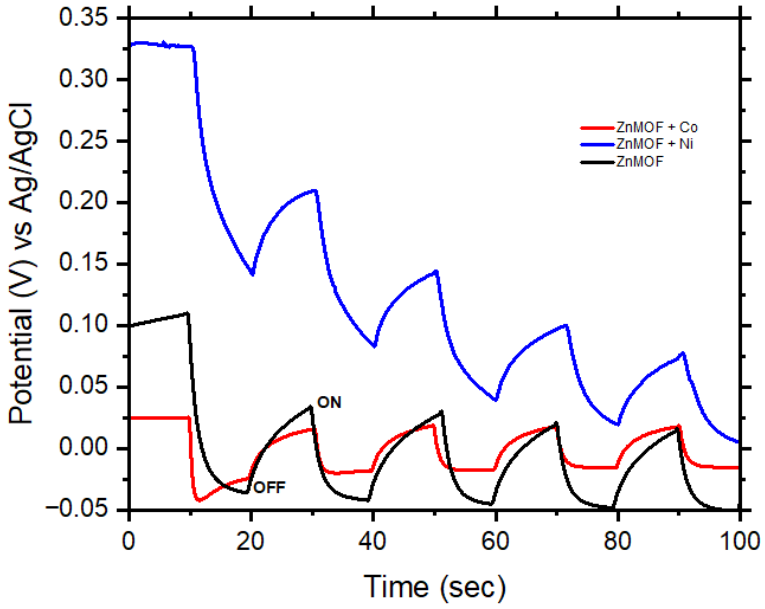

Figure 6.9: OCP Curves for Zn-MOF (black line) vs Zn-MOF+ Co (red line) vs Zn-MOF vs Zn-MOF+ Ni (Blue line).

In the open circuit potential curves shown in **Figure 6.9**, it was observed that once the light was switched on, the voltages became negative but when the light source was switched off, the potential became positive. This observation can be attributed to the nature of the photoelectrode, for n-type photoelectrodes, during open circuit potential measurements, when the light is switched on, the surface of the electrode becomes flooded by electrons (Hankin et al., 2019). When the light is switched off, recombination of the electron-hole pairs take place and this results less electrons on the photoelectrode surface hence the positive voltages. However, in the Mott-Schottky measurements the presence of p-type semiconductors was observed, this however is not observed in the OCP measurements, possibly because the n-type semiconductor (from the Zn^{2+} ions) is present in a larger concentration than the p-type semiconductors.

6.2.5.6 Overpotential

The overpotential was evaluated by running a Tafel plot from -1.5V to +1.5V at a scan rate of 0.01V/s. To evaluate and understand the OER mechanisms, Tafel plot analysis is often used.

Tafel plots are occasionally used to compare the catalytic properties of various photocatalysts that may be under study (Aralekallu et al., 2020).The overpotential is the slope (Tafel slope) of the Tafel plot and was measured at the linear part of the Tafel plot.

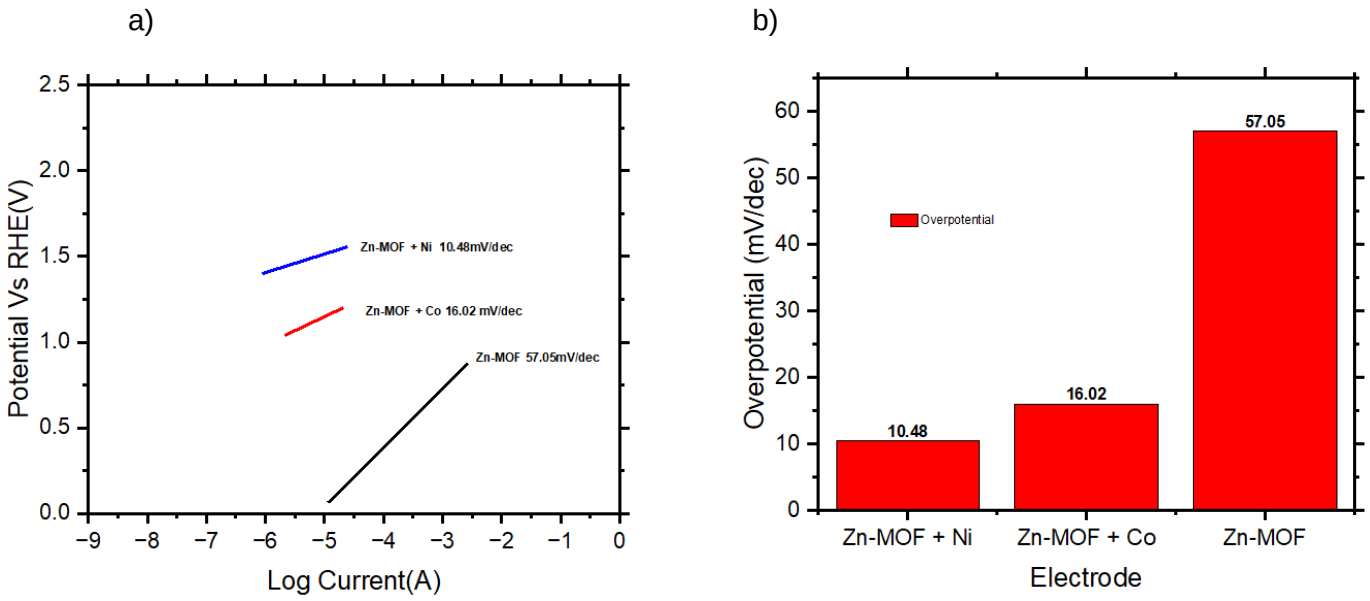

Figure 6.10: a) Tafel slope of Mixed Metal Zn-MOF showing overpotential in $mVdec^{-1}$ b) A bar chart showing the Mixed Metal Zn-MOF overpotentials

In **Figure 6.10,** a comparison of the overpotentials of the MM_MOFs vs the pristine Zn-MOF, show that the Zn-MOF a material that does not possess any ferromagnetism has an overpotential of 57.05mV/dec while Zn-MOF + Co exhibit an overpotential of 16.02 mV/dec and the Zn-MOF + Ni produced an overpotential of 10.48mV/dec. The decrease in the overpotential of the MM-MOFs can be attributed to the presence of the ferromagnetic metals Cobalt and Nickel. According to the CISS effect as described by Naaman and Waldeck (Naaman & Waldeck, 2012; Waldeck et al., 2021) electrons passing through a ferromagnetic material also get spin polarised, i.e ferromagnetic materials work in a manner similar to that of chiral molecules, where they offer spin filtration allowing electrons spinning in only one direction. Evidence in section 2.2.6.1, show that that overpotentials tend to be lower in inherently ferromagnetic materials while relatively high in non-ferromagnetic materials (Heard & Lennox, 2020). The presence of the cobalt and nickel ions in the photoelectrode resulted in the reduction of the overpotential significantly.

6.3 THE FABRICATION OF A TANDEM DEVICE FOR USE IN PHOTOELECTROCATALYTIC WATER SPLITTING

6.3.1 Introduction

Materials with a wide absorption band have been designed to improve the absorption of solar radiation and this has been achieved by stacking different narrow band absorbing materials into multiple junctions. When two or more donor materials are used in a multiple junction (tandem junction), it is expected that a broader range of the solar spectrum is covered (Hadipour et al., 2008). A tandem junction is made up of two or more light absorbing species which target different parts of the solar spectrum to generate voltage necessary for water splitting (Sherman et al., 2016). Tandem junctions are increasingly becoming popular in water splitting because they offer a possibility for the development of unassisted overall water splitting (Chen et al., 2018).

There are three different tandem cell configurations namely i) The PEC tandem cells ii) the integrated photovoltaic PEC/PV tandem cell and iii) the PV/Electrolyser hybrid (K. Zhang et al., 2016) and the simplest arrangement of a tandem cell is a one-sided light absorption semiconductor.

In a PEC tandem cell, the device configuration is made up of a two-sided light-absorption component with both the anode and cathode Spontaneous water redox takes place on the simultaneously excitable anode and cathode and reduces the basic requirement of band edge potentials, which is critical for the use of a single semiconductor (K. Zhang et al., 2016). Additionally, the two semiconductors can have smaller bandgaps because each need to provide only a half-reaction. Furthermore, the narrower bandgaps tend to increase the light absorption in the visible-wavelength radiation, which is the majority of photon flux from the sun (K. Zhang et al., 2016).

Another device configuration for the tandem junction, consists of an integrated PEC cell and photovoltaic (PV) device and is usually called the PEC/PV tandem cell. The PEC device is combined with a PV cell in a tandem configuration. When the solar energy reaches the rear PV device after passing through the front PEC electrode, the carrier (electron or hole) photoinduced by the PEC electrode is recombined with that from the PV component, the residual carrier contributes to the half-reaction of water splitting, and the charge remaining from the PV device is transferred to the counter electrode for another half-reaction of water splitting (K. Zhang et al., 2016). In this configuration, the photovoltage provided by a PV device is regarded as an external bias for unassisted water splitting. (K. Zhang et al., 2016)

The final tandem cell arrangement is a combined PV and electrolyser device. The PV device is used only as the photo-absorber to produce the charge carriers, which are transported to the electrolyser (K. Zhang et al., 2016). The PV devices provide direct current (DC) to enable the reduction reaction at the cathode, and the oxidation reaction takes place at the anode. These PV devices are separated from the water electrolyte physically, which can prevent the degradation of PV by water (K. Zhang et al., 2016).

Different oxides, including TiO_2, WO_3, ZnO CdS, CdSe, α-Fe_2O_3 and $BiVO_4$ have been used as photoelectrode materials (K. Zhang et al., 2016). Hematite (α-Fe_2O_3) is a promising transition metal oxide with a band gap of around 2.1 eV. Besides its relatively small band gap, α-Fe_2O_3 is the most stable form of iron oxide under ambient conditions. Iron is also abundant in the earth's upper crust and hematite is a favourable candidate for solar energy conversion on a scale proportionate with the global energy demand (Prévot & Sivula, 2013). According to the CISS effect electrons passing through a ferromagnetic material also get spin filtered (Naaman & Waldeck, 2012, 2015; Waldeck et al., 2021). Nanoparticles (small particles with all their critical dimensions on the nanoscale) offer a large surface area and are known to be highly reactive because of the large surface-area- to-volume ratio. Based on the above argument, α-Fe_2O_3 nanoparticles were found to be favourable for use and were selected for constructing the tandem junction.

6.3.2 Synthesis of the hematite, (α-Fe_2O_3) nanoparticles

In the synthesis of hematite, (α-Fe_2O_3), 7.5g of $FeCl_3 \cdot 6H_2O$ was dissolved in 100ml distilled water and stirred until the $FeCl_3 \cdot 6H_2O$ was completely dissolved. $NaBH_4$ was added to the $FeCl_3 \cdot 6H_2O$, drop by drop at room temperature using a dropper until finished. The mixture was stirred for an additional 10 minutes to ensure complete mixing. The iron oxide nanoparticles were harvested using centrifugation and then dried in an oven at 120 °C for 4 hours. The dried iron oxide nanoparticles were stored in an airtight container. The synthesised α-Fe_2O_3 nanoparticles were black in colour and highly magnetic.

6.3.3 Characterization

To ascertain the properties of the Iron oxide nanoparticles, characterization was carried out.

6.3.3.1 Photocatalytic Activity

a) b)

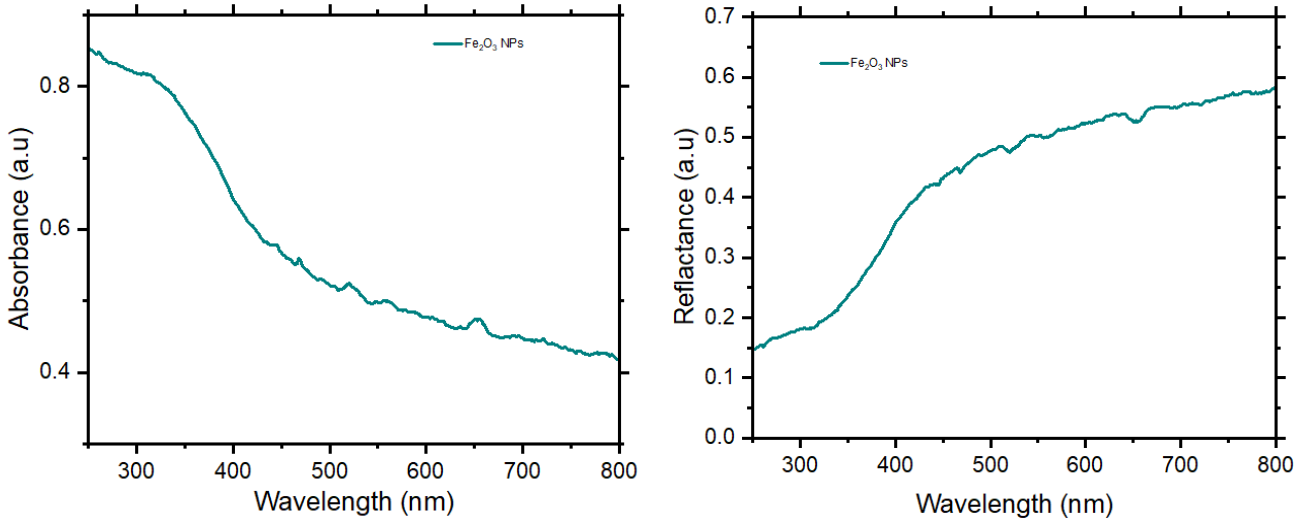

Figure 6.11: a) Uv-Vis Absorption Spectrum for the α-Fe_2O_3 nanoparticles and derivatives b) Diffuse Reflectance Spectrum for α-Fe_2O_3 nanoparticles.

In the absorption spectrum of the α-Fe_2O_3 nanoparticles shown in **Figure 6.11 a),** the absorption can be observed up to 800nm, indicating that the α-Fe_2O_3 nanoparticles are active in the visible range of the electromagnetic spectrum. **Figure 6.11 b),** shows the diffuse reflectance spectra of the α-Fe_2O_3 nanoparticles. DRS is used quantitatively to measure the colour and intensity of reflected light, it gives the light reflectance and absorbance of materials (Tran et al., 2023). To evaluate the band gap energies of the α-Fe_2O_3 nanoparticles, Tauc plots were plotted. The Tauc plots are used to estimate the band gap energy of the Iron Oxide nanoparticles. Tauc plots are drawn using the Tauc equation, given as **Equation 4.1.**

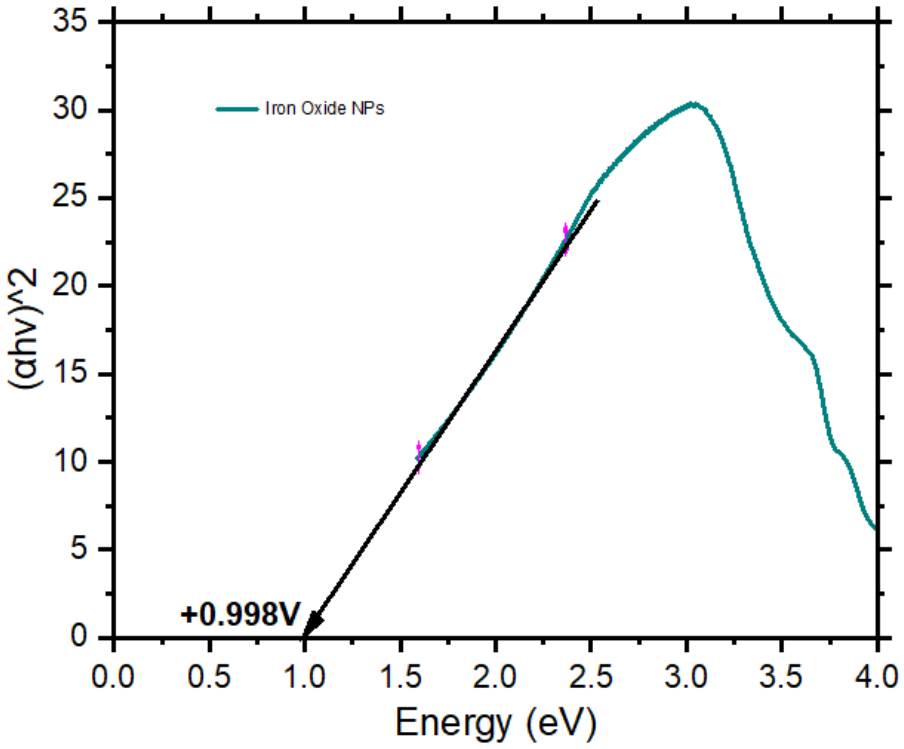

Figure 6.12: The Tauc plot for the iron oxide nanoparticles

In the Tauc plot for the iron oxide nanoparticles, shown in **Figure 6.12**, the estimated band gap energy of the Iron oxide nanoparticles is +0.998V ≈ +1.0V implying the nanoparticles are active in the visible range of the electromagnetic spectrum. The small band gap energy for the iron oxide nanoparticles can be attributed to the quantum confinement effect, as the particles become smaller, the electrons also become confined to a smaller space, hence the smaller band gap energy.

6.3.4 Preparation of tandem cell

The FTO substrates were boiled in acetone for 15 minutes, followed by 15 minutes of boiling in ethanol, and finally rinsed with de-ionized water. After rinsing, the substrates were dried in the air for 15 minutes. Two different Electrophoretic deposition (EPD) cycles were carried out, the first one to deposit TiO_2 nanoparticles and the second to deposit iron nanoparticles. The EPD was performed with a CHI electrochemical analyser, model 608E, using the Chronopotentiometry mode. During EPD, TiO_2 nanoparticles were prepared and deposited as reported Chapter 3. After deposition of TiO_2 nanoparticles, the FTO was annealed in a hot air oven at 80°C for 1 hour, to remove excess solvent. In the deposition of α-Fe_2O_3 nanoparticles, an electrolyte made up of 0.25g of α-Fe_2O_3 dissolved in 50 ml of deionized water was used. EPD was carried out in a manner similar to that reported for deposition of TiO_2 nanoparticles.

After deposition of the α-Fe_2O_3 nanoparticles, the FTO was annealed in a hot air oven at 80°C for 1 hour, to remove excess solvent The final tandem cell device was obtained by drop casting the MOF solutions onto the FTO/TiO_2/ α-Fe_2 O_3. 1 mM slurry solutions of the MOFs were made by dissolving the MOFs in ethanol and then carefully depositing 20µL of the MOF solution on the FTO/TiO_2/ α-Fe_2 O_3 surface. The electrodes were then left to dry under controlled humidity and temperature for a period of three weeks. The final tandem cell is as shown on **Figure 6.13**.

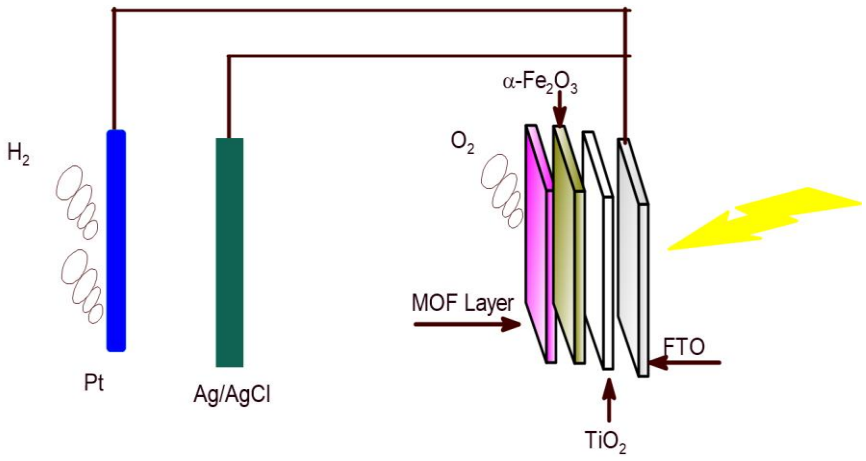

Figure 6.13: Structure of the tandem device

6.3.5 Water splitting experiments

Water splitting experiments were carried out as shown is section 6.2.4

6.3.5.1 Cyclic voltammetry

Cyclic Voltammetry from -0.35V to +1.35V (vs Ag/AgCl) with a positive initial polarity using a scan rate of 0.1V/s.

The cyclic voltammetry curve of the Iron Oxide nanoparticles **(Figure 6.14 a)),** shows remarkedly high current density, compared to the current density produced by the pristine Zn-MOF as shown in **Figure 4.17**. Similarly, the tandem cell shows remarkedly high current density, compared to the original Zn-MOF. The large current densities exhibited when the iron oxide nanoparticles are used, can be attributed to high reactivity exhibited by the iron oxide nanoparticles.

a) b)

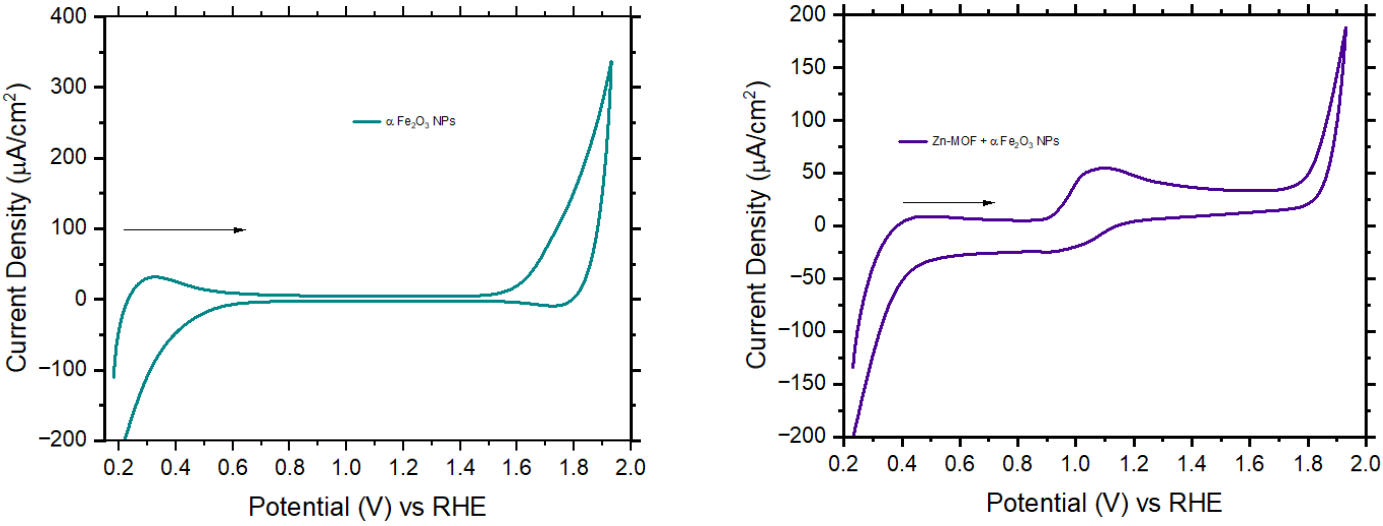

Figure 6.14: CV curves in 0.1M Na_2SO_4 of a) Iron Oxide NPs and b) Zn-MOF + Iron Oxide NPs at 0.1V/s

The Zn-MOF+ Iron Oxide nanoparticles has a sharp anodic peak at +1.08 V and a weak cathodic peak at +0.96 V, to give formal reduction potential of +1.02V. The differences in the anodic and cathodic area, suggest that the redox (Gazzotti et al., 2018) reaction is quasi-reversible. The steep gradient on the anodic peak suggest that the water splitting was very rigorous (Gazzotti et al., 2020). Due to the differences in the magnitude of the current densities between Zn-MOF and the tandem cell, when the curves are superimposed, the curve for Zn-MOF only appears as straight line.

6.3.5.2 OER evolution

To determine the OER performance of the fabricated photoanodes, Linear Sweep Voltammetry from 0.0 V to +1.4 V (vs Ag/AgCl) using a scan rate of 0.01 V/s under illumination and under darkness was carried out.

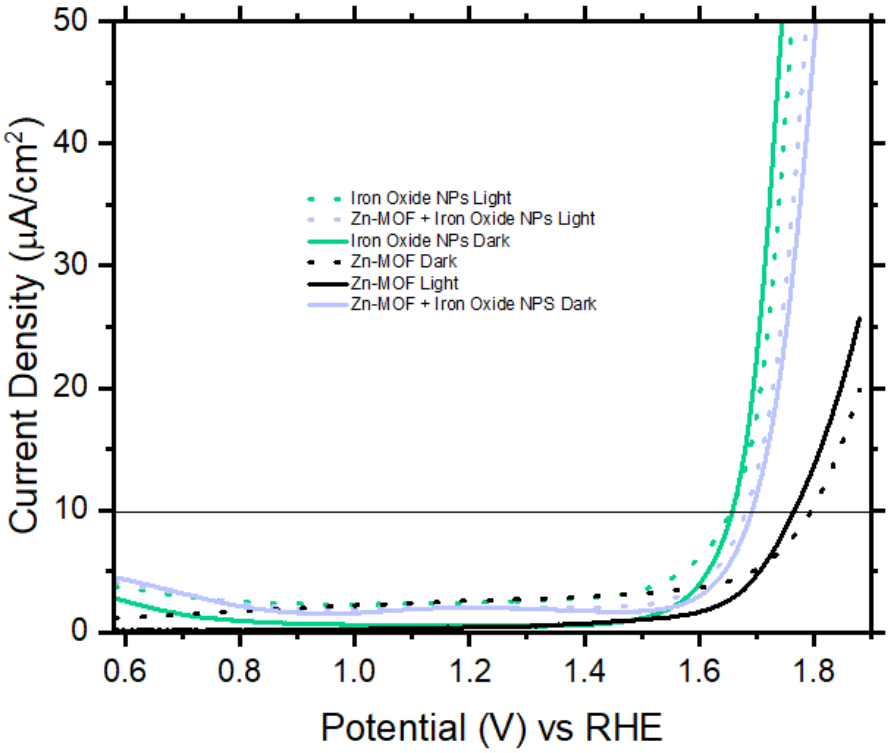

Figure 6.15: OER curves showing comparison between the Iron Oxide Nanoparticles (green line), (Zn-MOF + Iron Oxide Nanoparticles (tandem cell, blue line) and Zn-MOF (black line) carried out in 0.1M Na_2SO_4 at 0.01V/s

In the OER curves of the tandem cell, shown in **Figure 6.15**, a marked reduction in the OER voltage, is witnessed in the tandem cell which showed (+1.68V) vs Zn-MOF (+1.77). Iron oxide nanoparticles because of their nature, high reactivity due to the large surface area exhibited a smaller OER potential (+1.64V) as expected. In the tandem cell a reduction in the onset potential is witnessed compared to the value exhibited by Zn-MOF (+1.77V). The reduction in the onset potential can be attributed to the presence of the α-Fe_2O_3 nanoparticles. The α-Fe_2O_3 being ferromagnetic by nature assisted in the spin-filtering of the electrons that were released which is in agreement with the CISS effect (Naaman, Waldeck, et al., 2019; Naaman & Waldeck, 2012; Waldeck et al., 2021)

6.3.5.3 Photo response measurement for the tandem device

Chronoamperometry at +1.0 V under illumination with light of intensity 100mW/cm^2 chopping light ON/OFF at 10s intervals was carried out for transient photocurrent density measurements for the Zn-MOF+ Iron Oxide nanoparticles. From the curves shown in **Figure 6.16,** it can be noted that a swift and reproducible photocurrent densities are produced for all the photoelectrodes with the α-Fe_2O_3 nanoparticles exhibiting large current densities compared to

the Zn-MOF. In the chronoamperometry curves of the α-Fe_2O_3 nanoparticles and the tandem cell, when the light is chopped off the current is not going to zero instantly as expected.

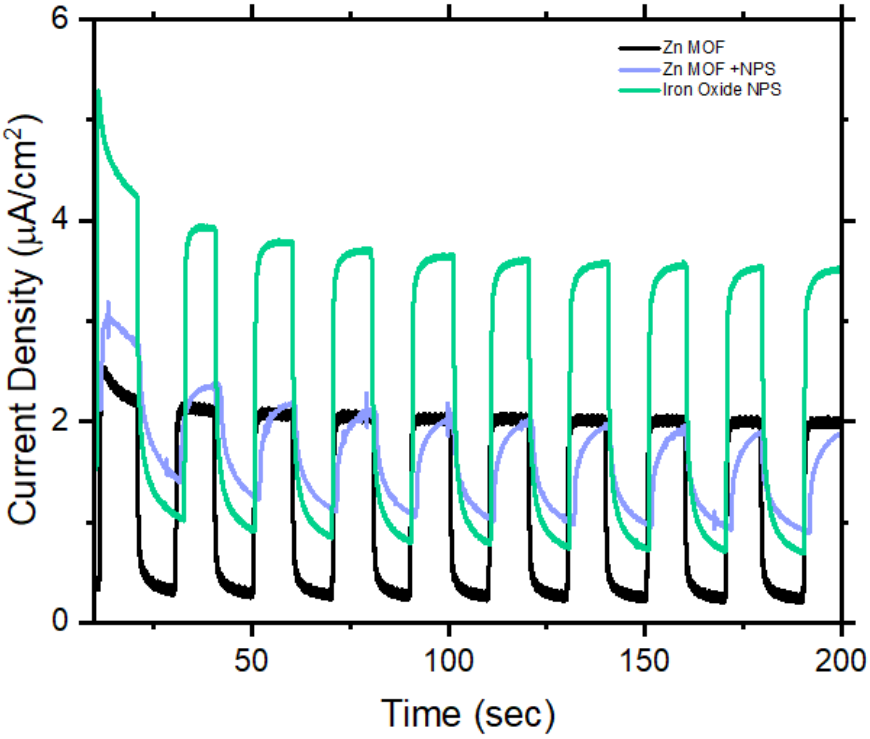

Figure 6.16: Chronoamperometry curves at 1.0V for Zn-MOF(black line), iron nanoparticles (green line) and Zn-MOF + Iron NPs (blue line) under illumination with light of intensity 100mW/cm^2 chopping light ON/OFF at 10s intervals in 0.1M Na_2SO_4 at 0.01V/s scan rate.

In the tandem cell shows low current densities within the 20 second cycle, although repeatable, over the 200 seconds the measurement was run were produced. The chronoamperometry curve for the tandem cell shows a moon shaped curve instead of the straight lines observed in the Zn-MOF photoelectrode. During chronoamperometry measurements the oxidative species must diffuse to the surface of the photoelectrode for the redox reaction to take place. The moon shaped curve can be attributed to the longer length that the oxidative species had to diffuse to get to the photoelectrode surface. Incorporating the α-Fe_2O_3 nanoparticles into the Zn-MOF structure may produce higher photocurrent densities.

It has also been observed that the spin filtering effected by chiral/ferromagnetic materials is not linear (Naaman, Waldeck, et al., 2019) as such more it is important to measure different electrochemical parameters to fully determine the properties of the photoelectrodes.

6.3.5.4 Electrochemical Impedance Spectroscopy

6.3.5.4.1 Mott Schottky

The electronic properties of the tandem cell were investigated using Mott-Schottky measurements. The flat band potential was determined by fitting the lower linear part of the data to **Equation 5.5**. The measurements were performed by sweeping voltages from 0.75V to -0.5V using an AC Voltage with an amplitude of 5mV and frequency of 1000Hz.

Figure 6.17 a) shows the Mott-Schottky curve for the photoelectrodes containing Zn-MOF + Iron Oxide while **Figure 6.17 b),** shows the Mott-Schottky curve for the as synthesised Zn-MOF under darkness and under illumination. In the Zn-MOF + Iron Oxide photoelectrodes, the flat band potential is observed at +0.58V compared to +0.68V that was observed in the Zn-MOF photoelectrodes. In both cases, the flat band potential was similar, indicating that the electronic properties of the TiO_2 was not affected by the materials added on the electrode (Mtangi et al., 2017). There is a reduction of the flat band potential in the tandem cell compared to the photoelectrodes fabricated using the pristine Zn-MOF.

a) b)

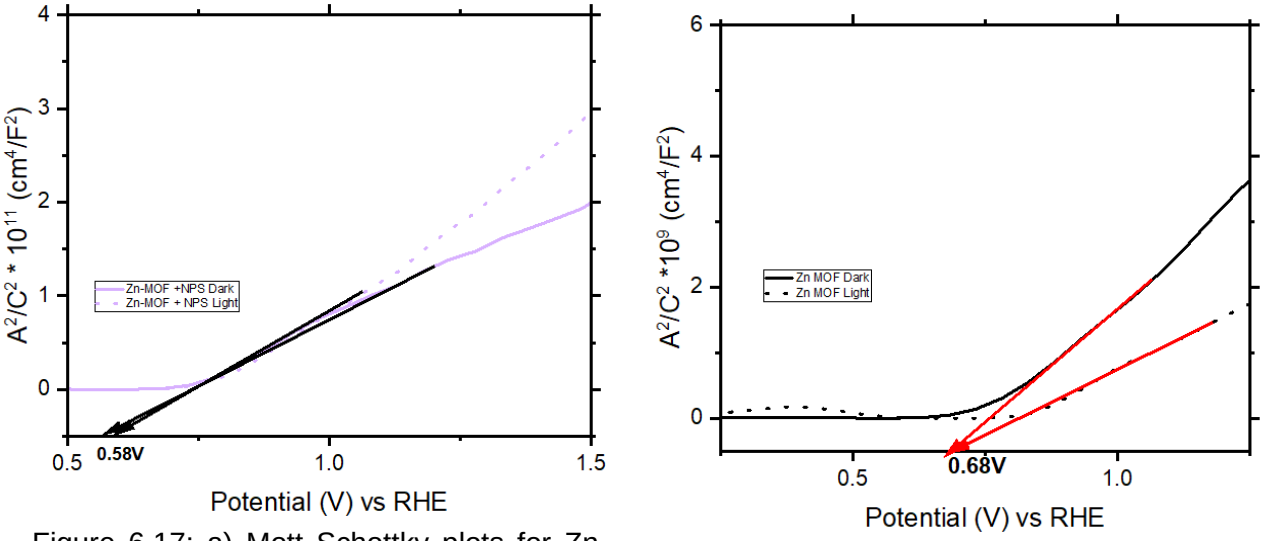

Figure 6.17: a) Mott Schottky plots for Zn-MOF + Iron Oxide NPs in 0.1M Na_2SO_4 b) Mott Schottky plots for Zn-MOF in 0.1M Na_2SO_4

The flat band potentials for the Zn-MOF + Iron Oxide NPs photoelectrode for measurements carried out under darkness and under illumination were found to be +0.58V compared to the +0.68V produced by the pristine Zn-MOF. A shift in the flat band potential of a photoelectrode towards the negative potentials promotes spontaneous water splitting (Guler et al., 2023). The

Mott-Schottky slope has a positive slope, implying that the tandem cell was more of an n-type device (Kusmierek, 2020).

6.3.5.4.2 Nyquist plots

Nyquist plots were used to evaluate the charge transfer mechanism. The Nyquist measurements were carried out by varying frequency between 1MHz and 0.1Hz, with an initial potential of 0V and an amplitude of 5mV.

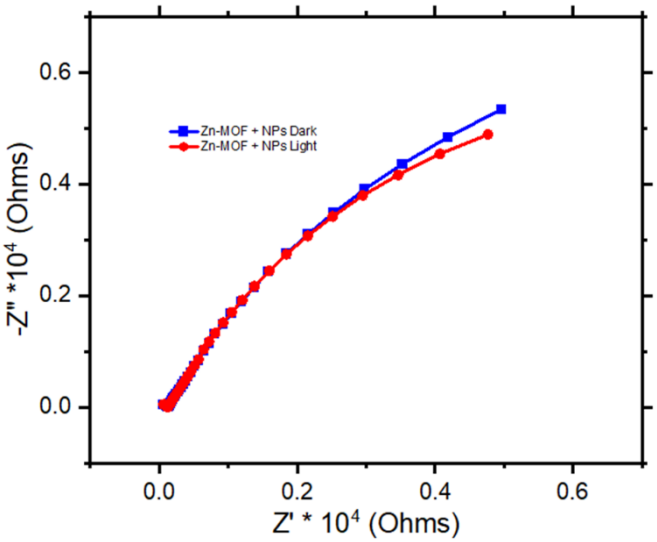

Figure 6.18: Nyquist plot for the tandem cell under darkness (blue curve) and under illumination (red curve)

In the Nyquist plots shown in **Figure 6.18**, two very small semicircles are observed. The magnitude of the resistances is very small when compared to the pristine Zn-MOF, implying very fast charge transfer kinetics in the tandem cell (Feng et al., 2023).

6.3.5.4.3 Bode Plots

Bode plots were used to further investigate the electronic properties of the photoelectrodes. The measurements were carried out by varying frequency between 1MHz and 0.1Hz, with an initial potential of 0V and an amplitude of 5mV under darkness and under illumination. A graph of Log_{10} frequency vs negative phase angle was plotted as shown in **Figure 6.19.**

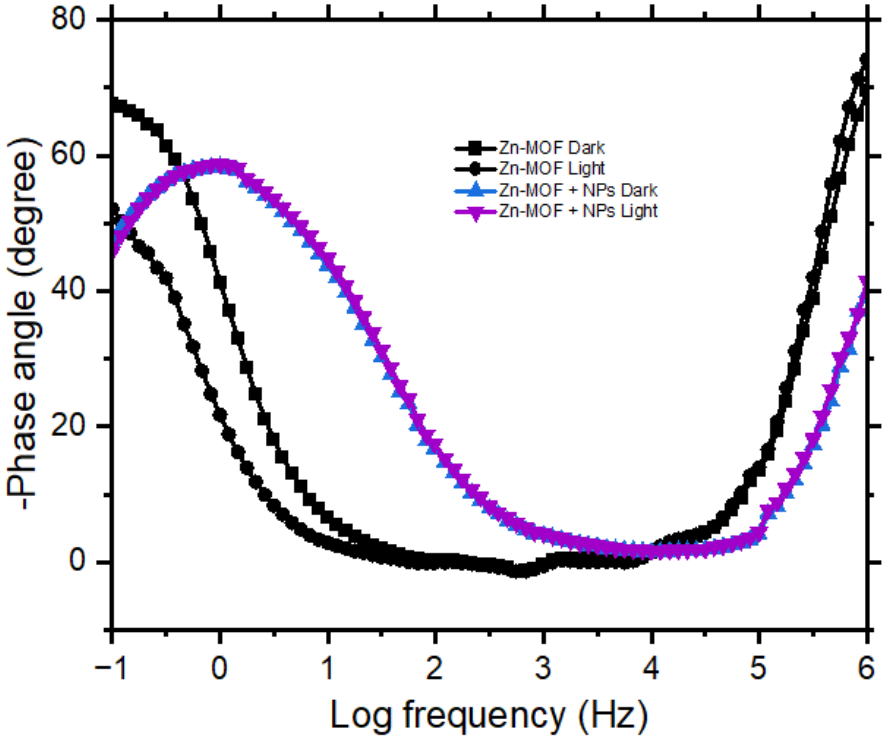

Figure 6.19: Bode plots for the tandem cell shown as a purple curve

In the Zn-MOF + Iron oxide curves, there is a reduction in the characteristic peak, indicating lower recombination rates in these photoelectrodes (Ali et al., 2017). The shift to higher frequencies is also noticeable, implying that the charge transfer processes are taking place in the electrode/electrolyte boundaries as opposed to the bulk electrolyte as is prevalent in the Zn-MOF (Toledo et al., 2017).

6.3.5.5 Activity

To investigate the activity of the tandem device, the open circuit potential, OCP in the dark and under illumination at zero current. The tandem device (Zn-MOF + iron oxide Nanoparticles) produced an OCP curve, indicating that an equilibrium was reached between the electrolyte and the device. During water splitting, when the semiconductor comes into contact with the electrolyte, the Fermi level of the semiconductor is adjusted to the Fermi level of the electrolyte (Gelderman et al., 2007).

In the open circuit potential measurements (**Figure 6.20**), it was observed that once the light was switched on, the voltages became negative but when the light source was switched off, the potential became more positive. This observation can be attributed to the nature of the photoelectrode, for n-type electrodes the tandem cell produced open circuit voltages under

illumination an indication that when the light was switched on, the surface of the electrode was flooded by electrons (Hankin et al., 2019).

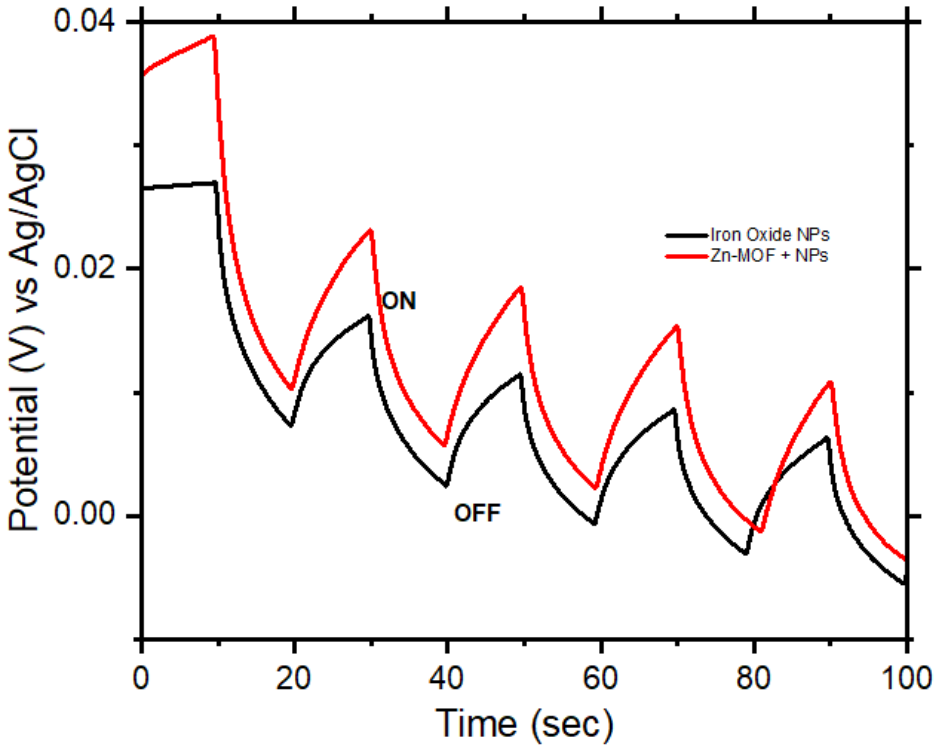

Figure 6.20: OCP Curves for Iron Oxide NPs vs Zn-MOF + Iron Oxide NPs in 0.1M Na_2SO_4 at 0.01V/s scan rate.

6.3.5.6 Overpotential

The overpotential was evaluated by running a Tafel plot from -1.5V to +1.5V at a scan rate of 0.01V/s. Oxygen evolution mechanisms as well as the reaction kinetics are assessed using Tafel plot analysis. Tafel plots are also used to evaluate the catalytic properties of photocatalyst materials that may be under study (Aralekallu et al., 2020). The reaction's rate-determining step can also be explained by the Tafel slope and it provides information on the sensitivity of current response to a given voltage. The catalyst which has a large current density and lower Tafel slope is treated as the good quality OER catalyst. The Tafel slope was obtained according to the Tafel equation (E = A + B *log j,) where E, j, and B correspond to potential, current density, and Tafel slope, respectively (Cardoso et al., 2015). To investigate the kinetics of chiral catalysts during OER the overpotential was determined and are shown in the plots in **Figure 6.21**.

a) b)

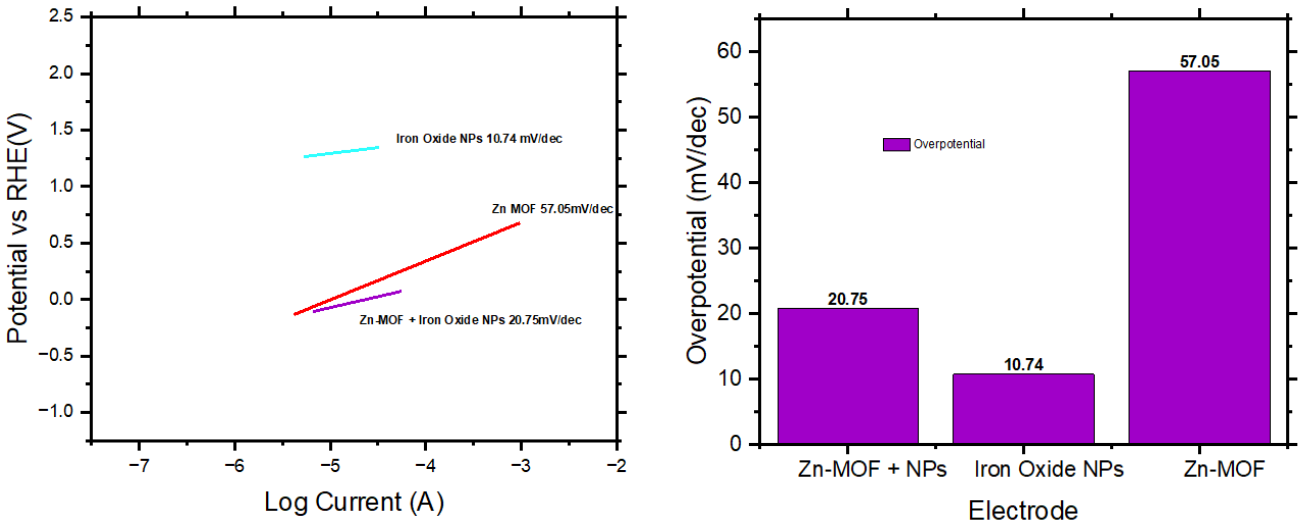

Figure 6.21: a) Tafel plot of Mixed Metal Zn-MOF showing overpotential in mVdec- [1] b) A bar chart showing the Mixed Metal Zn-MOF overpotentials.

A comparison of the overpotentials show that Zn-MOF a material that does not possess any ferromagnetism has an overpotential of 57.05mV/dec while the Iron oxide nanoparticles exhibit an overpotential of 10.74mV/dec. The photoelectrodes containing Zn-MOF and Iron Oxide Nanoparticles have an overpotential of 20.75mV/dec which is relatively small compared to the overpotential of the pristine Zn-MOF. The reduction of the overpotential in the Zn-MOF +Iron oxide nanoparticles is supported not only by the CISS effect (Naaman & Waldeck, 2012; Waldeck et al., 2021) but also evidence in section 2.2.6.1, where researchers have showed both theoretically (Torun et al., 2013) and experimentally (Heard & Lennox, 2020) that overpotentials tend to be lower in inherently ferromagnetic materials. The inclusion of the α-Fe_2O_3 nanoparticles into the electrode structure by fabricating a tandem cell have helped to reduce the overpotential significantly.

From the photocatalytic activity studies of the photocatalysts incorporated on the tandem device, an energy diagram can be drawn and this is shown in **Figure 6.22.**

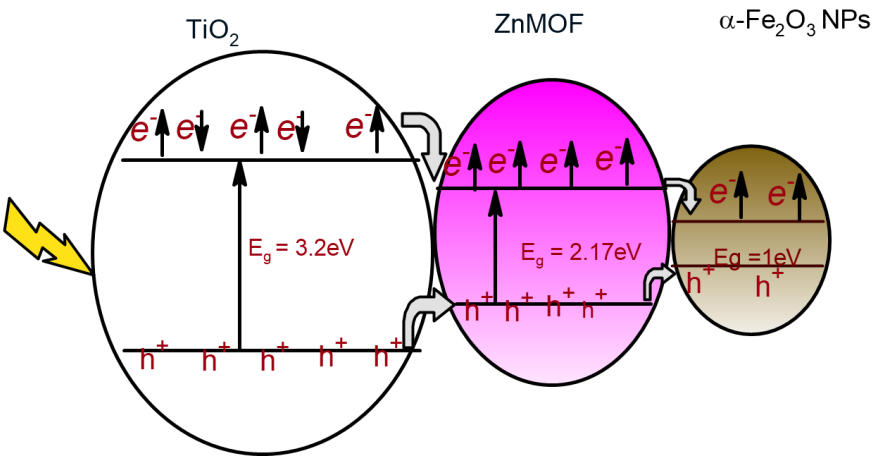

Figure 6.22 Proposed energy diagram for the Tandem device

The energy diagram shows how the different materials exhibit different energy band gaps and this shows how the tandem device is able to harness light from different wavelengths, hence energy. In the fabrication of a tandem device that incorporates chiral and/or ferromagnetic materials, the assumption that the materials will work in a linear is not always correct (Naaman, Waldeck, et al., 2019) It is important to comprehensively carry out the electrochemical techniques to fully determine the properties of the photoelectrodes.

6.4 CONCLUSION

Photoelectrodes incorporating ferromagnetic elements (cobalt and nickel) were successfully synthesised through transmetalation. The properties of the mixed metal MOFs were evaluated through XRD, Uv-Vis as well as ICP-OES. ICP-OES confirmed the presence of the Co^{2+} and Ni^{2+} in the MOF structure, while XRD revealed improved crystallinity in the mixed-metal MOFs. In OER measurements, the mixed-metal MOFs had a smaller onset potential compared to the parent Zn-MOF an indication that mixed-metal MOFs would perform better in water splitting compared to the parent MOF.

To further investigate effect of ferromagnetism in water splitting a tandem device incorporating α-Fe_2O_3 nanoparticles was fabricated. The nanoparticles were tested for photocatalytic activity, and found to be active in the visible range of the electromagnetic spectrum. In OER measurements are remarkable reduction in the onset potential was observed. However, in chronoamperometry the chronoamperometric curves exhibited a different shape as well as producing current densities were lower than expected and this was attributed to the large

distance that the oxidative species had to diffuse to get to the surface of the photoelectrode. The results from the tandem cell electrochemical measurements also show that a number of electrochemical techniques are needed to characterise the fabricated photoelectrodes to properly ascertain their properties

The inclusion of the ferromagnetic materials into the zinc-based photoelectrodes have shown a remarkable improvement in the performance of the PEC in both the mixed -metal MOFs and the tandem cell, however, further studies to further characterise and optimise both the tandem cell and the mixed-metal photoelectrodes are recommended.

6.5 REFERENCES

1) Ali, A., Li, X., Song, J., Yang, S., Zhang, W., Zhang, Z., Xia, R., Zhu, L., & Xu, X. (2017). Nature-mimic ZnO nanoflowers architecture: Chalcogenide quantum dots coupling with ZnO/ZnTiO3 Nanoheterostructures for efficient photoelectrochemical water splitting. *Journal of Physical Chemistry C*, *121*(39), 21096–21104. https://doi.org/10.1021/acs.jpcc.7b04701
2) Altaf, M., Sohail, M., Mansha, M., Iqbal, N., Sher, M., Fazal, A., Ullah, N., & Isab, A. A. (2018). Synthesis, Characterization, and Photoelectrochemical Catalytic Studies of a Water-Stable Zinc-Based Metal–Organic Framework. *ChemSusChem*, *11*(3), 542–546. https://doi.org/10.1002/cssc.201702122
3) Aralekallu, S., Sajjan, V. A., Palanna, M., Prabhu C P, K., Hojamberdiev, M., & Sannegowda, L. K. (2020). Ni foam-supported azo linkage cobalt phthalocyanine as an efficient electrocatalyst for oxygen evolution reaction. *Journal of Power Sources*, *449*. https://doi.org/10.1016/j.jpowsour.2019.227516
4) Bedoya-Lora, F. E., Holmes-Gentle, I., & Hankin, A. (2021). Electrochemical techniques for photoelectrode characterisation. In *Current Opinion in Green and Sustainable Chemistry* (Vol. 29). Elsevier B.V. https://doi.org/10.1016/j.cogsc.2021.100463
5) Cardoso, D. S. P., Amaral, L., Santos, D. M. F., Šljukić, B., Sequeira, C. A. C., Macciò, D., & Saccone, A. (2015). Enhancement of hydrogen evolution in alkaline water electrolysis by using nickel-rare earth alloys. *International Journal of Hydrogen Energy*, *40*(12), 4295–4302. https://doi.org/10.1016/j.ijhydene.2015.01.174
6) Chen, Q., Fan, G., Fu, H., Li, Z., & Zou, Z. (2018). Tandem photoelectrochemical cells for solar water splitting. In *Advances in Physics: X* (Vol. 3, Issue 1, pp. 863–884). Taylor and Francis Ltd. https://doi.org/10.1080/23746149.2018.1487267
7) Digdaya, I. A., Rodriguez, P. P., Ma, M., Adhyaksa, G. W. P., Garnett, E. C., Smets, A. H. M., & Smith, W. A. (2016). Engineering the kinetics and interfacial energetics of Ni/Ni-Mo catalyzed amorphous silicon carbide photocathodes in alkaline media. *Journal of Materials Chemistry A*, *4*(18), 6842–6852. https://doi.org/10.1039/c5ta09435f
8) Feng, T., Chen, W., Xue, J., Cao, F., Chen, Z., Ye, J., Xiao, C., & Lu, H. (2023). Spin Polarization of Chiral Amorphous Fe-Ni Electrocatalysts Enabling Efficient Electrochemical Oxygen Evolution. *Advanced Functional Materials*, *33*(27), 1-10. https://doi.org/10.1002/adfm.202215051
9) Gazzotti, M., Arnaboldi, S., Grecchi, S., Giovanardi, R., Cannio, M., Pasquali, L., Giacomino, A., Abollino, O., & Fontanesi, C. (2018). Spin-dependent electrochemistry:

Enantio-selectivity driven by chiral-induced spin selectivity effect. *Electrochimica Acta*, *286*, 271–278. https://doi.org/10.1016/j.electacta.2018.08.023

10) Gazzotti, M., Stefani, A., Bonechi, M., Giurlani, W., Innocenti, M., & Fontanesi, C. (2020). Influence of Chiral Compounds on the Oxygen Evolution Reaction (OER) in the Water Splitting Process. *Molecules*, *25*(17). https://doi.org/10.3390/molecules25173988
11) Gelderman, K., Lee, L., & Donne, S. W. (2007). Flat-Band Potential of a Semiconductor: W Using the Mott-Schottky Equation. In *In the Laboratory www.JCE.DivCHED.org,* (Vol. 84, Issue 4). www.JCE.DivCHED.org
12) Guler, A. C., Antos, J., Masar, M., Urbanek, M., Machovsky, M., & Kuritka, I. (2023). Comprehensive evaluation of photoelectrochemical performance dependence on geometric features of ZnO nanorod electrodes. *Nanoscale Advances*, *5*(11), 3091–3103. https://doi.org/10.1039/d3na00089c
13) Hadipour, A., de Boer, B., & Blom P.W.M (2008). Organic tandem and multi-junction solar cells, *Advanced Functional Materials* 18(2) 169-181 https://doi.org/10.1002/adfm.200700517
14) Hankin, A., Bedoya-Lora, F. E., Alexander, J. C., Regoutz, A., & Kelsall, G. H. (2019). Flat band potential determination: Avoiding the pitfalls. *Journal of Materials Chemistry A*, *7*(45), 26162–26176. https://doi.org/10.1039/c9ta09569a
15) Heard, D. M., & Lennox, A. J. J. (2020). Electrode Materials in Modern Organic Electrochemistry. *Angewandte Chemie*, *132*(43), 19026–19044. https://doi.org/10.1002/ange.202005745
16) Iacomi, F., Calin, G., Scarlat, C., Irimia, M., Doroftei, C., Dobromir, M., Rusu, G. G., Iftimie, N., & Sandu, A. V. (2011). Functional properties of nickel cobalt oxide thin films. *Thin Solid Films*, *520*(1), 651–655. https://doi.org/10.1016/j.tsf.2011.08.067
17) Jaryal, R., Kumar, R., & Khullar, S. (2022). Mixed metal-metal organic frameworks (MM-MOFs) and their use as efficient photocatalysts for hydrogen evolution from water splitting reactions. In *Coordination Chemistry Reviews* (Vol. 464). Elsevier B.V. https://doi.org/10.1016/j.ccr.2022.214542
18) Kusmierek, E. (2020). A CeO2 semiconductor as a photocatalytic and photoelectrocatalytic material for the remediation of pollutants in industrial wastewater: A review. In *Catalysts* (Vol. 10, Issue 12, pp. 1–54). MDPI. https://doi.org/10.3390/catal10121435
19) Masoomi, M. Y., Morsali, A., Dhakshinamoorthy, A., & Garcia, H. (2019). Mixed-Metal MOFs: Unique Opportunities in Metal–Organic Framework (MOF) Functionality and Design. *Angewandte Chemie*, *131*(43), 15330–15347. https://doi.org/10.1002/ange.201902229

20) Mtangi, W., Tassinari, F., Vankayala, K., Vargas Jentzsch, A., Adelizzi, B., Palmans, A. R. A., Fontanesi, C., Meijer, E. W., & Naaman, R. (2017). Control of Electrons' Spin Eliminates Hydrogen Peroxide Formation during Water Splitting. *Journal of the American Chemical Society*, *139*(7), 2794–2798. https://doi.org/10.1021/jacs.6b12971
21) Naaman, R., Paltiel, Y., & Waldeck, D. H. (2019). Chiral molecules and the electron spin. *Nature Reviews Chemistry*, *3*(4), 250–260. https://doi.org/10.1038/s41570-019-0087-1
22) Naaman, R., & Waldeck, D. H. (2012). Chiral-induced spin selectivity effect. *Journal of Physical Chemistry Letters*, *3*(16), 2178–2187. https://doi.org/10.1021/jz300793y
23) Naaman, R., & Waldeck, D. H. (2015). Spintronics and chirality: Spin selectivity in electron transport through chiral molecules. *Annual Review of Physical Chemistry*, *66*(January), 263–281. https://doi.org/10.1146/annurev-physchem-040214-121554
24) Naaman, R., Waldeck, D. H., & Paltiel, Y. (2019). Chiral molecules-ferromagnetic interfaces, an approach towards spin-controlled interactions. In *Applied Physics Letters* (Vol. 115, Issue 13). American Institute of Physics Inc. https://doi.org/10.1063/1.5125034
25) Petrucci, R. H., Geoffrey Herring, F., Madura, J. D., Bissonnette, C., P. (2011). *General Chemistry Principles and Modern Applications TENTH EDITION,* Pearson Canada, The Iron Triad,pp 1052-1054, Toronto, Canada.
26) Prévot, M. S., & Sivula, K. (2013). Photoelectrochemical tandem cells for solar water splitting. *Journal of Physical Chemistry C*, *117*(35), 17879–17893. https://doi.org/10.1021/jp405291g
27) Seenivasan, S., Moon, H., & Kim, D. H. (2022). Multilayer Strategy for Photoelectrochemical Hydrogen Generation: New Electrode Architecture that Alleviates Multiple Bottlenecks. *Nano-Micro Letters*, *14*(1). https://doi.org/10.1007/s40820-022-00822-8
28) Sherman, B. D., Sheridan, M. V., Wee, K. R., Marquard, S. L., Wang, D., Alibabaei, L., Ashford, D. L., & Meyer, T. J. (2016). A Dye-Sensitized Photoelectrochemical Tandem Cell for Light Driven Hydrogen Production from Water. *Journal of the American Chemical Society*, *138*(51), 16745–16753. https://doi.org/10.1021/jacs.6b10699
29) Toledo, R. P., Dias, C. E. S., Huanca, D. R., & Salcedo, W. J. (2017). Electrochemical impedance study of fresh and passivated macroporous silicon for sensors. *2017 32nd Symposium on Microelectronics Technology and Devices (SBMicro)*, 1–4. https://doi.org/10.1109/SBMicro.2017.8113011
30) Torun, E., Fang, C. M., De Wijs, G. A., & De Groot, R. A. (2013). Role of magnetism in catalysis: RuO2 (110) surface. *Journal of Physical Chemistry C*, *117*(12), 6353–6357. https://doi.org/10.1021/jp4020367

31) Tran, D. P. H., Pham, M. T., Nguyen, T. H., Wang, Y. F., & You, S. J. (2023). Photocatalytic membrane reactors (PMRs) for hydrogen production. In *Current Developments in Biotechnology and Bioengineering: Membrane Technology for Sustainable Water and Energy Management* (pp. 19–42). Elsevier. https://doi.org/10.1016/B978-0-443-19180-0.00022-5

32) Waldeck, D. H., Naaman, R., & Paltiel, Y. (2021). The spin selectivity effect in chiral materials. *APL Materials*, *9*(4). https://doi.org/10.1063/5.0049150

33) Wierzbicka, E., Szaniawska-Białas, E., Schultz, T., Basilio, A. O., Siemiaszko, D., Ray, K., Koch, N., Pinna, N., & Polański, M. (2024). Long-Term Stability of Light-Induced Ti3+ Defects in TiO2 Nanotubes for Amplified Photoelectrochemical Water Splitting. *ChemSusChem*, *17*(5). https://doi.org/10.1002/cssc.202301614

34) Wu, F., Cao, F., Liu, Q., Lu, H., & Li, L. (2016). Enhancing photoelectrochemical activity with three-dimensional p-CuO/n-ZnO junction photocathodes. *Science China Materials*, *59*(10), 825–832. https://doi.org/10.1007/s40843-016-5054-6

35) Xiao, Y., Guo, X., Yang, N., & Zhang, F. (2021). Heterostructured MOFs photocatalysts for water splitting to produce hydrogen. In *Journal of Energy Chemistry* (Vol. 58) 508-522. https://doi.org/10.1016/j.jechem.2020.10.008

36) Zahra, T., Ahmad, K. S., Thomas, A. G., Zequine, C., Gupta, R. K., Malik, M. A., & Sohail, M. (2020). Phyto-inspired and scalable approach for the synthesis of PdO-2Mn2O3: A nano-material for application in water splitting electro-catalysis. *RSC Advances*, *10*(50), 29961–29974. https://doi.org/10.1039/d0ra04571c

37) Zhang, J., Gong, W., Yin, H., Wang, D., Zhang, Y., Zhang, H., Wang, G., & Zhao, H. (2021). In Situ Growth of Ultrathin Ni(OH)2 Nanosheets as Catalyst for Electrocatalytic Oxidation Reactions. *ChemSusChem*, *14*(14), 2935–2942. https://doi.org/10.1002/cssc.202100811

38) Zhang, K., Ma, M., Li, P., Wang, D. H., & Park, J. H. (2016). Water Splitting Progress in Tandem Devices: Moving Photolysis beyond Electrolysis. In *Advanced Energy Materials* (Vol. 6, Issue 15). Wiley-VCH Verlag. https://doi.org/10.1002/aenm.201600602

39) Zhang, T., Jin, Y., Shi, Y., Li, M., Li, J., & Duan, C. (2019). Modulating photoelectronic performance of metal–organic frameworks for premium photocatalysis. In *Coordination Chemistry Reviews* (Vol. 380, pp. 201–229). Elsevier B.V. https://doi.org/10.1016/j.ccr.2018.10.001

40) Zhu, D., Liu, J., Wang, L., Du, Y., Zheng, Y., Davey, K., & Qiao, S. Z. (2019). A 2D metal-organic framework/Ni(OH) 2 heterostructure for an enhanced oxygen evolution reaction. *Nanoscale*, *11*(8), 3599–3605. https://doi.org/10.1039/c8nr09680e

7 CONCLUSIONS

7.1 SUMMARY

Hydrogen is a clean fuel which when combusted produces water. The use of hydrogen as a fuel has slowly been on the increase and hydrogen is projected as the leading fuel beyond 2050 (Espegren et al., 2021; Holechek et al., 2022; Staffell et al., 2019). Hydrogen fuel cells for use in electric vehicles as well as power generation is an emerging field. The declarations made by leading car manufacturers to phase out fossil by 2035 has made the search for new sustainable methods more competitive. The drive to find a green and renewable energy source has led to the production of hydrogen, through solar driven processes such as photobiological, photoelectrochemical and solar thermochemical methods. With the advent of the chiral induced spin selectivity (CISS) effect, research has moved towards the use of chiral based photoelectrodes for water splitting. The CISS effect states that electrons transmitted through a chiral photocatalyst, becomes spin filtered, allowing only electrons that are spinning in one direction to pass through (Naaman & Waldeck, 2012). Researchers have also looked at how the CISS effect can be used to improve the photoelectrochemical cells with some researchers developing chiral photoelectrodes (Feng et al., 2023; K. B. Ghosh et al., 2019; S. Ghosh et al., 2020; Mtangi et al., 2015, 2017; Vadakkayil et al., 2023; Zhang et al., 2018, 2021), while others used chiral electrolyte (Gazzotti et al., 2018, 2020). Various metal oxides (Khalid et al., 2021), perovskites (Huang et al., 2020) and metal organic frameworks (MOFs) have been investigated as possible photocatalysts for the photoelectrocatalytic splitting of water.

This thesis focused on the fabrication and characterization of chiral photoelectrodes for use in photoelectrocatalytic water splitting. The photoelectrodes were fabricated by depositing chiral MOFs synthesised using chiral molecules R (-) and S (+) Camphor Sulphonic Acid as well as L Cysteine. The chiral linkers were chosen because it was deemed their small size would not disrupt the MOF structures, while iron and zinc were selected because they are cheaper compared to other the metals that have been used as OER photocatalysts as well as being non-toxic. An amine functionalised form of both the Zn-MOF and the MIL 53 was also synthesised to assess its light harvesting properties when compared to the chiral MOFs.

The properties of the synthesised MOFs were evaluated using Fourier Transform Infrared Spectroscopy, Uv-Vis Spectroscopy, Thermogravimetric analysis, Scanning Electron Microscopy coupled with Energy Dispersive Spectroscopy and Field Emission Scanning Electron Microscopy.

Nuclear Magnetic Resonance Spectroscopy was used to evaluate the extent of the formation of one of the linkers (bpcda) that was synthesised *in-situ* based on chemical shifts of a proton or carbon. Powder X-ray diffraction was used to check the crystallinity of the MOFs as well as phase purity and phase transition of the prepared material. Inductively Couple Plasma Optical Emission was used in detecting and quantitatively determining the trace metal elements in the Mixed-Metal MOF.

7.2 PHOTOELECTROCATALYTIC WATER SPLITTING USING CHIRAL DOPED ZN-MOF

Chiral doped Zn-MOFs were synthesised using the solvothermal method using terephthalic acid and N,N'-bis(pyridin-4-ylmethylene)cyclohexane-1,4-diamine (bpcda) which was synthesised *in-situ* and the chiral molecules R (-) and S (+) Camphor Sulphonic Acid as well as L Cysteine. Successful synthesis of the linker, bpcda was assessed Nuclear Magnetic Resonance Spectroscopy (NMR). The appearance of chemical shifts for N-H (Amine), C=O (Carbonyl), Cyclohexyl, -CH_2- (Methylene) and Pyridyl groups of both ligands (4-Pyridylcarboxyldehyde and (1r,4r)-cyclohexane-1,4-diamine) in ^{1}H and ^{13}C NMR confirmed that the linker, N,N'-bis(pyridin-4-ylmethyl)cyclohexane-1,4-diamine was successfully synthesized

FTIR spectroscopy showed the successful formation of the Zn-O bond at 534 cm^{-1}. Successful incorporation of the linker was observed at 1220cm^{-1} attributed to the C-N stretching due to aromatic amine. In the chiral MOFs red shift was observed at 2088 cm^{-1}, a peak previously observed at 1923 cm^{-1} was now observed at 2088 $cm^{-1}$and this can be attributed to the formation of hydrogen bonds between the chiral moieties and the zinc salt. Successful synthesis of the Zn-MOF was assessed using PXRD by comparing the calculated PXRD pattern and experimental PXRD pattern of the Zn-MOF. PXRD was used to evaluate phase changes after the addition of the chiral dopants. Thermogravimetric analysis of the Zn-MOF, showed a 42% weight loss with the framework decomposing around 366°C

In the Uv-Vis measurements the reduction in the band gap energy was observed in Zn-MOF doped with L-Cysteine, R (-) camphor sulphonic acid as well as the amine functionalised Zn-MOF (Zn-MOF-NH_2). SEM revealed the lamellar structure of the Zn-MOF while FESEM further elucidated the surface morphology to show a flower petal like arrangement which offers a large surface area for the water splitting reaction. EDS was able to confirm the successful inclusion of the chiral motifs in the Zn-MOF. The difference in the signal produced in cyclic voltammetry curves during chiral recognition confirmed the chiral nature of the photoelectrodes.

In water splitting experiments, linear sweep voltammetry, cyclic voltammetry, chronoamperometry, open circuit potential, electrochemical impedance spectroscopy as well as Tafel plot measurements were carried out. In CV measurements, weak anodic and cathodic peaks were observed in the Zn-MOF curve while no peak was observed for Zn-MOF R CSA and Zn-MOF L Cysteine, while Zn-MOF S CSA showed a significant peak. In OER measurements the onset potential was significantly reduced in the chiral photoelectrodes. Photo response measurements confirmed that the chiral photoelectrodes are photocatalytic

in nature as witnessed by the sudden spikes in the current density when the light was switched on and the sudden decay when the light source was turned off.

Swift and reproducible photocurrents for all samples were observed during chronoamperometry measurements that were carried out under illumination with light intensity 100mW/cm^2 chopping light ON/OFF.

The photoelectrodes also exhibited great stability as they were able to sustain a constant current density over extended periods of time. In Mott Schottky measurements, the flat band potentials were found to be almost similar for all photoelectrodes when measured under illumination and under darkness and this was confirmation that the electronic properties of the TiO_2 was not affected by the deposited MOF pastes. The positive slope of the Mott Schottky measurements indicates that the zinc-based MOFs are n-type semiconductors and this was confirmed in OCP measurements. In OCP measurements the n-type nature of the electrodes was confirmed. During OCP measurements, when the electrodes were illuminated with light the OCP values became more negative indicating that when the light was switched on, electrons were released and made the surface of the electrode more negative. All the photoelectrodes produced OCP curves and this is an indication that they were all able to reach an equilibrium between photoelectrode and electrolyte.

Charge transfer kinetics were evaluated using Nyquist as well as Bode plots and it was observed that the chiral photoelectrodes produced small semicircle in the high frequency regions compared to the pristine Zn-MOF and this is an indication that charge transfer is faster in the chiral photoelectrodes.

To evaluate the kinetics of chiral photoelectrodes, the overpotential was determined using Tafel plot analysis. The chiral photoelectrodes displayed lower overpotentials of 32.14mV/dec and 22.48mV/dec for Zn-MOF S CSA and Zn-MOF L Cysteine respectively, vs 57.05mV/dec for the achiral Zn-MOF. The amount of H_2O_2 present was evaluated using spectrophotometric titration. Electrochemistry in the chronoamperometric mode was carried out at +1.23V for 40minutes while hydrogen and oxygen were evolved on the Platinum and the working electrode respectively. A sample of the electrolyte was treated with o-tolidine and assessed for the presence of hydrogen peroxide using the Uv-Vis spectrophotometer. Hydrogen peroxide was detected in the electrolytes from the PEC in which Bare TiO_2, Zn-MOF and Zn-MOF-NH_2 while no hydrogen peroxide was detected from the electrolyte in which chiral photoelectrodes were used. A modified Hoffman Apparatus was used to collect hydrogen using the best performing chiral Zn-MOF photoelectrode

7.3 APPLICATION OF IRON BASED CHIRAL METAL ORGANIC FRAMEWORKS IN PHOTOELECTROCATALYTIC WATER SPLITTING

Iron based chiral doped MOFs of the MIL 53 group were synthesised using the solvothermal method using terephthalic acid while chirality was induced by adding and the chiral molecules R (-) and S (+) Camphor Sulphonic Acid as well as L Cysteine.

FTIR spectroscopy showed the successful formation of the Fe-O bond in the fingerprint region at 551cm^{-1}. Successful incorporation of the linker was observed at observed at 1660 cm^{-1} which was assigned to the carboxylic C=O bonds stretching vibration confirming the absence of free ligand in the synthesized MIL 55 sample. A new peak was observed at new peak is observed at 2048 cm^{-1} in MIL 53 L-Cysteine and MIL 53 R while absent from MIL 53 and this was attributed to the formation of a C=S bond.

Successful synthesis of the MIL 53 was assessed using PXRD by comparing the calculated PXRD pattern and experimental PXRD pattern of the MIL 53. PXRD was used to evaluate phase changes after the addition of the chiral dopants. In thermogravimetric analysis of the MIL 53, a weight loss of 70% was observed with the framework decomposing around 348°C

In Uv-Vis measurements the reduction in the band gap energy was observed in all the three chiral derivatives of MIL 53. SEM revealed the regular morphology with uniform hexagonal bipyramid while FESEM confirmed the highly crystalline nature of the MIL 53. EDS confirmed the successful inclusion of the chiral moieties in the MIL 53. Cyclic voltammetry was used in chiral recognition, change in the signal produced in cyclic voltammetry curves confirmed the chiral nature of the photoelectrodes.

Linear sweep voltammetry, cyclic voltammetry, chronoamperometry, open circuit potential, Tafel plot analysis, and electrochemical impedance spectroscopy measurements were carried out during the water splitting measurements. In CV measurements, strong anodic and cathodic peaks were observed in all the chiral doped MIL 53 photoelectrodes with MIL 53 doped with L Cysteine going further to show two anodic and two cathodic peaks and this can be attributed to the possibility of different groups found in L-Cysteine bonding to the MIL 53. The strong anodic and cathodic peaks are proof of the intensity or extent of the water splitting that was taking place. In OER measurements remarkable photo current densities were produced by the chiral photoelectrodes at +1.23V compared to those produced by the pristine MIL 53. Photo response measurements confirmed the photocatalytic behaviour of the MOFs as witnessed by the rapid spikes in the current density when the light was switched on and the sudden decay when the light source was turned off.

In chronoamperometry measurements, instantaneous and reproducible photocurrents for were observed for all samples when the light was chopped ON/OFF.

Photoelectrodes also exhibited great stability as they were able to reproduce the same results even after being used for extended periods of time. In Mott Schottky measurements, the flat band potentials were found to be almost similar for all electrodes when measured under illumination and under darkness and this was confirmation that the electronic properties of the TiO_2 was not affected by the deposited MOF pastes. The positive slope of the Mott Schottky measurements indicate that the Iron based MOFs are n-type semiconductors and this was confirmed in OCP measurements. In OCP measurements the n-type nature of the photoelectrodes were confirmed. All the photoelectrodes produced OCP curves and this is an indication that they were all able to reach an equilibrium between photoelectrode and electrolyte.

Tafel plots were used to measure the overpotential of the chiral photoelectrodes. The chiral photoelectrodes exhibited lower overpotentials of 10.5 mV/dec and 17.5mV/dec for MIL 53 S CSA and MIL 53 L Cysteine respectively, vs 32.18mV/dec for the achiral MIL 53. The amount of H_2O_2 present was evaluated using spectrophotometric titration. Electrochemistry in the chronoamperometric mode was carried out at +1.23V for 40minutes while Hydrogen and Oxygen were evolved on the Platinum and the Working Electrode respectively. A sample of the electrolyte was treated with o-tolidine and assessed for the presence of Hydrogen Peroxide using the Uv-Vis spectrophotometer. Hydrogen peroxide was detected in the electrolytes from the PEC in which Bare TiO_2 was used as an electrode, while no hydrogen peroxide was detected from the electrolyte in which chiral photoelectrodes were used. A modified Hoffman Apparatus was used to collect hydrogen using the best performing chiral MIL 53 photoelectrode

7.4 FABRICATION AND CHARACTERIZATION OF FERROMAGNETIC BASED PHOTOELECTRODES.

To address the shortcomings of the Zn-MOF based photoelectrodes, doping using ferromagnetic metals (Cobalt and Nickel) was done to create mixed-metal MOFs. Mixed-Metal MOFs were synthesised by soaking the Zn-MOF with the appropriate salts in methanol over a period of 24hours. Characterisation was carried out using XRD to assess the change crystallinity, MM-MOFs are known to be more crystalline than their parent MOFs. ICP-OES was used to measure the amount of Co^{2+} as well as Ni^{2+} incorporated in the mixed-metal, metal organic framework. More Co^{2+} salts were incorporated in the same period compared to the Ni^{2+} ions. A measure of the photocatalytic activity of the MM-MOFs was carried out both MM-MOFs show high absorbances in a wide range of wavelengths from the ultra violet to near infrared region. Their photocatalytic activity was confirmed during photo response measurements in which the light was switched ON/OFF at constant intervals while running a Linear Sweep Voltammetry. When light was switched on current densities showed a huge spike, however, when the light was switched off, they current densities decayed to zero and this confirmed the photocatalytic activity of the MM-MOF based photoelectrodes.

In the OER measurements of the mixed-metal MOFs reduction in the OER voltage, was observed in both MM-MOFs, with Zn-MOF +Co showing +1.42V, Zn-MOF +Ni showing +1.72 vs Zn-MOF (+1.77V).

To further investigate this observation chronoamperometry measurement were carried out.

During chronoamperometry measurements, swift and reproducible photocurrent densities were produced for both the MM-MOF based photoelectrodes. Both forms of mixed metal MOFs exhibited increased current densities compared to the as synthesised MOFs. In open circuit potential measurements, the OCP curves were obtained, indicating that an equilibrium had been reached between the photoelectrodes and the electrolyte. In Mott Schottky measurements, the photoelectrodes exhibited two flat band potentials, one with a positive slope (n-type) and another with a negative slope (p-type). The presence of the two flat band potentials can also be used to confirm the successful inclusion of the cobalt and nickel salts in the MOF structure as the cobalt and nickel salts are known to form intrinsically p-type semiconductors.

A tandem cell was also fabricated by incorporating α-Fe_2O_3 nanoparticles on top of the TiO_2 film as well as the MOF paste. Tandem devices are often used to harness all the regions of the ultra-violet as well as visible regions of the electromagnetic spectrum. The α-Fe_2O_3 nanoparticles were synthesised by reduction using sodium borohydride. The tandem device was fabricated by depositing first TiO_2 nanoparticles using Electrophoretic Deposition (EPD), onto cleaned FTO slides, annealing them then depositing the α-Fe_2O_3 nanoparticles using

EPD and finally depositing a 20µL volume of a 1mmol MOF solution. An assessment of the photocatalytic activity of the α-Fe_2O_3 nanoparticles was carried out and a band gap energy of *circa* +1.0V was attained and the small band gap energy can be attributed to the quantum confinement experienced in nanomaterials.

In water splitting measurements, the cyclic voltammetry showed that the tandem cell produced greater current densities, compared to the pristine Zn-MOF, while the LSV showed an improved onset potential of +1.6V vs +1.77V shown by the pristine Zn-MOF. In chronoamperometry the tandem cell showed lower current density than expected, showing that the spin filtering is not always linear. Mott Schottky measurements conducted both under illumination and under darkness produced the same value for the flat band potential, indicating that deposited α-Fe_2O_3 nanoparticles as well as the MOF paste did not affect the electronic properties of the TiO_2 deposited on the FTO slide. Tafel plots were used to analyse the overpotential and the Tafel slope, which is the overpotential, was found to be 20.75mV/dec for the tandem device vs 57.05mV/dec for the pristine Zn-MOF again highlighting the effect of ferromagnetic materials in the reduction of overpotential.

7.5 CONCLUDING REMARKS AND FUTURE WORK

The objectives of the work outlined in this thesis as presented in section 1.5 were successfully accomplished. Chiral doped metal-organic frameworks based on Zn(II) and Fe(III) metal ions were prepared under solvothermal (hydrothermal) conditions using both N,N'-bis(pyridin-4-ylmethyl)cyclohexane-1,4-diamine (bpcda) and terephthalic acid (H2BDC or bdc) for the zinc-based MOF while the iron-based MOF was synthesised using terephthalic acid. Both types of MOFs were doped using R (-) and S (+) Camphor Sulphonic Acid as well as L Cysteine. In water splitting measurements, the as-synthesised MOFs, exhibited lower photocurrent densities in photo response measurements as well as transient photo measurements whereas all the chiral photoelectrodes had improved properties. All the chiral photoelectrochemical cells did not have hydrogen peroxide an indication that chiral photoelectrodes reduce the formation of hydrogen peroxide, through selectively spin filtering the produced electrons. These results demonstrate that chiral photoelectrodes improve the performance of the PEC.

Incorporation of the ferromagnetic elements, such as Cobalt, Nickel and Iron Oxide nanoparticles also showed that ferromagnetic materials also have the ability to filter the spin of the electrons and can be used in the photoelectrochemical cells, especially for the reduction of the OER potential, in the production of hydrogen.

Future work should focus on improving the work life of the photoelectrodes, optimising the use of ferromagnetic based photoelectrodes as well as expanding the research field by designing and fabricating chiral photoelectrodes for use in other multiple electron reactions.

7.6 REFERENCES

1) Espegren, K., Damman, S., Pisciella, P., Graabak, I., & Tomasgard, A. (2021). The role of hydrogen in the transition from a petroleum economy to a low-carbon society. *International Journal of Hydrogen Energy*, *46*(45), 23125–23138. https://doi.org/10.1016/j.ijhydene.2021.04.143
2) Feng, T., Chen, W., Xue, J., Cao, F., Chen, Z., Ye, J., Xiao, C., & Lu, H. (2023). Spin Polarization of Chiral Amorphous Fe-Ni Electrocatalysts Enabling Efficient Electrochemical Oxygen Evolution. *Advanced Functional Materials*, *33*(27), 1-10. https://doi.org/10.1002/adfm.202215051
3) Gazzotti, M., Arnaboldi, S., Grecchi, S., Giovanardi, R., Cannio, M., Pasquali, L., Giacomino, A., Abollino, O., & Fontanesi, C. (2018). Spin-dependent electrochemistry: Enantio-selectivity driven by chiral-induced spin selectivity effect. *Electrochimica Acta*, *286*, 271–278. https://doi.org/10.1016/j.electacta.2018.08.023
4) Gazzotti, M., Stefani, A., Bonechi, M., Giurlani, W., Innocenti, M., & Fontanesi, C. (2020). Influence of Chiral Compounds on the Oxygen Evolution Reaction (OER) in the Water Splitting Process. *Molecules*, *25*(17). https://doi.org/10.3390/molecules25173988
5) Ghosh, K. B., Zhang, W., Tassinari, F., Mastai, Y., Lidor-Shalev, O., Naaman, R., Möllers, P., Nürenberg, D., Zacharias, H., Wei, J., Wierzbinski, E., & Waldeck, D. H. (2019). Controlling Chemical Selectivity in Electrocatalysis with Chiral CuO-Coated Electrodes. *Journal of Physical Chemistry C*, *123*(5), 3024–3031. https://doi.org/10.1021/acs.jpcc.8b12027
6) Ghosh, S., Bloom, B. P., Lu, Y., Lamont, D., & Waldeck, D. H. (2020). Increasing the Efficiency of Water Splitting through Spin Polarization Using Cobalt Oxide Thin Film Catalysts. *Journal of Physical Chemistry C*, *124*(41), 22610–22618. https://doi.org/10.1021/acs.jpcc.0c07372
7) Holechek, J. L., Geli, H. M. E., Sawalhah, M. N., & Valdez, R. (2022). A Global Assessment: Can Renewable Energy Replace Fossil Fuels by 2050? *Sustainability (Switzerland)*, *14*(8) 1-22. https://doi.org/10.3390/su14084792
8) Huang, Y., Liu, J., Deng, Y., Qian, Y., Jia, X., Ma, M., Yang, C., Liu, K., Wang, Z., Qu, S., & Wang, Z. (2020). The application of perovskite materials in solar water splitting. In *Journal of Semiconductors* (Vol. 41, Issue 1). IOP Publishing Ltd. https://doi.org/10.1088/1674-4926/41/1/011701
9) Khalid, N. R., Ahmed, E., Tahir, M. B., Iqbal, T., Khalid, S., & Ahmed, W. (2021). Metal oxide semiconductors for photoelectrochemical water splitting. In *Emerging Nanotechnologies for Renewable Energy* (pp. 287–309). Elsevier. https://doi.org/10.1016/B978-0-12-821346-9.00004-3

10) Mtangi, W., Kiran, V., Fontanesi, C., & Naaman, R. (2015). Role of the Electron Spin Polarization in Water Splitting. *Journal of Physical Chemistry Letters*, *6*(24), 4916–4922. https://doi.org/10.1021/acs.jpclett.5b02419
11) Mtangi, W., Tassinari, F., Vankayala, K., Vargas Jentzsch, A., Adelizzi, B., Palmans, A. R. A., Fontanesi, C., Meijer, E. W., & Naaman, R. (2017). Control of Electrons' Spin Eliminates Hydrogen Peroxide Formation during Water Splitting. *Journal of the American Chemical Society*, *139*(7), 2794–2798. https://doi.org/10.1021/jacs.6b12971
12) Naaman, R., & Waldeck, D. H. (2012). Chiral-induced spin selectivity effect. *Journal of Physical Chemistry Letters*, *3*(16), 2178–2187. https://doi.org/10.1021/jz300793y
13) Staffell, I., Scamman, D., Velazquez Abad, A., Balcombe, P., Dodds, P. E., Ekins, P., Shah, N., & Ward, K. R. (2019). The role of hydrogen and fuel cells in the global energy system. In *Energy and Environmental Science* (Vol. 12, Issue 2, pp. 463–491). Royal Society of Chemistry. https://doi.org/10.1039/c8ee01157e
14) Vadakkayil, A., Clever, C., Kunzler, K. N., Tan, S., Bloom, B. P., & Waldeck, D. H. (2023). Chiral electrocatalysts eclipse water splitting metrics through spin control. *Nature Communications*, *14*(1). https://doi.org/10.1038/s41467-023-36703-w
15) Zhang, W., Banerjee-Ghosh, K., Tassinari, F., & Naaman, R. (2018). Enhanced Electrochemical Water Splitting with Chiral Molecule-Coated Fe3O4 Nanoparticles. *ACS Energy Letters*, *3*(10), 2308–2313. https://doi.org/10.1021/acsenergylett.8b01454
16) Zhang, W., Wang, W., Hu, Y., Guan, H., & Hao, L. (2021). Take a cue from nature: Promoting electrocatalytic watersplitting with a helping hand of hemoglobin. *International Journal of Hydrogen Energy*, *46*(5), 3504–3509. https://doi.org/10.1016/j.ijhydene.2020.10.154

8 APPENDICES

APPENDIX A NMR SPECTRA FOR BPCDA

Proton NMR for the synthesised linker (bpcda)

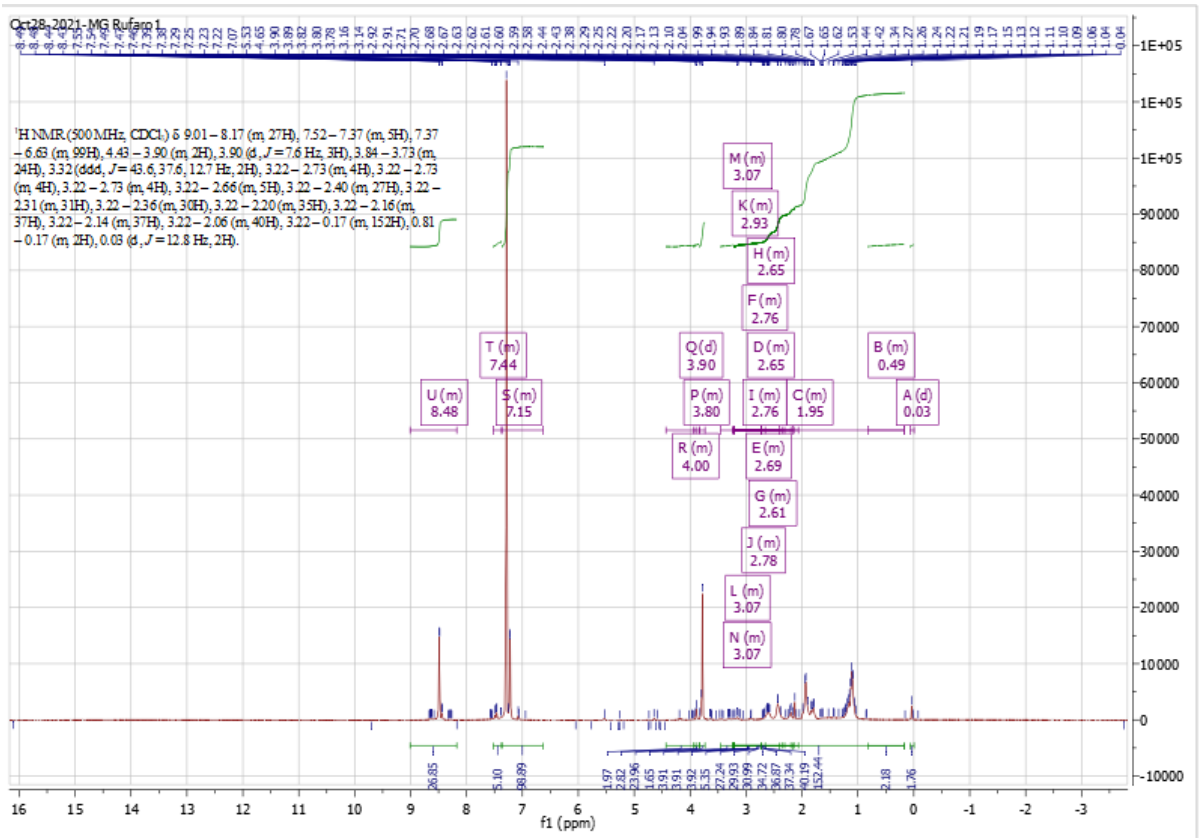

Figure 8.1: Proton NMR for the synthesized linker (bpcda)

Carbon-13 NMR for bpcda

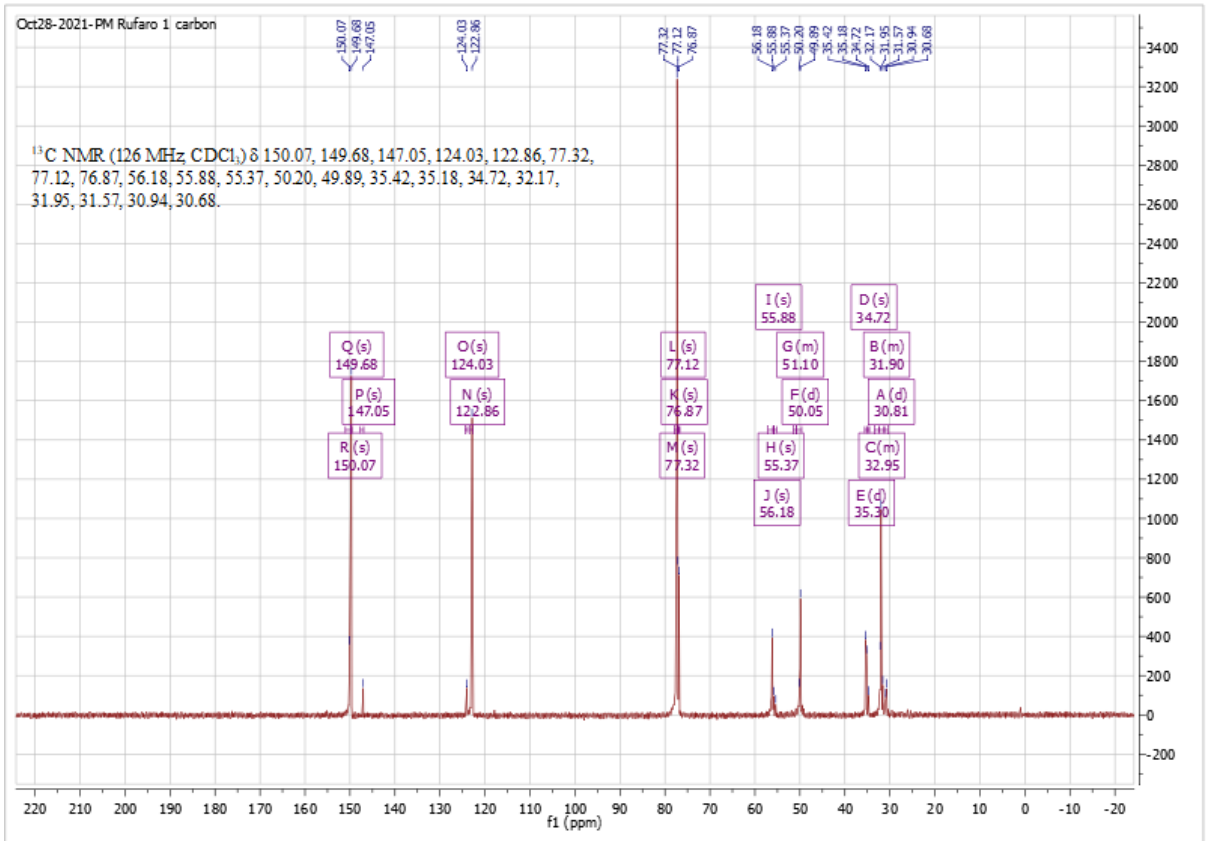

Figure 8.2: ^{13}C NMR for the synthesised linker (bpcda)

ChemNMR ^{1}H Estimation

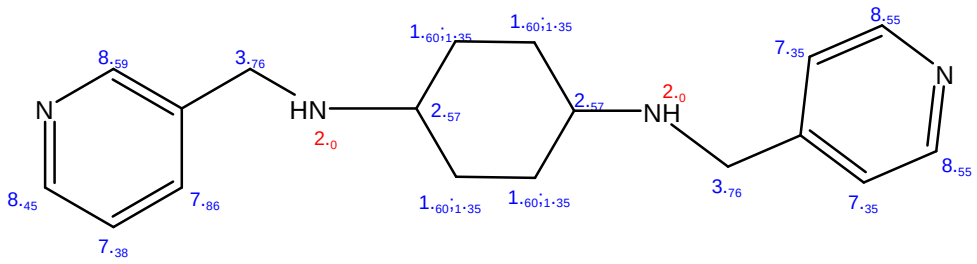

Estimation quality is indicated by color: good, medium, rough

Protocol of the H-1 NMR Prediction:

Node	Shift	Base + Inc.	Comment (ppm rel. to TMS)
NH	2.0	2.00	amine
NH	2.0	2.00	amine
CH	8.55	8.59	4-pyridine, in DMSO
		0.01	1 -C-N
		-0.05	general corrections
CH	8.45	8.59	3-pyridine, in DMSO
		0.00	1 -C-N
		-0.14	general corrections
CH	8.59	8.59	3-pyridine, in DMSO
		0.16	1 -C-N
		-0.16	general corrections
CH	8.55	8.59	4-pyridine, in DMSO
		0.01	1 -C-N
		-0.05	general corrections
CH	2.57	1.44	cyclohexane
		1.13	1 alpha -N from methine
CH	2.57	1.44	cyclohexane
		1.13	1 alpha -N from methine
CH	7.35	7.38	4-pyridine, in DMSO
		0.03	1 -C-N
		-0.06	general corrections
CH	7.35	7.38	4-pyridine, in DMSO
		0.03	1 -C-N
		-0.06	general corrections
CH	7.38	7.38	3-pyridine, in DMSO
		0.04	1 -C-N
		-0.04	general corrections
CH	7.86	7.75	3-pyridine, in DMSO
		0.13	1 -C-N
		-0.02	general corrections
CH2	1.60;1.345000	1.44	cyclohexane
		0.08	1 beta -N-C from methylene
		-0.05	general corrections
CH2	1.60;1.345000	1.44	cyclohexane
		0.08	1 beta -N-C from methylene
		-0.05	general corrections
CH2	1.60;1.345000	1.44	cyclohexane
		0.08	1 beta -N-C from methylene
		-0.05	general corrections
CH2	1.60;1.345000	1.44	cyclohexane
		0.08	1 beta -N-C from methylene
		-0.05	general corrections
CH2	3.76	1.37	methylene
		1.22	1 alpha -C*R
		1.22	1 alpha -N-C
		-0.05	general corrections
CH2	3.76	1.37	methylene
		1.22	1 alpha -C*R
		1.22	1 alpha -N-C
		-0.05	general corrections

ChemNMR ^{13}C Estimation

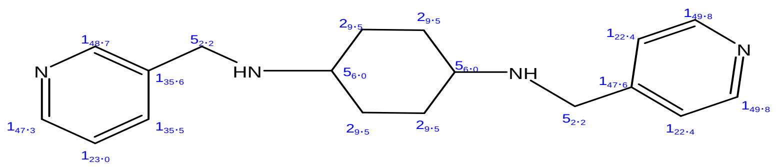

Estimation quality is indicated by color: good, medium, rough

```
Protocol of the C-13 NMR Prediction:

Node     Shift     Base + Inc.    Comment (ppm rel. to TMS)

CH   149.8          149.8      4-pyridine
                      0.5         1 -C
                     -0.5         general corrections
CH   147.3          149.8      3-pyridine
                     -2.3         1 -C
                     -0.2         general corrections
CH   148.7          149.8      3-pyridine
                      1.3         1 -C
                     -2.4         general corrections
CH   149.8          149.8      4-pyridine
                      0.5         1 -C
                     -0.5         general corrections
CH   56.0            -7.4      cyclohexane
                     18.2         2 alpha -C from aliphatic
                     28.3         1 alpha -N from aliphatic
                     28.2         3 beta -C from aliphatic
                     -2.6         1 gamma -1:C*R*R*R*R*R*1 from aliphatic
                     -2.5         1 gamma -C from aliphatic
                      0.0         1 delta -N from aliphatic
                     -6.2         general corrections
CH   56.0            -7.4      cyclohexane
                     18.2         2 alpha -C from aliphatic
                     28.3         1 alpha -N from aliphatic
                     28.2         3 beta -C from aliphatic
                     -2.6         1 gamma -1:C*R*R*R*R*R*1 from aliphatic
                     -2.5         1 gamma -C from aliphatic
                      0.0         1 delta -N from aliphatic
                     -6.2         general corrections
C    135.6          123.6      3-pyridine
                      9.0         1 -C
                      3.0         general corrections
C    147.6          135.7      4-pyridine
                     10.8         1 -C
                      1.1         general corrections
CH   122.4          123.6      4-pyridine
                      0.8         1 -C
                     -2.0         general corrections
CH   122.4          123.6      4-pyridine
                      0.8         1 -C
                     -2.0         general corrections
CH   123.0          123.6      3-pyridine
                     -0.8         1 -C
                      0.2         general corrections
CH   135.5          135.7      3-pyridine
                      0.2         1 -C
                     -0.4         general corrections
CH2 29.5             -7.4      cyclohexane
                     18.2         2 alpha -C from aliphatic
                     18.8         2 beta -C from aliphatic
                     11.3         1 beta -N from aliphatic
                     -5.0         2 gamma -C from aliphatic
                     -5.1         1 gamma -N from aliphatic
                      0.3         1 delta -1:C*R*R*R*R*R*1 from aliphatic
                      0.3         1 delta -C from aliphatic
                     -1.9         general corrections
CH2 29.5             -7.4      cyclohexane
                     18.2         2 alpha -C from aliphatic
                     18.8         2 beta -C from aliphatic
                     11.3         1 beta -N from aliphatic
                     -5.0         2 gamma -C from aliphatic
                     -5.1         1 gamma -N from aliphatic
                      0.3         1 delta -1:C*R*R*R*R*R*1 from aliphatic
                      0.3         1 delta -C from aliphatic
                     -1.9         general corrections
CH2 29.5             -7.4      cyclohexane
                     18.2         2 alpha -C from aliphatic
                     18.8         2 beta -C from aliphatic
                     11.3         1 beta -N from aliphatic
                     -5.0         2 gamma -C from aliphatic
                     -5.1         1 gamma -N from aliphatic
                      0.3         1 delta -1:C*R*R*R*R*R*1 from aliphatic
                      0.3         1 delta -C from aliphatic
                     -1.9         general corrections
CH2 29.5             -7.4      cyclohexane
                     18.2         2 alpha -C from aliphatic
                     18.8         2 beta -C from aliphatic
                     11.3         1 beta -N from aliphatic
                     -5.0         2 gamma -C from aliphatic
                     -5.1         1 gamma -N from aliphatic
                      0.3         1 delta -1:C*R*R*R*R*R*1 from aliphatic
                      0.3         1 delta -C from aliphatic
                     -1.9         general corrections
CH2 52.2             -2.3      aliphatic
                     24.3         1 alpha -1:C*R*R*R*R*R*1
                     28.3         1 alpha -N
                      9.4         1 beta -C
                     -5.0         2 gamma -C
                      0.6         2 delta -C
                     -3.1         general corrections
CH2 52.2             -2.3      aliphatic
                     24.3         1 alpha -1:C*R*R*R*R*R*1
                     28.3         1 alpha -N
                      9.4         1 beta -C
                     -5.0         2 gamma -C
                      0.6         2 delta -C
                     -3.1         general corrections
```

CVs Zn-MOF derivatives

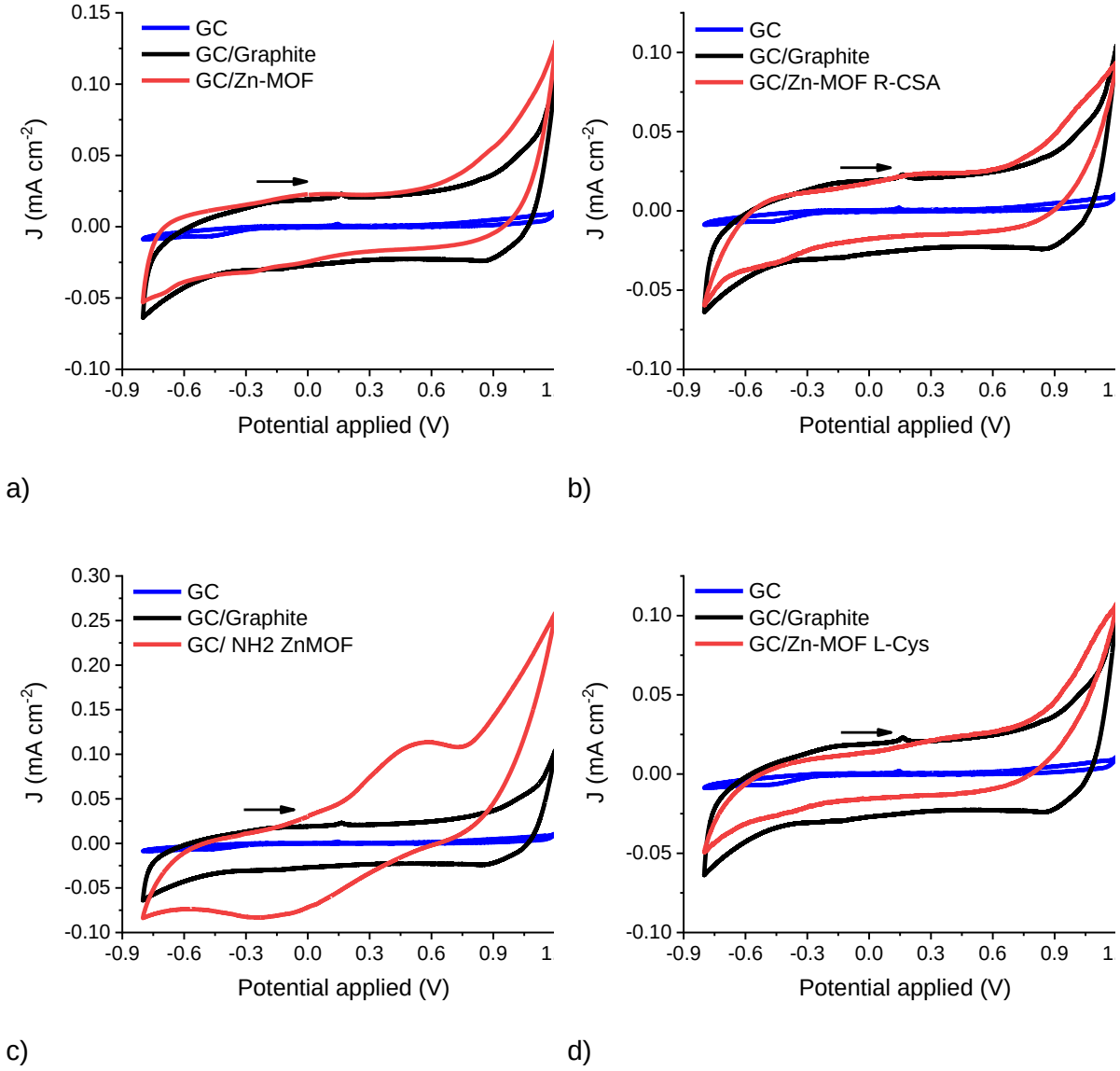

Figure 8.3: Cyclic Voltammetry curves in aqueous 0.1 M Potassium Chloride (KCl) the working electrodes, a) GC/Zn-MOF, b) Zn-MOF R-CSA, c) GC/ZnMOF-NH_2, d) Zn-MOF L vs $Ag/AgCl/KCl_{sat}$ (Reference Electrode) at a scan rate 0.01V s^{-1}.

APPENDIX C HYDROGEN PEROXIDE CALIBRATION CURVE

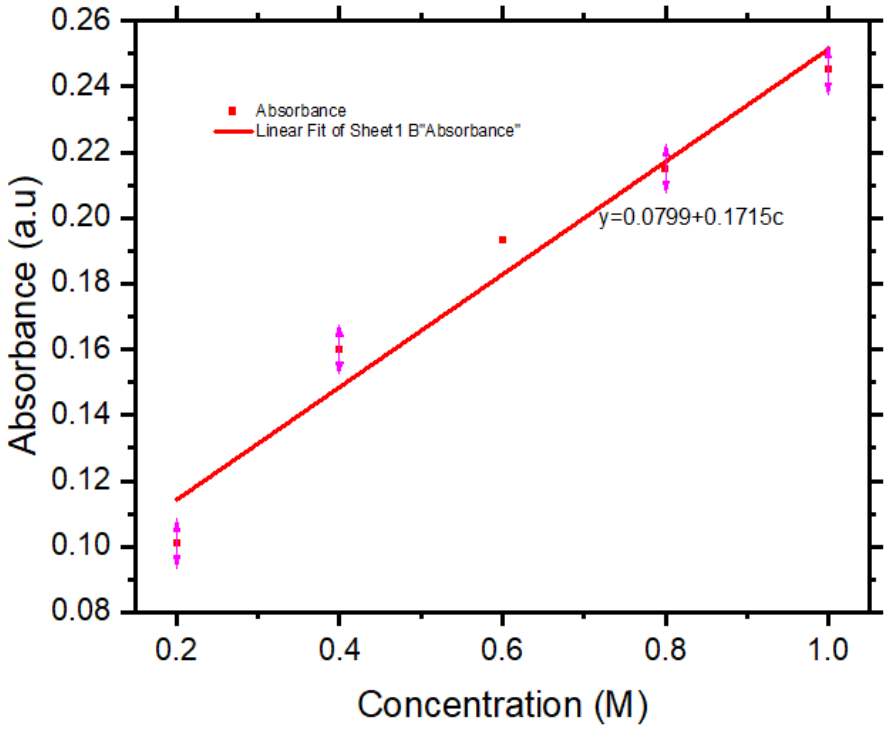

Figure 8.4: Hydrogen Peroxide Calibration Curve

APPENDIX D CALCULATED PXRD PATTERN FROM MATCH!*

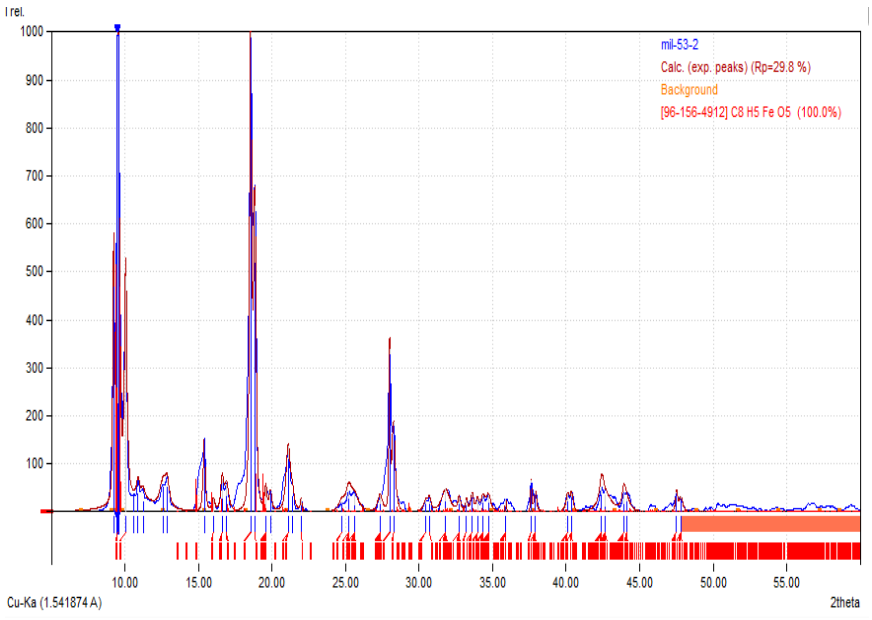

Figure 8.5: Calculated MIL 53 PXRD pattern using Match!*

APPENDIX E EVALUATION OF MIL 53 PHOTOCATALYTIC PERFORMANCE

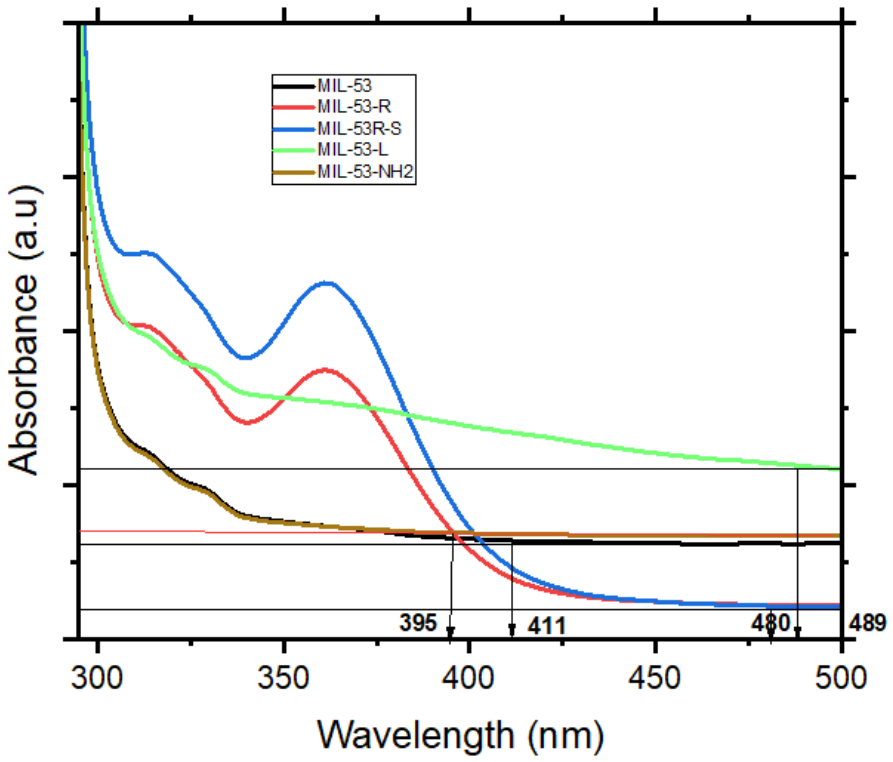

Figure 8.6: Evaluation of photocatalytic activity of MIL 53 and its derivatives

CVs MIL53 derivatives

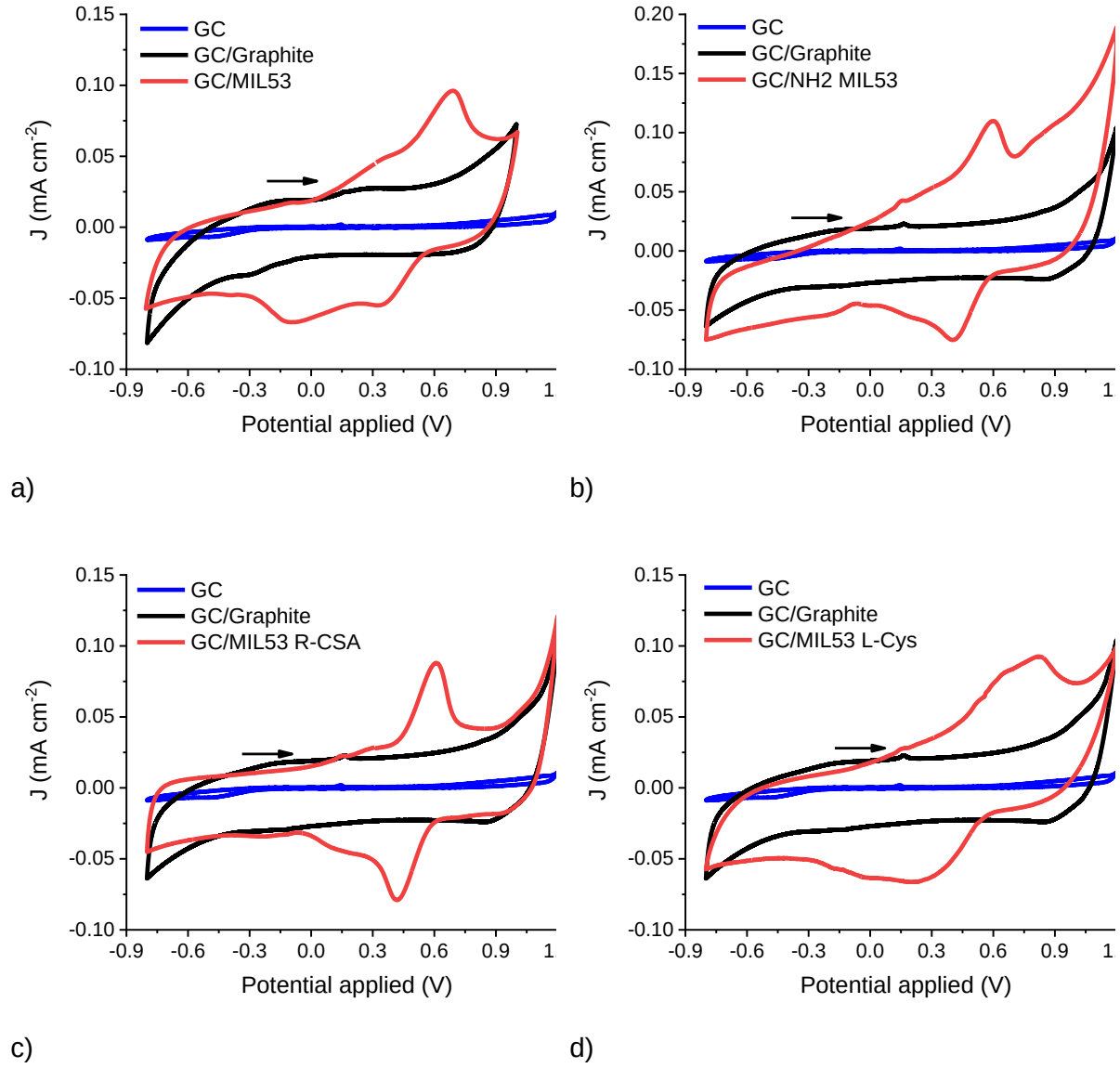

Figure 8.7: Cyclic Voltammetry curves in aqueous 0.1 M Potassium Chloride (KCl) the working electrodes, of a) GC/MIL53, b) GC/NH2 MIL53, c) GC/MIL53 R-CSA, GC/MIL53 L-Cys.

APPENDIX F EXTENDED OPTICAL ACTIVITY

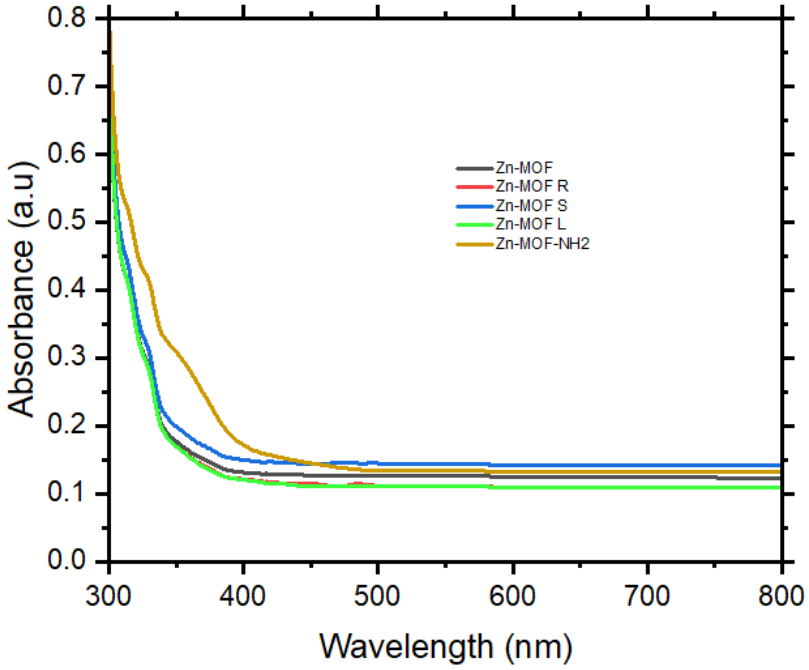

Figure 8.8: Uv-vis spectra of Zn-MOF and its derivatives

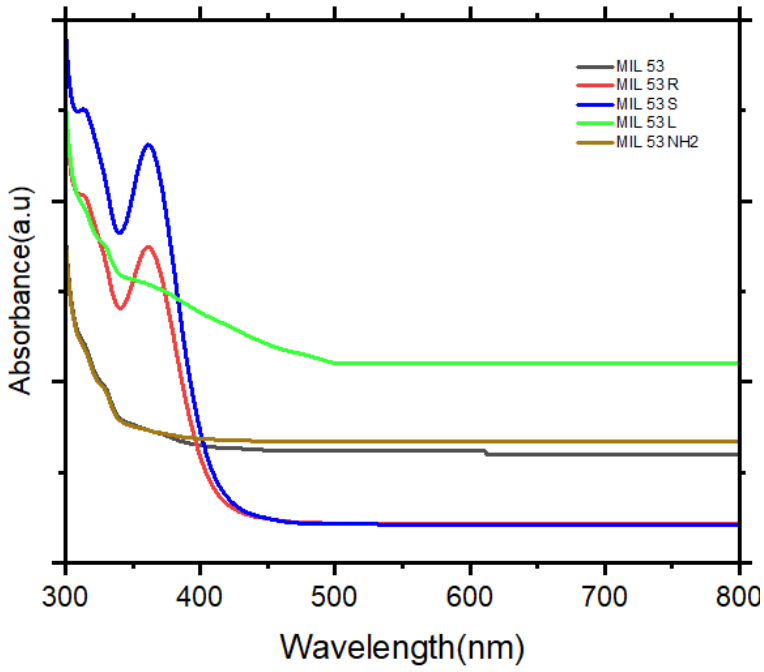

Figure 8.9: Uv-Vis Spectra of MIL 53 and its derivatives

Similarity Report

Similarity Report

PAPER NAME
Rufaro Kawondera Corrected Thesis.docx

AUTHOR
Rufaro Kawondera

WORD COUNT
60081 Words

CHARACTER COUNT
338192 Characters

PAGE COUNT
261 Pages

FILE SIZE
13.7MB

SUBMISSION DATE
Oct 22, 2024 3:17 PM GMT+2

REPORT DATE
Oct 22, 2024 3:21 PM GMT+2

17% Overall Similarity

The combined total of all matches, including overlapping sources, for each database.

- 10% Internet database
- 13% Publications database
- Crossref database
- Crossref Posted Content database
- 5% Submitted Works database

Excluded from Similarity Report

- Bibliographic material
- Small Matches (Less then 10 words)

Summary